2007

Characterization of inorganic mesoporous materials, nanoparticles and organometallic complexes by multinuclear solid-state NMR spectroscopy

Andy Y. H. Lo
University of Windsor

Recommended Citation
Lo, Andy Y. H., "Characterization of inorganic mesoporous materials, nanoparticles and organometallic complexes by multinuclear solid-state NMR spectroscopy" (2007). *Electronic Theses and Dissertations*. 4630.
https://scholar.uwindsor.ca/etd/4630

Characterization of Inorganic Mesoporous Materials, Nanoparticles and Organometallic Complexes by Multinuclear Solid-State NMR Spectroscopy

By

Andy Y. H. Lo

A Dissertation Submitted to the
Department of Chemistry & Biochemistry
in Partial Fulfillment of the Requirements for the
Doctor of Philosophy Degree
in Chemistry at the
University of Windsor

Windsor, Ontario, Canada

2007

Library and
Archives Canada

Published Heritage
Branch

395 Wellington Street
Ottawa ON K1A 0N4
Canada

Bibliothèque et
Archives Canada

Direction du
Patrimoine de l'édition

395, rue Wellington
Ottawa ON K1A 0N4
Canada

Your file Votre référence
ISBN: 978-0-494-35101-7
Our file Notre référence
ISBN: 978-0-494-35101-7

NOTICE:
The author has granted a non-exclusive license allowing Library and Archives Canada to reproduce, publish, archive, preserve, conserve, communicate to the public by telecommunication or on the Internet, loan, distribute and sell theses worldwide, for commercial or non-commercial purposes, in microform, paper, electronic and/or any other formats.

The author retains copyright ownership and moral rights in this thesis. Neither the thesis nor substantial extracts from it may be printed or otherwise reproduced without the author's permission.

AVIS:
L'auteur a accordé une licence non exclusive permettant à la Bibliothèque et Archives Canada de reproduire, publier, archiver, sauvegarder, conserver, transmettre au public par télécommunication ou par l'Internet, prêter, distribuer et vendre des thèses partout dans le monde, à des fins commerciales ou autres, sur support microforme, papier, électronique et/ou autres formats.

L'auteur conserve la propriété du droit d'auteur et des droits moraux qui protège cette thèse. Ni la thèse ni des extraits substantiels de celle-ci ne doivent être imprimés ou autrement reproduits sans son autorisation.

In compliance with the Canadian Privacy Act some supporting forms may have been removed from this thesis.

While these forms may be included in the document page count, their removal does not represent any loss of content from the thesis.

Conformément à la loi canadienne sur la protection de la vie privée, quelques formulaires secondaires ont été enlevés de cette thèse.

Bien que ces formulaires aient inclus dans la pagination, il n'y aura aucun contenu manquant.

Canada

Reproduced with permission of the copyright owner. Further reproduction prohibited without permission.

Abstract

This thesis is to demonstrate the use of solid-state NMR (SSNMR) spectroscopy, along with complementary techniques such as ab initio calculations and X-ray diffraction (XRD) experiments, for the characterization of various systems at the molecular level, including vanadates, niobium metallocenes, mesoporous transition-metal oxides (M-TMS1) and composite materials, lanthanide (Ln)-doped LaF_3 nanoparticles (NPs), and mesoporous aerogels and xerogels made of CdSe NPs.

Theoretical ^{51}V electric field gradient (EFG) tensor components and orientations in a series of pyrovanadates and metavanadates are studied using Restricted Hartree-Fock and hybrid density functional theory calculations. Effects of basis set, cluster size and termination, and long-range electrostatic interactions were considered.

^{93}Nb and ^{13}C SSNMR experiments, along with other complementary techniques, are applied for the characterization of structures and dynamics in various half-sandwich niobium(I) and (V) metallocenes. It is demonstrated that ^{93}Nb NMR parameters are sensitive to changes in temperature, Cp′ ring substitution and oxidation state. Solvation of Nb(V) metallocenes can also be easily detected via SSNMR experiments.

Multinuclear SSNMR spectroscopy is used to investigate M-TMS1 loaded with various guest materials. ^{15}N SSNMR experiments are used to characterize the nitrogen-containing species in Ti-TMS1/bis(toluene)Ti composites. Structure and dynamics of bis(benzene)Cr(0) and Cr(I) complexes, in pure form and loaded onto V-doped Nb-TMS1/bis(benzene)Cr(0) composites, are investigated by ^{2}H SSNMR spectroscopy. ^{23}Na and ^{7}Li SSNMR experiments are utilized to characterize the channel and framework Na^+

and Li^+ ions in reduced Ti-TMS1/Na- and Li-naphthalenide composites. Redox reactions occurring in the Ta-TMS1/Rb-naphthalenide and/or Rb_3C_{60} composites are studied by ^{87}Rb and ^{13}C SSNMR spectroscopy.

^{139}La, ^{19}F and ^{45}Sc SSNMR spectroscopy is applied to characterize the LaF_3 NP cores and dopant positions in the NPs. ^{1}H and ^{31}P SSNMR spectra aid in probing the nature of the capping ligands. In the aerogels and xerogels, ^{111}Cd and ^{77}Se SSNMR experiments are used to characterize the CdSe NPs. Mobile surface ligands are examined with ^{1}H, ^{13}C and ^{19}F SSNMR spectroscopy. Cross-polarization experiments are used for both classes of NPs to probe the connectivity and interaction between surface ligands and NPs.

Co-Authorship

For the niobium metallocene complexes presented in Chapter 3, all compounds were synthesized by Professor Thomas Bitterwolf at the University of Idaho, with the exception of $CpNbCl_4$•THF compound which was synthesized at the University of Windsor under the supervision of Professor Charles MacDonald. The crystal structure refinement was performed by Professor MacDonald as well.

All transition-metal oxide mesoporous composites (Chapters 4) were synthesized by Professor David Antonelli and his students (University of Windsor). Dr. Trudeau (Hydro-Quebec Research Institute) and the research group of Professor Antonelli are responsible for all other characterization methods applied to these materials.

The syntheses of all LaF_3 nanoparticles (Chapter 5) were conducted by the research group of Professor Frank van Veggel (University of Victoria).

Professor Stephanie Brock and her research group (Wayne State University) are responsible for the preparation of CdSe aerogel and xerogel samples (Chapter 6).

Dedication to

my *Family* and Carol *(Bo Bo)* Kong

Acknowledgements

I must first thank Professor Robert W. Schurko, who allowed me to work in his lab during my many years (seven? Longer than I can remember) of undergraduate and graduate studies. It was Rob who introduced solid-state NMR spectroscopy to me, and I enjoyed every minute working with the spectrometer. Rob has also been immeasurably patient with me when explaining NMR concepts as well as correcting my manuscripts. He has provided me with much guidance, from things as simple as basic English sentence structure to professional scientific writing, during my studies. He is not only my supervisor but also an excellent English teacher.

I thank Professors Charles L. B. MacDonald and David M. Antonelli for being my internal dissertation examiners. I thank Professor Karl T. Mueller and Lisa A. Porter for being my external university and external departmental readers, respectively.

There is no doubt that I have received much help from the former and the current group members including Dr. Ivan Hung, Mathew Willans, Cory Widdifield, Josh Mutus, Joel Tang, Aaron Rossini, Hiyam Hamaed, Andre Sutrisno, Jenna Pawlowski and Bryan Lucier. Joel, Aaron and Hiyam are acknowledged from proofreading my Ph.D. thesis. Although it is sometimes too noisy in the office with this size of research group, we have had very good communication to each other. Especially during the lunch-style group meetings, which are unforgettable. I enjoyed very much listening to others explaining interesting NMR experiments, while chewing a delicious shrimp dumpling at the same time.

Department staff such as Mr. Mike Fuerth (NMR spectrometer manager) and Mrs.

Marlene Bezaire (graduate secretary) are also acknowledged for their help in conducting solution-state NMR experiments and all of the complicated administrative work, respectively.

Professor Thomas E. Bitterwolf (University of Idaho) is thanked for his kind supply of all of the niobium organometallic samples. I also thank Professors Charles L. B. MacDonald and Samuel Johnson for their assistance with the syntheses and sublimation experiment for the niobocene project, respectively.

I thank Professor Lyndon Emsley (ENS-Lyon) for helpful discussions for the work involving CdSe aerogel and xerogel.

I am grateful to Dr. Victor Terskikh (NRC), who showed me the state-of-art of the 900 MHz high field spectrometer. His assistance for the acquisition of high field ^{45}Sc NMR spectra is also acknowledged.

The Centre for Catalysis and Materials Research (CCMR) at the University of Windsor, Imperial Oil, NSERC CRD and Ontario Graduate Scholarship (OGS) program are acknowledged for additional funding.

Most importantly, I thank my parents for all financial support. Mrs. Lo especially, who does all of the cooking and house work for me, so that I can stay 16 hours a day in the office with no worries.

Finally, I thank Carol for all her love and support. I also thank her for not leaving me during the time I was writing the thesis.

Statement of Originality

I certify that this thesis, and the research to which it refers, are the product of my own work. Ideas or quotations (published or not) from the work of other people are fully acknowledged and are properly cited using standard referencing practices of the discipline. I acknowledge the helpful guidance and support of my supervisor, Professor Robert W. Schurko.

This thesis is based on the following publications:

Chapter 2:	Andy Y. H. Lo and Robert W. Schurko. A Theoretical Study of ^{51}V Electric Field Gradient Tensors in Pyrovanadates and Metavanadates. *Solid State Nucl. Magn. Reson. (submitted)*, February 2007.
Chapter 3:	Andy Y. H. Lo, Thomas E. Bitterwolf, Charles L. B. MacDonald, and Robert W. Schurko. Solid-State ^{93}Nb and ^{13}C NMR Investigations of Half-Sandwich Niobium (I) and Niobium (V) Cyclopentadienyl Complexes. *J. Phys. Chem. A* **2005**, *109*, 7073–7087; DOI: 10. 1021/jp0521499.
Chapter 4:	Melissa Vettraino, Michel Trudeau, Andy Y. H. Lo, Robert W. Schurko, and David Antonelli. Room-Temperature Ammonia Formation from Dinitrogen on a Reduced Mesoporous Titanium Oxide Surface with Metallic Properties. *J. Am. Chem. Soc.* **2002**, *124*, 9567–9573; DOI: 10.1021/ja020313p. Xun He, Andy Y. H. Lo, Michel Trudeau, Robert W. Schurko, and David Antonelli. Compositional and ^{2}H NMR Studies of Bis(benzene)chromium Composites of Mesoporous Vanadium-Niobium Mixed Oxides. *Inorg. Chem.* **2003**, *42*, 335–347; DOI: 10.1021/ic020559v. Andy Y. H. Lo, Robert W. Schurko, Melissa Vettraino, Boris O. Skadtchenko, Michel Trudeau, and David M. Antonelli. Solid-State ^{23}Na and ^{7}Li NMR Investigations of Sodium- and Lithium-Reduced Mesoporous Titanium Oxides. *Inorg. Chem.* **2006**, *45*, 1828–1838; DOI: 10.1021/ic051654h.

Boris O. Skadtchenko, Michel Trudeau, Andy Y. H. Lo, Robert W. Schurko, David M. Antonelli. Electronic Properties and Solid-State ^{87}Rb and ^{13}C NMR Studies of Mesoporous Tantalum Oxide Rubidium Fulleride Composites. *Chem. Mater.* **2005**, *17*, 1467–1478; DOI: 10.1021/cm048174t.

Chapter 5: Andy Y. H. Lo, Vasanthakumaran Sudarsan, Sri Sivakumar, Frank van Veggel, and Robert W. Schurko. Multinuclear Solid-State NMR Spectroscopy of Doped Lanthanum Fluoride Nanoparticles. *J. Am. Chem. Soc.* **2007**, *129*, 4987–4700, DOI: 10.1021/ja068604b.

Table of Contents

List of Tables

List of Figures

List of Abbreviations

B3LYP	Becke's three parameter exchange functional and the correlation functional of Lee, Yang and Parr
CT	central transition
CS	chemical shielding, chemical shift
CSA	chemical shielding anisotropy
CP	cross polarization
Cp	cyclopentadienyl ligand, C_5H_5
DFT	density functional theory
ECMO	embedded cluster molecular orbital
EFG	electric field gradient
EPR	electron spin resonance
Et	ethyl group, CH_3CH_2–
FID	free induction decay
GIAO	gauge including atomic orbital
Ln	lanthanide
MAS	magic-angle spinning
Me	methyl group, CH_3–
MO	molecular orbital
MQMAS	multiple quantum magic angle spinning
C_n	n-fold rotation
NP	nanoparticle

NMR	nuclear magnetic resonance
o.d.	outer diameter
Cp*	pentamethylcyclopentadienyl ligand, $C_5(CH_3)_5$
PAS	principal axis system
Ph	phenyl group, C_6H_5–
ppm	parts per million
QCPMG	Quadrupolar Carr-Purcell Meiboom-Gill NMR pulse sequence
rf	radio frequency
RHF	restricted Hartree-Fock
S/N	signal-to-noise ratio
ST	satellite transition
STMAS	satellite-transition magic-angle spinning
SATRAS	satellite-transition spectroscopy
SCF	self consistent field
SQ	single quantum
SR	spin rotation
THF	tetrahydrofuran
TMS	tetramethyl silane
VACP	variable-amplitude cross polarization
VT	variable temperature
XRD	X-ray diffraction

List of Symbols

η_Q	asymmetry of the electric field gradient tensor
k	Boltzmann constant (1.38065×10^{-23} J K^{-1})
σ	chemical shielding tensor
σ^d, σ^p	diamagnetic and paramagnetic contributions, respectively, to the principal chemical shielding component σ_{ii} according to Ramsey's formulation of chemical shielding
R_{DD}	dipolar coupling constant
T_2*	effective transverse (or spin-spin) relaxation time constant
e	elementary electron charge (1.602×10^{-19} C)
$\mathbf{V}$	electric field gradient tensor
α, β, γ	Euler angles
$\mathbf{B_0}$	external static magnetic field
$\Delta\nu_{1/2}$	full width at half height
γ	gyromagnetic ratio
$\mathbf{H}$	Hamiltonian
η^x	hapticity of metallocene complexes
δ_{iso}	isotropic chemical shift
σ_{iso}	isotropic chemical shielding
ν_0	Larmor frequency
ω_0	Larmor frequency in radian unit
T_1	longitudinal (or spin-lattice) relaxation time constant

$T_{1\rho}$	longitudinal (or spin-lattice) relaxation time constant in the rotating frame
μ	magnetic moment
$\mathbf{M_0}$	magnetization at thermal equilibrium
Q	nuclear quadrupole moment
I	nuclear spin quantum number
h	Planck constant (6.626×10^{-34} J s)
δ_{11}, δ_{22}, δ_{33}	principal components of the chemical shift tensor
δ_{xx}, δ_{yy}, δ_{zz}	principal components of the chemical shift tensor in Haeberlen convention
σ_{11}, σ_{22}, σ_{33}	principal components of the chemical shielding tensor
V_{11}, V_{22}, V_{33}	principal components of the electric field gradient tensor
ν_Q	quadrupolar frequency
C_Q	quadrupole coupling constant
ν_1	radio-frequency of NMR pulses
B_1	radio-frequency field strength of NMR pulses
ν_{rot}	rotational frequency
κ	skew of the chemical shielding tensor
Ω	span of the chemical shielding tensor
T_2	transverse (or spin-spin) relaxation time constant

Chapter 1

Introduction

1.1 Nuclear Magnetic Resonance Spectroscopy

The first attempts at carrying out nuclear magnetic resonance (NMR) experiments on condensed matter were performed by a physicist named Gorter, and were unsuccessful due to improper experimental setup.[1] Ten years later, Purcell et al. and Bloch et al. from two research groups simultaneously reported the successful magnetic resonance experiments on solid paraffin[2] and liquid water,[3,4] respectively. Synthetic chemists use NMR spectroscopy to structurally characterize chemical compounds on a daily basis. For solid materials, single-crystal X-ray diffraction (XRD) has traditionally been the technique of choice for structural characterization, though its application is constrained to crystalline samples from which appropriate crystals can be grown. In many cases, single crystals isolated from larger samples do not always represent the bulk material, e.g., polymorphous materials. For micro- or nano-crystalline samples, crystal structure information such as cell dimension and space group may be obtained from powder XRD data; however, atomic positions must be calculated via Rietveld analysis,[5] which is a time-consuming and complicated process.

Solid-state NMR spectroscopy has proven to be an excellent means of probing molecular structures of and dynamic motions in crystalline materials[6-8] and a variety of amorphous systems including heterogeneous catalysts and support materials,[9] polymers,[10-12] self-assembled monolayers (SAMs),[13] glasses,[12,14,15] zeolitic materials,[12,16] mesoporous composite materials,[17-19] and biological materials.[12,20-22] Solid-state NMR experiments provide valuable information on local magnetic/electronic and coordination environments, local symmetry, bond character, internuclear distances as well as intra- and intermolecular motions.

In order to understand solid-state NMR experiments, basic concepts in NMR must be reviewed. We start by considering the simplest case, an ensemble of identical proton spins. The nuclear spin quantum number of a proton is $I = 1/2$, which means there are two possible spin states, $m_I = +1/2$ or $-1/2$ (which are often designated as α and β, respectively).[23] In the absence of an external magnetic field (denoted as $\mathbf{B}_0$, and $\mathbf{B}_0 = (0, 0, B_0)$), the energies of the two possible spin states are degenerate. However, in the presence of $\mathbf{B}_0$, the degeneracy of two quantized states, α and β, is removed (Figure 1.1).

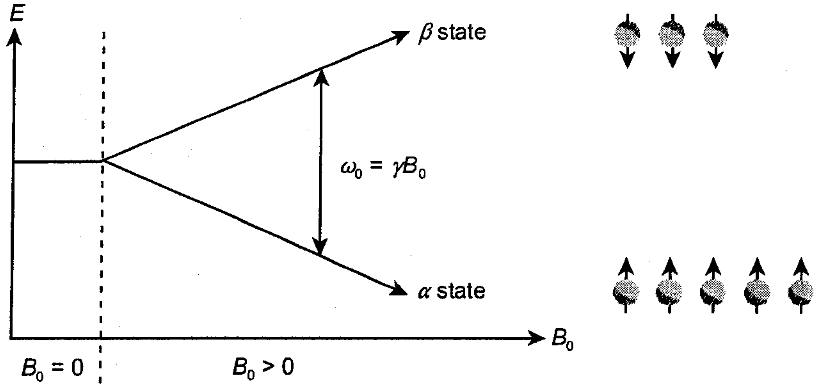

Figure 1.1. On the left, energy states of a proton nucleus in the absence and presence of an external magnetic field ($\mathbf{B}_0$). On the right, the lower energy (α) state is more populated according to Boltzmann distribution.

The proton has an intrinsic property known as the gyromagnetic ratio (γ), which describes the rate of precession of the nucleus about an applied field as a function of field strength. Hence, the spins precess about the magnetic field, with increasing magnetic fields leading to a faster precession. The α-spins precess about axes parallel to the applied field, while the β-spins precess about an antiparallel axis, and are therefore referred to as "spin-up" and "spin-down", respectively. The rate of precession of the nuclear spins is known as the Larmor frequency. The Larmor frequency is related to the magnitude of γ and the strength of the field along the z-direction, such that $\gamma = \omega_0/B_0$.

1.2 NMR Interactions

Zeeman interaction. The largest interaction in NMR experiments is the Zeeman interaction when an external magnetic filed is applied. The Zeeman Hamiltonian is written as,

$$\mathbf{H}_z = \boldsymbol{\mu}\cdot\mathbf{B}_0 = -\hbar\gamma B_0\mathbf{I}_z = -\omega_0\hbar\mathbf{I}_z \qquad [1.1]$$

where μ is the magnetic moment and $\mathbf{I}_z$ is the quantum mechanical spin operator. The energy levels for α and β spin states (E_α and E_β) are,

$$E_\alpha = -\frac{1}{2}\hbar\omega_0,\ E_\beta = +\frac{1}{2}\hbar\omega_0 \qquad [1.2]$$

where $\hbar$ is the Planck's constant (h) divided by 2π. From classical thermodynamics, the Boltzmann distribution predicts the populations that associate with the energy states, and that the lower energy state (α) is more populated at thermoequilibrium (Figure 1.1). For a system containing *N* proton spins, the ratio of the populations of α and β spin states can be calculated as,

$$\frac{N_\beta}{N_\alpha} = \frac{e^{-\frac{E_\beta}{kT}}}{e^{-\frac{E_\alpha}{kT}}} = e^{-\frac{(E_\beta - E_\alpha)}{kT}} = e^{\frac{-\hbar\omega_0}{kT}} \qquad [1.3]$$

where *k* is the Boltzmann constant, and *T* is the temperature. In Eq. 1.3, at normal temperatures, the value of *kT* in the denominator of the exponent is ca. six order of magnitude larger than the value of ($\hbar\omega_0$) in the numerator. Therefore, the population difference between α and β spin states is very small under ambient conditions. This makes NMR a relatively insensitive technique when compared to other forms of spectroscopy such as infra-red or UV-visible spectroscopy.

The population difference between the two spin states yields a net magnetization ($\mathbf{M}_0$) pointing along the *z* direction (Figure 1.2).

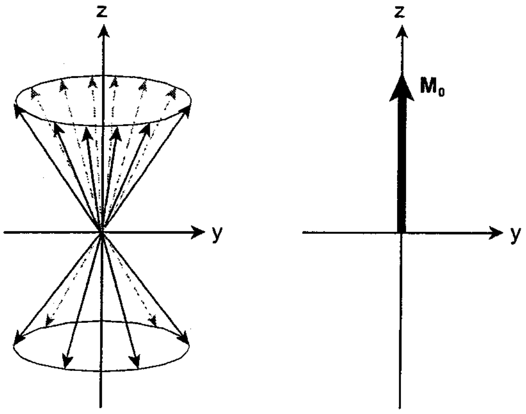

Figure 1.2. Precession of nuclear spins about the *z*-axis in the lab frame (left) and a net magnetization (right).

Note that the population difference between α and β spin states becomes larger, and hence the sensitivity of the NMR experiment becomes higher, with increasing B_0 and/or decreasing temperature, according to Eq. 1.4:

$$\Delta N = N_\alpha - N_\beta = \frac{N\gamma\hbar B_0}{2kT} \qquad [1.4]$$

Radiofrequency interaction. In the rotating frame, which is the frame of the spin precession about the *z*-axis at the Larmor frequency, all magnetic moments are stationary, yet there is still a net magnetization. The effect of the absence of spin precession in the rotating frame on the system is as if $\mathbf{B}_0$ has "vanished". In pulse NMR experiments, if a radiofrequency (rf) field generated by the NMR transmitter oscillates at or near the Larmor frequency, then the applied oscillating magnetic field ($\mathbf{B}_1$), which is perpendicular to the initial $\mathbf{B}_0$, appears stationary in the rotating frame. The oscillating $\mathbf{B}_1$ field is the result of an applied AC current in the NMR sample coil. The rf field strength of $\mathbf{B}_1$ is much smaller than that of $\mathbf{B}_0$. Since $\mathbf{B}_1$ is stationary in the rotating frame, magnetization will precess about $\mathbf{B}_1$. The rf Hamiltonian is written as,

$$\mathbf{H}_{\mathbf{rf}} = -h\omega_1 \sum_k I_{xk}\cos[(\omega_0+\omega)t+\theta] - I_{yk}\sin[(\omega_0+\omega)t+\theta] \qquad [1.5]$$

where ω_1 is the frequency of precession about $\mathbf{B}_1$, ω is the offset frequency relative to the Larmor frequency, θ is the phase offset, and I_x and I_y are the nuclear spin operators. Thus $\mathbf{H}_{\mathbf{rf}}$ represents the interaction between nuclear spins and the $\mathbf{B}_1$ field. When a rf pulse of frequency ω_1 is applied along the *x* direction with the duration τ_p, the magnetization tips from the *z* direction onto the *y*-axis in the Zeeman frame. The tip angle θ_p is determined by τ_p, such that $\theta_p = \gamma B_1\tau_p = \omega_1\tau_p$.

Other NMR interactions. The Zeeman and the rf interactions are considered to be the external NMR interactions.[24,25] Under the high-field approximation, that is, the Zeeman interaction is much larger than all other internal NMR interactions, which are treated as small perturbations on the Zeeman interaction. The total Hamiltonian of the system is thus,

$$\begin{aligned}\mathbf{H}_{\mathbf{tot}} &= \mathbf{H}_j^{\mathrm{ext}} + \mathbf{H}_k^{\mathrm{int}} \\ &= (\mathbf{H}_{\mathbf{Z}} + \mathbf{H}_{\mathbf{rf}}) + (\mathbf{H}_{\mathbf{CS}} + \mathbf{H}_{\mathbf{D}} + \mathbf{H}_{\mathbf{J}} + \mathbf{H}_{\mathbf{Q}} + \mathbf{H}_{\mathbf{SR}})\end{aligned} \qquad [1.6]$$

where $\mathbf{H}_{\mathbf{CS}}$, $\mathbf{H}_{\mathbf{D}}$, $\mathbf{H}_{\mathbf{J}}$, $\mathbf{H}_{\mathbf{Q}}$ and $\mathbf{H}_{\mathbf{SR}}$ are the chemical shielding (CS), direct spin-spin (dipolar), indirect spin-spin (*J*-coupling), quadrupolar (Q) and spin-rotation (SR) Hamiltonians, respectively, and are classified as internal NMR interactions.[24,25] Herein, a brief summary of NMR interactions is presented in the next paragraph; full treatments and full mathematical formalisms have been published elsewhere.[24-28] Structural analysis of the materials in this thesis is largely focussed on the interpretation of the CS and quadrupolar parameters, hence, these interactions are discussed in more detail below. The effects of CS and quadrupolar parameters on the appearance of solid powder patterns are further discussed in section 1.2.

Chemical shielding interaction. Chemical shielding arises from the interaction between the nuclear spins and local magnetic fields ($\mathbf{B}^{\mathrm{loc}}$) generated by the motion of electrons induced by $\mathbf{B}_0$, such that,

$$\mathbf{B}_j^{\mathrm{loc}} = \mathbf{B}_0 + \mathbf{B}_j^{\mathrm{ind}} \qquad [1.7]$$

where $\mathbf{B}^{\mathrm{ind}}$ is the magnetic field arising from the induced circulation of electrons by $\mathbf{B}_0$.

The subscript j represents a site j of the molecule. The local fields at different nuclear sites in a molecule are dependent upon the electronic environment, giving rise to distinct chemical shifts, which of course are extremely useful in molecular structural characterization. $\mathbf{B}_j^{\mathrm{ind}}$ is related to the CS tensor (σ) and $\mathbf{B}_0$ in the form,

$$\mathbf{B}_j^{\mathrm{ind}} = \boldsymbol{\sigma}_j \cdot \mathbf{B}_0 \qquad [1.8]$$

and the chemical shielding Hamiltonian is given by:

$$\mathbf{H}_{\mathrm{CS}} = \gamma\hbar \cdot \boldsymbol{\sigma} \cdot \mathbf{B}_0 \qquad [1.9]$$

The pioneer of chemical shielding theory was Ramsey,[29] who partitioned the CS interaction into diamagnetic and paramagnetic contributions. For chemical shielding in molecules, the diamagnetic shielding contribution (σ^{d}) arises from magnetically-induced circulation of electrons, in occupied molecular orbitals (MOs) and is dependent upon the ground state electronic configuration of the molecule/atom. The resulting local field is antiparallel to $\mathbf{B}_0$, and serves to magnetically shield the nucleus. The paramagnetic shielding contribution (σ^{p}) results from magnetically-induced mixing of MOs, and is usually responsible for magnetic deshielding (i.e., the local induced field is parallel to the direction of $\mathbf{B}_0$). Theoretical evaluation of the paramagnetic contribution is considerably more difficult than that for the diamagnetic contribution, since the excited MOs must also be taken into account. That is, there are contributions from (i) mixing of ground- and excited-state MOs and (ii) mixing of ground-state MOs.

The CS tensor is an orientation-dependent property. The anisotropic nature of chemical shielding can be described by a second-rank tensor (3 × 3 matrix). The CS tensor is composed of symmetric ($\sigma_{ij} = \sigma_{ji}$) and anti-symmetric ($\sigma_{ij} \neq \sigma_{ji}$) components; however, since the latter do not affect the appearance of NMR spectra,[30] they are ignored in the discussion. The symmetric CS tensor can be described relative to an arbitrary Cartesian axis system (e.g., a molecular frame) by six components, and can be diagonalized to yield the three principal components of its principal axis system (PAS):

$$\boldsymbol{\sigma}_{symm} = \begin{bmatrix} \sigma_{xx} & \sigma_{xy} & \sigma_{xz} \\ \sigma_{yx} & \sigma_{yy} & \sigma_{yz} \\ \sigma_{zx} & \sigma_{zy} & \sigma_{zz} \end{bmatrix} \xrightarrow{-diagonalization} \begin{bmatrix} \sigma_{11} & 0 & 0 \\ 0 & \sigma_{22} & 0 \\ 0 & 0 & \sigma_{33} \end{bmatrix}_{PAS} \qquad [1.10]$$

The principal components are assigned such that $\sigma_{11} \leq \sigma_{22} \leq \sigma_{33}$, in the order of lowest to highest magnetic shielding. Theoretical calculations and certain other experimental techniques yield chemical shielding values, which describe the degree of magnetic shielding with respect to the bare nucleus. In practice however, the chemical shift is measured in NMR experiments, which describes the degree of chemical shielding with respect to an arbitrarily chosen reference compound. The chemical shift and chemical shielding are related by

$$\begin{aligned} \delta_{sample} &= \frac{(\nu_{sample} - \nu_{ref})}{\nu_{ref}} \times 10^6 \\ &\approx \sigma_{ref} - \sigma_{sample} \end{aligned} \qquad [1.11]$$

Since the signs of the chemical shift and chemical shielding scales are opposite to one another, the principal components of the chemical shift tensor are defined such that $\delta_{11} \geq \delta_{22} \geq \delta_{33}$, still in the order of lowest to highest shielding.

Quadrupolar interaction. The quadrupolar interaction is distinct from all other internal NMR interactions, since (i) it applies only to nuclei with spin $I > 1/2$ and (ii) the interaction is electric in origin, not magnetic. Quadrupolar nuclei are distinguished from spin-1/2 nuclei in that they have spherically asymmetric nuclear charge distributions (while those of spin-1/2 nuclei are spherically symmetric). The degree of spherical asymmetry is described to second order by nuclear electric quadrupole moments (eQ), or nuclear quadrupole moments (NQM). NQM interacts with non-vanishing electric field gradients (EFGs) which are of molecular origin, and dependent only upon the ground electronic state of the molecule. The quadrupolar Hamiltonian has the form,

$$\begin{aligned}\mathbf{H}_{\mathrm{Q}} &= \frac{eQ}{6I(2I-1)}\mathbf{I}\cdot\mathbf{V}\cdot\mathbf{I} \\ &= \frac{e^2Qq_{zz}}{4I(2I-1)}\left[(3I_z^2-\mathbf{I}^2)+\frac{\eta_{\mathrm{Q}}}{2}(I_+^2+I_-^2)\right]\end{aligned} \qquad [1.12]$$

where $I_\pm = I_x \pm iI_y$. The e^2Qq_{zz} term is related to the quadrupolar coupling constant (C_{Q}); while η_{Q} is the asymmetry parameter of the EFG tensor, $\mathbf{V}$. The quadrupolar frequency, ν_{Q}, can be related to C_{Q} by:

$$\nu_{\mathrm{Q}} = \frac{3C_{\mathrm{Q}}}{2I(2I-1)} \qquad [1.13]$$

The quadrupolar interaction also has anisotropic characteristics, which can be used to study the local electronic environment of the nucleus and the symmetry of the molecule. The anisotropic quadrupolar interaction has its origin in the nature of the EFG tensor, which is a second-rank tensor. The EFG tensor is symmetric and traceless, and can be defined in both a Cartesian frame with six components, or in its own principle axis system, with three components:

$$\mathbf{V} = \begin{bmatrix} V_{xx} & V_{xy} & V_{xz} \\ V_{yx} & V_{yy} & V_{yz} \\ V_{zx} & V_{zy} & V_{zz} \end{bmatrix} \; \textit{-diagonalization} \rightarrow \begin{bmatrix} V_{11} & 0 & 0 \\ 0 & V_{22} & 0 \\ 0 & 0 & V_{33} \end{bmatrix}_{PAS} \qquad [1.14]$$

where $V_{ij} = V_{ji}$, and $|V_{11}| \le |V_{22}| \le |V_{33}|$. Since the EFG tensor is traceless, it is described by two parameters: $C_Q = e^2Qq_{zz}/h = eQV_{33}/h$ with eq_{zz} equal to V_{33}, and $\eta_Q = (V_{11} - V_{22})/V_{33}$. The former is a measure of spherical or platonic symmetry of the tensor, while the latter describes the axial symmetry of the tensor.

The quadrupolar interaction may be broken down into first-order and second-order contributions, depending on ν_Q. Thus, the quadrupolar Hamiltonian can be written as,

$$\mathbf{H}_Q = \mathbf{H}_Q^{(1)} + \mathbf{H}_Q^{(2)} \qquad [1.15]$$

where $\mathbf{H}_Q^{(1)}$ and $\mathbf{H}_Q^{(2)}$ are the first- and second-order quadrupolar Hamiltonians, respectively. The size of ν_Q relative to ν_0 determines whether or not the second-order quadrupolar interaction must be considered. Consider the simple case involving a spin-3/2 quadrupolar nucleus, there are $2I + 1 = 4$ quantized eigenstates: the -1/2, -3/2, +1/2 and +3/2 spin states (Figure 1.3A). There are three observable single-quantum (SQ or 1Q) transitions: the +1/2↔-1/2 transition is called the central transition (CT), and all other transitions are referred to as satellite transitions (STs, and in this case, +3/2↔+1/2 and -1/2↔-3/2). Under the high field approximation ($\nu_0 >> \nu_Q$), the quadrupolar interaction is primarily first order. The frequency associated with the SQ transitions is given by,

$$\nu^{(1)}_{m_I,m_{I\pm1}} = \left(\frac{\nu_Q}{4}\right)(1-2m_I)(3\cos^2\theta - 1 + \eta_Q\sin^2\theta\cos 2\Phi) \qquad [1.16]$$

where θ and Φ are the polar angles describing the EFG tensor orientation relative to $\mathbf{B}_0$. The angle θ is between V_{33} and $\mathbf{B}_0$, and Φ is the angle between V_{11} and the projection of $\mathbf{B}_0$ onto the plane of V_{11} and V_{22}.

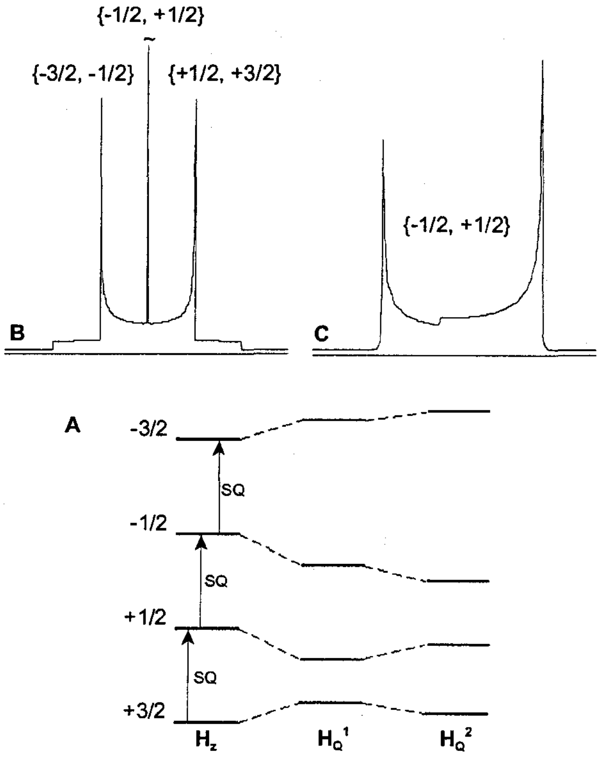

Figure 1.3. (A) Energy diagram of spin states under first- and second-order quadrupolar perturbation from the Zeeman level. (B) NMR powder pattern including CT and STs, with the former remains unchanged and the latter are broadened. (C) The CT is broadened dramatically by second-order quadrupolar effects.

When the quadrupolar interaction is corrected to first order, only the STs are affected and CT remains unchanged. However, as ν_Q becomes larger, all three transitions are affected by the second-order quadrupolar effects. The frequency associated with the CT can be calculated as,

$$
\begin{aligned}
\nu^{(2)}_{+1/2,-1/2} = \left(\frac{\nu_Q^2}{12\nu_0}\right) & \{\frac{3}{2}\sin^2\theta\,[(A+B)\cos^2\theta - B] \\
& -\eta_Q\cos 2\Phi\sin^2\theta\,[(A+B)\cos^2\theta + B] \qquad [1.17a] \\
& +\left(\frac{\eta_Q}{6}\right)[A-(A+4B)\cos^2\theta-(A+B)\cos^2\Phi(\cos^2\theta-1)^2]\}
\end{aligned}
$$

where

$$
\begin{aligned}
A &= 24m_I(m_I-1)-4I(I+1)+9 \\
B &= \left(\frac{1}{4}\right)[6m_I(m_I-1)-2I(I+1)+3] \qquad [1.17b]
\end{aligned}
$$

When the size of the quadrupolar interaction approaches that of the Zeeman interaction, the high field approximation collapses, and the full treatment of combined Zeeman and quadrupolar interactions is needed.[31]

Direct dipole-dipole and indirect spin-spin interactions. Both CS and quadrupolar interactions are one-spin interactions, while a pair of spins are involved in the dipolar (or dipole-dipole) and the indirect spin-spin interactions. Both dipole-dipole and indirect spin-spin interactions can be used to examine the intra- and intermolecular interactions, as well as the bonding between spin pairs involved in the interactions. The dipole-dipole interaction is the interaction between a homonuclear or heteronuclear pair of spins through space, i.e., a formal chemical bond between the spin pair is not required. The dipolar Hamiltonian is written as,

$$\begin{aligned}\mathbf{H}_{\mathbf{D}} &= \mathbf{I}\cdot\mathbf{D}\cdot\mathbf{S} \\ &= \hbar R_{\mathrm{dd}}\left[\frac{\mathbf{I}\cdot\mathbf{S}-3(\mathbf{I}\cdot\mathbf{r}_{IS})(\mathbf{S}\cdot\mathbf{r}_{IS})}{r_{IS}^{2}}\right]\end{aligned} \qquad [1.18]$$

where R_{dd} is known as the dipolar coupling constant, which is related to the gyromagnetic ratios of the spin pair involved in the interaction as well as their internuclear distances:

$$R_{\mathrm{dd}} = \left(\frac{\mu_0}{4\pi}\right)\frac{\hbar\gamma_I\gamma_S}{2\pi}\left\langle r_{IS}^{-3}\right\rangle \qquad [1.19]$$

The indirect spin-spin interaction involves the interaction between the spin pair through electrons, i.e., chemical bonds. The indirect spin-spin Hamiltonian is described by,

$$\mathbf{H}_{\mathbf{J}} = \hbar\mathbf{I}\cdot\mathbf{J}\cdot\mathbf{S} \qquad [1.20]$$

The *J*-coupling interaction between *I* and *S* nuclear spins results in splitting of peaks in the *I* NMR spectrum into $2S + 1$ evenly spaced lines, and vice versa. The orientation-dependent property of **J** is completely averaged to zero in solution state by rapid tumbling motions of molecules. The resulting isotropic value of the **J** tensor is known as the *J*-coupling constant. This constant can be used to examine the strength of bonding between the spin pair, as well as to estimate the torsion angle in aliphatic organic compounds via the Karplus relationship.

1.3 NMR Experiments of Solid Samples

The orientation-dependent properties of all first-order interaction tensors are averaged to zero in the solution state, due to rapid, isotropic tumbling of the molecules. Spectral acquisition in solution NMR experiments is generally easier compared to solid-state NMR experiments due to this averaging; however, much more structural information is present in the latter. For a stationary microcrystalline powder sample, which contains crystallites oriented in all possible directions, individual tensor orientations yield different NMR frequencies. A solid-state NMR spectrum is a superimposition of many sharp resonances with different frequencies and intensities, giving rise to a powder pattern. Since the NMR signal is distributed over a range of frequencies, the signal intensity is greatly reduced (Figure 1.4) in comparison to that of the corresponding solution NMR spectrum.

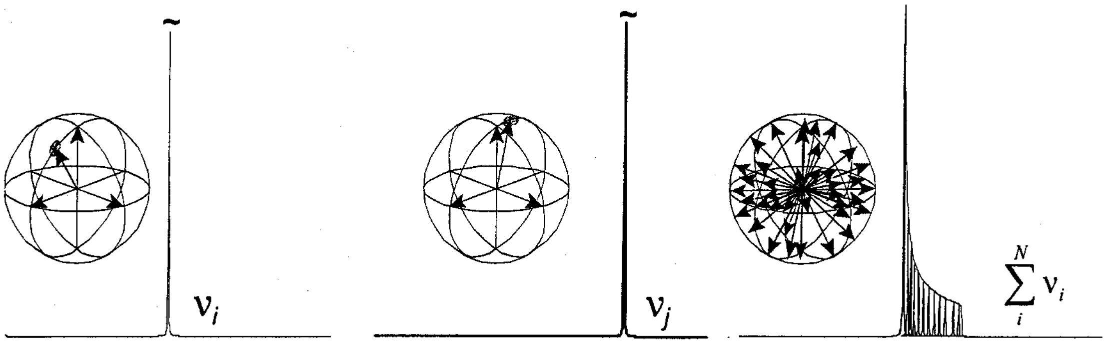

Figure 1.4. An NMR CS powder pattern consists of different NMR frequencies (right) corresponding to different crystallite orientations, examples of which are shown above (left and middle).

Chemical shielding powder patterns. A commonly used convention, which is called the Herzfeld-Berger convention, conveniently defines the CS tensor with three parameters: the isotropic chemical shift, $\delta_{iso} = (\delta_{11} + \delta_{22} + \delta_{33})/3$; the span, $\Omega = (\delta_{11} - \delta_{33})$;

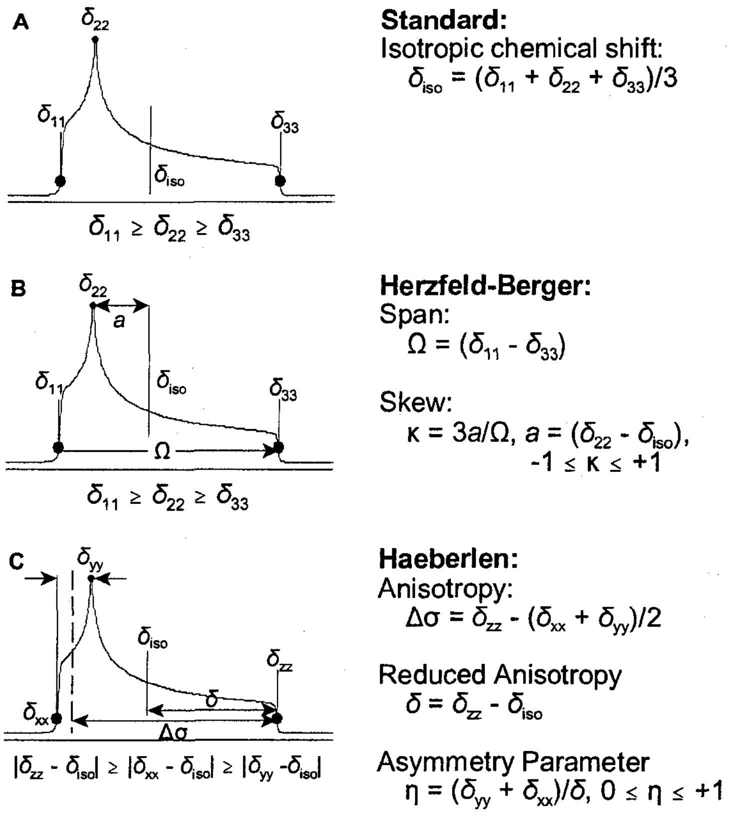

Figure 1.5. Illustration of relationship between CS tensor parameters and static NMR spectra in (A) standard, (B) Herzfeld-Berger and (C) Haeberlen conventions.

and the skew, $\kappa = 3(\delta_{22} - \delta_{iso})/\Omega$, where $-1 \geq \kappa \geq +1$ (Figure 1.5B). These parameters describe the position, breadth and shape of a chemical shift powder pattern. The span describes that degree of anisotropy, or range of chemical shifts, whereas the skew defines the degree of axial symmetry of the CS tensor. Another commonly used convention is the Haeberlen convention (Figure 1.5C). In the Haeberlen convention, δ_{xx}, δ_{yy} and δ_{zz} are used. They are defined such that $|\delta_{zz} - \delta_{iso}| \geq |\delta_{xx} - \delta_{iso}| \geq |\delta_{yy} - \delta_{iso}|$. The anisotropy ($\Delta\sigma$) (or sometimes the reduced anisotropy (δ)), and asymmetry parameter (η) are used in describing the size and axial symmetry of the CS tensor, respectively. The definition of these two parameters are included in Figure 1.5C.

Quadrupolar powder patterns. Solid-state NMR studies of quadrupolar nuclei are becoming increasingly important since the majority of the periodic table consists of quadrupolar nuclei ($I > 1/2$), and many of these are associated with scientifically and technologically important inorganic and organometallic materials.[32-35] For instance, solid-state NMR studies on quadrupolar nuclei have been reported on a variety of systems including an assortment of organic[7] and inorganic complexes,[8,36,37] glasses,[38] zeolites,[39] porous materials, catalysts[40] and biological compounds.[41] The analysis of the powder patterns for quadrupolar nuclei is more complicated in comparison to that of spin-1/2 nuclei, due to the second-order quadrupolar effects which complicate the NMR spectra. For solid patterns affected by the first-order quadrupolar interaction only, the intensity of the CT is the largest since the CT is unaffected, while all other STs are broadened by the first-order quadrupolar effects (Figure 1.3B); hence, their apparent intensities are reduced. Additionally, the shape and breadth of the two STs (for spin-3/2 nuclei) are the same but are mirror-imaged to one another. The position of all SQ transitions can be explained by the energy diagram which is shown in Figure 1.3A. The energy difference (ΔE) is the biggest for $\{-1/2 \leftrightarrow -3/2\}$ ST; hence, the frequency range of such transition, which can be calculated according to Eq. 1.16, is positioned at the higher frequency in the spectrum. Conversely, ΔE for the $\{+3/2 \leftrightarrow +1/2\}$ ST transition is the smallest, the pattern is thus located to the low frequency direction. The CT is greatly broadened by the second-order quadrupolar effects (Figure 1.3C), and all STs can be barely detected since they are severely broadened and effectively disappear into the noise of the baseline. Figure 1.6 illustrates the effects of C_Q and η_Q on the appearance of static powder patterns of central transitions which are dominated by the second-order quadrupolar interaction.

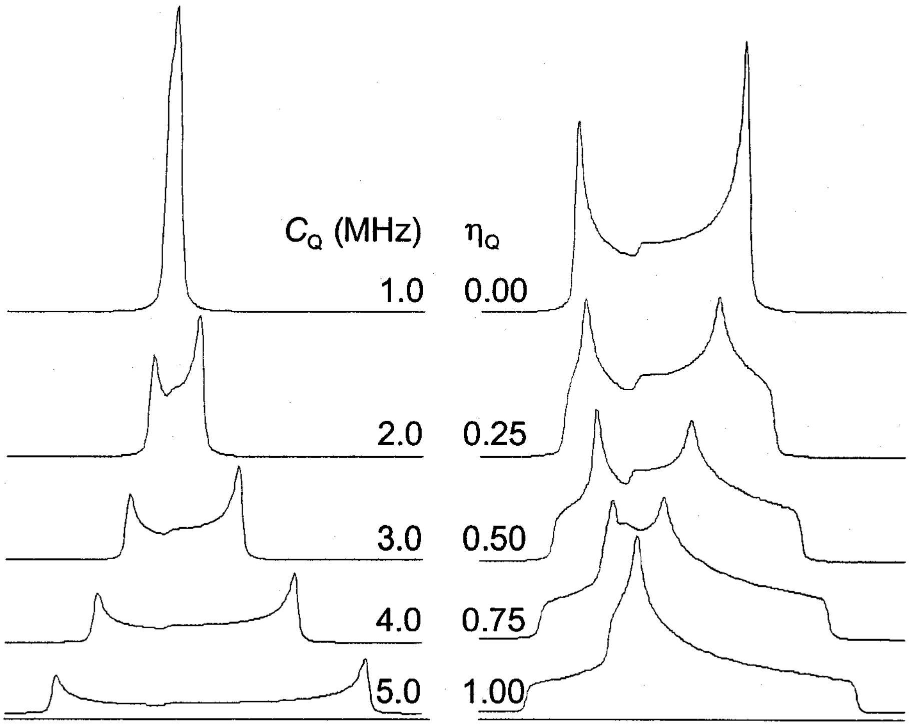

Figure 1.6. Effects of the change of C_Q (left, with η_Q being fixed and equals to 0.0) and η_Q (right, with C_Q being fixed and equals 3.0 MHz) on the CT powder patterns.

Euler angles. The CS and EFG tensors need not to have the same orientation in the molecular frame; thus, a set of angles, $\{\alpha, \beta, \gamma\}$, which are called Euler angles, are used to define their relative orientation. In this thesis, all spectral analytical simulations were performed using the computer program called WSOLIDS,[42] in which a positive or counterclockwise rotation (Arfken convention,[43]) of the coordinate system is used. Before the rotation operations, the CS and the EFG tensors are coincident, i.e., V_{33}/σ_{33}, V_{22}/σ_{22} and V_{11}/σ_{11} are parallel to the x-, y- and z-axes. After the rotation operations by Euler angles, the CS tensor is brought into its PAS while the EFG tensor remains

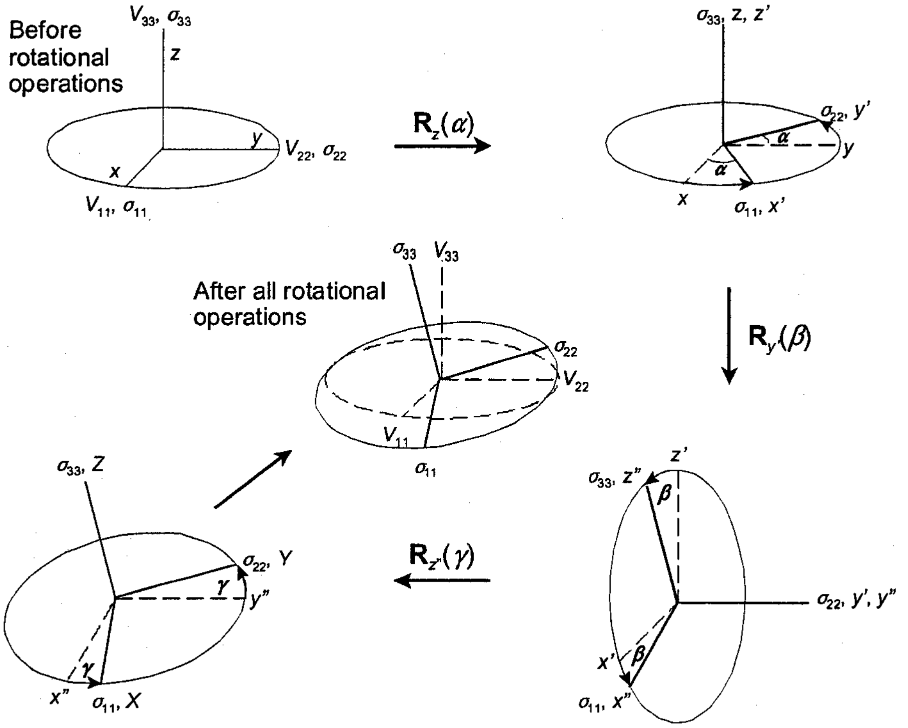

Figure 1.7. Illustration of positive rotation performed on the CS tensor from the coincident tensor frames (x, y, z) into its PAS (X, Y, Z) by the Euler angles $\{\alpha, \beta, \gamma\}$.

stationary throughout (i.e., the two NMR tensors do not coincide in the end). The rotational operations which relate the two tensor frames are outlined as follows: first, a rotation with an angle α about σ_{33} is performed. The resultant frame has x', y', and z' coordinate system, and are parallel to the new σ_{33}, σ_{22} and σ_{11} principal components. A subsequent rotation about y' by β yields another frame with x''-, y''- and z''-axes. Finally, the last rotation about z'' by the angle γ makes the CS tensors coincide with the X, Y and Z coordinate system. Determination of Euler angles is crucial when simulating solid-state NMR spectra of nuclei which are influenced by both chemical shielding and quadrupolar interactions.

1.4 Common Solid-State NMR Experiments

Magic-angle spinning. All first-order NMR Hamiltonians contain the geometrical term ($3\cos^2\theta - 1$) where θ represents the angle between the *z*-axis of the interaction tensor (i.e., the largest component in the PAS) and $\mathbf{B}_0$. For powder samples which contain all possible orientations, rotation of the samples about the rotor axis changes the value of θ. The expectation value of the geometrical term ($<3\cos^2\theta - 1>$) has to be calculated. The angle between the rotor axis and $\mathbf{B}_0$ is θ_R, and β is the angle between the rotor and *z*-axes of first-order NMR interaction tensors. Then the relationship between all three angles can be written as:

$$\langle 3\cos^2\theta - 1 \rangle = \frac{1}{2}(3\cos^2\beta - 1)(3\cos^2\theta_R - 1) \qquad [1.21]$$

By setting θ_R to be 54.74°, then the right-hand side of Eq. 1.21 becomes zero and so does the left-hand side. Hence, all first-order NMR interactions may be averaged to zero by mechanically spinning the samples at θ_R at 54.74°, which is known as the magic angle. First-order NMR interactions can be completely averaged out if the rotational frequency is larger than the interaction in Hz. This spinning technique is called magic-angle spinning (MAS) and was first reported by Andrew and Lowe.[44-46] Spectral acquisition under such conditions narrows the NMR resonances substantially, resulting in solution-like spectra provided that spinning speeds are fast enough. The NMR spectra obtained from

MAS experiments consist of the isotropic peak flanked by its spinning sidebands, where the peak separation equals the spinning frequency. Since all of the signal of MAS spectra is localized into a set of NMR peaks, the signal-to-noise ratio (S/N) is greatly increased when compared to that of broad static powder patterns. For chemical shielding patterns of spin-1/2 nuclei, the spinning side manifold allows one to extract the CS tensor parameters via Herzfeld-Berger analysis (HBA).[47]

Cross-polarization MAS. Dilute nuclei refer to nuclei with low natural abundances (e.g., ^{13}C, ^{15}N, ^{109}Ag, ^{77}Se, etc.), which as a result do not form a complicated network of homonuclear dipolar coupled spins. The absence of fluctuating homonuclear dipole-dipole interactions often results in very long T_1 relaxation time constants (i.e., inefficient longitudinal relaxation). The time taken to acquire solid spectra for such nuclei using single-pulse (Bloch-decay) NMR experiments is very long. Further, Bloch-decay MAS NMR experiments on dilute nuclei often yield poor S/N NMR spectra.

The problem of acquiring spectra of dilute spins with potentially long relaxation times may be addressed by performing cross-polarization MAS (CP/MAS) NMR experiments. The CP/MAS NMR experiment was first introduced by Pines et al.[48] and is based on the cross-polarization theory developed by Hartmann and Hahn.[49] Upon the introduction of the CP/MAS technique, it became the method of choice for NMR experiments to observe dilute spin-1/2 nuclei (e.g., see references [50-55]). The detailed theoretical background for CP/MAS can be found elsewhere,[56,57] but a brief explanation is given herein. In CP/MAS NMR experiments, polarization transfer from the abundant nucleus to the dilute nucleus is mediated by their dipolar interactions, i.e., the

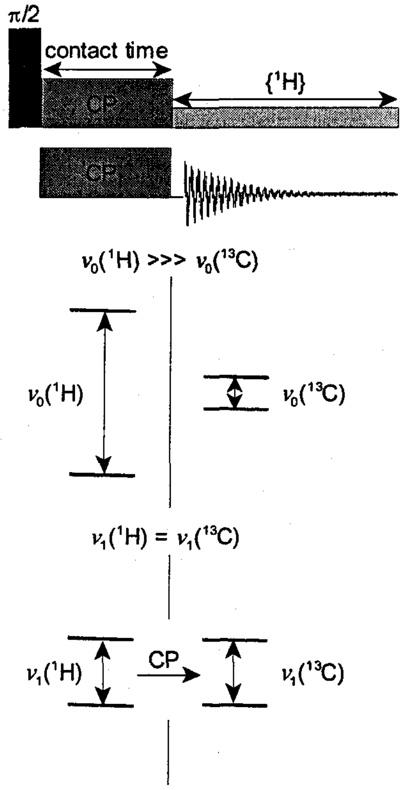

Figure 1.8. A basic CP/MAS pulse sequence (top), energy diagram of ^{1}H and ^{13}C at the Zeeman level: no CP is allowed (middle), and energy diagram in the rotating frame during spin-lock (bottom).

two nuclei must be dipolar coupled. Figure 1.8 shows the most basic CP/MAS NMR pulse sequence. The NMR experiment utilizes two channels, one of which irradiates the abundant nuclei (^{1}H) and the other the dilute nuclei (^{13}C). The initial ^{1}H magnetization (along the z direction) is brought into the xy-plane after the initial $\pi/2$ pulse, immediately follow by a spin-lock pulse along the $-y$ direction on both channels with rf fields $B_1(^1\text{H})$ and $B_1(^{13}\text{C})$. The ^{1}H and ^{13}C magnetization is locked along the same direction in their own frame of reference. During this spin-locked pulses, the rf fields for both nuclei experience time dependent oscillations in the lab frame. Under the consideration of doubly rotating frame, the oscillatory time dependency of the rf fields disappear so that the Zeeman splitting is comparable for both spins (Figure 1.8, bottom). The polarization transfer is accomplished by matching the two spin-lock fields such that the two B_1 fields nutate at the same frequency.

$$\begin{aligned} \gamma_H B_1(^1\mathrm{H}) &= \gamma_C B_1(^{13}\mathrm{C}) \\ \nu_1(^1\mathrm{H}) &= \nu_1(^{13}\mathrm{C}) \end{aligned} \qquad [1.22]$$

Eq. [1.22] is known as the Hartmann-Hahn match condition. The rate of magnetization buildup in the ^{13}C channel (i.e., efficiency of the CP process) depends on the strength of the heteronuclear dipolar interaction, and the length of contact time. Several factors can influence the strength of the dipolar interaction: (i) internuclear distance, (ii) dynamic motions which partially average the dipolar interaction, and (iii) the strength of the homonuclear ^{1}H-^{1}H dipolar interactions in the ^{1}H spin network. In (i), the smaller the distance, the stronger the dipolar interaction due to the $1/r^3$ dependence (Eq. [1.19]). Point (ii) stems from both the cross relaxation between the ^{1}H-^{13}C spin pair (T_{CH}) and the relaxation of ^{1}H spins during the spin-lock period ($T_{1\rho}$). Efficient relaxation (i.e., fast motions) may decrease the CP efficiency, but may also reduce the ^{1}H T_1, allowing a faster recycle rate. Finally, for (iii), the CP process does not involve isolated spin pairs in most cases. Rather, the ^{1}H spins involved in the CP process are part of a strongly coupled ^{1}H spin bath. The initial stage of the CP process occurs between the ^{13}C and the most proximate ^{1}H spin pair when the ^{1}H magnetization begins to transfer to the ^{13}C spin. To maintain the polarization transfer, ^{1}H magnetization must be redistributed from all other ^{1}H spins within the strongly coupled ^{1}H spin bath, so that the polarization transfer continues. Thus, CP efficiency may decrease if the ^{1}H spins are far apart from each other in the network;[57] however, strongly coupled ^{1}H spin bath also results in efficient $T_{1\rho}$.

The last stage of the CP/MAS pulse sequence is acquisition on the channel of the dilute spin accompanied by simultaneous proton decoupling (denoted as {^{1}H} in Figure 1.8). High-power proton decoupling with rf-field near 100 kHz is generally required to suppress the strong heteronuclear dipole-dipole interaction (for ^{13}C-^{1}H spin pairs). Both factors can broaden and complicate the NMR spectrum.

When the heteronuclear dipolar interaction of ^{1}H and ^{13}C becomes too weak (e.g., experiments with high spinning frequencies), variable-amplitude CP/MAS (VACP/MAS)[58] or RAMP-CP/MAS[59] NMR experiments are used. Such NMR experiments are similar to a standard CP/MAS experiment, with the exception that the matching power during the CP period in one of the channels is ramped up (or ramped down). The effect of this is to sample a more broad range of Zeeman splittings and increase the CP efficiency.

1.5 Complementary Techniques

Often, other complementary techniques such as single-crystal XRD, powder XRD, ab initio calculations, etc., are used along with solid-state NMR experiments to gain a better understanding of molecular structures, dynamics and long-range chemical interactions. Powder XRD experiments can act as a fingerprinting tool to identify purity and phase of the bulk samples, by comparing experimental diffraction patterns to those calculated from known crystal structures.[60-63]

First principles calculations are used to correlate the orientation of NMR interaction tensors in the frame of the molecule. Accurate calculations of NMR interaction tensor parameters allow the examination of the tensor orientations in the molecular frame. One can then rationalize the nature of NMR tensors with respect to molecular structures, symmetry and bonding motifs. For cases where the crystal structure or molecular structure is unknown, structural predictions and interpretation may be accomplished by theoretical studies. Direct determination of the relative orientation can be obtained from NMR experiments conducted on single crystals;[64-67] however, a large crystal size and special instrumentation are often required.

There are an enormous number of theoretical studies of NMR interaction tensors (see references [68-72]). Ab initio (Hartree-Fock) and density functional theory (DFT) molecular orbital calculations are full quantum-mechanical treatments and are generally used for molecular compounds. DFT is distinct from Hartree-Fock (restricted HF or RHF for diamagnetic systems) methods since the former accounts for electron correlation in a semi-empirical fashion. Calculations on extended solids usually employ a variety of plane-wave calculations.[73,74] The latter category is beyond the scope of this thesis, and is not discussed further in this sections.

Regardless of the use of RHF or DFT methods, the choice of basis sets is also very important for calculations of NMR tensors. Basis sets are utilized to describe the atomic orbitals (AOs), which are linearly combined to construct the MOs.[75] Generally speaking, the larger the basis set, the better it can describe the MOs of the system. In practice, however, large basis sets are avoided in some cases to reduce the computational time or when they are applied on less important atoms (e.g., atoms that are used for charge balance purposes for large ionic clusters). Further discussion on ab initio calculations is presented in chapter 2.

1.6 Context of Research

The purpose of this thesis is to demonstrate applications of solid-state NMR spectroscopy characterization of molecular structure and dynamic motions in a broad range of inorganic, organometallic and composite chemical systems.

In chapter 2, the use of RHF and DFT calculations on small molecular clusters, to study ^{51}V EFG tensors in a series of vanadates, is discussed. Cluster calculations serve as an alternative method for theoretical studies on extended solids like vanadates. We have determined that it is possible, with the appropriate basis sets and molecular orbital calculations, to accurately calculate ^{51}V EFG tensor parameters in vanadates. These methods will have predictive value in examining a variety of vanadium oxide systems with unknown molecular structures, such as vanadia and even a wide range of supported vanadia heterogeneous catalysts.[76]

Many metallocene complexes involving a variety of quadrupolar metal nuclei positioned within different organometallic architectures have been studied by solid-state NMR spectroscopy in our research group.[61,62,77-83] In chapter 3, a comprehensive characterization of a series of organometallic half-sandwich niobium(I) and niobium(V) complexes by solid-state ^{93}Nb and ^{13}C NMR is presented. Results from complementary XRD experiments and ab initio calculations are also discussed. The sensitivity of the ^{93}Nb NMR spectra to ring substitution, metal oxidation state and solvent coordination is demonstrated.

In chapter 4, solid-state multinuclear NMR experiments are used to characterize a series of guest materials in different mesoporous transition-metal oxide materials. The host materials include mesoporous titanium oxide, vanadium-niobium mixed oxides and tantalum oxide. The guest materials include bis(toluene)titanium, neutral bis(arene)chromium(0) and cationic bis(arene)chromium(I), sodium, lithium and rubidium naphthalenides, and rubidium fulleride. Molecular dynamics are also studied by variable-temperature NMR experiments and relaxation measurements. Interesting chemical reactions occur within the walls and channels of these materials, such as ammonia generation from dinitrogen and water, as well as redox reactions; all of these can be probed in great detail with solid-state NMR.

Chapters 5 and 6 describe the characterization of nanoparticles, which is an area of rapidly expanding interest, due to their size-dependent chemical and physical properties. While a variety of microscopic techniques are used to examine NPs at the micro- and nano-scaled dimensions, multinuclear solid-state NMR spectroscopy can be used to characterize NP systems at the molecular level, leading to much insight into their structure and preparation. In chapter 5, a series of luminescent lanthanide-doped lanthanum fluoride NPs coated with alkyl organic ligands are investigated. Degrees of crystallinity, structural changes and dopant positions in the inorganic core, the nature of surface ligands, as well as the connectivity between the NP surface and organic ligands are discussed in detail. In Chapter 6, the preliminary phase of a comprehensive investigation of mesoporous aerogels and xerogels comprised of CdSe NPs is presented. NMR characterization of the NP cores and surfaces, nature of the surface ligands, and their connectivity and interaction are examined.

Bibliography

[1] Gorter, C.J. *Physica* **1936**, *3*, 995.

[2] Purcell, E.M., Torrey, H.C., Pound, R.V. *Phys. Rev.* **1946**, *69*, 37.

[3] Bloch, F., Hansen, W.W., Packard, M. *Phys. Rev.* **1946**, *70*, 474.

[4] Bloch, F., Hansen, W.W., Packard, M. *Phys. Rev.* **1946**, *69*, 127.

[5] Rietveld, H.M. *J. Appl. Crystallogr.* **1969**, *2*, 65.

[6] Bernard, G.M., Wasylishen, R.E. *Phys. Organomet. Chem.* **2002**, *3*, 165.

[7] Lemaitre, V., Smith, M.E., Watts, A. *Solid State Nucl. Magn. Reson.* **2004**, *26*, 215.

[8] Bryce, D.L., Sward, G.D. *Magn. Reson. Chem.* **2006**, *44*, 409.

[9] Wachs, I.E. *Catal. Today* **2005**, *100*, 79.

[10] Andreis, M., Koenig, J.L. In *Polysoaps/Stabilizers/Nitrogen-15 NMR*; Springer-Verlag Berlin: Berlin, 1995; Vol. 124, pp 191-237.

[11] Kuroki, S., Kimura, H., Ando, I. In *Advances in Solid State NMR Studies of Materials and Polymers: A Special Volume Dedicated to Isao Ando*; Academic Press Ltd: London, 2004; Vol. 52, pp 201-243.

[12] Dybowski, C., Bai, S., van Bramer, S. *Anal. Chem.* **2004**, *76*, 3263.

[13] Badia, A., Lennox, R.B., Reven, L. *Accounts Chem. Res.* **2000**, *33*, 475.

[14] Eckert, H. *Angew. Chem.-Int. Edit. Engl.* **1989**, *28*, 1723.

[15] Eckert, H. *Prog. Nucl. Magn. Reson. Spectrosc.* **1992**, *24*, 159.

[16] Suib, S.L. *Chem. Rev.* **1993**, *93*, 803.

[17] Anderson, M.W. *Topics in Catalysis* **1996**, *3*, 195.

[18] Smith, M.E. *Nucl. Magn. Reson.* **2000**, *29*, 251.

[19] Khimyak, Y.Z. *NATO ASI Ser., Ser. C* **2004**, *165*, 261.

[20] Legrand Andre, P., Bresson, B., Guidoin, R., Famery, R. *J. Biomed. Mater. Res.* **2002**, *63*, 390.

[21] Baldus, M. *Curr. Opin. Struct. Biol.* **2006**, *16*, 618.

[22] Hong, M. *Structure* **2006**, *14*, 1731.

[23] Zumbulyadis, N. *Concepts Magn. Reson.* **1991**, *3*, 89.

[24] Mehring, M. *Principles of High Resolution NMR in Solids. 2nd Ed*, 1983.

[25] Levitt, M. *Spin Dynamics: Basic Principles of NMR Spectroscopy*, 2001.

[26] Abragam, A. *Principles of Nuclear Magnetism*; Oxford University Press: Ely House, London W.1, 1961.

[27] Schmidt-Rohr, K., Spiess, H.W. *Multidimensional Solid-State NMR And Polymers*; Academic Press Inc.: San Diego, 1994.

[28] Duer, M.J. *Introduction to Solid-State NMR Spectroscopy*; Blackwell Science Ltd.: Oxford, 2004.

[29] Ramsey, N.F. *Phys. Rev.* **1950**, *78*, 699.

[30] Anet, F.A.L., O'Leary, D.J. *Concepts Magn. Reson.* **1991**, *3*, 193.

[31] Bain, A.D. *Mol. Phys.* **2003**, *101*, 3163.

[32] Smith, M.E. *Applied Magnetic Resonance* **1993**, *4*, 1.

[33] Smith, M.E., Van Eck, E.R.H. *Prog. Nucl. Magn. Reson. Spectrosc.* **1999**, *34*, 159.

[34] Duer, M.J., Farnan, I. In *Solid State NMR Spectrosc.*; Blackwell Science Ltd.: Oxford, 2002, pp 179-215.

[35] Ashbrook, S.E., Duer, M.J. *Concepts Magn. Reson.* **2006**, *28A*, 183.

[36] Fitzgerald, J.J., DePaul, S.M. *ACS Symposium Series* **1999**, *717*, 2.

[37] Wasylishen, R.E. In *Calculation of NMR and EPR Parameters*; Wiley-VCH Verlag GmbH & Co.: Weinheim, 2004, pp 433-447.

[38] Eckert, H. *Series on Directions in Condensed Matter Physics* **2000**, *17*, 283.

[39] Koller, H. *Stud. Surf. Sci. Catal.* **2004**, *149*, 105.

[40] Pruski, M., Amoureux, J.P., Fernandez, C. *NATO ASI Ser., Ser. C* **2002**, *76*, 107.

[41] Wu, G. *Biochem. Cell Biol.* **1998**, *76*, 429.

[42] Eichele, K., Wasylishen, R.E., v. 1.17.30, Tübingen, 2001.

[43] Arfken, G.B. *Mathematical Methods for Physicists*; Academic Press: New York, 1985.

[44] Andrew, E.R., Bradbury, A., Eades, R.G. *Nature* **1958**, *182*, 1659.

[45] Andrew, E.R., Newing, R.A. *Proc. Phys. Soc.* **1958**, *72*, 959.

[46] Lowe, I.J. *Phys. Rev. Lett.* **1959**, *2*, 285.

[47] Herzfeld, J., Berger, A.E. *J. Chem. Phys.* **1980**, *73*, 6021.

[48] Pines, A., Gibby, M.G., Waugh, J.S. *J. Chem. Phys.* **1973**, *59*, 569.

[49] Hartmann, S.R., Hahn, E.L. *Phys. Rev.* **1962**, *128*, 2042.

[50] Fyfe, C.A., Mueller, K.T., Wong-Moon, K.C. *NATO ASI Ser., Ser. C* **1994**, *447*, 447.

[51] Sebald, A. *Nucl. Magn. Reson.* **1994**, *31*, 91.

[52] Ambrosius, F., Klaus, E., Schaller, T., Sebald, A. *Z. Naturforsch., A: Phys. Sci.* **1995**, *50*, 423.

[53] Cook, R.L., Langford, C.H. *Polym. News* **1999**, *24*, 6.

[54] Amoureux, J.P., Pruski, M. *Mol. Phys.* **2002**, *100*, 1595.

[55] Taylor, R.E. *Concepts Magn. Reson.* **2004**, *22A*, 37.

[56] Fyfe, C.A. In *Solid State NMR for Chemists*; C.F.C Press: Guelph, 1983, pp 268-526.

[57] Duer, M.J. In *Introduction to Solid-State NMR Spectroscopy*; Blackwell Science Ltd.: Oxford, 2004, pp 96-106.

[58] Peersen, O.B., Wu, X., Kustanovich, I., Smith, S.O. *J. Magn. Reson. Ser. A* **1993**, *104*, 334.

[59] Metz, G., Wu, X., Smith, S.O. *J. Magn. Reson. Ser. A* **1994**, *110*, 219.

[60] Lo, A.Y.H., Bitterwolf, T.E., Macdonald, C.L.B., Schurko, R.W. *J. Phys. Chem. A* **2005**, *109*, 7073.

[61] Widdifield, C.M., Schurko, R.W. *J. Phys. Chem. A* **2005**, *109*, 6865.

[62] Rossini, A.J., Schurko, R.W. *J. Am. Chem. Soc.* **2006**, *128*, 10391.

[63] Tang, J.A., Masuda, J.D., Boyle, T.J., Schurko, R.W. *ChemPhysChem* **2006**, *7*, 117.

[64] Veeman, W.S. *Philos. Trans. R. Soc. London, A* **1981**, *299*, 629.

[65] Kennedy, M.A., Ellis, P.D. *Concepts Magn. Reson.* **1989**, *1*, 109.

[66] Kennedy, M.A., Ellis, P.D. *Concepts Magn. Reson.* **1989**, *1*, 35.

[67] Dye, J.L. *NATO ASI Ser., Ser. C* **1996**, *485*, 313.

[68] Jackowski, K. *Bull. Pol. Acad. Sci., Chem.* **1998**, *46*, 91.

[69] Jameson, C.J., De Dios, A.C. *Nucl. Magn. Reson.* **1999**, *28*, 42.

[70] Sanders, L.K., Arnold, W.D., Oldfield, E. *J. Porphyrins Phthalocyanines* **2001**, *5*, 323.

[71] Vaara, J., Jokisaari, J., Wasylishen, R.E., Bryce, D.L. *Prog. Nucl. Magn. Reson. Spectrosc.* **2002**, *41*, 233.

[72] Aliev, A.E., Law, R.V. *Nucl. Magn. Reson.* **2003**, *32*, 238.

[73] Schwarz, K. *J. Solid State Chem.* **2003**, *176*, 319.

[74] Schwarz, K., Blaha, P. *Comput. Mater. Sci.* **2003**, *28*, 259.

[75] Foresman, J.B., Frisch, A. In *Exploring Chemistry with Electronic Structure Methods: A Guide to Using Gaussian*; 1 ed.; Gaussian, Inc.: Pittsburgh, 1993, pp 107-112.

[76] Lapina, O.B., Mastikhin, V.M., Shubin, A.A., Krasilnikov, V.N., Zamaraev, K.I. *Prog. Nucl. Magn. Reson. Spectrosc.* **1992**, *24*, 457.

[77] Schurko, R.W., Hung, I., Schauff, S., Macdonald, C.L.B., Cowley, A.H. *J. Phys. Chem. A* **2002**, *106*, 10096.

[78] Schurko, R.W., Hung, I., Macdonald, C.L.B., Cowley, A.H. *J. Am. Chem. Soc.* **2002**, *124*, 13204.

[79] Hung, I., Schurko, R.W. *Solid State Nucl. Magn. Reson.* **2003**, *24*, 78.

[80] Willans, M.J., Schurko, R.W. *J. Phys. Chem. B* **2003**, *107*, 5144.

[81] Hung, I., Schurko, R.W. *J. Phys. Chem. B* **2004**, *108*, 9060.

[82] Hung, I., Macdonald, C.L.B., Schurko, R.W. *Chem.-Eur. J.* **2004**, *10*, 5923.

[83] Hamaed, H., Lo, A.Y.H., Lee, D.S., Evans, W.J., Schurko, R.W. *J. Am. Chem. Soc.* **2006**, *128*, 12638.

Chapter 2

A Theoretical Study of ^{51}V Electric Field Gradient Tensors in Pyrovanadates and Metavanadates

2.1 Introduction

Vanadium oxides or oxovanadium complexes are of great interest in coordination chemistry, material science and mineralogy due to their structural variety in naturally occurring minerals and synthetic materials.[1] In particular, supported (e.g., onto Al_2O_3, SiO_2 and TiO_2) and unsupported vanadium pentoxides, V_2O_5, and other vanadium mixed oxides (e.g., V–P–O, V–Mg–O, V–Sb–O, V–Fe–O systems, etc.) have importance in industrial catalytic processes, such as oxidative dehydrogenation (ODH) of hydrocarbons and selective catalytic reduction (SCR) of NO by ammonia.[2-19] A special class of vanadia known as vanadates, which are involved in syntheses of supported–V_2O_5 catalysts,[6,20,21] insulin–mimetic agents,[22,23] and rechargeable Li batteries,[24,25] are of great interest.

Vanadates are classified in pyrovanadate, orthovanadate and metavanadate categories based upon the structural differences between the vanadium-oxygen units. Pyrovanadates have the general formula $M_2V_2O_7$ (M = Zn, Mg, Cd, Ca, etc.),[26-29] though some mixed-metal "double pyrovanadates" are well known (e.g., $BaCaV_2O_7$).[30] The anionic $V_2O_7^{4-}$ complex ions (i.e., pyro units, Figure 2.1A) are isolated units where both vanadium atoms are corner shared. The pyro units are classified as either "thortveitite" or "dichromate" structural types, which have staggered and eclipsed conformations, respectively. The orthovanadates are structurally simple as well, featuring isolated VO_4 units.[25,31-33]

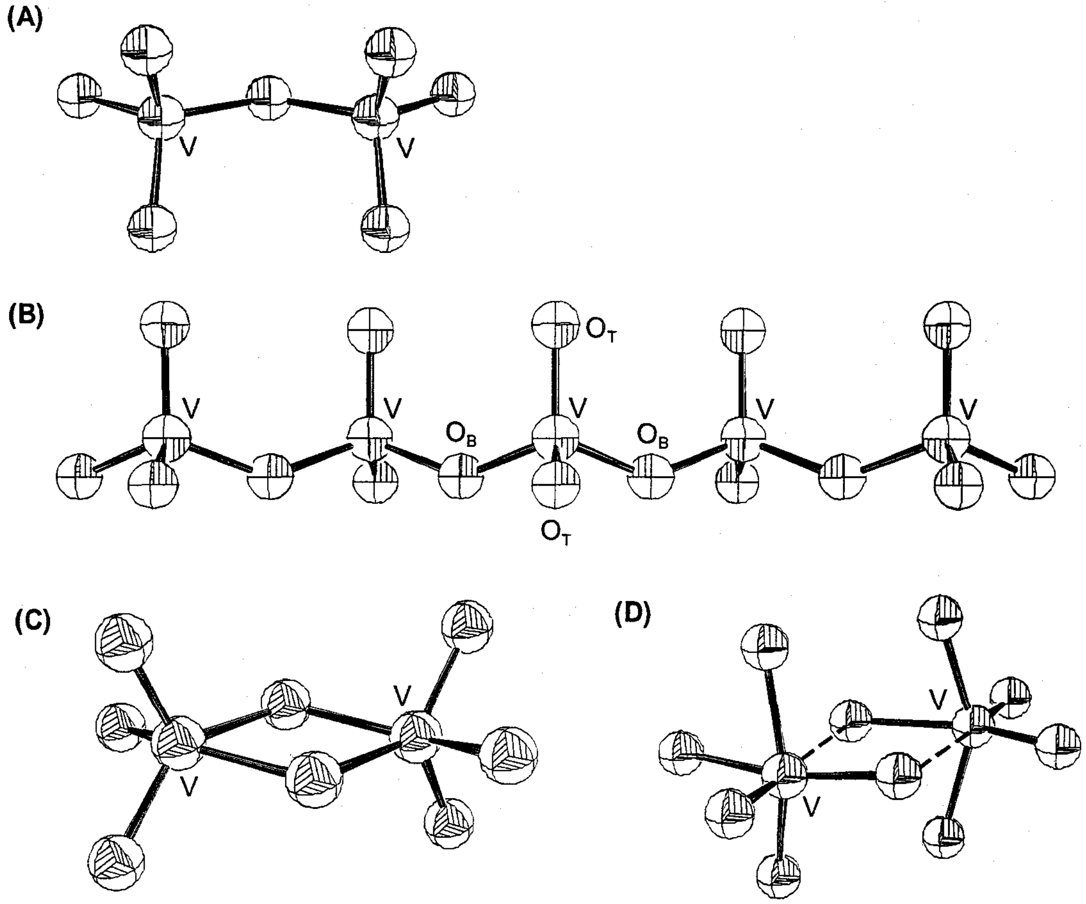

Figure 2.1. Various structural types of vanadium–oxygen units in (A) pyrovanadates, and (B) to (D) metavanadates. O_B and O_T refer to bridging and terminal oxygen atoms, respectively.

In metavanadates the vanadium-oxygen units have extensive structural variety. For instance, the pyroxene family, with the general molecular formula MVO_3 (M = Li, Tl, NH_4, K and Na in the high temperature phase of $NaVO_3$ (α-$NaVO_3$)),[34-37] is comprised of infinitely zig-zagging chains of corner-shared, distorted VO_4 tetrahedra (Figure 2.1B).

The low temperature phase of $NaVO_3$ (β-$NaVO_3$) has distorted, edge-sharing VO_5 units (Figure 2.1C).[38] Another group of metavanadates possesses the brannerite structure of $ThTi_2O_6$, (MV_2O_6, M = Mg, Ba, Cd, Ca, Zn, Pb, and Sr).[39-45] With the exception of M = Ca and Ba, the vanadium atoms in MV_2O_6 are located at the centre of corner-shared, distorted VO_6 octahedra (Figure 2.1D). Structures with increasingly complex vanadium-oxygen units can be found in the alkali-metal trivalent vanadates (MV_3O_8, M = K, Rb and Cs),[46] which are composed of V_3O_8 layers. These V_3O_8 layers consist of distorted V_aO_6 octahedra and edge-sharing V_bO_5-V_bO_5 square pyramids.

Solid-state ^{51}V NMR is an important technique for structural characterization of vanadates. Vanadium has two NMR-active isotopes which are quadrupolar nuclei (i.e., nuclear spin $I > ½$). ^{50}V has $I = 6$ and a natural abundance of 0.2%, while ^{51}V has a spin of 7/2 and a natural abundance of 99.8%. Solid-state ^{51}V NMR experiments are relatively easy to perform due to its high natural abundance and small nuclear quadrupole moment ($Q = 0.052 \times 10^{-28}$ m^2).[47] Magic-angle spinning (MAS) is commonly used in ^{51}V NMR investigations of vanadia-based catalysts[48-61] and vanadates.[57,62-71] The appearance of solid-state ^{51}V NMR powder patterns mainly depends upon the vanadium chemical shielding (CS) and ^{51}V electric field gradient (EFG) tensors, as well as their relative orientation. These tensors reflect different aspects of the local magnetic and electronic environments about the ^{51}V nucleus, and hence are sensitive probes of molecular structure.

Theoretical calculations of tensor parameters often complement solid-state ^{51}V NMR experiments conducted on powdered samples.[60,65,67-69,72,73] However, first principles calculation of ^{51}V EFG tensors in solid vanadates is challenging, since the individual units comprising vanadates form extended periodic lattices; thus long range electrostatic interactions may have to be considered. Aside from empirical "point-charge" calculations, there are two common modern methods for accurate calculation of EFG tensors in solids: plane wave calculations on large periodic lattices and molecular orbital (MO) calculations on isolated clusters. Plane wave calculations are considered to be one of the most accurate methods of calculating the electronic band structure of extended solids.[74,75] Plane wave calculations have been applied to calculate the EFGs of numerous nuclei across the periodic table.[76-91] MO calculations of EFG tensors using Hartree-Fock (HF) and/or density functional theory (DFT) methods are sometimes inaccurate due to the effects of truncating the extended structure (i.e., a calculation on an isolated cluster does not account for long-range electrostatic interactions or charges in bonding resulting from corner, edge and/or face sharing with neighbouring units). The embedded cluster MO (ECMO) approach or the analogous embedded ion method (EIM) can sometimes be utilized to accurately model long-range electrostatic interactions, and have been applied to numerous systems to calculate NMR interaction tensors.[92-111] In ECMO calculations, the isolated cluster is embedded within a lattice of empirically determined or theoretically calculated point charges, providing an inexpensive means of approximating the extended lattice about the cluster. However, the usefulness of this method is limited by the size and shape of the lattice, as well as the "correctness" of the surrounding point charges. Nonetheless, (EC)MO calculations of ^{51}V EFG tensor parameters in various vanadium-oxide systems have been reported.[108,112-114]

Herein, we present a comprehensive set of theoretically calculated ^{51}V EFG tensors for a series of well-characterized pyrovanadates and metavanadates (i.e., the crystal structures have been experimentally determined and quadrupolar parameters have been measured) to complement similar theoretical studies reported by other research groups.[108,114] RHF and B3LYP methodologies are applied on a series of isolated clusters which are unique to each class of vanadates, and a systematic set of results for isolated and embedded clusters are carefully examined. In order to see if such calculations can correctly predict experimentally measured ^{51}V EFG tensors, several important factors are taken into account, including the level of calculations (method and basis sets), cluster size, cluster charge, nature of termination of the cluster (where necessary), and necessity for ECMO calculations.

2.2 Experimental

Materials. Structural parameters of all pyrovanadates: α-$Zn_2V_2O_7$,[26] $Cd_2V_2O_7$,[28] β-$Mg_2V_2O_7$,[27] $BaCaV_2O_7$[30], and metavanadates: $LiVO_3$,[34] α-$NaVO_3$,[35] KVO_3,[37] ZnV_2O_6[43] and MgV_2O_6,[39] were obtained from experimentally determined crystal structures. The ^{51}V EFG tensors of vanadates were calculated for both isolated and embedded clusters. For ECMO calculations, the cluster is positioned at the centre of a spherical lattice of point charges with a radius of 20 Å (the number of point charges in the sphere varies from ca. 2000 to 5600, depending upon the molecular structure). The point charges of individual atoms (i.e., V and O) were obtained from Mulliken population analyses, whereas the point charges of atoms other than those in the embedded cluster (e.g., alkali cations) were set to be equal to their oxidation states.

Calculation methods and basis sets. Restricted Hartree-Fock (RHF) and hybrid density functional theory (Becke's three-parameter hybrid density functional[115,116] with Lee, Yang and Parr correlation functional[117]; B3LYP) calculations were carried out using the Gaussian 98 software package[118] on a Dell Precision 420 workstation with dual 733 MHz Pentium III processors. Two all-electron basis sets: 14s8p5d(4F) and 14s8p5d(6D) which correspond to the valence shell electron configurations of $3d^3 4s^2$ and $3d^4 4s^1$, respectively,[119] were used for the vanadium atoms. Double- and triple-zeta basis sets with the addition of both polarization functions, 6-31G** and 6-311G**, and diffuse functions, 6-311+G** and 6-311++G**, were used for all other atoms in the cluster.

Calculation models. The terminal oxygen atoms in metavanadates have different charges than those at the bridging positions (Figure 2.1B), since the latter have bonding interactions with vanadium atoms in the second coordination sphere. Therefore, a hydrogen atom is appended to each bridging oxygen site to produce an $H_2VO_4^-$ cluster. This serves to approximate the second-coordination sphere bonding interaction, as well as decreasing the negative charge of the cluster, both of which can have significant effects on the calculated EFG tensor components. In addition, the computational time is greatly reduced compared to calculations on larger clusters.[108,113,120,121] The positions of the hydrogen atoms are fixed in the direction of second-coordination sphere vanadium sites, but with geometry-optimized O-H bond lengths. Terminal protonation of such clusters has been used in numerous studies of the electronic structure of solid V_2O_5,[113,120] magnetic exchange interactions in μ-hydroxo bridged vanadium(IV) dimers,[121] and ^{51}V EFG tensor calculations on orthovanadates.[108]

2.3 Results and Discussion

Pyrovanadates, α-$Zn_2V_2O_7$ and $Cd_2V_2O_7$. α-$Zn_2V_2O_7$[26] and $Cd_2V_2O_7$[28] have space groups *C*2/c and *C*2/m (β = 111.37° and 103.35°), respectively. The Zn and Cd cations, which are five- and six-coordinate, respectively, are at distorted trigonal bipyramidal and octahedral sites. The ZnO_5 and CdO_6 units are edge-shared with their neighbours, resulting in two-dimensional, hexagonal layers in the *ab*-planes, stacking along the *c*-axes of the unit cells (Figure 2.2). In both pyrovanadates, there is only a single crystallographically distinct vanadium site, positioned between the ZnO_5 (or CdO_6) layers (Figure 2.2B,D). The V-V vectors within the pyro units are directed close to the *a*-axes of the unit cells with $\angle V-V-a$-axis = 14° in both cases. Figure 2.3A depicts the V_2O_7 unit in α-$Zn_2V_2O_7$, which has C_2 symmetry. The bridging oxygen atom (O1, hereafter denoted as O_B) connects the two four-coordinate vanadium atoms in a bent arrangement ($\angle(V-O_B-V) \approx 150°$), and the terminal oxygen atoms (O2, O3 and O4, hereafter denoted as O_T) are coordinated by two, two and one Zn atoms, respectively. The V_2O_7 unit of $Cd_2V_2O_7$ has C_{2h} symmetry (Figure 2.3B) and possesses a linear V-O1-V arrangement, with each O_T weakly coordinated by two Cd atoms. The C_2 axes of the pyro units are along the crystallographically unique *b*-axes of the unit cells in both α-$Zn_2V_2O_7$ and

$Cd_2V_2O_7$.

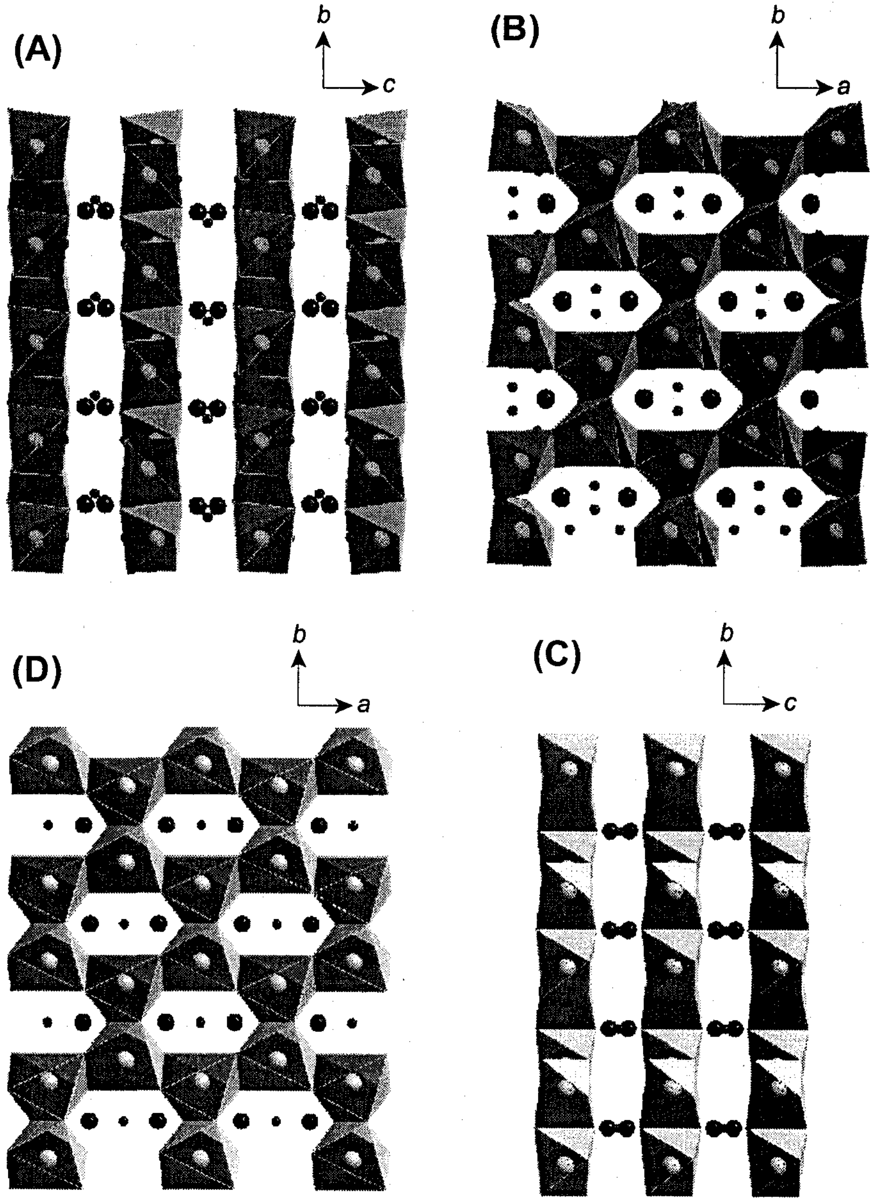

Figure 2.2. (A) and (B) ZnO_5, and (C) and (D) CdO_6 polyhedra in α-$Zn_2V_2O_7$ and $Cd_2V_2O_7$ pyrovanadates, respectively, looking along particular crystallographic axes as shown in the pictures. Cation layers stacking along *c*-axis is shown in (A) and (C), while "porous" structure can be seen in (B) and (D). Big, medium and small circles indicate counter cations, V and O atoms, respectively.

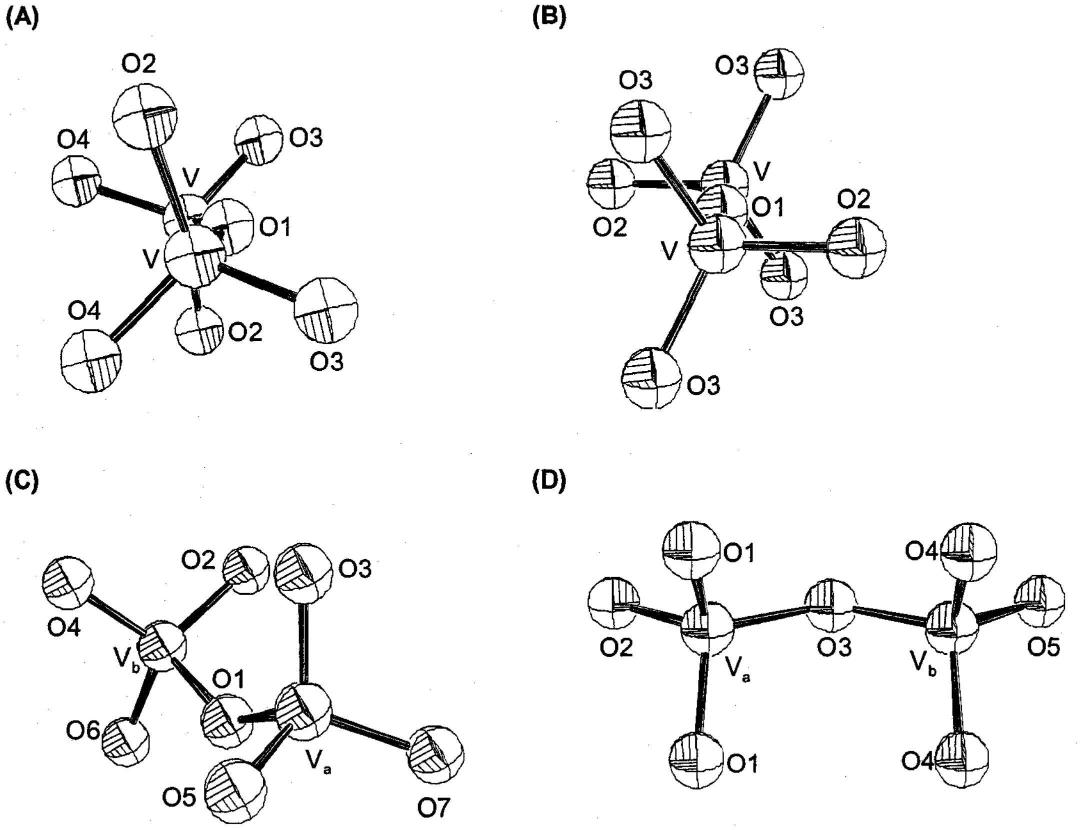

Figure 2.3. Vanadium–oxygen (pyro) units in (A) α-$Zn_2V_2O_7$, (B) $Cd_2V_2O_7$, (C) β-$Mg_2V_2O_7$, and (D) $BaCaV_2O_7$ pyrovanadates.

Calculations on the $V_2O_7^{4-}$ clusters yielded parameters in reasonably good agreement with experiment (Table 2.1), while those on truncated VO_4^{3-} clusters yielded poor agreement (see Appendices, Table A.2.1). The B3LYP/4F/6-311+G** calculation on an isolated $V_2O_7^{4-}$ cluster of α-ZnV_2O_7 agrees best with experiment, with the quadrupolar coupling constant, $C_Q = 3.41$ MHz, and the asymmetry parameter, $\eta_Q = 0.69$ (see Table 2.1 footnotes for definitions of all quadrupolar and EFG tensor parameters). Interestingly, the C_Q (3.94 MHz) predicted from B3LYP/6D/6-311G** calculation has better agreement. However, calculations involving basis sets smaller than 6-311+G** on the O atoms are relatively inconsistent, in that the calculated quadrupolar parameters are

Table 2.1. Selected ^{51}V EFG Tensor Parameters of α-$Zn_2V_2O_7$ and $Cd_2V_2O_7$ Pyrovanadates.

Vanadate	Cluster[a]	Level of Theory[b]	V_{11} (a.u.)[c]	V_{22} (a.u.)	V_{33} (a.u.)	$\lvert C_Q\rvert$[d]	η_Q[e]
α-$Zn_2V_2O_7$	–	**Experimental[f]**	–	–	–	**3.86**	**0.56**
	$V_2O_7^{4-}$	iR411+	0.0066	0.222	-0.2285	2.79	0.94
	$V_2O_7^{4-}$	iR611+	-0.0183	-0.2184	0.2367	2.89	0.85
	$V_2O_7^{4-}$	iB411+	0.0439	0.2349	-0.2788	3.41	0.69
	$V_2O_7^{4-}$	iB611+	0.0224	0.2537	-0.2761	3.37	0.84
	$V_2O_7^{4-}$	eR411+	0.2007	0.2714	-0.4721	5.77	0.15
	$V_2O_7^{4-}$	eR611+	0.2290	0.2854	-0.5144	6.28	0.11
	$V_2O_7^{4-}$	eB411+	0.1721	0.3158	-0.4879	5.96	0.29
	$V_2O_7^{4-}$	eB611+	0.2130	0.3183	-0.5313	6.49	0.20
$Cd_2V_2O_7$	–	**Experimental[f]**	–	–	–	**6.00**	**0.41**
	$V_2O_7^{4-}$	iR411+	0.1225	0.2893	-0.4118	5.03	0.41
	$V_2O_7^{4-}$	iR611+	0.1032	0.2993	-0.4025	4.92	0.49
	$V_2O_7^{4-}$	iB411+	0.1419	0.2988	-0.4407	5.38	0.36
	$V_2O_7^{4-}$	iB611+	0.1305	0.3131	-0.4437	5.42	0.41
	$V_2O_7^{4-}$	eR411+	0.0634	0.4582	-0.5216	6.37	0.76
	$V_2O_7^{4-}$	eR611+	0.0476	0.4969	-0.5445	6.65	0.83
	$V_2O_7^{4-}$	eB411+	0.0129	0.5757	-0.5886	7.19	0.96
	$V_2O_7^{4-}$	eB611+	0.0370	0.6009	-0.6379	7.79	0.88

[a] Cluster sizes utilized in calculations; [b] isolated (i) or embedded (e) cluster calculation in the form methods/basis sets (V)/basis sets (all other atoms). R = RHF, B = B3LYP, 4 = 4F, 6 = 6D all-electron basis sets, and 1, 11, 11+ and 11++ = 6-31G**, 6-311G**, 6-311+G** and 6-311++G** basis sets, respectively. For instance, iR411+ = RHF/4F/6-311+G** calculation on an isolated cluster; [c] principal components of the EFG tensor with $|V_{11}|\leq|V_{22}|\leq|V_{33}|$ in atomic units; [d] absolute values of quadrupolar coupling constant ($C_Q = eQV_{zz}/h$) of ^{51}V EFG tensor in MHz, and were obtained from multiplying the V_{33} in a.u. by 9.7177×10^{21} $V{\cdot}m^{-2} \times eQ/h$; [e] asymmetric parameters of ^{51}V EFG tensor, $\eta_Q = (V_{11} - V_{22})/V_{33}$; [f] obtained from reference [69].

quite random and only seem to match with experimental data by chance; hence, these calculations are not listed in Table 2.1 nor discussed further. In addition, ECMO calculations fail to reproduce experimental quadrupolar parameters; in fact, the C_Q and η_Q are always over- and underestimated, respectively (Tables 2.1 and A.2.1). The EFG tensor orientation from B3LYP/4F/6-311+G** calculations is depicted in Figure 2.4A. The largest component of the ^{51}V EFG tensor, V_{33}, is oriented near to both the bridging

V-O_B bond ($\angle V_{33}$-V-O_B = 10.7°) and the *a*-axis of the unit cell (with an angle of ca. 6°). The intermediate component, V_{22}, is directed close to one of the V-O_T (V-O4) bonds with $\angle V_{22}$-V-O4 = 12°.

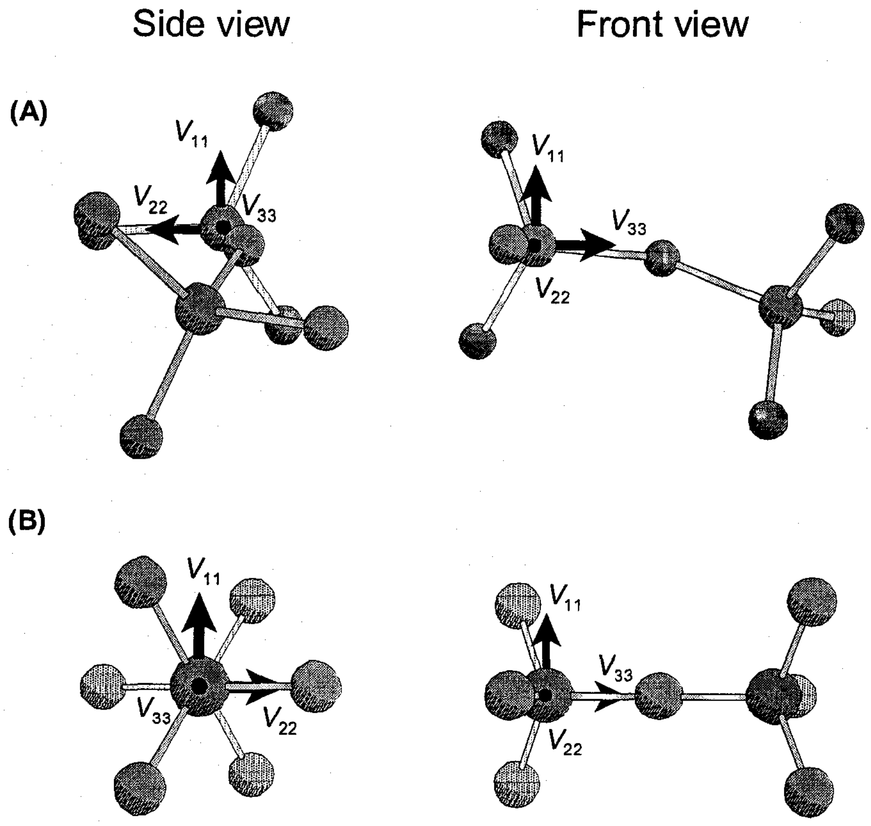

Figure 2.4. Calculated orientation of the ^{51}V EFG tensor in (A) α-$Zn_2V_2O_7$ and (B) $Cd_2V_2O_7$ pyrovanadates.

For $Cd_2V_2O_7$, good agreement between calculated and experimental quadrupolar parameters is also obtained, notably for the B3LYP/(4F and 6D)/6-311+G** calculations on isolated $V_2O_7^{4-}$ clusters (Tables 2.1 and A.2.2). All calculations predict similar ^{51}V EFG tensor orientations, with the orientation from the B3LYP/4F/6-311+G** calculation depicted in Figure 2.4B. As in the case of α-$Zn_2V_2O_7$, V_{33} is oriented near the V-O_B bond

($\angle V_{33}$–V–O_B = 4.0°) and *a*-axis (10°). V_{22} is directed close to the shortest V-O_T (O2) bond with $\angle V_{22}$-V-O2 = 18°, as well as the crystallographic *c*-axis ($\angle V_{22}$-V-*c*-axis = 24°), while V_{11} is parallel to the crystallographically unique *b*-axis. Furthermore, V_{22} and V_{33} are in the σ_h mirror plane. The smaller value of $C_Q(^{51}V)$ in α-$Zn_2V_2O_7$ in comparison to $Cd_2V_2O_7$ indicates that the former has higher spherical symmetry at the vanadium site, due to smaller variation in the O-V-O bond angles in the former (between 108.2° and 110.6°) compared to the latter (between 104.1° and 112.6°).

β-$Mg_2V_2O_7$ and $BaCaV_2O_7$. β-$Mg_2V_2O_7$ and $BaCaV_2O_7$, with space groups $P\bar{1}$ (α = 81.42°, β = 106.82°, γ = 130.33°),[27] and *Pnma*,[30] respectively, have two crystallographically distinct vanadium sites, hereafter denoted as V_a and V_b. In β-$Mg_2V_2O_7$, there are two cationic sites, Mg1 and Mg2, both of which are in distorted octahedral environments (Figure 2.5).

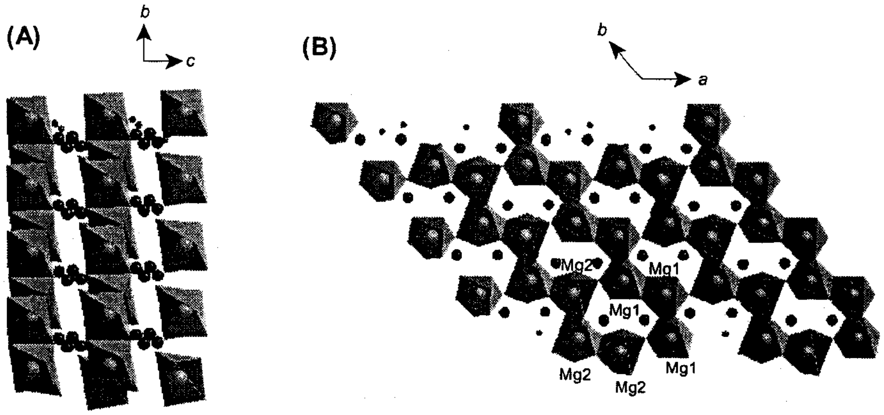

Figure 2.5. MgO_6 polyhedra in β-$Mg_2V_2O_7$ pyrovanadates, looking along the crystallographic (A) *a*- and (B) *c*-axes. Cation layers stacking along *c*-axis is shown in (A) and "porous" structure can be seen in (B). Big, medium and small circles indicate counter cations, V and O atoms, respectively.

Similar to α-$Zn_2V_2O_7$ and $Cd_2V_2O_7$, the cation-oxygen polyhedra of β-$Mg_2V_2O_7$ form a hexagonal 2D layer in the *ab*-plane, but with a slightly different arrangement of atoms (Figure 2.5A). The V atoms are located between layers comprised of $Mg1O_6$ and $Mg2O_6$ units (Figure 2.5B), and the V_2O_7 units have V-O bond lengths ranging from 1.629 to 1.817 Å (Figure 2.3C).

Table 2.2. Selected ^{51}V EFG Tensor Parameters of β-$Mg_2V_2O_7$ and $BaCaV_2O_7$ Pyrovanadates.

Vanadate	Cluster[a]	Site	Level of Theory[b]	V_{11} (a.u.)[c]	V_{22} (a.u.)	V_{33} (a.u.)	$\lvert C_Q\rvert$[d]	η_Q[e]
β-$Mg_2V_2O_7$	–	**a**	**Experimental[f]**	–	–	–	**4.80**	**0.39**
	–	**b**		–	–	–	**10.10**	**0.44**
	$V_2O_7^{4-}$	a	iR411+	0.1487	0.2033	-0.3521	4.30	0.16
		b		0.1826	0.7524	-0.9350	11.43	0.61
	$V_2O_7^{4-}$	a	iR611+	0.1496	0.2020	-0.3517	4.30	0.15
		b		0.1929	0.8203	-1.0133	12.38	0.62
	$V_2O_7^{4-}$	a	iB411+	0.1868	0.2184	-0.4052	4.95	0.08
		b		0.2017	0.6684	-0.8701	10.63	0.54
	$V_2O_7^{4-}$	a	iB611+	0.1875	0.2232	-0.4107	5.02	0.09
		b		0.2212	0.7504	-0.9716	11.87	0.54
$BaCaV_2O_7$	–	**a**	**Experimental[f]**	–	–	–	**2.57**	**0.32**
	–	**b**		–	–	–	**3.20**	**0.85**
	$V_2O_7^{4-}$	a	iR411+	-0.0725	-0.1292	0.2017	2.46	0.28
		b		-0.0484	-0.2646	0.3129	3.82	0.69
	$V_2O_7^{4-}$	a	iR611+	-0.0864	-0.1414	0.2278	2.78	0.24
		b		-0.0452	-0.3062	0.3514	4.29	0.74
	$V_2O_7^{4-}$	a	iB411+	-0.0097	-0.1821	0.1917	2.34	0.90
		b		-0.1211	-0.1867	0.3078	3.76	0.21
	$V_2O_7^{4-}$	a	iB611+	-0.0213	-0.1914	0.2127	2.60	0.80
		b		-0.1207	-0.2236	0.3443	4.21	0.30

[a-e] See footnotes of Table 2.1; [f] obtained from reference [69].

Several calculations, most notably the B3LYP/4F/6-311+G** calculation, predict the value of C_Q fairly accurately; however, η_Q is underestimated in all cases (Tables 2.2 and A.2.3). All calculations predict that V_{33} at both V sites are oriented near the V-O_B bonds (Figure 2.6A), with $\angle V_{33}$-V_a-O_B = 6.0° and $\angle V_{33}$-V_b-O_B = 19.4° for the B3LYP/4F/6-311+G** calculation. Since the pyro unit has C_1 symmetry, V_{11} and V_{22} are not constrained by any symmetry elements. The disparate values of C_Q for V_a and V_b arise from the slight geometrical differences between the VO_4 units. The V-O bond lengths in the V_aO_4 and V_bO_4 pseudo-tetrahedra are similar: 1.629 to 1.817 Å and 1.665 to 1.785 Å, respectively. However, the O-V-O bond angles in V_aO_4 and V_bO_4 range from 108° to 110° and 104° to 124°, respectively; hence, the less spherically symmetric environment at V_b produces larger EFGs.

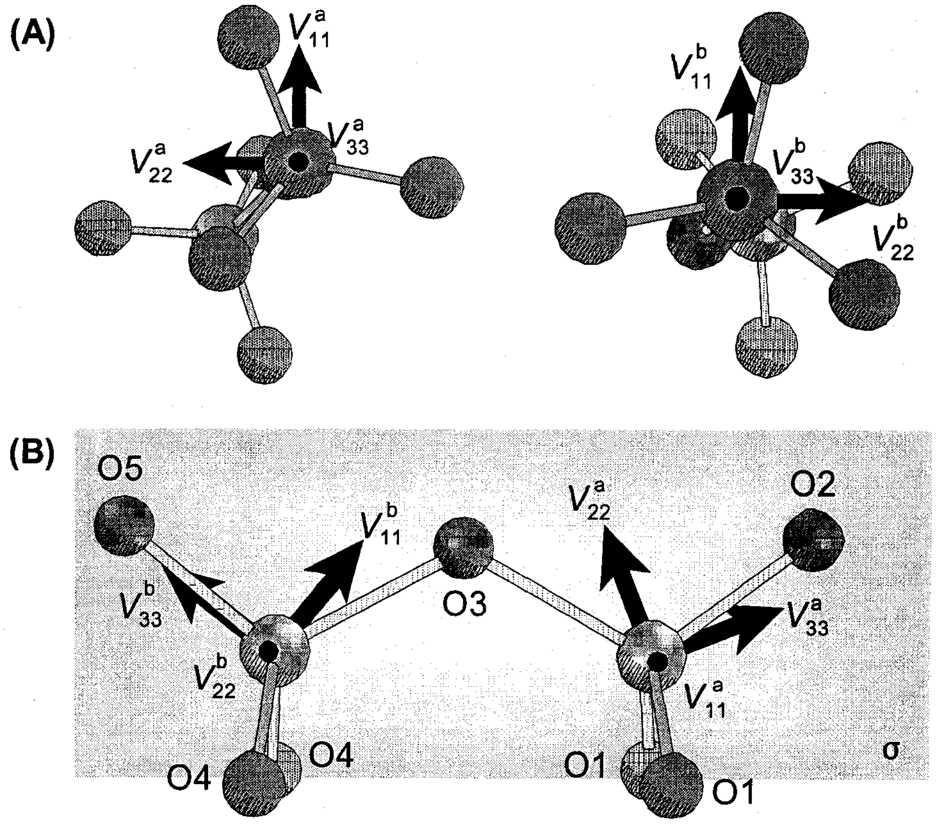

Figure 2.6. Theoretically determined ^{51}V EFG tensor orientations of (A) β-$Mg_2V_2O_7$ at V_a (left) and V_b (right) sites, and (B) $BaCaV_2O_7$ pyrovanadates. The mirror plane in the vanadium-oxygen unit in (B) is denoted as σ.

In $BaCaV_2O_7$, the Ba and Ca cations are eight- and six-coordinate, respectively. Each of the CaO_6 (trigonal prism) and BaO_8 (doubly-capped trigonal prism) units are edge and corner shared, respectively, to their neighbours (Figure 2.7). The "dichromate"-type $V_2O_7^{4-}$ cluster (Figure 2.3D) has no rotational symmetry axis, but a mirror plane (σ) is present which is parallel to the *ac*-plane (i.e., the pyro unit has a C_s symmetry). The O2, V_a, O3, V_b and O5 atoms are contained with σ, which reflects two O1 and two O4 atoms with V–O bond lengths of 1.692 Å and 1.710 Å, respectively. The coordination environments of V_a and V_b are very similar to one another (V–O bond lengths and O-V-O

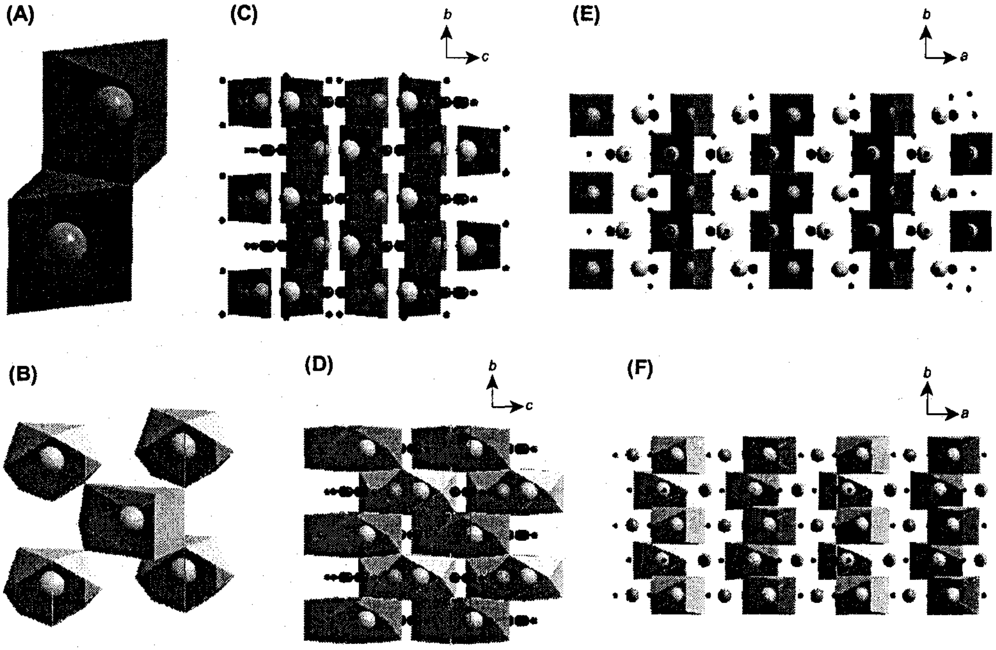

Figure 2.7. (A) Two edge-shared, trigonal prisms for CaO_6 units, (B) five corner-shared, doubly-capped trigonal prism for BaO_8 units, (C) the edge-shared CaO_6 units extend in the *b* direction, (D) corner-shared BaO_8 units form a two-dimensional layer on the *bc*-plane, (E) and (F) both one- and two-dimensional CaO_6 chains and BaO_8 layers stack along the *a*-axis.

bond angles in V_aO_4 and V_bO_4 pseudo-tetrahedra differ by only ca. 0.2 Å and 2°, respectively), accounting for the similarity of the experimentally measured C_Q at these sites.

Unlike in the previously discussed systems, both RHF/4F/6-311+G** and RHF/6D/6-311+G** calculations are in good agreement with experimental values (Tables 2.2 and A.2.4). The corresponding B3LYP calculations predict C_Q fairly closely, but the values of η_Q are incorrect (Table 2.2). Figure 2.6B shows the ^{51}V EFG tensors at both V_a and V_b sites. In contrast to the thortveitite mineral type pyrovanadates (which have staggered pyro units), V_{33} at both sites are not oriented towards the O_B atom, but rather, are contained within σ and directed near the terminal O2 and O5 atoms ($\angle V_{33}^{a}$-V_a-O2 = 15° and $\angle V_{33}^{b}$-V_b-O5 = 1.4°). The V_{22}^{a} and V_{11}^{b} components (the latter is the pseudo-unique component) are contained within σ, consistent with distinct values of η_Q at V_a and V_b sites (Table 2.2). Finally, V_{11}^{a} and V_{22}^{b} are perpendicular to σ as well as the *b*-axis of the unit cell.

Comparison of calculations between isolated and embedded clusters reveals that inclusion of a surrounding lattice of point charges does not lead to any significant improvement in agreement with experimental values of C_Q, though the longer range electrostatic interactions from the lattice may have some influence on values of η_Q in certain systems. This suggests that for pyrovanadates, the local structure and symmetry of the pyro units are predominant in determining the magnitude and symmetry of the ^{51}V EFG tensors, and the surrounding lattice is of little importance. B3LYP/4F/6-311+G** calculations consistently provide good correspondence between experimental and theoretical quadrupolar parameters in the "thortveitite" structural type (staggered V_2O_7 units), while RHF/{4F,6D}/6-311+G** calculations succeed for the "dichromate" structural type (eclipsed V_2O_7 units). This difference in the success of these methodologies may have to do with the orientation of V_{33} in each mineral type: the thortveitite systems have V_{33} directed along or near the V-O_B bond, while the dichromate system has V_{33} oriented towards the terminal O atoms.

Metavanadates. Owing to the wide range of different structural types present in metavanadates, a large variety of test calculations were carried out using an assortment of cluster sizes, calculation methods and basis sets. The vanadium atom within the vanadium-oxygen unit is typically four- or six-coordinate (Figure 2.1B,D). In addition, the vanadium-oxygen units are not isolated; rather, they are corner or edge shared, giving rise to infinite one-dimensional chains or two-dimensional layers. In order to reduce cluster sizes, while still approximating the bridging V-O-V interactions and reducing the overall negative charge on the cluster, certain V-O bridging bonds are terminated with hydrogen atoms (see experimental section for details).

$LiVO_3$, α-$NaVO_3$ and KVO_3. The crystal structure of $LiVO_3$ (space group *C2/c*, β = 110.48°)[34] reveals two distinct cationic sites, Li1 and Li2, which are both at the centre of distorted, edge-shared octahedra (Figure 2.8A). The vanadium atoms are located between the lithium-oxygen layers (Figure 2.8B,C), and only a single crystallographic site is present. The vanadium atom is at the centre of a distorted tetrahedron, with V-O bond lengths ranging from 1.63 Å to 1.82 Å.[34] O3 and O3a are corner-shared with the neighbouring VO_4 units (Figures 2.1B and 2.9A), giving rise to zig-zagging one-dimensional chains extending in the *c* direction of the unit cell. For α-$NaVO_3$ (space group *C*2/*c*, β = 108.47°), the cationic (Na), V and O sites are arranged similarly to those in $LiVO_3$, since these structures are isomorphic.[35]

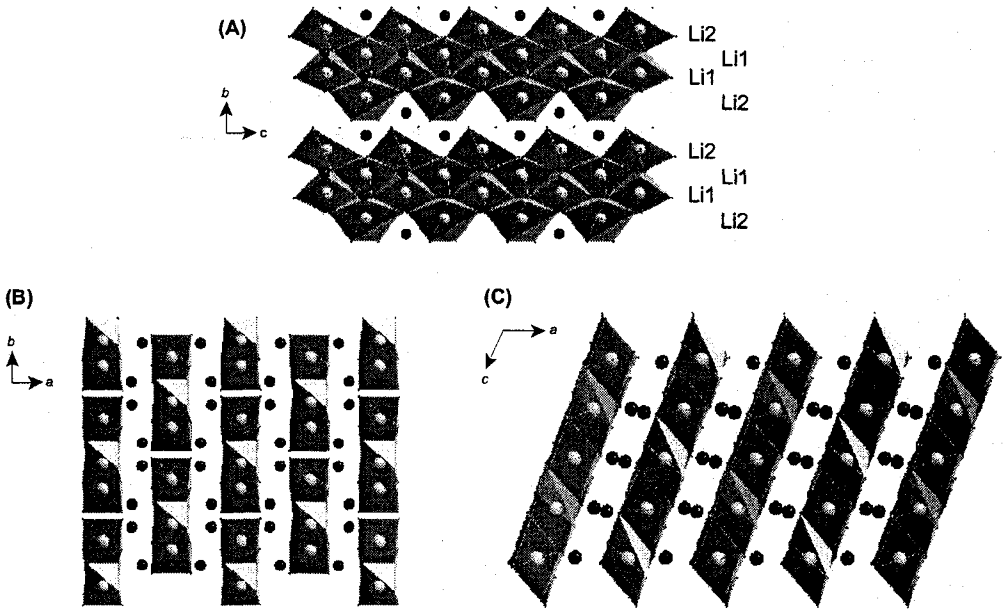

Figure 2.8. (A) Alternating, edge-shared $Li1O_6$ and $Li2O_6$ units in a zig-zag arrangement extend along the *c*-axis, giving rise to discrete two-dimensional sheets, and (C) and (D) the $Li1O_6$-$Li2O_6$ two-dimensional sheets stack along *a*-axis in $LiVO_3$ metavanadate. Big, medium and small circles indicate counter cations, V and O atoms, respectively.

For $LiVO_3$, initial calculations conducted on both isolated and embedded VO_4^{3-} clusters were not successful, with the value of C_Q consistently overestimated by a minimum of 1 MHz (Table A.2.5). Similar results were obtained by Vorotilova *et al.*, who reported a theoretical study of ^{51}V EFG tensors in $LiVO_3$, α-$NaVO_3$ and KVO_3 metavanadates by ab initio cluster calculations.[114] To improve the accuracy of calculated EFG parameters, these same authors performed calculations on an extended

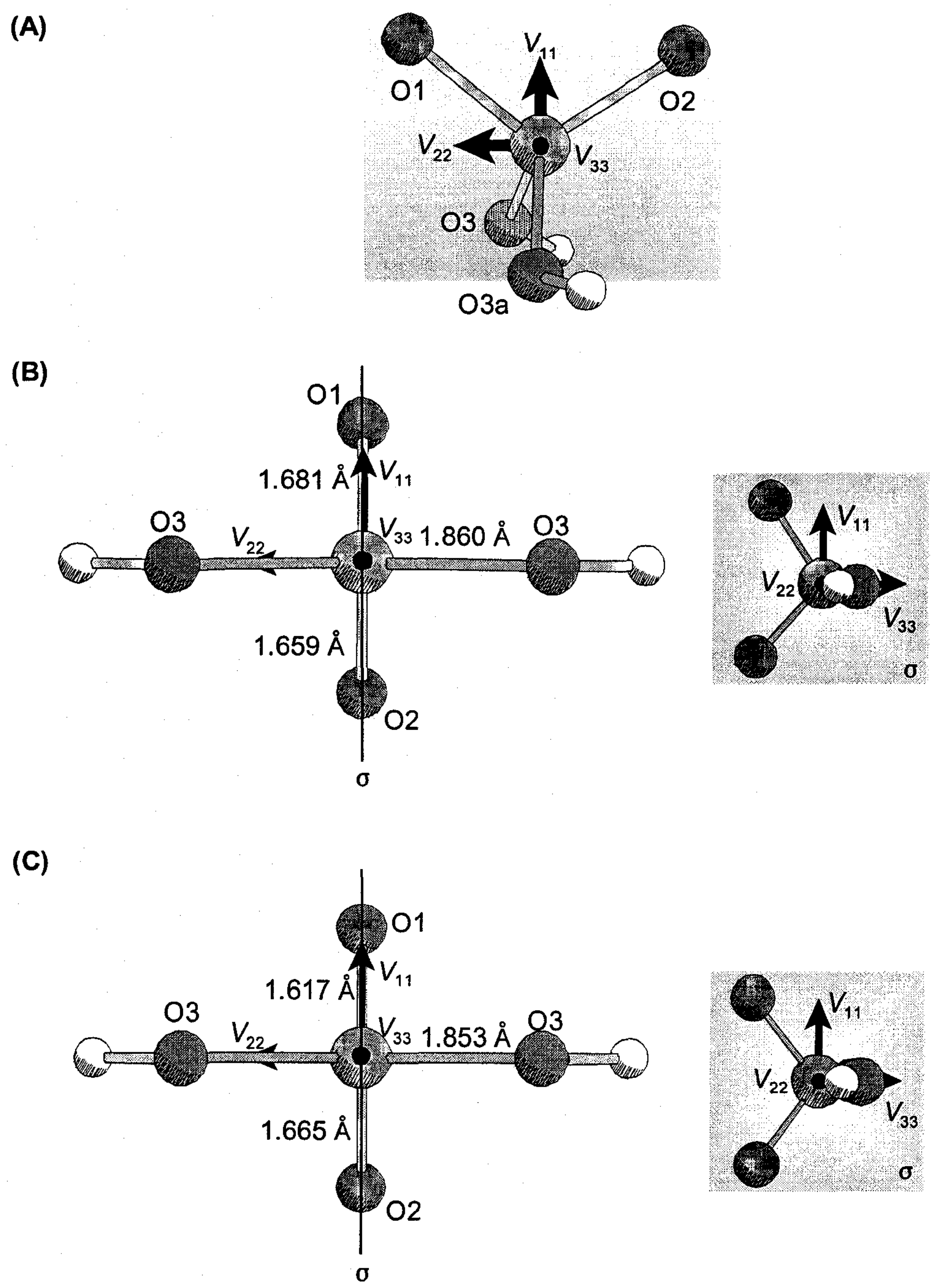

Figure 2.9. Theoretically determined ^{51}V EFG tensor orientations for (A) $LiVO_3$, (B) ZnV_2O_6 and (C) MgV_2O_6 metavanadates. Mirror planes of vanadium-oxygen units are denoted with σ. Insets in (B) and (C) show side views of the molecule.

cluster, $V_3O_{10}^{5-}$; however, even though the agreement for η_Q improved, poorer agreement was obtained for values of C_Q. In order to avoid the large and computationally expensive $V_3O_{10}^{5-}$ clusters, and also to reduce the overall negative charge, we have differentiated the O_B and O_T sites in the small VO_4 units by terminating the former with hydrogen atoms (i.e., $H_2VO_4^-$ clusters). While this improves agreement between experiment and theory, even better agreement can be obtained from ECMO calculations on $H_2VO_4^-$ clusters. In particular, both B3LYP/4F/{6-311+G**, 6-311++G**} calculations yield the best

Table 2.3. Selected[a] ^{51}V EFG Tensor Parameters of $LiVO_3$, ZnV_2O_6 and MgV_2O_6 Metavanadates.

Vanadates	Cluster[b]	Levels of Theory[c]	V_{11} (a.u.)[d]	V_{22} (a.u.)	V_{33} (a.u.)	$\lvert C_Q\rvert$[e]	η_Q[f]
$LiVO_3$	–	**Experimental[g]**	–	–	–	**3.25**	**0.88**
	$H_2VO_4^-$	iR41	-0.0463	-0.2891	0.3354	4.10	0.72
	$H_2VO_4^-$	eR411+	-0.0216	-0.3220	0.3436	4.20	0.87
	$H_2VO_4^-$	eR411++	-0.0215	-0.3223	0.3437	4.20	0.87
	$H_2VO_4^-$	eB41	0.0414	0.3003	-0.3419	4.18	0.76
	$H_2VO_4^-$	eB411	0.0370	0.3302	-0.3672	4.49	0.80
	$H_2VO_4^-$	eB411+	-0.0163	-0.3017	0.3180	3.89	0.90
	$H_2VO_4^-$	eB411++	-0.0163	-0.3019	0.3182	3.89	0.90
ZnV_2O_6	–	**Experimental[h]**	–	–	–	**6.86**	**0.40**
	$H_2VO_4^-$	iR411+	0.1527	0.4035	-0.5562	6.80	0.45
	$H_2VO_4^-$	iR411++	0.1483	0.4027	-0.5510	6.73	0.46
MgV_2O_6	–	**Experimental[h]**	–	–	–	**7.50**	**0.34**
	$H_2VO_4^-$	iR411+	0.1660	0.4186	-0.5846	7.14	0.43
	$H_2VO_4^-$	iR411++	0.1612	0.4176	-0.5789	7.07	0.44
	$H_2VO_4^-$	iB41	0.2110	0.3577	-0.5687	6.95	0.26
	$H_2VO_4^-$	eR411+	0.2203	0.4183	-0.6386	7.80	0.31
	$H_2VO_4^-$	eR411++	0.2170	0.4178	-0.6348	7.76	0.32
	$H_2VO_4^-$	eB411+	0.2326	0.3926	-0.6253	7.64	0.26
	$H_2VO_4^-$	eB411++	0.2310	0.3936	-0.6247	7.63	0.26
	$H_2VO_4^-$	iB611+	0.2531	0.442	-0.6951	8.49	0.27
	$H_2VO_4^-$	iB611++	0.2524	0.4438	-0.6962	8.51	0.27
	$H_2VO_4^-$	eB611+	0.1930	0.4838	-0.6767	8.27	0.43
	$H_2VO_4^-$	eB611++	0.1965	0.4816	-0.6781	8.29	0.42

[a] Calculated ^{51}V EFG parameters that are within the cutoff of experimental C_Q ± 1 MHz and experimental η_Q ± 0.1 are listed in the Table; [b-f] see footnotes of Table 2.1; [g] obtained from reference [66]; [h] obtained from reference [68].

parameters (Tables 2.3 and A.2.5). Since the parameters are almost identical for a number of calculations with these basis sets (Table 2.3), the additional diffuse orbitals are deemed to be unnecessary (i.e., the 6-311+G** basis set will suffice). The V_{33} is predicted to be nearly perpendicular to the O_T-V-O_T (O1-V-O2 in the figure) plane (Figure 2.9A), with a dihedral angle of V_{33}-V-O_T-O_T $\approx$ 85°, and is also near the *c*-axis of the unit cell (< 10°). Consequently, both V_{22} and V_{11} are almost within the O_T-V-O_T plane, and the latter, which is the unique component of the ^{51}V EFG tensor, is near the intersection between the O_T-V-O_T and O_B-V-O_B planes.

For α-NaVO$_3$, almost all calculations on isolated VO_4^{3-} clusters yielded quadrupolar parameters that are overestimated (Table A.2.6). ECMO calculations improve the value of η_Q but not C_Q. Surprisingly, calculations on isolated and embedded $H_2VO_4^-$ clusters yielded even poorer agreement with experimental data. Reasonably good agreement between experiment and theory is observed for certain calculations on embedded VO_4^{3-} or isolated $H_2VO_4^-$ clusters in KVO_3 (Table A.2.7). The discrepancy of the calculated EFG tensors in alkali metavanadates likely arises from two major sources: (i) the proton termination may be insufficient for modeling the nature of the extended chains of VO_4 units, (ii) the EFG tensors in the VO_4 units are dramatically affected by second-coordination sphere structure and charges, which may be not properly modeled with simple ECMO methods and/or the embedded ion method (EIM).[96-100,102-105,108-111] It is also important to mention again that increased cluster sizes yield even worse agreement between experiment and theory.[114]

ZnV_2O_6 and MgV_2O_6. ZnV_2O_6 and MgV_2O_6 ($\beta = 111.37°$ and $111.77°$, respectively) have the same space group (*C*2/*m*).[39,43] The cations are at the centre of distorted octahedra, with Zn-O and Mg-O bond lengths ranging from 1.98 to 2.25 and 2.02 to 2.20 Å, respectively. The vanadium-oxygen units in both complexes can be thought of as distorted tetrahedra (with V-O bond lengths ranging from 1.66 to 1.85 Å) or distorted octahedra with two relatively long V-O contacts (2.08 and 2.67 Å; Figures 2.1D and 2.10). The VO_4 units (Figure 2.9B,C) possess mirror planes containing two V-O_T bonds (O1 and O2), and bisecting two longer V-O_B (O3) bonds. In addition, the mirror plane in both complexes is parallel to the *ac*-plane of the unit cells, with zig-zagging, corner-shared VO_4 units along the *b*-axis.

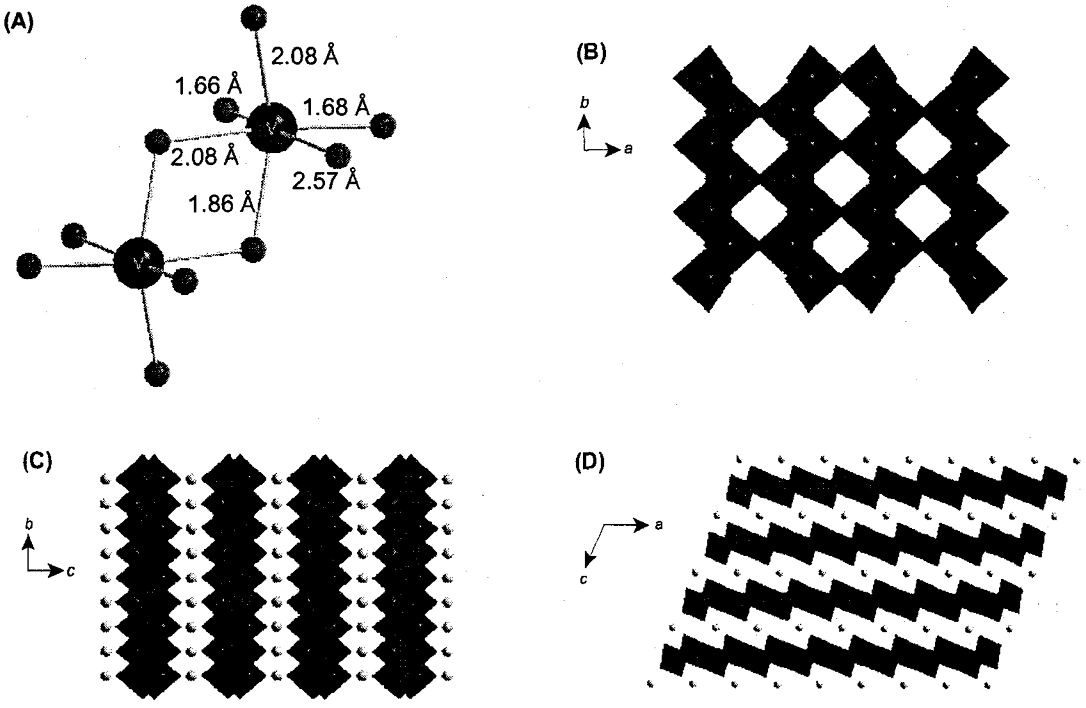

Figure 2.10. (A) Edge-sharing VO_6 units in ZnV_2O_6 metavanadates. (B) Two-dimensional sheet that is composed of VO_6 octahedra extend parallel to the *ab* plane. (C) and (D) Two-dimensional VO_6 sheets stack along the *c*-axis of the unit cell.

For ZnV_2O_6 and MgV_2O_6, ab initio calculations were conducted on both isolated and embedded tetrahedra and octahedra. Poor agreement was obtained (or calculations sometimes failed to converge) for all calculations conducted on isolated and embedded VO_6^{7-} and VO_5^{5-} (in MgV_2O_6 only; Figure 2.1D) clusters in both ZnV_2O_6 and MgV_2O_6 (Tables A.2.8 and A.2.9). Although reasonable values of C_Q were predicted in some cases, the values of η_Q were largely overestimated (Table A.2.9). On the other hand, much better results are obtained in calculations on $H_2VO_4^-$ clusters, with RHF/4F/{6-311+G**, 6-311++G**} calculations yielding the best agreement (Table 2.3). ECMO calculations at the same level of theory for MgV_2O_6 slightly improve theoretically predicted values of C_Q and η_Q, but slightly poorer agreement is obtained for ZnV_2O_6 (Table A.2.8). The differences in EFG components are not large in these cases, but the exact reasons for the seemingly random influence of the surrounding lattice are unknown at the present time.

The orientation of the calculated ^{51}V EFG tensors of isolated $H_2VO_4^-$ clusters in ZnV_2O_6 and MgV_2O_6 are depicted in Figure 2.9B,C. For both ZnV_2O_6 and MgV_2O_6, V_{11} and V_{33} are contained within σ, with the latter oriented along the intersection of the O_T-V-O_T and O_B-V-O_B planes, as well as the *c*-axis of the unit cell. Since σ is in the *ac*-plane, V_{22} is along the unique *b*-axis. The ECMO calculations on MgV_2O_6 result in a different EFG tensor orientation despite the similarity of the parameters: the directions of V_{22} and V_{33} interchange, and all three components are no longer constrained by the σ element (Figure 2.11). Similar effects on tensor orientation are seen for calculations on the $H_2VO_4^-$ cluster of ZnV_2O_6; however, the principle components are quite distinct between the two calculations. The inclusion of a lattice of point charges can clearly influence not only the magnitude of the components, but the orientation of the EFG tensor in smaller clusters.

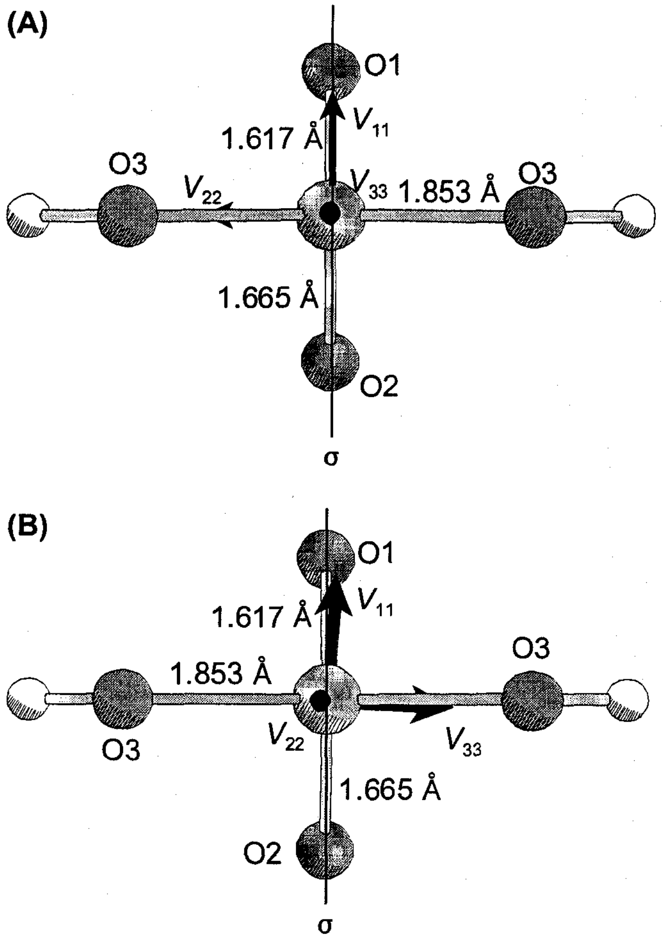

Figure 2.11. Theoretical ^{51}V tensor orientation of (A) isolated and (B) embedded $H_2VO_4^-$ clusters in MgV_2O_6 metavanadate.

Ab initio calculations on $H_2VO_4^-$ clusters in metavanadates provide EFG tensor parameters which are in good agreement with experimental data (with the exception of some vanadates from the pyroxene family); calculations on computationally demanding

Table 2.4. Theoretical ^{51}V EFG Tensor Parameters Obtained from 4F and 6-311+G Basis Sets for all Vanadates Presented in This Work.**

Vanadates	Site	Levels of Theory[a]	V_{11} (a.u.)[b]	V_{22} (a.u.)	V_{33} (a.u.)	$\|C_Q\|$[c]	η_Q[d]
α-$Zn_2V_2O_7$	**---**	**Experimental[e]**	–	–	–	**3.86**	**0.56**
	---	iB411+	0.0439	0.2349	-0.2788	3.41	0.69
	---	iR11+[e]	0.0449	0.1519	-0.1967	2.40	0.54
	---	iB11+	0.0676	0.2254	-0.2930	3.58	0.54
$Cd_2V_2O_7$	**---**	**Experimental[e]**	–	–	–	**6.00**	**0.41**
	---	iB411+	0.1419	0.2988	-0.4407	5.38	0.36
	---	iR11+	0.1729	0.2729	-0.4458	5.45	0.22
	---	iB11+	0.1813	0.3248	-0.5061	6.18	0.28
β-$Mg_2V_2O_7$	**a**	**Experimental[e]**	–	–	–	**4.80**	**0.39**
	b		–	–	–	**10.10**	**0.44**
	a	iB411+	0.1868	0.2184	-0.4052	4.95	0.10
	b		0.2017	0.6684	-0.8701	10.63	0.54
	a	iR11+	0.0688	0.2851	-0.3539	4.32	0.61
	b		0.1895	0.8389	-1.0283	12.56	0.63
	a	iB11+	0.1474	0.2795	-0.4269	5.22	0.31
	b		0.2432	0.8121	-1.0553	12.89	0.54
$BaCaV_2O_7$	**a**	**Experimental[e]**	–	–	–	**2.57**	**0.32**
	b		–	–	–	**3.20**	**0.85**
	a	iR411+	-0.0725	-0.1292	0.2017	2.46	0.28
	b		-0.0484	-0.2646	0.3129	3.82	0.69
	a	iR11+	-0.1059	-0.1404	0.2463	3.01	0.14
	b		0.0286	0.2904	-0.3191	3.90	0.82
	a	iB11+	-0.0624	-0.1647	0.2272	2.78	0.45
	b		-0.0853	-0.255	0.3403	4.16	0.50
$LiVO_3$	**---**	**Experimental[f]**	–	–	–	**3.25**	**0.88**
	---	eB411+	-0.0163	-0.3017	0.3180	3.89	0.90
	---	eR11+	-0.0532	-0.2355	0.2887	3.53	0.63
	---	eB11+	-0.1208	-0.3013	0.4221	5.16	0.43
ZnV_2O_6	**---**	**Experimental[g]**	–	–	–	**6.86**	**0.40**
	---	iR411+	0.1527	0.4035	-0.5562	6.80	0.45
	---	iR11+	0.0656	0.8396	-0.9052	11.06	0.86
	---	iB11+	0.3649	0.5871	-0.9520	11.63	0.23
MgV_2O_6	**---**	**Experimental[g]**	–	–	–	**7.5**	**0.34**
	---	iR411+	0.1660	0.4186	-0.5846	7.14	0.43
	---	iR11+	0.0776	0.8541	-0.9317	11.38	0.83
	---	iB11+	0.3706	0.6044	-0.9750	11.91	0.24

[a-d] See footnotes of Table 2.1; [e] iR11+ = RHF/6-311+G** calculation on an isolated cluster. The clusters that are utilized in all calculations are identical to what are presented in Tables 2.1 to 2.3; [e] obtained from reference [69]; [f] obtained from reference [66]; [g] obtained from reference [68].

larger clusters with increased anionic charges can be avoided. Termination of the bridging oxygen atoms with protons oriented in the direction of the neighbouring vanadium atom proves to be a suitable means of approximating the extended structure of these clusters, at least for the purposes of calculating EFG tensors. RHF and B3LYP calculations should likely both be tested, as neither seems to particularly predominate in achieving good agreement with experimental results; however, a minimum basis set level of 4F and 6-311+G** on vanadium and oxygen (and hydrogen) atoms, respectively, can be used to predict fairly accurate EFG parameters. ECMO calculations clearly have an influence on the EFG tensors of metavanadate $H_2VO_4^-$ clusters, and therefore should be considered when conducting such calculations. The surrounding point charges can alter the magnitude of the EFG tensor components as well as the tensor orientation, as observed for all three cases. The metavanadates examined herein, which feature corner-shared VO_4 units, have $V_{33}(^{51}V)$ oriented along the intersection of the O_B-V-O_B and O_T-V-O_T planes, which contain the V_{11} or V_{22} components.

Choice of basis set for the vanadium atom. It was recently demonstrated by Gee that the 6-311+G** basis set can be used on vanadium atoms in VO_4^{3-} clusters of orthovanadates to accurately predict the ^{51}V EFG tensor parameters.[108] We also applied this basis set in calculations on several systems presented in this work (Table 2.4). Reasonably good agreement with experiment was obtained for all pyrovanadates involving isolated $V_2O_7^{4-}$ clusters; however, calculated tensors are in extremely poor agreement for metavanadates which involve bridging vanadium-oxygen units. The all-electron basis sets are clearly more suitable for EFG calculations on proton-terminated models of extended vanadate structures.

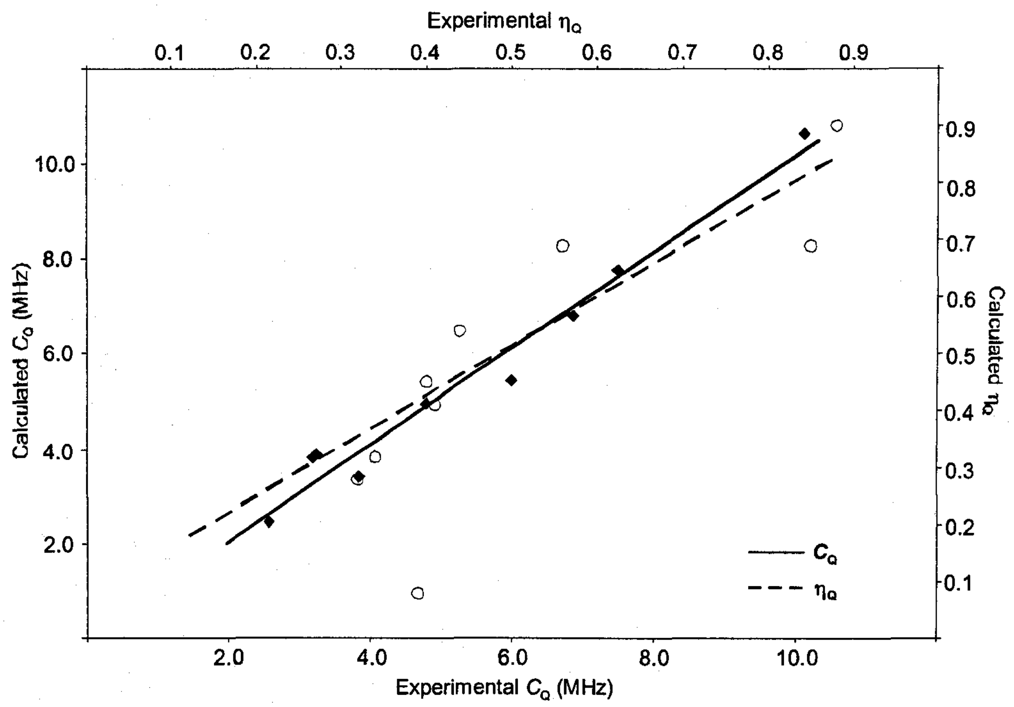

Figure 2.12. Correlation between experimental and calculated ^{51}V quadrupolar parameters (◆ for C_Q and ○ for η_Q) of all pyrovanadates and metavanadates. The correlation coefficients (R^2) are 0.97 and 0.84 (when $\eta_Q(V_b)$ in β-$Mg_2V_2O_7$ pyrovanadate is excluded) for C_Q and η_Q, respectively.

2.4 Conclusion

Theoretical ^{51}V EFG tensors in a series of pyrovanadates and metavanadates were examined by first principle calculations on both isolated and embedded clusters of varying shapes and sizes. Overall, the agreement between experimental and theoretical quadrupolar parameters (C_Q and η_Q) is quite good; notably, calculations utilizing 4F basis set often provide the best agreement (Table 2.4 and Figure 2.12). From a systematic trial and error investigation, we have made basic recommendations on the suitability of calculation methods and basis sets, as well as choice of structural features such as cluster size, proton termination and the necessity of a surrounding lattice. We anticipate that this work will encourage others to use efficient, inexpensive ab initio calculations of EFG tensors and their orientations, in combination with experimental NMR data, to make structural predictions for all classes of vanadates (and perhaps other vanadium oxide systems) for which structural data may be unavailable or unobtainable (e.g., disordered solids, glasses, nano-scaled materials, etc.).

Bibliography

[1] Hagrman, P.J., Finn, R.C., Zubieta, J. *Solid State Sci.* **2001**, *3*, 745.

[2] Abon, M., Volta, J.C. *Appl. Catal., A* **1997**, *157*, 173.

[3] Bielanski, A., Najbar, M. *Appl. Catal., A* **1997**, *157*, 223.

[4] Blasco, T., Nieto, J.M.L. *Appl. Catal., A* **1997**, *157*, 117.

[5] Blasco, T., Concepcion, P., Nieto, J.M.L., Perezpariente, J. *J. Catal.* **1995**, *152*, 1.

[6] Blasco, T., Nieto, J.M.L., Dejoz, A., Vazquez, M.I. *J. Catal.* **1995**, *157*, 271.

[7] Bond, G.C. *Appl. Catal., A* **1997**, *157*, 91.

[8] Bruckner, A., Baerns, M. *Appl. Catal., A* **1997**, *157*, 311.

[9] Busca, G., Lietti, L., Ramis, G., Berti, F. *Appl. Catal., B* **1998**, *18*, 1.

[10] Cavani, F., Trifiro, F. *Appl. Catal., A* **1997**, *157*, 195.

[11] Centi, G., Perathoner, S., Trifiro, F. *Appl. Catal., A* **1997**, *157*, 143.

[12] Conte, V., DiFuria, F., Licini, C. *Appl. Catal., A* **1997**, *157*, 335.

[13] Courtine, P., Bordes, E. *Appl. Catal., A* **1997**, *157*, 45.

[14] Forzatti, P., Tronconi, E., Elmi, A.S., Busca, G. *Appl. Catal., A* **1997**, *157*, 387.

[15] Tichy, J. *Appl. Catal., A* **1997**, *157*, 363.

[16] Wachs, I.E., Weckhuysen, B.M. *Appl. Catal., A* **1997**, *157*, 67.

[17] Grzybowska-Swierkosz, B. *Appl. Catal., A* **1997**, *157*, 263.

[18] Grzybowska-Swierkosz, B. *Appl. Catal., A* **1997**, *157*, 409.

[19] Kung, H.H., Kung, M.C. *Appl. Catal., A* **1997**, *157*, 105.

[20] Livage, J., Gharbi, N., Leroy, M.C., Michaud, M. *Mater. Res. Bull.* **1978**, *13*,

1117.

[21] Livage, J. *Chem. Mat.* **1991**, *3*, 578.

[22] Rehder, D. et al. *J. Biol. Inorg. Chem.* **2002**, *7*, 384.

[23] Thompson, K.H., McNeill, J.H., Orvig, C. *Chem. Rev.* **1999**, *99*, 2561.

[24] Pistoia, G., Wang, G., Zane, D. *Solid State Ionics* **1995**, *76*, 285.

[25] Amarilla, J.M., Casal, B., RuizHitzky, E. *J. Mater. Chem.* **1996**, *6*, 1005.

[26] Gopal, R., Calvo, C. *Can. J. Chem.* **1973**, *51*, 1004.

[27] Gopal, R., Calvo, C. *Acta Crystallogr., Sect. B: Struct. Sci.* **1974**, *30B*, 2491.

[28] Au, P.K.L., Calvo, C. *Can. J. Chem.* **1967**, *45*, 2297.

[29] Trunov, V.K., Velikodnyi, I.A., Murashova, E.V., Zhuravlev, V.D. *Dokl. Akad. Nauk SSSR* **1983**, *270*, 886.

[30] Murashova, E.V., Velikodnyi, Y.A., Trunov, V.K. *Zhurnal Neorg. Khimii* **1989**, *34*, 1388.

[31] Krishnamachari, N., Calvo, C. *Can. J. Chem.* **1971**, *49*, 1629.

[32] Gopal, R., Calvo, C. *Can. J. Chem.* **1971**, *49*, 3056.

[33] Sleight, A.W., Chen, H.Y., Ferretti, A., Cox, D.E. *Mater. Res. Bull.* **1979**, *14*, 1571.

[34] Shannon, R.D., Calvo, C. *Can. J. Chem.* **1973**, *51*, 265.

[35] Marumo, F., Isobe, M., Iwai, S., Kondo, Y. *Acta Crystallogr., Sect. B: Struct. Sci.* **1974**, *30, Pt. 6*, 1628.

[36] Ganne, M., Piffard, Y., Tournoux, M. *Can. J. Chem.* **1974**, *52*, 3539.

[37] Wyckoff, R.W.G. In *Crystal Structures*; Interscience Publishers: New York, 1963;

Vol. 2, pp 430 - 431.

[38] Kato, K., Takayama, E. *Acta Crystallogr., Sect. B: Struct. Sci.* **1984**, *40*, 102.

[39] Ng, H.N., Calvo, C. *Can. J. Chem.* **1972**, *50*, 3619.

[40] Yao, T., Oka, Y., Yamamoto, N. *Inorg. Chim. Acta* **1995**, *238*, 165.

[41] Bouloux, J.C., Perez, G., Galy, J. *Bull. Soc. Fr. Mineral. Cristallogr.* **1972**, *95*, 130.

[42] Perez, G., Frit, B., Bouloux, J.C., Galy, J. *C. R. Acad. Sci., Ser. C* **1970**, *270*, 952.

[43] Andreetti, G.D., Calestani, G., Montenero, A., Bettinelli, M. *Z. Kristallogr.* **1984**, *168*, 53.

[44] Jordan, B.D., Calvo, C. *Can. J. Chem.* **1974**, *52*, 2701.

[45] Karpov, O.G., Simonov, M.A., Krasnenko, T.I., Zabara, O.A. *Kristallografiya* **1989**, *34*, 1392.

[46] Oka, Y., Yao, T., Yamamoto, N. *Mater. Res. Bull.* **1997**, *32*, 1201.

[47] Pyykko, P. *Mol. Phys.* **2001**, *99*, 1617.

[48] Le Coustumer, L.R., Taouk, B., Lemeur, M., Payen, E., Guelton, M., Grimblot, J. *J. Phys. Chem.* **1988**, *92*, 1230.

[49] Taouk, B., Guelton, M., Grimblot, J., Bonnelle, J.P. *J. Phys. Chem.* **1988**, *92*, 6700.

[50] Eckert, H., Wachs, I.E. *J. Phys. Chem.* **1989**, *93*, 6796.

[51] Lapina, O.B., Mastikhin, V.M., Shubin, A.A., Krasilnikov, V.N., Zamaraev, K.I. *Prog. Nucl. Magn. Reson. Spectrosc.* **1992**, *24*, 457.

[52] Das, N., Eckert, H., Hu, H.C., Wachs, I.E., Walzer, J.F., Feher, F.J. *J. Phys.*

Chem. **1993**, *97*, 8240.

[53] Chary, K.V.R., Kishan, G. *J. Phys. Chem.* **1995**, *99*, 14424.

[54] Blasco, T., Nieto, J.M.L. *Colloid Surf. A-Physicochem. Eng. Asp.* **1996**, *115*, 187.

[55] Gheorghe, C., Gee, B. *Chem. Mat.* **2000**, *12*, 682.

[56] Lapina, O.B., Khabibulin, D.F., Shubin, A.A., Bondareva, V.M. *J. Mol. Catal. A-Chem.* **2000**, *162*, 381.

[57] Lapina, O.B., Bodart, P.R., Amoureux, J.P. *NATO ASI Ser., Ser. C* **2002**, *76*, 355.

[58] Grasser, S., Haessner, C., Koehler, K., Lefebvre, F., Basset, J.-M. *Phys. Chem. Chem. Phys.* **2003**, *5*, 1906.

[59] Gee, B.A., Wong, A. *J. Phys. Chem. B* **2003**, *107*, 8382.

[60] Pooransingh, N., Pomerantseva, E., Ebel, M., Jantzen, S., Rehder, D., Polenova, T. *Inorg. Chem.* **2003**, *42*, 1256.

[61] Nielsen, U.G., Topsoe, N.-Y., Brorson, M., Skibsted, J., Jakobsen, H.J. *J. Am. Chem. Soc.* **2004**, *126*, 4926.

[62] Andronenko, S.I., Dmitrieva, L.V., Molodchenko, N.G., Moskalev, V.V., Zoni, Z.N. *Fiz. Tverd. Tela (Leningrad)* **1979**, *21*, 914.

[63] Hayashi, S., Hayamizu, K. *Bull. Chem. Soc. Jpn.* **1990**, *63*, 961.

[64] Davis, J., Tinet, D., Fripiat, J.J., Amarilla, J.M., Casal, B., Ruizhitzky, E. *J. Mater. Res.* **1991**, *6*, 393.

[65] Skibsted, J., Nielsen, N.C., Bildsoe, H., Jakobsen, H.J. *J. Am. Chem. Soc.* **1993**, *115*, 7351.

[66] Skibsted, J., Jacobsen, C.J.H., Jakobsen, H.J. *Inorg. Chem.* **1998**, *37*, 3083.

[67] Bodart, P.R., Dumazy, Y., Amoureux, J.P., Fernandez, C. *Magn. Reson. Chem.* **1999**, *37*, 223.

[68] Nielsen, U.G., Jakobsen, H.J., Skibsted, J. *Inorg. Chem.* **2000**, *39*, 2135.

[69] Nielsen, U.G., Jakobsen, H.J., Skibsted, J. *J. Phys. Chem. B* **2001**, *105*, 420.

[70] Nielsen, U.G., Boisen, A., Brorson, M., Jacobsen, C.J.H., Jakobsen, H.J., Skibsted, J. *Inorg. Chem.* **2002**, *41*, 6432.

[71] Nielsen, U.G., Jakobsen, H.J., Skibsted, J. *Solid State Nucl. Magn. Reson.* **2003**, *23*, 107.

[72] Marichal, C., Kempf, J.Y., Maigret, B., Hirschinger, J. *Solid State Nucl. Magn. Reson.* **1997**, *8*, 33.

[73] Huang, W.L., Todaro, L., Francesconi, L.C., Polenova, T. *J. Am. Chem. Soc.* **2003**, *125*, 5928.

[74] Schwarz, K. *J. Solid State Chem.* **2003**, *176*, 319.

[75] Schwarz, K., Blaha, P. *Comput. Mater. Sci.* **2003**, *28*, 259.

[76] Petrilli, H.M., Blochl, P.E., Blaha, P., Schwarz, K. *Phys. Rev. B: Condens. Matter Mater. Phys.* **1998**, *57*, 14690.

[77] Jager, B., Paluch, S., Wolf, W., Herzig, P., Zogal, O.J., Shitsevalova, N., Paderno, Y. *J. Alloys Compd.* **2004**, *383*, 232.

[78] Blaha, P., Schwarz, K., Faber, W., Luitz, J. *Hyperfine Interact.* **2000**, *126*, 389.

[79] Iglesias, M., Schwarz, K., Blaha, P., Baldomir, D. *Phys. Chem. Miner.* **2001**, *28*, 67.

[80] Zhou, B., Sherriff, B.L. *Am. Mineral.* **2004**, *89*, 377.

[81] Ravindran, P., Delin, A., James, P., Johansson, B., Wills, J.M., Ahuja, R., Eriksson, O. *Phys. Rev. B: Condens. Matter Mater. Phys.* **1999**, *59*, 15680.

[82] Lalic, M.V., Mestnik-Filho, J., Carbonari, A.W., Saxena, R.N. *Solid State Commun.* **2003**, *125*, 175.

[83] Laskowski, R., Blaha, P., Schwarz, K. *Phys. Rev. B: Condens. Matter Mater. Phys.* **2003**, *67*, 075102/1.

[84] Soldner, T., Troger, W., Butz, T., Blaha, P., Schwarz, K. *Z. Naturfors. Sect. A-J. Phys. Sci.* **1998**, *53*, 411.

[85] Errico, L.A., Fabricius, G., Renteria, M. *Hyperfine Interact.* **2001**, *136*, 749.

[86] Devine, R.A.B., Dixon, J.M. *Phys. Rev. B* **1973**, *7*, 4902.

[87] Yamaguchi, M., Asano, S. *Physica B (Amsterdam, Neth.)* **1998**, *254*, 73.

[88] Body, M., Silly, G., Legein, C., Buzare, J.Y., Calvayrac, F., Blaha, P. *Chem. Phys. Lett.* **2006**, *424*, 321.

[89] Siegel, R., Hirschinger, J., Carlier, D., Menetrier, M., Delmas, C. *Solid State Nucl. Magn. Reson.* **2003**, *23*, 243.

[90] Truflandier, L., Paris, M., Payen, C., Boucher, F. *J. Phys. Chem. B* **2006**, *110*, 21403.

[91] Hansen, M.R., Madsen, G.K.H., Jakobsen, H.J., Skibsted, J. *J. Phys. Chem. B* **2006**, *110*, 5975.

[92] Hemmingsen, L., Ryde, U. *J. Phys. Chem.* **1996**, *100*, 4803.

[93] Lewandowski, A.C., Wilson, T.M. *J. Comput. Phys.* **1996**, *129*, 233.

[94] Mitchell, D.W. et al. *Phys. Rev. B: Condens. Matter* **1996**, *53*, 7684.

[95] Bryant, P.L., Harwell, C.R., Wu, K., Fronczek, F.R., Hall, R.W., Butler, L.G. *J. Phys. Chem. A* **1999**, *103*, 5246.

[96] Stueber, D., Guenneau, F.N., Grant, D.M. *J. Chem. Phys.* **2001**, *114*, 9236.

[97] Stueber, D., Grant, D.M. *J. Am. Chem. Soc.* **2002**, *124*, 10539.

[98] Stueber, D., Orendt, A.M., Facelli, J.C., Parry, R.W., Grant, D.M. *Solid State Nucl. Magn. Reson.* **2002**, *22*, 29.

[99] Stueber, D., Grant, D.M. *Solid State Nucl. Magn. Reson.* **2002**, *22*, 439.

[100] Barich, D.H., Clawson, J.S., Stueber, D., Strohmeier, M., Pugmire, R.J., Grant, D.M. *J. Phys. Chem. A* **2002**, *106*, 11375.

[101] Willans, M.J., Schurko, R.W. *J. Phys. Chem. B* **2003**, *107*, 5144.

[102] Strohmeier, M., Stueber, D., Grant, D.M. *J. Phys. Chem. A* **2003**, *107*, 7629.

[103] Strohmeier, M., Grant, D.M. *J. Am. Chem. Soc.* **2004**, *126*, 966.

[104] Clawson, J.S., Anderson, K.L., Pugmire, R.J., Grant, D.M. *J. Phys. Chem. A* **2004**, *108*, 2638.

[105] di Fiori, N., Orendt, A.M., Caputo, M.C., Ferraro, M.B., Facelli, J.C. *Magn. Reson. Chem.* **2004**, *42*, S41.

[106] Widdifield, C.M., Schurko, R.W. *J. Phys. Chem. A* **2005**, *109*, 6865.

[107] Lo, A.Y.H., Bitterwolf, T.E., Macdonald, C.L.B., Schurko, R.W. *J. Phys. Chem. A* **2005**, *109*, 7073.

[108] Gee, B.A. *Solid State Nucl. Magn. Reson.* **2006**, *30*, 171.

[109] Orendt, A.M. *Magn. Reson. Chem.* **2006**, *44*, 385.

[110] Strohmeier, M., Barich, D.H., Grant, D.M., Miller, J.S., Pugmire, R.J., Simons, J.

J. Phys. Chem. A **2006**, *110*, 7962.

[111] Stueber, D. *Concepts Magn. Reson. A* **2006**, *28A*, 347.

[112] Grant, C.V., Cope, W., Ball, J.A., Maresch, G.G., Gaffney, B.J., Fink, W., Britt, R.D. *J. Phys. Chem. B* **1999**, *103*, 10627.

[113] Hermann, K., Witko, M., Druzinic, R. *Faraday Discuss.* **1999**, 53.

[114] Vorotilova, L.S., Dmitrieva, L.V., Lavrov, S.A., Shchegolev, B.F. *Phys. Solid State* **2002**, *44*, 1864.

[115] Becke, A.D. *Phys. Rev. A: At., Mol., Opt. Phys.* **1988**, *38*, 3098.

[116] Becke, A.D. *J. Chem. Phys.* **1993**, *98*, 5648.

[117] Lee, C., Yang, W., Parr, R.G. *Phys. Rev. B: Condens. Matter Mater. Phys.* **1988**, *37*, 785.

[118] Frisch, M.J. et al., Revision A.9, Gaussian, Inc., Pittsburgh, PA, 1998.

[119] Huzinaga, S., Andzelm, J. In *Gaussian basis sets for molecular calculations*; Elsevier: New York, 1984, pp 124 - 134.

[120] Michalak, A., Witko, M., Hermann, K. *Surf. Sci.* **1997**, *375*, 385.

[121] Zhang, L., Chen, Z.D. *Chem. Phys. Lett.* **2001**, *345*, 353.

Chapter 3

Solid-State ^{93}Nb and ^{13}C NMR Investigations of Half-Sandwich Niobium(I) and Niobium(V) Cyclopentadienyl Complexes

3.1 Introduction

Since the discovery of ferrocene,[1,2] metallocenes have captured the imagination of many chemists, due to their assortment of fascinating structures, variation in coordination chemistries and their prevalence in many technologically important materials and industrial processes.[3-9] Solid-state structures of the monomeric half-sandwich niobium metallocenes of the forms Cp′Nb(I)(CO)$_4$ and Cp′Nb(V)Cl$_4$, along with other metallocenes of this motif, have been of great interest over the past ten years. Cp′ is generally an η^5-coordinated cyclopentadienyl ring which may be substituted by a variety of functional groups. The carbonyl niobocenes can be synthesized under high-pressure from Cp′NbCl$_4$,[10,11] and can potentially serve as building blocks in photochemically reactive organometallic polymers.[12,13] They are also used to produce phosphine derivatives, which may exhibit catalytic behavior in homogeneous H- and CO-transfer reactions.[14] The Cp′Nb(CO)$_4$ complexes have been characterized with single-crystal X-ray diffraction (XRD),[10,11,15,16] IR spectroscopy,[10,11,14] gas-phase photoelectron spectroscopy,[17] microwave spectroscopy,[18] and ^{93}Nb solution NMR.[10,14,16,19] The chloride niobocenes have been used extensively in the syntheses of half-sandwich (imido)niobium complexes;[20,21] however, in comparison to Nb(I) complexes, fewer structural characterizations have been reported. For instance, phosphine adducts of $CpNbCl_4$[22] and Cp^*NbCl_4[23] ($Cp^* = C_5Me_5$) have been structurally characterized by single-crystal X-ray diffraction, multinuclear solution NMR, IR, EPR, and mass spectroscopy. In terms of solid-state NMR, attempts at structural characterization of this class of compounds include a preliminary report on the solid-state ^{93}Nb NMR spectroscopy of $CpNb(CO)_4$,[24] and ^{31}P NMR experiments on a series of phosphine derivatives of half-sandwich niobium metallocenes.[25,26]

Standard ^{13}C, ^{1}H and ^{2}H solid-state NMR experiments have long been used for the characterization of structure and dynamics in organometallic complexes such as metallocenes and bis-arene complexes.[27-40] More recently, experiments focusing upon the metal nuclei at the "heart" of metallocenes have proven to be excellent assessors of molecular structure and symmetry, intramolecular dynamics and sample purity. Recent work in our research group has focused upon metallocenes containing half-integer quadrupolar nuclei (i.e., nuclear spin $I = 3/2, 5/2, 7/2, 9/2$), including ^{9}Be, ^{11}B, ^{23}Na, ^{25}Mg, ^{27}Al and ^{91}Zr.[35,36,38,40-42] In addition, a number of other research groups have reported solid-state NMR studies of metallocenes containing both spin-1/2 and half-integer quadrupolar nuclei.[43-50]

Niobium has only one NMR-active isotope, ^{93}Nb, which has $I = 9/2$ and 100% natural abundance. However, its moderately sized nuclear quadrupole moment ($Q(^{93}\text{Nb}) = -0.32 \times 10^{-28}$ m^2)[51] often results in severe quadrupolar broadening of central-transition NMR powder patterns, which in some cases is prohibitive in terms of routine spectral acquisition and interpretation. Nonetheless, solid-state ^{93}Nb NMR has been used to study a variety of different systems, including inorganic niobium halides,[52] intercalated H-bronzes of $NbVO_5$,[53] niobium borides and deuterides,[54,55] and a variety of niobates.[56-70] There have also been a number of ^{93}Nb NMR studies featuring a variety of modern two-dimensional (2D) solid-state NMR experiments, including multiple quantum magic-angle spinning (MQMAS) and satellite-transition magic-angle spinning (STMAS) experiments, which are used for resolving peaks which may be obscured due to broad overlapping quadrupolar NMR patterns, as well as nutation and 2D-exchange NMR.[71-76]

Given the relatively favorable NMR characteristics of ^{93}Nb, solid-state ^{93}Nb NMR experiments on niobocene complexes could potentially act as fast, powerful probes of molecular structure, identity and/or presence of solid phase impurities, as well as lending insight into the fundamental origins of NMR interaction tensors in an important structural theme in organometallic chemistry. To these ends, we present a comprehensive solid-state ^{93}Nb and ^{13}C NMR study of niobium(I) carbonyl and niobium(V) chloride cyclopentadienyl complexes, including the parent compound, $CpNb(CO)_4$; complexes with singly-substituted cyclopentadienyl rings, $(\eta^5\text{-}C_5H_4R)Nb(CO)_4$ (where R = COMe, CO_2Me, CO_2Et and $COCH_2Ph$); and niobium(V) chlorides $CpNbCl_4$ and $CpNbCl_4$•THF (Chart 3.1). For complexes which have extremely broad central-transition powder patterns, the quadrupolar Carr-Purcell Meiboom-Gill (QCPMG) pulse sequence[77] is applied to acquire sub-spectra in a piecewise manner, which are then co-added to produce the final ultra-wideline ^{93}Nb NMR spectrum. The QCPMG pulse sequence has the potential to provide signal enhancement by an order of magnitude over standard spin-echo

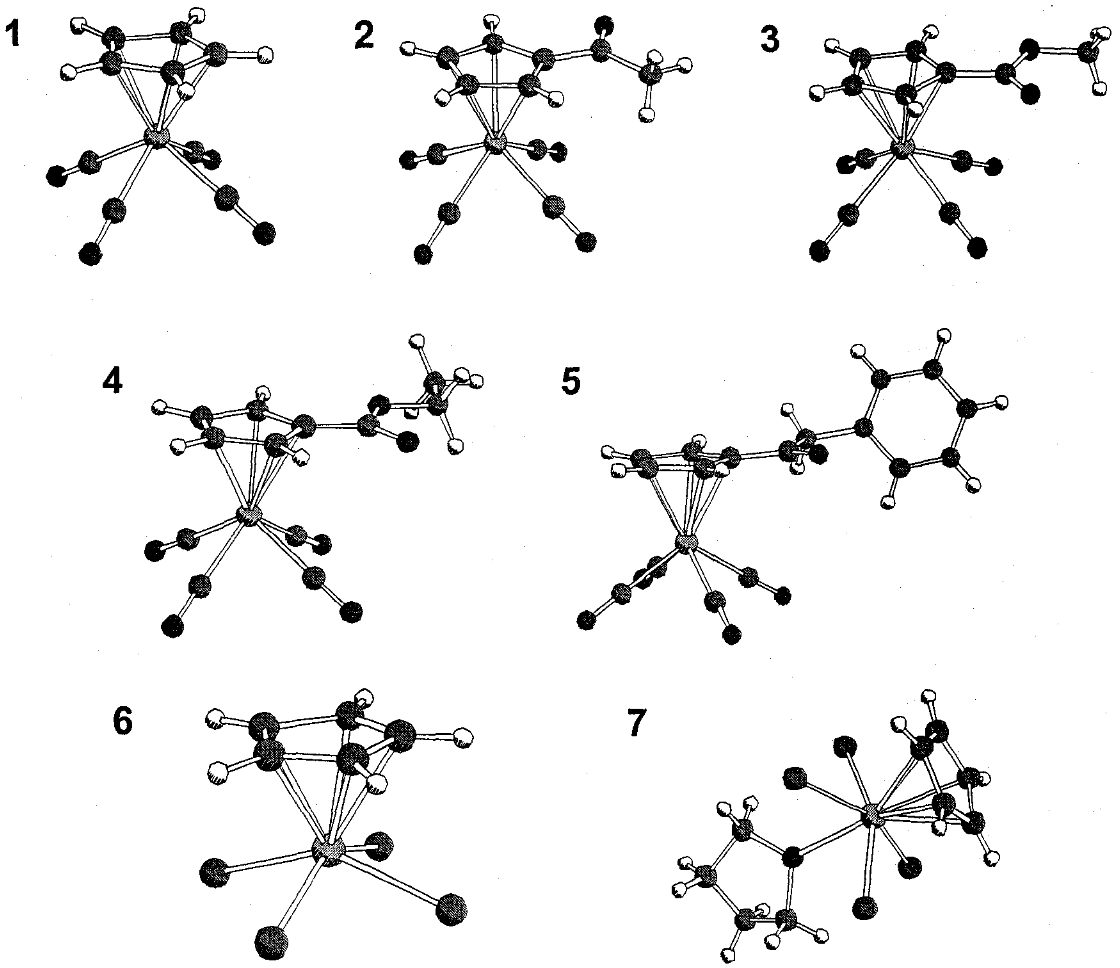

Chart 3.1. Molecular Structures of Half-Sandwich Niobium Metallocenes. Key: (**1**) (η^5-C_5H_5)Nb(CO)$_4$, (**2**) (η^5-MeOC-C_5H_4)Nb(CO)$_4$, (**3**) (η^5-MeO$_2$C-C_5H_4)Nb(CO)$_4$, (**4**) (η^5-EtO$_2$C-C_5H_4)Nb(CO)$_4$, (**5**) (η^5-PhCH$_2$OC-C_5H_4)Nb(CO)$_4$, (**6**) (η^5-C_5H_5)NbCl$_4$, and (**7**) (η^5-C_5H_5)NbCl$_4$•THF.

experiments, though its efficiency is limited by the T_2 relaxation time constant of the nucleus under study. QCPMG has also recently been coupled with MQMAS to produce spectra with high S/N and individually resolved sites.[78] Analytical and numerical simulations of magic-angle spinning (MAS) and static (i.e., stationary) ^{93}Nb NMR powder patterns are used to obtain the ^{93}Nb electric field gradient (EFG) and chemical shift (CS) tensor parameters. The ^{93}Nb NMR tensors are then correlated to molecular structure with the aid of theoretical calculations and/or X-ray data. Solid-state ^{13}C MAS and cross-polarization MAS (CP/MAS) NMR experiments are used to determine carbon CS tensors for Cp′ ring carbons, to assess sample purity and identity, and to measure ^{1}J-coupling between ^{13}C and ^{93}Nb.

3.2 Experimental

Materials. All Cp′Nb(CO)$_4$ compounds with Cp′ = C$_5$H$_4$R, where R = H (**1**), COMe (**2**), CO$_2$Me (**3**), CO$_2$Et (**4**), and COCH$_2$Ph (**5**), were synthesized as previously described in the literature[10,15] and were used without further purification unless otherwise stated. CpNb(CO)$_4$ (**1**) was sublimed at 100 ± 10 °C prior to use (orange, needle-shaped crystals). CpNbCl$_4$ (**6**) was obtained from Aldrich, and CpNbCl$_4$•THF (**7**) was synthesized by the recrystallization of CpNbCl$_4$ in THF in a dry, nitrogen-filled glovebox. The THF was dried on a series of Grubb's type columns.[79] The CpNbCl$_4$/THF solution was stirred for 2 days to ensure all of the CpNbCl$_4$ solid dissolved into the solution. Solvent was then decanted and residual solvent was removed under vacuum for 2 hours. Isolated crystals were needle-shaped with a pink/purple coloration.

Solid-state NMR. Solid-state ^{93}Nb and ^{13}C NMR experiments were conducted on a Varian Infinity Plus NMR spectrometer with an Oxford 9.4 T wide bore magnet operating at $\nu_0(^{93}\text{Nb})$ = 97.6 MHz and $\nu_0(^{13}\text{C})$ = 100.5 MHz, employing high-power proton-decoupling ($\nu_1(^{1}\text{H}) \approx$ ca. 35 kHz to 110 kHz). Most of the NMR spectra were acquired using Varian/Chemagnetics 2.5 mm HX MAS and 4 mm HX MAS probes, while

^{93}Nb ultra-wideline static NMR spectra of CpNbCl$_4$ were acquired using a 5 mm HX static probe. All samples were ground into fine powders under an inert atmosphere and tightly packed into zirconium oxide rotors, which were sealed with air-tight Teflon caps.

Niobium chemical shifts were referenced to a 0.4 M NbCl$_5$ solution in dry CH$_3$CN with $\delta_{\text{iso}}(^{93}\text{Nb}) = 0.0$ ppm. A conventional Bloch decay sequence was employed for most MAS and static experiments. A Hahn-echo pulse sequence of the form $[(\pi/2)_x\text{-}\tau_1\text{-}(\pi)_y\text{-}\tau_2\text{-}$acq.] was employed to acquire a satellite-transition spectrum (SATRAS)[80] of **1**, static spectra of samples **2** and **5**, and both the MAS and static spectra of **7**, in order to avoid losing points in the beginning of the FIDs which may cause baseline distortions in the Fourier-transformed spectra. All Hahn-echo experiments acquired under conditions of MAS were rotor synchronized. For MAS experiments, samples were spun at 5 kHz to 27 kHz, 330 to 370000 transients were collected and calibrated recycle times ranged from 0.2 s to 1.0 s. The central-transition selective 90° pulse width ranged from 0.44 μs to 7.90 μs, corresponding to rf fields from 6.3 kHz to 113.6 kHz. For static echo experiments, inter-pulse delays ranged from 60 μs to 75 μs, and between 220 and 21000 transients were collected. For the static ^{93}Nb QCPMG experiments on **6**, selective 90° pulses were 0.84 μs ($\nu_1(^{93}\text{Nb}) = 59.5$ kHz), inter-pulse delays were ca. 60 μs, calibrated recycle times were 0.5 s and 30 MG loops were collected with 128 points per echo. Five sub-spectra were collected at 100 kHz transmitter offsets, with 4400 scans per spectrum. Variable-temperature (VT) static ^{93}Nb NMR experiments ranging from +100 °C to -140 °C were conducted on samples **1** and **7** using parameters similar to those above (temperatures are accurate to within ±2 °C, based on previous calibrations). Additional static ^{93}Nb experiments were conducted on samples **1**, **3**, **5** and **7** using a Bruker DRX 500 spectrometer ($\nu_0(^{93}\text{Nb})$ = 122.2 MHz), equipped with a broad band 5 mm HX probe. Selective 90° pulse width of 2.5 μs ($\nu_1(^{93}\text{Nb})$ = 20.0 kHz) was used for **1** and **3**; while 36° (1.25 μs) and 30° (0.67 μs) pulses, corresponding to rf fields of 15.8 kHz and 25 kHz, respectively, were used for **5** and **7**.

Carbon chemical shifts were referenced to TMS ($\delta_{\text{iso}}(^{13}\text{C})$ = 0 ppm) by setting the high-frequency resonance of solid adamantane to 38.57 ppm. Solid-state ^{13}C{^{1}H} MAS, CP/MAS and variable-amplitude (VA) CP/MAS (in cases where fast spinning was utilized) NMR experiments were performed on all samples. The 90° pulse widths for ^{13}C MAS experiments ranged from 3.5 μs to 6.0 μs. Samples were spun between 1.95 kHz and 14.0 kHz, the number of transients collected ranged from 420 to 3500, and calibrated recycle times ranged from 29 s to 40 s. For ^{13}C CP/MAS NMR experiments, the ^{1}H 90° pulse widths were 1.9 μs to 3.5 μs, between 370 and 13000 transients were collected, and recycle times varied from 5 s to 20 s. Optimal contact times varied from sample to sample, ranging from 4 ms to 19 ms. During the contact time in VACP/MAS experiments, 10 or 15 steps of 4 to 19 ms length were applied, linearly ramping from 13.2 to 92.6 kHz on the ^{13}C channel. Several static ^{13}C CP experiments were attempted, but discontinued due to difficulties with orientation-dependent CP efficiencies. VT ^{13}C CP/MAS NMR experiments were conducted on **6**, with ν_{rot} = 1.9 kHz and between 252 and 444 scans were collected.

Spectral simulations. The EFG and CS parameters of all ^{93}Nb static and MAS spectra were obtained with analytical simulations using the WSOLIDS simulation package.[81] SIMPSON[82] was used to obtain numerical simulations of the ^{93}Nb SATRAS spectrum of **1** and the MAS NMR spectrum of **7**, and was run on a Dell Precision 420 workstation with dual 733 MHz pentium III processors running Red Hat Linux 6.2. The simulation was carried out by the *direct* method of powder averaging using the *zcw4180* crystal file, which is provided with the package. I_{1z} and I_{1p} were set as the start and the detect operators, respectively. The number of gamma angles was set to 100 and 30 for **1** and **7**, respectively.

Theoretical Calculations. Structural parameters of **1** through **5** used in the calculations were obtained from experimentally determined crystal structures,[10,11,15] with the exception of **4**, for which a structural geometry based on **3** was theoretically determined. The structure of **6** was constructed with geometry-optimized Cl positions, starting with a geometry based on **1**. The structure of **7** used in the calculations was obtained from a single crystal X-ray diffraction experiment (*vide infra*). The Cp′ ring proton positions were optimized for all complexes at corresponding levels of theory.

Restricted Hartree-Fock (RHF) and hybrid density functional theory (B3LYP) calculations were carried out using the Gaussian 98 and 03 software packages[83,84] on a Dell Precision 420 workstation with dual 733 MHz Pentium III processors. Two different all-electron basis sets, 16s10p7d (4F) and 16s10p7d (6D),[85] were used for the Nb atoms, which correspond to valence shell electron configurations of $4d^35s^2$ and $4d^45s^1$, respectively. The 6-31G** and 6-311G** basis sets were used for all other atoms, while 6-311G(2d,p) and 6-311G(2df,p) basis sets, with and without diffuse functions, were applied in select calculations.

Calculations of NMR tensor parameters on the optimized gas-phase structures of **1** and **6** were also performed at select levels of theory. Embedded cluster molecular orbital (ECMO) calculations were also conducted on select species. In the ECMO calculations, a cluster (in this case, a neutral, isolated molecule) was embedded in a spherical lattice of point charges (e.g., with a radius of ca. 20 Å), which are determined from Mulliken population analyses or arbitrarily assigned.

The value of $C_Q(^{93}\mathrm{Nb})$ in MHz is obtained by multiplying the largest component of the EFG tensor (eq or V_{33}, expressed in a.u.) by $(eQ/h) \times 9.7177 \times 10^{21}$ V m^{-2},[86] where $e = 1.602 \times 10^{-19}$ C, $Q(^{93}\mathrm{Nb}) = -0.32 \times 10^{-28}$ m^2,[51] and h is Planck's constant. Niobium CS tensors were calculated using the gauge-including atomic orbitals (GIAO) method.[87,88] The absolute shielding of the niobium nucleus is converted to the niobium chemical shift scale, using $\mathrm{NbCl_6^-}$ ($\delta_{\mathrm{iso}} = 0.0$ ppm) as the primary reference. The absolute shielding of the reference compound was obtained from a geometry-optimized $\mathrm{NbCl_6^-}$ ion using all levels of theory and all previously mentioned basis sets. Theoretical isotropic niobium chemical shifts can be obtained from $\delta_{\mathrm{iso}} \approx \sigma_{\mathrm{ref}} - \sigma_{\mathrm{sample}}$.

X-ray crystallography of CpNbCl$_4$•THF. The crystal used for the diffraction experiments was handled, selected and coated in mineral oil prior to data collection. The data were collected on a Bruker Apex CCD diffractometer using a graphite monochromator with MoKα radiation (λ = 0.71073 Å). A total of 1800 frames of data were collected using ω-scans with a scan range of 0.3° and a counting time of 30 seconds per frame. The data were collected at -100 °C using a Kryoflex low temperature device. Details of crystal data, data collection and structure refinement are listed in appendix A

(Table A.3.1). Data reduction was performed using SAINT.[89] The structure was solved by direct methods using SIR97[90] and refined by full-matrix least-squares on F^2 with anisotropic displacement parameters for most of the non-H atoms using SHELXL-97.[91] The cyclopentadienyl carbon was highly-disordered and was modeled using rings composed of isotropic carbon atoms in two different orientations; the relative occupancies of the orientations were refined to a ratio of 61:39. The corresponding carbon atoms in each ring were constrained to have identical temperature factors; however, no additional constraints were applied to the rings. All hydrogen atoms were placed in calculated positions (AFIX 23 for the methylene hydrogens and AFIX 43 for the aromatic hydrogens). The function, $\Sigma w(|F_o|^2 - |F_c|^2)^2$, was minimized, where $w = 1/[(\sigma(F_o))^2 + (0.0227{*}P)^2 + (1.3514{*}P)]$ and $P = (|F_o|^2 + 2\,|F_c|^2)/3$. No correction for secondary extinction effects was necessary. Neutral atom scattering factors and values used to calculate the linear absorption coefficient are from the International Tables for X-ray Crystallography (1992).[92] All figures were generated using SHELXTL.[93] Tables of positional, thermal, and metrical parameters are provided in the supporting information (Table A.3.2). In addition, powder XRD experiments were conducted using a Bruker AXS D8 Discover powder X-ray diffractometer, to assess the purity of bulk samples of **6** and **7**. Samples were loaded into 1.0 mm diameter capillary tubes and sealed under an inert atmosphere. Simulation of the powder XRD patterns from their corresponding known crystal structure was performed using PowderCell software.[94]

3.3 Results and Discussion

Solid-State ^{93}Nb NMR of Cp′Nb(CO)$_4$ Complexes. ^{93}Nb MAS NMR spectra of the parent CpNb(CO)$_4$ (**1**) and singly-substituted analogues (**2** to **5**) are shown in Figure 3.1, and corresponding static ^{93}Nb NMR spectra for compounds **1**, **3** and **5** are displayed in Figure 3.2. Compound **1** possesses a very small quadrupolar interaction and does not

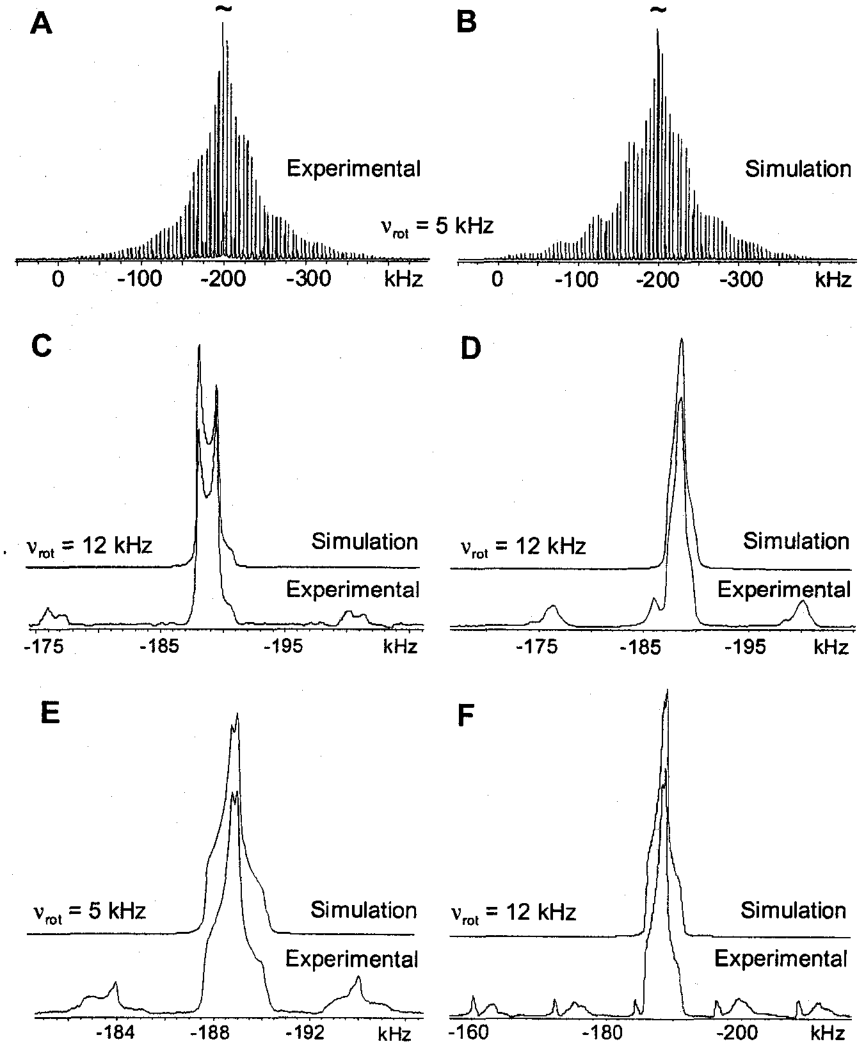

Figure 3.1. ^{93}Nb MAS NMR spectra of (A) **1** (experimental), (B) SIMPSON simulation of (A), and experimental and simulated simulated spectra of (C) **2**, (D) **3**, (E) **4**, and (F) **5** acquired at 9.4 T.

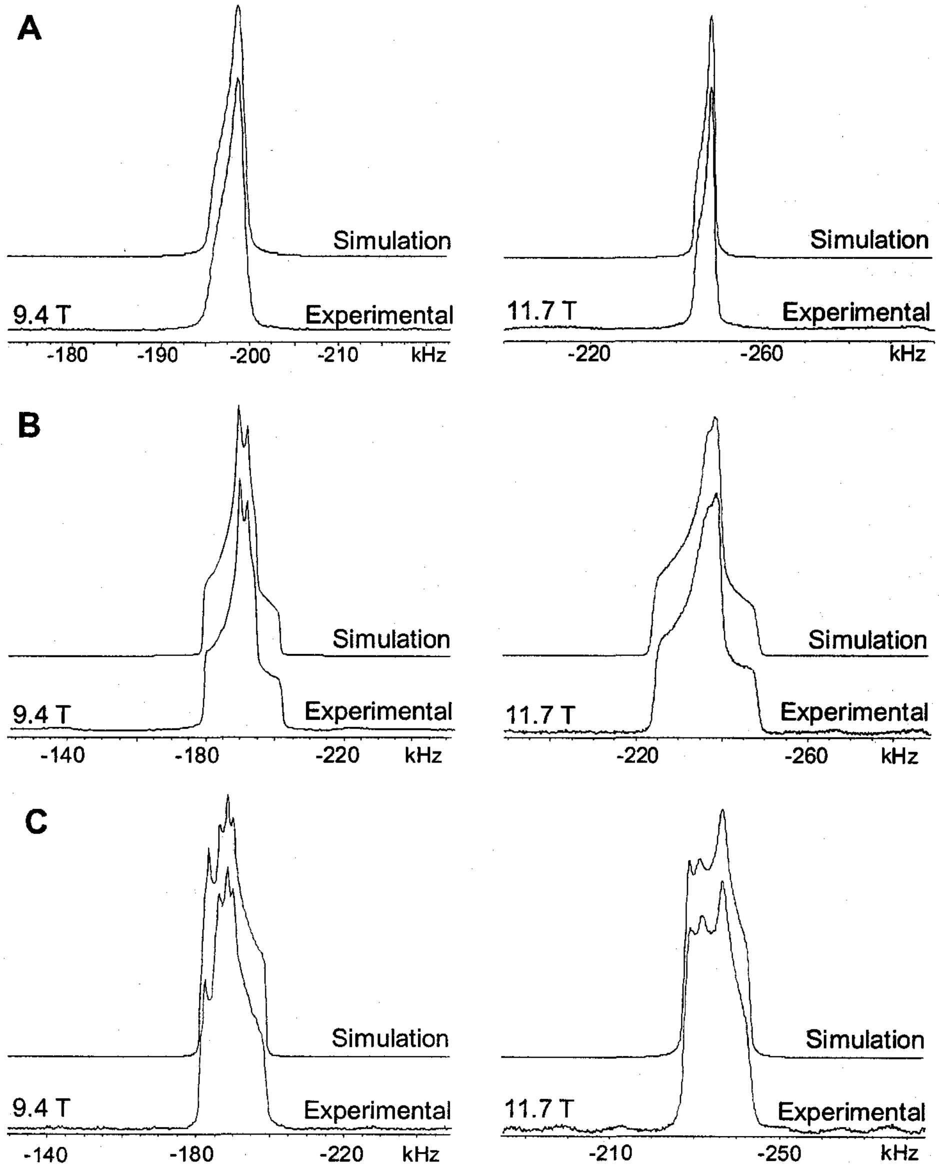

Figure 3.2. Experimental and analytically simulated static ^{93}Nb NMR spectra of (A) **1**, (B) **3**, and (C) **5** acquired at 9.4 and 11.7 T.

display a second-order quadrupolar pattern in the MAS spectrum at 9.4 T. Simulations of the MAS spectrum of the complete spinning sideband manifold (Figure 3.1A), as well as a static powder pattern at two different magnetic field strengths (Figure 3.2A), were used to extract the values of $C_Q(^{93}\text{Nb}) = 1.0(2)$ MHz and $\eta_Q = 0.80(10)$ (Table 3.1). The value of

Table 3.1. Experimental ^{93}Nb NMR Parameters for Cp′NbX$_4$ Complexes.

Parameters	H, **1**[a]		COMe, **2**	CO$_2$Me, **3**		CO$_2$Et, **4**	COCH$_2$Ph, **5**		CpNbCl$_4$, **6**	CpNbCl$_4$•THF, **7**	
B_0 (T)	9.4	11.7	9.4	9.4	11.7	9.4	9.4	11.7	9.4	9.4	11.7
C_Q (MHz)[b]	1.0(2)	1.2(2)	9.7(1)	9.0(3)	9.3(3)	8.7(4)	12.0(3)	12.3(3)	54.5(5)	38.4(4)	38.0(4)
η_Q[c]	0.80(10)	0.70(10)	0.10(2)	0.79(4)	0.79(3)	0.89(9)	0.81(3)	0.84(3)	0.83(3)	0.17(7)	0.10(7)
δ_{iso} (ppm)[d]	-2027(4)	-2023(4)	-1922(2)	-1924(4)	-1920(4)	-1920(1)	-1910(6)	-1904(6)	-600(30)	-703(12)	-715(12)
Ω (ppm)[e]	35.0(5)	35.0(10)	125(3)	135(5)	140(5)	120(2)	91(4)	95(4)	150	320(10)	320(10)
κ[f]	-0.90(5)	-0.90(5)	0.00(2)	0.10(5)	0.10(5)	0.20(4)	-0.4(2)	-0.2(2)	-0.6	-0.4(2)	-0.2(2)
α[g]	90(20)	90(20)	70(5)	105(15)	120(15)	166(1)	36(7)	29(7)	90	155(2)	155(1)
β	0(10)	0(10)	54(1)	44(3)	41(3)	63(1)	110(1)	109(1)	74	90(4)	86(4)
γ	0(25)	0(30)	48(1)	62(23)	85(23)	34(1)	23(8)	31(8)	15	0(5)	0(1)

[a] Singly substituted (η^5-C$_5$H$_4$R)Nb(CO)$_4$ complexes, with the substituents, R, being specified in the Table for samples **1** to **5**; [b, c] the quadrupolar coupling constant and the asymmetry parameter of the ^{93}Nb EFG tensor, are defined as $C_Q = eQV_{33}/h$, and $\eta_Q = (V_{11} - V_{22})/V_{33}$, respectively; [d, e, f] the isotropic value, span and skew, respectively, of the niobium CS tensor, are defined as $\delta_{iso} = (\delta_{11} + \delta_{22} + \delta_{33})/3$, $\Omega = \delta_{11} - \delta_{33}$, and $\kappa = 3(\delta_{22} - \delta_{iso})/\Omega$;

[g] α, β, and γ are the Euler angles between the ^{93}Nb EFG tensor and the niobium CS tensor in degrees.

$C_Q(^{93}Nb)$ is similar to that determined from gas phase microwave experiments ($C_Q(^{93}Nb)$ = -1.8(6) MHz);[18] however, both C_Q and η_Q are in disagreement with a previous solid-state static ^{93}Nb NMR study on polycrystalline CpNb(CO)$_4$, where C_Q was determined to be 2.26 MHz and η_Q was assumed to be zero.[24] This discrepancy likely exists because, in this previous work, both the presence of niobium chemical shift anisotropy (CSA) and the fact that η_Q might be non-zero were not taken into account. To deconvolute the contributions from the second-order quadrupolar interaction and the niobium CSA, two different fields are necessary.[95] Simulations of the complete MAS spinning sideband manifold (Figure 3.1B), as well as the static NMR spectra (Figure 3.2A), reveal a span of Ω = 35.0(5) ppm and κ = -0.90(5). The niobium chemical shift, δ_{iso} = -2027(4) ppm, indicates one of the most shielded ^{93}Nb nuclei reported in the literature,[96] and is similar to values previously reported from solution NMR studies on CpNb(CO)$_4$, which range from ca. -2000 ppm to -2050 ppm (different shift values are likely due to temperature and solvent effects).[10,14,16] The low chemical shift indicates a highly shielded niobium nucleus, which results from the Cp′-metal π-bonding interactions.[38,97] High magnetic shielding of niobium nuclei have also been observed in the ^{93}Nb NMR spectra of a variety of analogous systems.[14,19,98-100]

^{93}Nb MAS NMR spectra of compounds **2** through **5** are shown in Figure 3.1C to 3.1F. All of the spectra display partially averaged second-order quadrupolar powder patterns and an array of spinning sidebands, indicating that the values of C_Q are large in comparison to **1**. The $C_Q(^{93}Nb)$ is observed to increase in the order **4** < **3** < **2** < **5** (Table 3.1); however, there is no general relationship between the nature of the substituents and the magnitude of C_Q (though C_Q in **5** is the largest in this series, possibly due to the bulkiness of the phenyl-containing substituent). The small value of C_Q in compound **1**, in comparison to those in compounds **2** through **5**, may arise from some sort of Cp′ ring motion in the former which serves to dynamically reorient the ^{93}Nb EFG tensor (*vide infra*). The relatively large substituents on the Cp′ rings in the latter complexes would prevent such motional averaging, and correspondingly, larger values of C_Q are observed. Interestingly, compounds **2** through **5** have higher isotropic chemical shifts than the parent compound, meaning that the niobium nuclei are slightly deshielded with respect to **1** due to substitution at the Cp′ ring. However, again there is no clear trend relating the nature or size of the substituents and the relative shift. Nevertheless, the combination of δ_{iso}, C_Q and η_Q can be used to differentiate these chemically and structurally similar species. The rapidity with which these spectra can be acquired (i.e., 1 to 5 minutes) makes ^{93}Nb MAS NMR a useful "fingerprinting" tool for such compounds.

Static ^{93}Nb NMR spectra of compounds **3** and **5** acquired at 9.4 T and 11.7 T are shown in Figure 3.2B,C. Compounds **3** and **5** have an increased niobium CSA with respect to **1** (see Table 3.1, and Figure B.3.1 in appendix section for similar spectra of **2** and **4**). In compound **1**, the CS tensor is near axially symmetric (i.e., $\kappa = -0.90$, and δ_{11} is the pseudo-unique component); however, the presence of a substituent on the Cp ring results in non-axial niobium CS tensors in all substituted complexes, attesting to the influence of substitution on the metal chemical shift tensor. In all cases, the ^{93}Nb EFG and CS tensors are not coincident. In fact, Euler angles obtained from simulations of the spectra indicate that relative orientations vary greatly between compounds (Table 3.1).

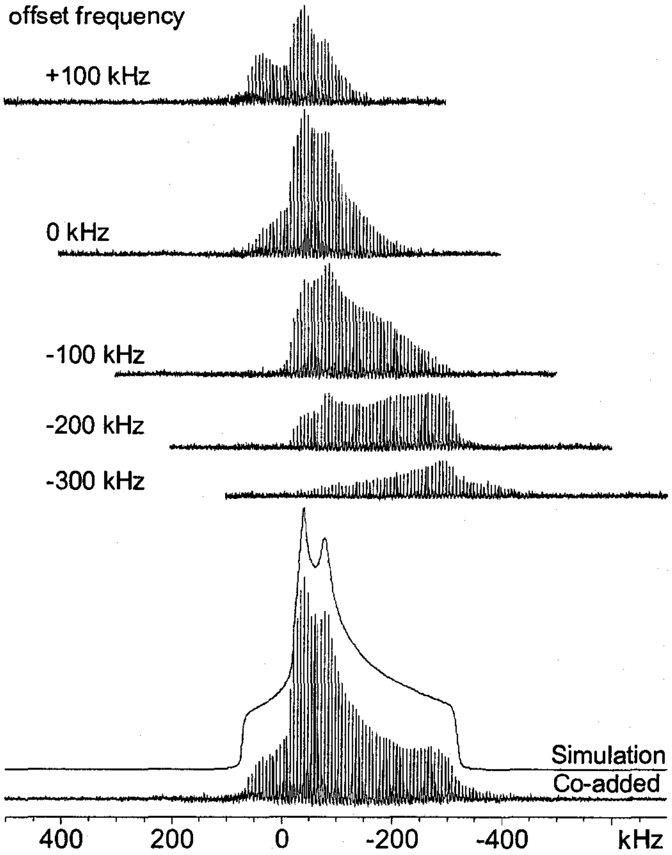

Figure 3.3. Piecewise static ^{93}Nb QCPMG NMR spectrum and analytical simulation of **6**, along with the transmitter offset frequencies of each sub-spectrum.

The relationship between tensor orientation and molecular structure will be addressed in the discussion of theoretically calculated tensor orientations (*vide infra*).

Solid-State ^{93}Nb NMR and X-ray Diffraction of CpNbCl$_4$ and CpNbCl$_4$•THF. Static ^{93}Nb NMR spectra reveal that the magnitudes of C_Q(^{93}Nb) in the niobium(V) half-sandwich complexes are very large compared to those in the niobium(I) complexes. In the case of CpNbCl$_4$ (**6**), the quadrupolar interaction is so large that the spectrum must be acquired in a piecewise fashion (Figure 3.3), since the entire breadth of the pattern cannot be uniformly excited with a single short pulse. Individual sub-spectra are acquired using a short excitation pulse and 100 kHz offset frequencies. The offsets are chosen such that the sinc-like excitation profiles in the frequency domain, when co-added, form a rectangular excitation profile.[101] The final spectrum can be produced by either co-adding the sub-spectra[102,103] or skyline projection (see Figure B.3.2).[104] Simulation of the powder pattern yields $\delta_{\mathrm{iso}} = -600(30)$ ppm, $C_Q = 54.5(5)$ MHz and $\eta_Q = 0.83(3)$. The replacement of the neutral CO ligands with negatively charged Cl ligands and the higher oxidation state of Nb result in a drastically different ^{93}Nb EFG tensor with an extremely augmented V_{33} component (as $C_Q = eQV_{33}/h$). The piecewise QCPMG spectra were only acquired at 9.4 T, so accurate extraction of CS tensor parameters is troublesome. Simulations reveal that a slightly better fit can be obtained with $\Omega = 150$ ppm and $\kappa = -0.6$ (Figure B.3.2). Ab initio calculations presented later in the chapter predict a larger Ω on the order of 450 ppm; this is clearly not the case, as a noticeable change in the breadth of the powder pattern and/or positions of the discontinuities would be apparent. The CSA makes a very small contribution to the quadrupolar-dominated pattern and the span likely has an upper limit near 300 ppm. Thus, it is difficult to extract the CSA in this case unless extremely high magnetic field strengths were to be applied.

The molecular structure of $CpNbCl_4$ has not been determined by X-ray diffraction methods, due to the difficulty in obtaining single crystals suitable for single-crystal X-ray diffraction experiments. In order to isolate a single crystal of $CpNbCl_4$, a recrystallization from dry THF was attempted (THF was tested to have the greatest solubility in comparison to MeCN, CH_2Cl_2, and toluene). The MAS and static ^{93}Nb NMR spectra of a fine powder of these crystals, along with numerical and analytical simulations, are shown

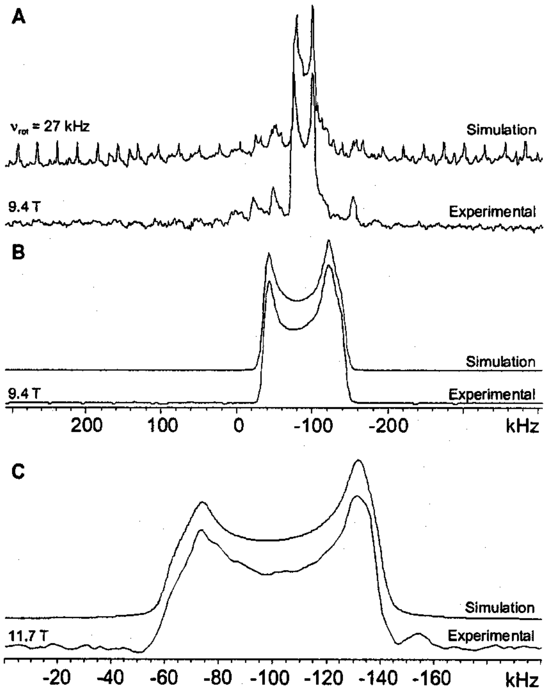

Figure 3.4. Experimental and simulated ^{93}Nb NMR spectra of **7**: (A) MAS and (B and C) static NMR powder patterns at two different magnetic field strengths. In part A, the numerical simulation includes excited central and satellite transitions, and assumes uniform excitation, accounting for the high intensities of the spinning sidebands in the simulated pattern.

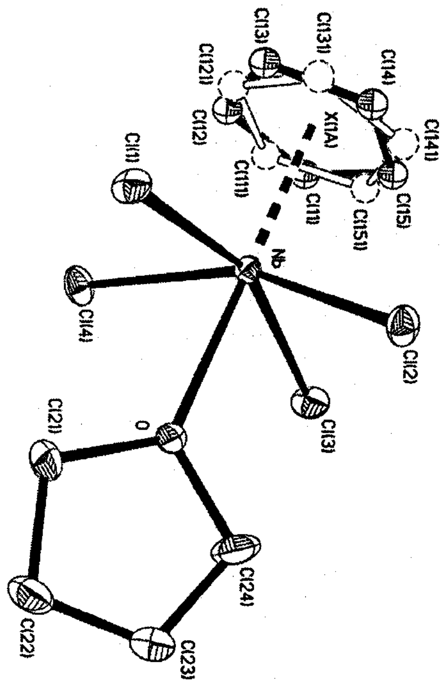

Figure 3.5. Thermal ellipsoid plot (30% probability surface) of the molecular structure of **7**. C11 and C15 (solid ellipsoids) represent the major occupancy atomic position (61%). Note that X(1A) represents the centroid of the Cp ring with the highest occupancy. H atoms are omitted for clarity.

in Figure 3.4. All of the NMR powder patterns and extracted parameters are very distinct from those of **6**, and the combination of ^{93}Nb NMR, ^{13}C NMR and X-ray crystallographic data (*vide infra*) suggests that a single THF molecule coordinates from beneath the four Cl ligands (Chart 1, $CpNbCl_4$•THF (**7**)). The THF ligand significantly alters the ^{93}Nb EFG and CS tensors. The quadrupolar parameters and isotropic chemical shift are obtained from fast-spinning MAS (ν_{rot} = 27 kHz) spectra as δ_{iso} = -703(12) ppm, C_Q = 38.4(4) MHz and η_Q = 0.17(7). The breadth of the static pattern of **7** at 9.4 T is only 125 kHz, which is considerably less than the 450 kHz breadth of **6**; thus, the spectrum can be acquired in a single experiment at both 9.4 and 11.7 T. The value of $\eta_Q = 0.17$ in **7** implies that V_{33} is the pseudo-unique component of the EFG tensor, in contrast to the $\eta_Q = 0.83$ in **6**. In addition, the niobium nucleus is slightly more shielded due to a fairly dramatic change in the CS tensor. The span of the CS tensor is larger than those measured in all of the other complexes, though it is still non-axial, with $\Omega = 320(10)$ ppm and $\kappa = -0.4(2)$.

Single-crystal X-ray diffraction experiments yielded a refined crystal structure which indicates that the $CpNbCl_4$ unit is directly coordinated at the niobium by a THF molecule (Figure 3.5). Powder X-ray patterns for **6** taken directly from the sample bottle and the recrystallized **7** are very different from one another (Figure 3.6A,B, respectively). Simulation of the powder XRD pattern of 7 (Figure 3.6C) using the refined single-crystal structural data indicates that the molecular structure in the powdered microcrystalline sample is identical to that in the single crystal phase. The structure of 7 is

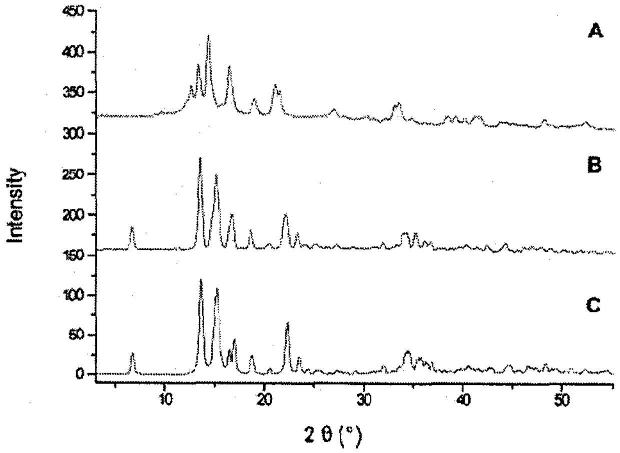

Figure 3.6. Experimental powder XRD patterns of (A) **6** and (B) **7**, and (C) simulation of (B).

similar to those observed for phosphine and cyanide adducts of $CpNbCl_4$ and Cp^*NbCl_4 complexes.[22,23,105] Attempts to sublime **6** were unsuccessful at producing suitable single crystals for XRD experiments; however, the combination of the NMR data and ab initio calculations presented below are used to propose potential solid-state structures for this system (*vide infra*).

Solid-State ^{13}C NMR. Carbon-13 MAS and CP/MAS NMR spectra were acquired for all samples, and were utilized to measure carbon CS tensors, ^{13}C-^{93}Nb *J*-couplings, assess Cp ring dynamics, and ascertain the identity and purity of each sample. Carbon chemical shift assignments are summarized for all complexes in Table 3.2, and theoretically calculated carbon CS tensors of selected compounds are presented in Table 3.3.

The ^{13}C CP/MAS NMR spectra of complexes with unsubstituted Cp rings, $CpNb(CO)_4$ (**1**), $CpNbCl_4$ (**6**) and $CpNbCl_4$•THF (**7**), are shown in Figure 3.7A,B,C, respectively. Herzfeld-Berger analysis[106] of these spectra yields δ_{iso} = 96.6(1) ppm, Ω = 120(1) ppm and κ = 0.94(2) for **1**, which is quite distinct from that of **6** and **7**, with δ_{iso} = 131.4(1) ppm, Ω = 167(1) ppm, κ = 0.65(1) and δ_{iso} = 130.4(1) ppm, Ω = 155(5) ppm, κ = 0.7(1), respectively. The Ω and κ for **6** and **7** are quite unusual. For instance, Sayer[107] and Kentgens *et al.*[108] used solid-state ^{13}C NMR to study carbon CSA in some neutral and cationic half-sandwich Fe metallocenes, and measured carbon CS tensors with spans on the order of ca. 100 ppm and high axial symmetry ($\kappa \approx 1.0$). The much larger spans in **6** and **7** account for the higher isotropic chemical shifts, and result from decreased shielding in the plane of the Cp ring (i.e., increase in the chemical shifts of δ_{11}

Table 3.2. Structural Assignments of Experimental ^{13}C NMR Spectra for Cp′NbX$_4$ Complexes.

H, **1**[a]	COMe, **2**	CO$_2$Me, **3**	CO$_2$Et, **4**	COCH$_2$Ph, **5**	CpNbCl$_4$, **6**	CpNbCl$_4$•THF, **7**
Cp, 96.6(1)	CH$_3$, 26.4(3)	CH$_3$, 53.3(2)	CH$_3$, 16.0(2)	CH$_2$, 45.3(2)	Cp, 131.4(1)	THF(C_β), 26.8(3)
	Cp(C_α),[b] 94.1(1), 104.3(1)	Cp(C_β), 95.3(1)	CH$_2$, 60.6(2)	Cp($C_{\alpha,\beta}$), 98.8(2)		THF(C_α), 75.8(2)
	Cp(C_β), 100.1(1)	Cp(C_α), 98.2(1)	Cp($C_{\alpha,\beta}$), 99.1(1)	Cp(C_{ipso}), 111.7(3)		Cp, 130.4(1)
	Cp(C_{ipso}), 110.0(3)	Cp(C_{ipso}), 100.3(3)	Cp(C_{ipso}), 100.6(1)	Ph(C_p), 128.4(2)		
	Me-CO, 195.8(1)	Me-CO$_2$, 166.1(1)	Et-CO$_2$, 165.5(2)	Ph(C_o), 129.5(2)		
		OC-Nb, 250(5)		Ph(C_{ipso}), 132.6(2)		
				Ph(C_m), 134.6(2)		
				O$_2$$C$-CH$_2$, 195.2(2)		
				OC-Nb, 250.7(3)		

[a] Singly substituted (η^5-C$_5$H$_4$R)Nb(CO)$_4$ complexes, with the substituents, R, being specified in the Table for samples **1** to **5**; [b] C_α, C_β and C_{ipso} resonances of the Cp ring are well resolved only in the ^{13}C NMR spectrum of **2**.

Table 3.3. Carbon Chemical Shielding Tensor of the Cyclopentadienyl Ligand in Unsubstituted $CpNbX_4$ Complexes.

Source	δ_{11} (ppm)[a]	δ_{22} (ppm)	δ_{33} (ppm)	δ_{avg} (ppm)[b]	δ_{iso} (ppm)[c]	Ω (ppm)	κ
$CpNb(CO)_4$, **1**	**137.8**[d]	**134.2**	**17.8**	136	**96.6(1)**	**120(1)**	**0.94(2)**
RHF/6-311G**	152.8	90.1	8.8	121.5	83.9	144	0.13
B3LYP/6-311G**	167.2	95.5	16.2	131.4	93	151	0.05
$CpNbCl_4$, **6**	**196.8**	**167.6**	**29.8**	182.2	**131.4(1)**	**167(1)**	**0.65(1)**
RHF/6-311G**	188.3	157.9	9.3	173.1	118.5	179	0.66
B3LYP/6-311G**	189.3	150.3	23.3	169.8	121	166	0.53
$CpNbCl_4$•THF, 7	**189.8**	**166.6**	**34.8**	178.2	**130.4(1)**	**155(5)**	**0.7(1)**
RHF/6-311G**	177.8	162.2	4.8	170	114.9	173	0.82
B3LYP/6-311G**	179.9	160.6	18.9	170.3	119.8	161	0.76

[a] δ_{ii} are the principal components of the niobium CS tensor such that $\delta_{11} \geq \delta_{22} \geq \delta_{33}$; [b] average value of δ_{11} and δ_{22}, with $\delta_{avg} = (\delta_{11} + \delta_{22})/2$; [c] carbon CS tensor parameters: $\delta_{iso} = (\delta_{11} + \delta_{22} + \delta_{33})/3$, $\Omega = \delta_{11} - \delta_{33}$, and $\kappa = 3(\delta_{22} - \delta_{iso})/\Omega$. Carbon chemical shifts are referenced to TMS (experimental) or CO (theoretical), see experimental section for details. Averaged theoretical δ_{iso}, Ω and κ are reported over the five distinct carbon sites of the Cp ring; [d] experimental values are provided in boldface for comparison.

and δ_{22}). More interesting are the skews of the CS tensors. In **1**, the skew is near axially symmetric, resulting from time-averaging of the δ_{11} and δ_{22} components of the carbon CS tensor. This is indicative of unhindered rotation of the η^5-Cp rings, which normally occurs at temperatures greater than 77 K.[109] This is supported by theoretical calculations on **1**, which predict a non-axially symmetric CS tensor; however, when the δ_{11} and δ_{22} components are averaged (representative of rapid, five-fold reorientation of the Cp ring), there is a very good agreement between experiment and theory. In **6** and **7**, the non-axially symmetric skew might be a sign of hindered Cp ring rotation, which was previously observed by Gay *et al.* in VT ^{13}C NMR experiments on solid $CpMo(CO)_3R$, where R = Me, Et.[110] This assumption is also supported by the theoretical calculations, which predict CS tensor parameters in very good agreement with experimental values. The hindered rotation in **6** and **7** could be intramolecular and/or intermolecular in origin.

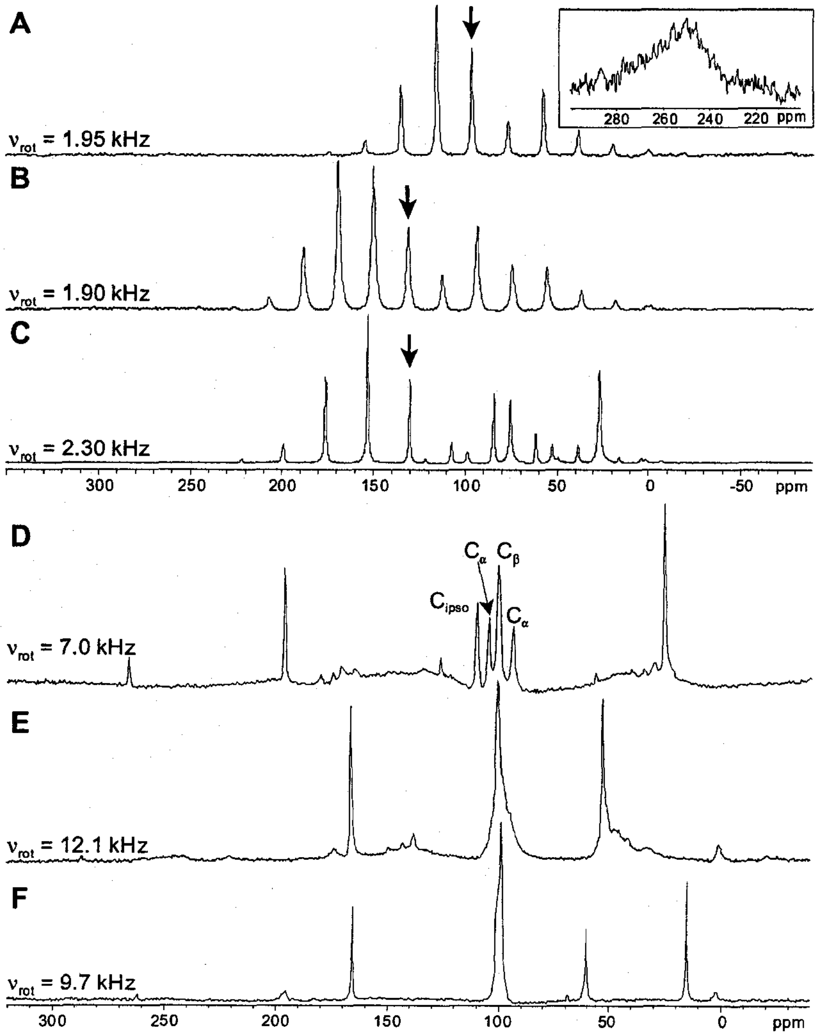

Figure 3.7. ^{13}C VACP/MAS NMR spectra for (A) **1**, (B) **6**, (C) **7**, (D) **2**, (E) **3**, and (F) **4** at 9.4 T. Arrows indicate isotropic resonances. Inset: The extremely low intensity of the O*C*-Nb resonance in the ^{13}C MAS NMR spectrum of **1** is presented.

Examination of the crystal structure of **7** reveals intermolecular contacts between the Cl ligands and the nearest H atom on the Cp ring (i.e., Cl···H ranging from 2.9 to 3.0 Å, Figure B.3.3). Weak interactions of this kind were proposed by Blaurock *et al.* in the phosphine adducts of $CpNbCl_4$ complexes, in which almost identical Cl···H distances were observed (2.90 Å), resulting in polymeric ladders or dimers in the lattice.[23] Intermolecular interactions of this sort do not exist in the $CpNb(CO)_4$ molecule, accounting for the unhindered Cp rotation at temperatures above 77 K. Interestingly, our own VT ^{13}C CP/MAS experiments on **6** from +100 °C to -90 °C reveal no substantial changes in the carbon CSA (Figure B.3.4), suggesting that unhindered Cp ring rotation may only occur near the decomposition temperature of $CpNbCl_4$ (which we have measured at ca. 130 to 140 °C).

In the ^{13}C CP/MAS NMR spectra of $CpNb(CO)_4$, a resonance corresponding to the carbonyl ligands is not observed, regardless of the length of the contact time. However, ^{13}C MAS NMR spectra acquired using a recycle time of 29 s reveal a very broad (spanning ca. 40 ppm), low intensity resonance centred at ca. 250 ppm (Figure 3.7A, inset). This resonance has a similar shift to that observed in the solution ^{13}C NMR spectrum of labeled $CpNb(^{13}CO)_4$ (250 ppm), in which a ten peak multiplet is observed arising from $^{1}J(^{93}Nb, ^{13}C) = 222$ Hz.[10]

Single substitution of the Cp ring breaks the five-fold symmetry and results in a number of different Cp-ring carbon peaks. The substituted carbon is denoted as C_{ipso}, the neighbouring carbons C_α and the remaining carbons C_β. For instance, in the solid-state ^{13}C VACP/MAS NMR spectrum of **2**, the isotropic chemical shifts for C_{ipso}, C_β and C_α are assigned as 110.0(3) ppm, 100.1(1) ppm, and 94.1(1) ppm and 104.3(1) ppm, respectively (Figure 3.7D). There are two separate C_α peaks, since the rigid positioning of the side chain differentiates the electronic environments of these carbon sites. The assignments are made based upon both carbon chemical shielding parameters from ab initio calculations presented herein and analogous assignments made in the literature.[15] The wavy baseline arises from an overlap between the spinning sidebands, and the background signal from the Torlon-containing drive tip, and top and bottom spacers,[111] found exclusively in the 2.5 mm rotors used for **2**. In compounds **3** and **4** (Figure 3.7E,F), the various Cp carbon sites cannot easily be differentiated, due to either line broadening and/or the Cp ring ^{13}C nuclei having similar magnetic environments.

As in the case of **1**, NMR powder patterns corresponding to the carbonyl groups are either not observed or very weak and broad for **2**, **3** and **4**. Interestingly, in the ^{13}C MAS NMR spectrum of **5** (Figure 3.8), which was acquired with a recycle time of 40 s, a very intense multiplet is observed which corresponds to the niobium-bound carbonyl groups. The ^{13}C multiplet has ten peaks, which result from indirect spin-spin coupling (*J*-coupling) with the ^{93}Nb nucleus (^{93}Nb is spin 9/2 and 100% naturally abundant). The

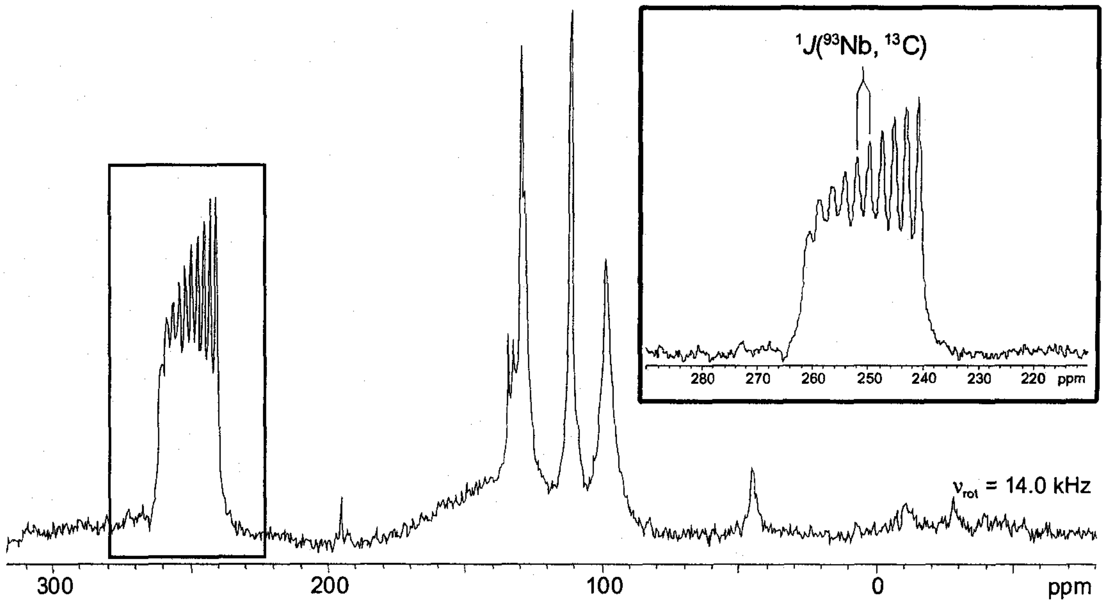

Figure 3.8. ^{13}C MAS NMR spectrum of **5** at 9.4 T. Inset: Expansion of the O*C*-Nb resonance showing the $^1J(^{93}Nb, ^{13}C)$ pattern.

asymmetric appearance of the multiplet is the result of residual dipolar coupling[112] between ^{13}C and ^{93}Nb, which causes differential peak spacing and broadening within the multiplet. The value of $^{1}J(^{13}\text{C}, ^{93}\text{Nb})$ is measured from the separation between the central peaks of the multiplet to be 220(1) Hz, which is very similar to that observed for labeled CpNb(^{13}CO)$_4$.[10] It is often very difficult to observe such *J*-couplings between spin-1/2 and quadrupolar nuclei in solution and solid-state NMR experiments, due to rapid relaxation at the quadrupolar nucleus and scalar relaxation of the second kind at the spin-1/2 nucleus. There are a few other reported cases of similar couplings between spin-1/2 and spin-9/2 nuclei in the solid-state, including $^{1}J(^{31}\text{P}, ^{93}\text{Nb})$ in a series of phosphine-containing half-sandwich niobium complexes,[25,26] $^{1}J(^{31}\text{P}, ^{115}\text{In})$ in the ^{31}P NMR spectra of a 1:1 adduct of indium tribromide and a triarylphosphine,[113] and $^{2}J(^{29}\text{Si}, ^{93}\text{Nb})$ in a niobium silicate ($Rb_4(NbO)_2(Si_8O_{21})$).[114] To the best of our knowledge, there has not been any report of $^{1}J(^{13}\text{C}, ^{93}\text{Nb})$ measured in solid-state ^{13}C NMR experiments.

Niobium NMR interaction tensors. In this section, we will first discuss the ^{93}Nb EFG tensors for the Nb(I) complexes, followed by the Nb(V) complexes, and then move on to a brief discussion of theoretical niobium chemical shielding tensors. We also present VT ^{93}Nb NMR spectra of complexes **1** and **7**, in an effort to make a prefatory examination on the effects of intramolecular motion on ^{93}Nb EFG tensor orientation. The theoretically calculated ^{93}Nb EFG and CS tensor parameters are presented in Tables 3.4 to 3.7, along with the corresponding experimental values for comparison (other relevant data is reported elsewhere and is not included in this thesis due to the large number of calculations).[115]

Table 3.4. Theoretical ^{93}Nb EFG Tensor Parameters in Nb(I) Complexes.

Source[a]	V_{11} (a.u.)[b]	V_{22} (a.u.)	V_{33} (a.u.)	$\lvert C_Q \rvert$ (MHz)[c]	η_Q
$CpNb(CO)_4$, **1**	—	—	—	**1.0(2)**[d]	**0.80(10)**
RHF/4F/6-311G**	-0.1334	-0.1821	0.3155	23.7	0.15
RHF/6D/6-311G**	-0.1083	-0.1892	0.2974	22.4	0.27
B3LYP/4F/6-311G**	-0.1172	-0.1565	0.2737	20.6	0.14
B3LYP/6D/6-311G**	-0.0941	-0.1715	0.2655	20	0.29
$(MeOC)CpNb(CO)_4$, **2**	—	—	—	**9.7(1)**	**0.10(2)**
RHF/4F/6-311G**	-0.0083	-0.0889	0.0973	7.3	0.83
RHF/6D/6-31G**	-0.085	-0.115	0.1999	15	0.15
RHF/6D/6-311G**	-0.0139	-0.0861	0.1	7.5	0.72
B3LYP/4F/6-311G**	0.0137	0.1067	-0.1204	9.1	0.77
B3LYP/6D/6-311G**	0.0027	0.116	-0.1187	8.9	0.95
$(MeO_2C)CpNb(CO)_4$, **3**	—	—	—	**9.0(3)**	**0.79(4)**
RHF/4F/6-311G**	-0.0187	-0.0885	0.1072	8.1	0.65
RHF/6D/6-311G**	-0.0067	-0.1188	0.1255	9.4	0.89
B3LYP/4F/6-311G**	-0.0119	-0.0714	0.0833	6.3	0.71
B3LYP/6D/6-311G**	0.0228	0.0952	-0.118	8.9	0.61
$(EtO_2C)CpNb(CO)_4$, **4**	—	—	—	**8.7(4)**	**0.89(9)**
RHF/4F/6-311G**	-0.0169	-0.0897	0.1066	8	0.68
RHF/6D/6-311G**	-0.0058	-0.1174	0.1232	9.3	0.91
B3LYP/4F/6-311G**	-0.0259	-0.0681	0.094	7	0.45
B3LYP/6D/6-311G**	0.0151	0.0992	-0.1143	8.6	0.74
$(PhH_2COC)CpNb(CO)_4$, **5**	—	—	—	**12.0(3)**	**0.81(3)**
RHF/4F/6-311G**	0.0154	0.1589	-0.1742	13.1	0.82
RHF/6D/6-311G**	0.0196	0.1533	-0.1729	13	0.77
B3LYP/4F/6-311G**	0.0551	0.1768	-0.2319	17.4	0.52
B3LYP/6D/6-311G**	0.0493	0.1774	-0.2267	17.1	0.57

[a] Source from theoretical work is in the form method/basis set (Nb)/basis set (all other atoms); [b] V_{ii} are the principal components of the ^{93}Nb EFG tensor such that $|V_{33}| \geq |V_{22}| \geq |V_{11}|$; [c] absolute value of the C_Q, where $C_Q = eQV_{33}/h$, and $\eta_Q = (V_{11} - V_{22})/V_{33}$; theoretical C_Q are converted from atomic units to MHz (see experimental section for details); [d] experimental values are provided in boldface for comparison.

^{93}Nb EFG Tensors. The theoretical values of C_Q(^{93}Nb) are overestimated for **1** by more than an order of magnitude at all levels of theory. It is unlikely that the discrepancy between experiment and theory arises from insufficiently large basis sets or low levels of theory, since there are reasonable agreements between experiment and theory for compounds **2** through **5**, which are larger molecules, and where the substituted Cp rings do not rotate freely (Table 3.4). The experimental $\eta_Q = 0.8$ implies that V_{33} is not directed along the pseudo-rotational axis of the molecule (i.e., the molecular axis), and that V_{11} is the pseudo-unique component. Calculated ^{93}Nb EFG tensor orientations support this hypothesis, with V_{11} oriented nearly perpendicular to the central mirror plane, and V_{22} and V_{33} contained within the mirror plane, approximately along the direction of the Nb-CO bonds (e.g., $\angle(V_{22}\text{-Nb-Cp}_{\text{cen}}) = 42°$ and $\angle(V_{33}\text{-Nb-Cp}_{\text{cen}}) = 48°$ according to RHF/6-311G** calculations, Figure 3.9A). However, the theoretical values of η_Q lie closer to the case of axial symmetry where $|V_{11}| \approx |V_{22}| < |V_{33}|$, in disagreement with experiment. This is puzzling, given that V_{22} and V_{33} appear to be oriented in very similar chemical environments.

It is very probable that the experimentally measured C_Q is the result of time averaging of the EFG tensor orientation resulting from some sort of intramolecular motion (i.e., the measured C_Q results from a time average of different orientations of V_{33}, perhaps from Cp ring rotation). Theoretical calculations of the SCF energy as a function of Cp ring rotation on both solid-state and gas-phase structures reveal four-fold rotational barriers on the order of 12 to14 kJ mol^{-1} and 5.5 kJ mol^{-1}, respectively (Figure 3.9B,C). Given the relatively low rotational barriers of Cp rings predicted by theory, it is likely that VT experiments conducted below 77 K could slow down this intramolecular motion enough to observe the completely unaveraged EFG tensor components.[109] VT static ^{93}Nb NMR experiments conducted from +100 °C to -140 °C (Figure 3.10) partially

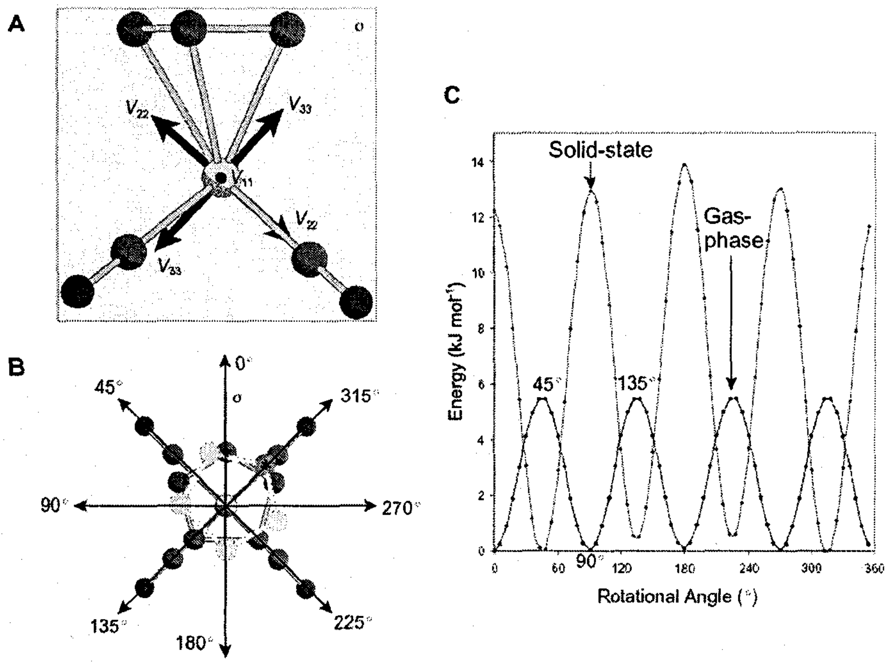

Figure 3.9. (A) ^{93}Nb EFG tensor orientation with respect to the molecular mirror plane, and (B) schematic picture of the 5-fold rotation of the Cp ring about the molecular axis in **1**. In (B), 0° rotation is defined such that the mirror plane contains the unique Cp carbon (marked with an asterisk). (C) A plot correlates the SCF energy with the Cp ring rotation, defined in part B, for **1**.

support this hypothesis, revealing that C_Q increases as the temperature is decreased and η_Q changes from 1.0 (i.e., $V_{22} = V_{33}$) at high temperatures to 0.56 at the lowest temperature, meaning the tensors components are at least partially distinguished. These results suggest that higher temperatures result in averaging of the V_{22} and V_{33} components, while at lower temperatures, reduced motion results in their differentiation. Theoretical calculations also demonstrate that the magnitude and sign of C_Q, the value of η_Q and the EFG tensor orientation all change as the orientation of the Cp ring is altered; however, a detailed experimental and theoretical study of this temperature-dependent EFG variation in **1** is beyond the scope of this thesis (preliminary results are reported elsewhere).[115]

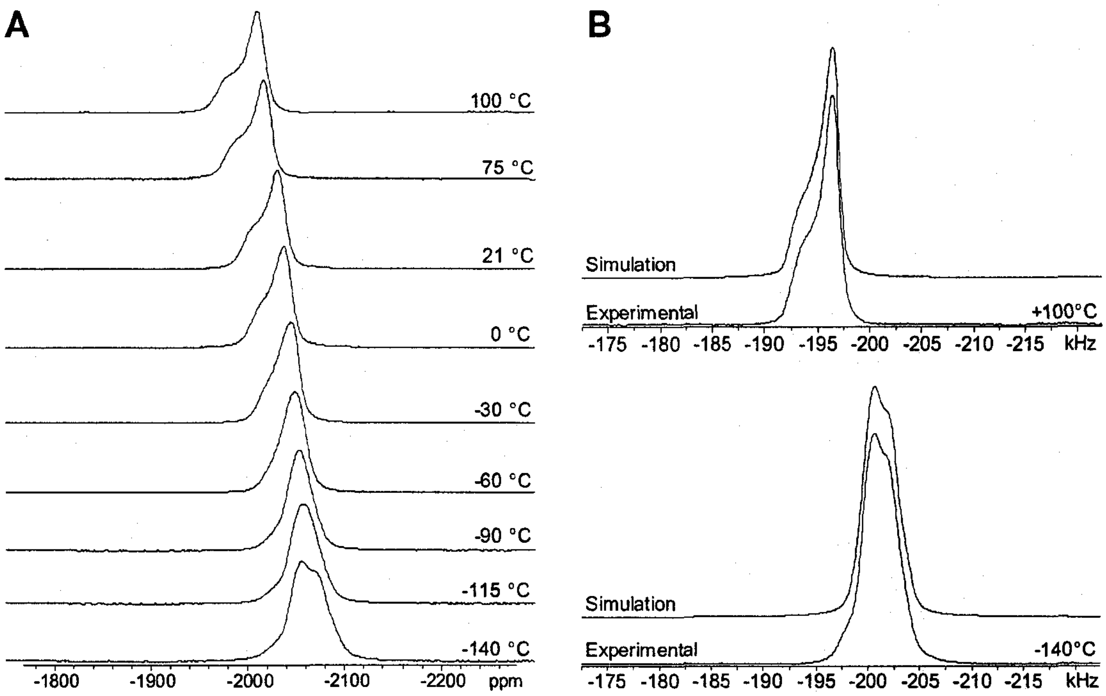

Figure 3.10. (A) VT static ^{93}Nb NMR spectra of **1** at 9.4 T. (B) Simulation reveals C_Q = 2.0(10) MHz, η_Q = 1.00(1), δ_{iso} = -2005.5(10) ppm, Ω = 43(2) ppm, κ = -1.00(2), α = 70(10)°, β = 0(10)°, and γ = 20(20)° for +100 °C powder pattern in part A; and C_Q = 5.0(2) MHz, η_Q = 0.56(6), δ_{iso} = -2056.0(10) ppm, Ω = 34(2) ppm, κ = -0.95(5), α = 90(20)°, β = 75(2)°, and γ = 45(45)° for -140 °C powder pattern in part A.

Calculations on **2** using the 6-311G** basis set are relatively close to the experimental value of C_Q; however, in all cases, η_Q is predicted to be in the 0.7 to 1.0 range, in disagreement with experiment. The experimental value of η_Q = 0.10(2) is anomalous in this series of Nb(I) complexes, implying that V_{11} and V_{22} are similar, and that V_{33} is oriented in a distinct electronic environment. Higher level calculations using 6-311G(2d,p) and 6-311G(2df,p) basis sets, with and without diffuse functions, did not result in improved agreement with experiment.[115] Interestingly, lower level RHF/6-31G** calculations overestimate C_Q considerably, but predict that η_Q = 0.15. From this particular calculation, the V_{33} component is oriented approximately towards the

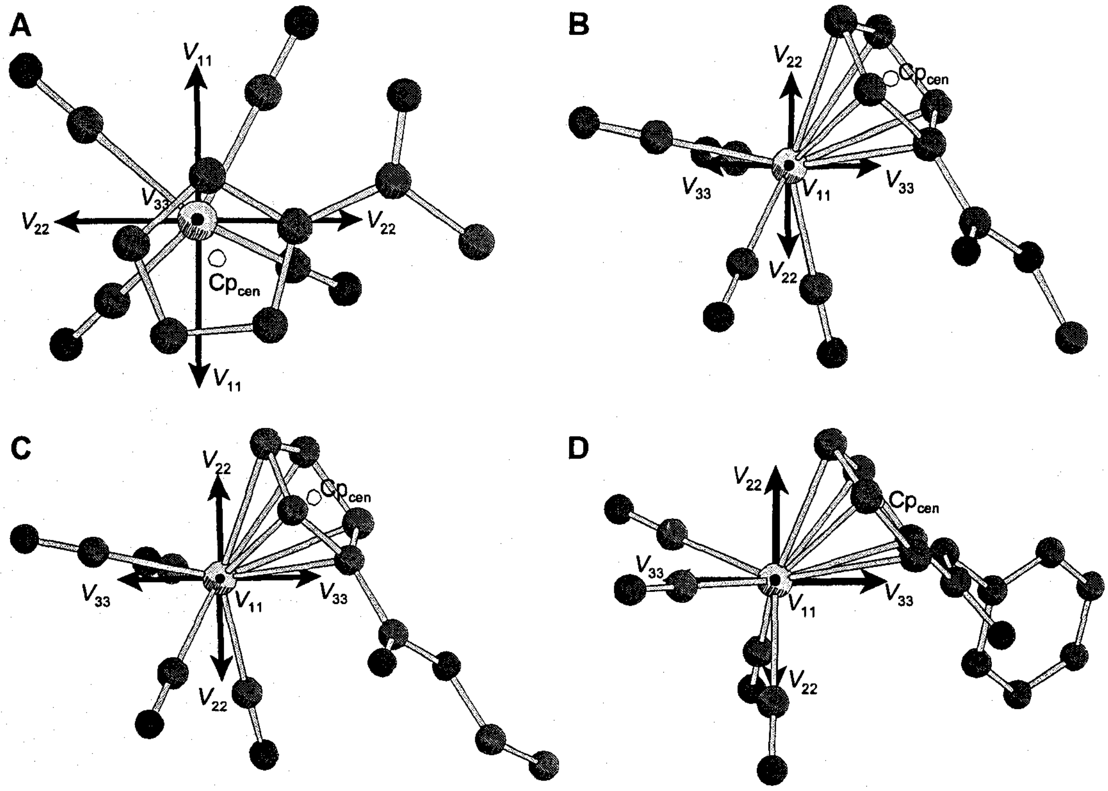

Figure 3.11. ^{93}Nb EFG tensor orientations for (A) **2**, (B) **3**, (C) **4**, and (D) **5**. Note that in part D, V_{22} is directed close to one of the Nb-CO bonds with $\angle(V_{22}\text{-Nb-CO}) \approx 20°$.

Cp ring ($\angle(V_{33}\text{-Nb-Cp}_{\text{cen}}) = 17.4°$), and the V_{22} points approximately in the direction of the side chain of the Cp ring (Figure 3.11A). The reason for the atypical EFG tensor in **2** compared to the others in this series of complexes is unknown at this time. On a side note of consequence, embedded cluster molecular orbital (ECMO) calculations do not alter the values of C_Q and η_Q significantly for **1**, **2**, or any of the other complexes discussed herein, suggesting that EFGs of intramolecular origin are dominant, and that major discrepancies between theory and experiment do not arise from intermolecular effects.

Calculations on complexes **3**, **4** and **5** are in reasonable agreement with theory; notably, the RHF calculations of C_Q and η_Q are in good agreement with experimental values. The ^{93}Nb EFG tensors for **3** and **4** have similar orientations predicted at all levels of theory: V_{33} is oriented ca. 10° from an Nb-CO bond and V_{22} is in a similar environment. V_{11}, the pseudo-distinct component, is directed away from the Nb-CO bonds and the Cp ring (Figure 3.11B,C). Calculations predict that C_Q is smaller in all substituted complexes in comparison to the parent complex; this could in part be due to the Nb-Cp$_{cen}$ distance, which is 2.090(2) Å for all substituted complexes, and 2.069(2) Å for the parent. In comparing **3** and **4** with **5**, the larger C_Q in the latter undoubtedly results from the decreased ground state electronic symmetry resulting from substitution with the voluminous $COCH_2Ph$ group. However, the EFG orientation in **5** is very similar to that encountered in the former complexes (Figure 3.11D).

All calculations on the Nb(V) complexes, **6** and **7**, predict a large increase in C_Q relative to the Nb(I) complexes, though there are some difficulties in obtaining quantitative agreement with experiment in both cases (Table 3.5). Since a crystal structure is not available for **6**, the solid-state structure had to be approximated from analogous crystal structures (details in experimental section). Calculations on a geometry-optimized gas-phase $CpNbCl_4$ molecule[115] consistently results in an overestimation of C_Q and near zero η_Q, in disagreement with experiment. Approximating the structure of **6** by simply using the $CpNbCl_4$ framework from **7** without the THF ligand results in a severe overestimation of C_Q (as high as ca. 94 MHz), also implying the important role of THF in altering the ^{93}Nb EFG tensor. Using the approximated solid-state structure of **6**, with a Nb-Cp$_{cen}$ distance of 2.06 Å, there is reasonable agreement between experimental and theoretical C_Q, but the values of η_Q are in disagreement. Theoretical calculations align V_{33}

Table 3.5. Theoretical ^{93}Nb EFG Tensor Parameters in Nb(V) Complexes.

Source[a]	V_{11} (a.u.)[b]	V_{22} (a.u.)	V_{33} (a.u.)	$\lvert C_Q \rvert$ (MHz)[c]	η_Q
$CpNbCl_4$, **6**	—	—	—	**54.5(5)**[d]	**0.83(3)**
RHF/4F/6-311G**	0.2085	0.4721	-0.6806	51.2	0.39
RHF/6D/6-311G**	0.1937	0.4426	-0.6363	47.8	0.39
B3LYP/4F/6-311G**	0.338	0.5143	-0.8523	64.1	0.21
B3LYP/6D/6-311G**	0.301	0.4714	-0.7724	58.1	0.22
$CpNbCl_4$•THF, 7	—	—	—	**38.4(4)**	**0.17(7)**
61% occ. RHF/4F/6-311G**[e]	0.1507	0.2257	-0.3764	28.3	0.2
61% occ. RHF/6D/6-311G**	0.1001	0.1816	-0.2817	21.2	0.29
61% occ. B3LYP/4F/6-311G**	0.3651	0.4372	-0.8023	60.3	0.09
61% occ. B3LYP/6D/6-311G**	0.297	0.36	-0.657	49.4	0.1
39% occ. RHF/4F/6-311G**	0.0916	0.2406	-0.3322	25	0.45
39% occ. RHF/6D/6-311G**	0.0394	0.1865	-0.226	17	0.65
39% occ. B3LYP/4F/6-311G**	0.3282	0.4461	-0.7743	58.2	0.15
39% occ. B3LYP/6D/6-311G**	0.2576	0.3656	-0.6232	46.9	0.17

[a-d] See footnotes of Table 3.4; [e] calculations were conducted upon molecular coordinates taken from both the major (61%) and minor (39%) occupancies used to refine the crystal structure structures.

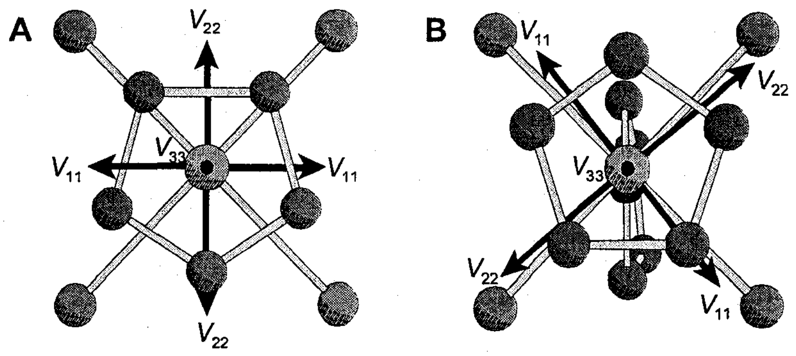

Figure 3.12. ^{93}Nb EFG tensor orientations for (A) **6** and (B) **7**.

along the molecular axis; however, experimental parameters imply that V_{11} is the unique component, and that V_{22} and V_{33} are oriented in electronically similar environments, contrary to these predictions (Figure 3.12A). In light of the pseudo-octahedral structure of 7, and previously reported dimeric structures of related compounds in the form

$[Cp'ZrLCl_3]_2$,[116-120] it is possible that compound **6** forms a centro-symmetric bis-μ^2-chlorine-bridged dimer of the type depicted in Chart 3.2, which may account for the discrepancy between experimental and theoretical parameters. However, we have not attempted to theoretically approximate the molecular structure of the dimer at this time, though future structural characterizations will focus on this problem.

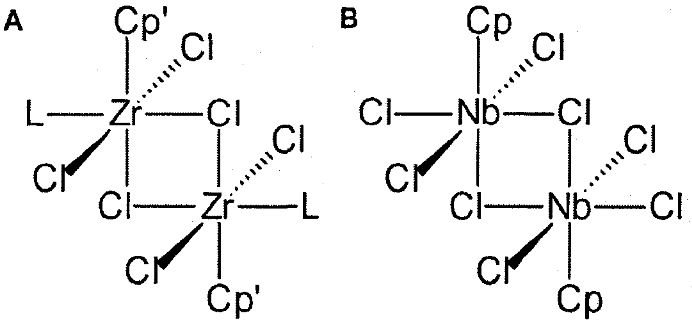

Chart 3.2. (A) Previously reported dimeric structures of compounds related to **6** in the form $[Cp'ZrLCl_3]_2$. (B) Possible structure of **6** which forms a centro-symmetric bis-μ^2-chlorine-bridged dimer.

Calculations on **7** were conducted upon molecular coordinates taken from both the major (61%) and minor (39%) occupancies used to refine the crystal structure. The value of C_Q is underestimated and overestimated by RHF and B3LYP calculations, respectively, though all calculations correctly predict C_Q to be larger than in the Nb(I) complexes and smaller than in compound **6**. The value of η_Q is predicted to have nearly axial symmetry in all cases except the RHF calculations on the structure with minor occupancy. The RHF and B3LYP calculations orient V_{33} very close to the direction of the Nb-O bond, with $\angle V_{33}$-Nb-O ca. 11° to 16° and 3° to 5°, respectively. V_{11} and V_{22} are in very similar electronic environments: for instance, in the B3LYP/6D calculations, both are directed towards the four Nb-Cl bonds (with dihedral angles, $\angle(V_{33}\text{-Nb-Cp}_{cen}\text{-Cl})$, ranging from 6°

to 7°, Figure 3.12B). The crystal structure of **7** used for these calculations was obtained at – 100 °C, so it might be expected that temperature-dependent structural changes are responsible for the divergence between experiment and theory. However, VT ^{93}Nb NMR experiments on **7** reveal that there are relatively small changes in both the EFG and CS tensor parameters with changing temperature (Figure B.3.5). As the temperature drops, C_Q decreases (Figure B.3.6), which is different from the VT behaviour in **1**. This distinct VT behaviour in **7**, unlike in **1**, occurs because V_{33} is oriented near to the Nb-Cp$_{cen}$ direction, and its magnitude is influenced by changes in Nb-Cp$_{cen}$ distance.[36]

Niobium Chemical Shielding Tensors. There are several general observations that can be made after a review of the niobium CS tensor data (Tables 3.6 and 3.7). Isotropic chemical shifts are not quantitatively predicted, though qualitative trends are observed. For instance, for a given set of calculations, Nb(I) complexes are predicted to have highly shielded ^{93}Nb nuclei in comparison to Nb(V) complexes. The lack of quantitative agreement between experiment and theory can be attributed to the overestimation of the spans of the niobium chemical shielding tensors. For **1**, calculations overestimate the experimentally measured span by an order of magnitude, perhaps suggesting that motional averaging of the CS tensor is taking place (a similar observation was made for the ^{93}Nb EFG tensor above). For complexes **2** through **5**, RHF and B3LYP calculations consistently overestimate the spans, by about two times for the former and four times for the latter. RHF calculations predict the skews accurately for **1** and **2**, B3LYP calculations for **3** and **4**, while no calculation seems to predict the proper skew for **5**. For **6** and **7**, the spans are overestimated by a factor of ca. three. The application of

Table 3.6. Theoretical Niobium CS Tensor Parameters in Nb(I) Complexes.

Source[a]	δ_{11} (a.u.)[b]	δ_{22} (a.u.)	δ_{33} (a.u.)	δ_{iso} (ppm)[c]	Ω (ppm)	κ
$CpNb(CO)_4$, **1**	**-2004.3**[d]	**-2037.5**	**-2039.3**	**-2027(4)**	**35.0(5)**	**-0.90(5)**
RHF/4F/6-311G**	-1722.3	-1972.1	-1980.9	-1892	259	-0.93
RHF/6D/6-311G**	-1554	-1800	-1805.9	-1720	252	-0.95
B3LYP/4F/6-311G**	-2132.6	-2311.1	-2634.4	-2359	502	0.29
B3LYP/6D/6-311G**	-1949.3	-2120.1	-2428.8	-2166	479	0.29
$(MeOC)CpNb(CO)_4$, **2**	**-1859.5**	**-1922**	**-1984.5**	**-1922(2)**	**125(3)**	**0.00(2)**
RHF/4F/6-311G**	-1771	-1888.7	-2025.3	-1895	254	0.07
RHF/6D/6-311G**	-1615.9	-1716.5	-1838.3	-1724	222	0.1
B3LYP/4F/6-311G**	-2126.5	-2246	-2648.4	-2340	522	0.54
B3LYP/6D/6-311G**	-1951.1	-2058.4	-2437.8	-2149	487	0.56
$(MeO_2C)CpNb(CO)_4$, **3**	**-1858.8**	**-1919.5**	**-1993.8**	**-1924(4)**	**135(5)**	**0.10(5)**
RHF/4F/6-311G**	-1704.9	-1913.4	-1938.7	-1852	234	-0.78
RHF/6D/6-311G**	-1548.8	-1739	-1755.4	-1681	207	-0.84
B3LYP/4F/6-311G**	-2080.9	-2262.1	-2615.8	-2320	535	0.32
B3LYP/6D/6-311G**	-1905.3	-2071.9	-2405.7	-2128	500	0.33
$(EtO_2C)CpNb(CO)_4$, **4**	**-1864**	**-1912**	**-1984**	**-1920(1)**	**120(2)**	**0.20(4)**
RHF/4F/6-311G**	-1699.1	-1894.8	-1922.3	-1839	223	-0.75
RHF/6D/6-311G**	-1821.8	-2003.5	-2019.7	-1948	198	-0.84
B3LYP/4F/6-311G**	-2082.5	-2250.6	-2608.6	-2314	526	0.36
B3LYP/6D/6-311G**	-2168	-2326.6	-2663.5	-2386	495	0.36
$(PhH_2COC)CpNb(CO)_4$, **5**	**-1858.4**	**-1922.1**	**-1949.4**	**-1910(6)**	**91(4)**	**-0.40(20)**
RHF/4F/6-311G**	-1785.2	-1879.1	-1992.1	-1885	207	0.09
RHF/6D/6-311G**	-1625	-1714.3	-1805.6	-1715	181	0.01
B3LYP/4F/6-311G**	-2145.8	-2220.1	-2640.6	-2336	495	0.7
B3LYP/6D/6-311G**	-1967.8	-2038.1	-2428.7	-2145	461	0.69

[a] Source from theoretical work is in the form method/basis set (Nb)/basis set (all other atoms); [b] δ_{ii} are the principal components of the niobium CS tensor such that $\delta_{11} \geq \delta_{22} \geq \delta_{33}$; [c] niobium CS tensor parameters: $\delta_{iso} = (\delta_{11} + \delta_{22} + \delta_{33})/3$, $\Omega = \delta_{11} - \delta_{33}$, and $\kappa = 3(\delta_{22} - \delta_{iso})/\Omega$. Niobium chemical shifts are referenced to 0.4 M $NbCl_5$ solution in CH_3CN (experimental) or $NbCl_6^-$ (theoretical), see experimental section for details; [d] experimental values are provided in boldface for comparison.

Table 3.7. Theoretical Niobium CS Tensor Parameters in Nb(V) Complexes.

Source[a]	δ_{11}[b]	δ_{22}	δ_{33}	δ_{iso}[c]	Ω	κ
$CpNbCl_4$, **6**	**-510.0**[d]	**-630**	**-660**	**-600(30)**	**150(30)**	**-0.60(4)**
RHF/4F/6-311G**	-356.6	-474.3	-791.3	-541	435	0.46
RHF/6D/6-311G**	-254.5	-468.6	-738.3	-487	484	0.11
B3LYP/4F/6-311G**	-121.8	-507.4	-581.5	-404	460	-0.68
B3LYP/6D/6-311G**	-97.9	-498.8	-566	-388	468	-0.71
$CpNbCl_4$•THF, **7**	**-521.7**	**-745.7**	**-841.7**	**-703(12)**	**320(10)**	**-0.40(20)**
61% occ. RHF/4F/6-311G**[e]	-582.9	-1305	-1402	-1097	819	-0.76
61% occ. RHF/6D/6-311G**	-434.5	-1205	-1301	-980	866	-0.78
61% occ. B3LYP/4F/6-311G**	-239.1	-1193	-1254	-895	1015	-0.88
61% occ. B3LYP/6D/6-311G**	-167	-1119	-1180	-822	1012	-0.88
39% occ. RHF/4F/6-311G**	-596.7	-1328	-1429	-1118	832	-0.76
39% occ. RHF/6D/6-311G**	-446	-1230	-1326	-1001	880	-0.78
39% occ. B3LYP/4F/6-311G**	-241.9	-1196	-1285	-907	1043	-0.83
39% occ. B3LYP/6D/6-311G**	-168.7	-1123	-1209	-834	1040	-0.83

[a] Source from theoretical work is in the form method/basis set (Nb)/basis set (all other atoms); [b] δ_{ii} are the principal components of the niobium CS tensor in ppm such that $\delta_{11} \geq \delta_{22} \geq \delta_{33}$; [c] niobium CS tensor parameters: δ_{iso} (ppm) = $(\delta_{11} + \delta_{22} + \delta_{33})/3$, Ω (ppm) = $\delta_{11} - \delta_{33}$, and $\kappa = 3(\delta_{22} - \delta_{iso})/\Omega$. Niobium chemical shifts are referenced to 0.4 M $NbCl_5$ solution in CH_3CN (experimental) or $NbCl_6^-$ (theoretical), see experimental section for details; [d] experimental values are provided in boldface for comparison; [e] calculations were conducted upon molecular coordinates taken from both the major (61%) and minor (39%) occupancies used to refine the crystal structure.

larger 6-311G(2d,p) and 6-311G(2df,p) basis sets, with and without diffuse functions, did not result in significant improvement.[115] For instance, higher level calculations on **2** get closer to the experimentally predicted span, while incorrectly predicting the isotropic chemical shift. It is possible that the future use of relativistic DFT calculations incorporating the zeroth-order regular approximation (ZORA)[121,122,123] or the advent of superior Nb basis sets could improve quantitative agreement between experiment and theory.

All calculations predict similar CS tensor orientations, lending insight into the distinct magnetic shielding characteristics in Nb(I) and Nb(V) metallocenes. RHF

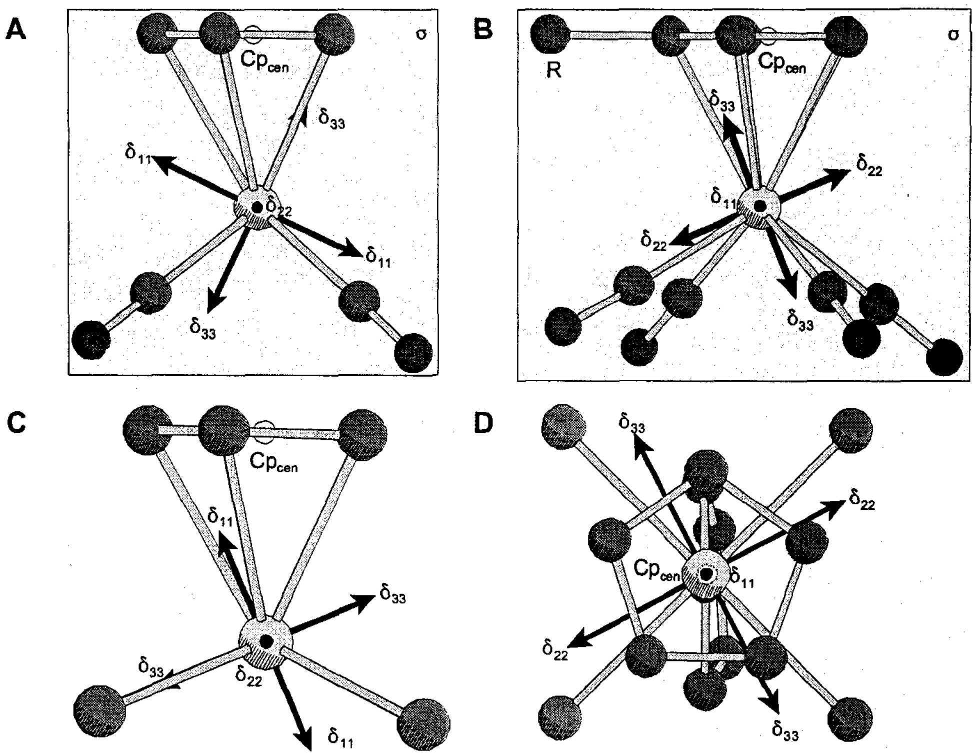

Figure 3.13. Niobium CS tensor orientations for (A) **1**, (B) **2** through **5**, (C) **6**, and (D) **7**.

calculations on the Nb(I) complexes predict that the most shielded CS tensor component, δ_{33}, is oriented towards the Cp ring, with $\angle(\mathrm{Cp_{cen}}\text{-Nb-}\delta_{33})$ angles ranging from 10° to 35°, whereas the B3LYP calculations consistently predict $\angle(\mathrm{Cp_{cen}}\text{-Nb-}\delta_{33})$ angles even closer to zero. Both RHF and B3LYP calculations predict that the δ_{33} and V_{33} components are oriented in similar directions, with notably reduced $\angle(V_{33}\text{-Nb-}\delta_{33})$ angle in the latter. Furthermore, in **1**, δ_{33} and δ_{11} are contained within the molecular mirror plane (Figure 3.13A); whereas in **2** through **5**, δ_{33} and δ_{22} are contained approximately in the pseudo-mirror planes of the molecule (i.e., planes that contain the first atom in the R groups, Figure 3.13B). In contrast, for the Nb(V) complexes, both RHF and B3LYP calculations predict that the least shielded component, δ_{11}, points toward the Cp ring. In

6, δ_{11} is predicted to be oriented slightly away from the Cp ring centroid (Figure 3.13C), with $\angle(\mathrm{Cp_{cen}}\text{-Nb-}\delta_{11})$ between 15° and 26°. However, in **7**, $\angle(\mathrm{Cp_{cen}}\text{-Nb-}\delta_{11})$ is closer to 0° and $\angle(\text{O-Nb-}\delta_{11}) \approx 3°$ to 5° (Figure 3.13D), suggesting that the presence of the THF ligand plays a major role in determining both the magnitude of the tensor components as well as their orientations in the molecular frame. Interestingly and uniquely in **7**, δ_{22} and δ_{33} point approximately towards the Nb-Cl bonds. Most calculations predict that $\angle(\delta_{33}\text{-Nb-}V_{33})$ are on the order of 90° (i.e., δ_{11} and V_{33} are relatively close to one another), in reasonable agreement with experimentally predicted tensor orientations.

A simplistic explanation for the large difference in chemical shifts between Nb(I) and Nb(V) complexes might be that since Nb(I) has more electron density than Nb(V), it should correspondingly be more shielded. However, the more accurate explanation is that chemical shielding tensor orientation and magnitude of its components are altered as a result of differing interactions between Nb and the Cp ring, and Nb and the CO or Cl ligands. For Nb(I) complexes, δ_{33} is consistently oriented towards the Cp ring in the direction of the R group, while in the Nb(V) complexes, δ_{11} is oriented towards the Cp ring centroid. In $\mathrm{CpNbCl_4{\bullet}THF}$, there are occupied and virtual MOs which are close in energy and undergo symmetry-allowed magnetic-dipole mixing, oriented perpendicular to the $\mathrm{Nb\text{-}Cp_{cen}}$ direction, resulting in deshielding parallel to the $\mathrm{Nb\text{-}Cp_{cen}}$ direction. Such MOs are absent in the Nb(I) complexes, where CS tensor spans are much smaller, accounting for the large difference in shielding parameters. Thus, though the exact CS tensor orientations are not duplicated in all calculations, there is still the overall inference that very different chemical shielding mechanisms are at work in the Nb(I) and Nb(V) complexes. Future detailed MO analyses will provide further insight into the magnetic shielding of transition metals in this important class of compounds.

3.4 Conclusion

Solid-state ^{93}Nb, complemented by ^{13}C NMR experiments, has been shown to be a very sensitive and rapid probe of molecular structure and purity in half-sandwich metallocenes. Static, MAS and piecewise ^{93}Nb echo and QCPMG NMR experiments can be conducted with relative ease, and provide spectra which are rich in information on structure and dynamics. Subtle functional group changes on the Cp′ ring result in observable changes in the ^{93}Nb quadrupolar and chemical shift parameters. An immense increase in the quadrupolar interaction is witnessed upon changing the nature of the other coordinating ligands (CO to Cl) and formal oxidation state of the Nb atom (I to V). The increased quadrupolar interaction in $CpNbCl_4$ results in a pattern whose breadth exceeds uniform excitation bandwidths using 1 kW amplifiers and standard magnetic field strengths; notwithstanding, piecewise QCPMG experiments can be applied to rapidly acquire a powder pattern from which relevant NMR tensor parameters can be extracted. Attempts to grow a single crystal of pure $CpNbCl_4$ have resulted in the isolation of a new solvent-coordinated species, $CpNbCl_4$•THF, which has been characterized by both solid-state NMR and X-ray crystallographic methods. The presence of THF results in a dramatic alteration of the ^{93}Nb quadrupolar interaction and spectral appearance, so much so, that it can be acquired within a single experiment, contrary to its unligated parent complex. Preliminary theoretical calculations of NMR tensor parameters do not display high levels of precision in terms of quantitative agreement with experiment, in a few cases due to the approximate nature of the available models used for calculations. Qualitative trends however, in both quadrupolar and chemical shielding parameters are well reproduced, and most importantly, EFG and CS tensor orientations lend insight into the origins of NMR interactions and their relationships to molecular structure, symmetry and dynamics. This comprehensive study of niobium metallocenes suggests that complimentary data derived from solid-state ^{93}Nb and ^{13}C NMR experiments, X-ray diffraction techniques and first principles calculations will be very useful in characterizing organometallic niobium species in a variety of crystalline and disordered solid materials of fundamental, technological and/or industrial importance.

Bibliography

[1] Wilkinson, G., Rosenblum, M., Whiting, M.C., Woodward, R.B. *J. Am. Chem. Soc.* **1952**, *74*, 2125.

[2] Bochmann, M. *Organometallics 2, Complexes with Transition Metal-carbon π-bonds*; Oxford University Press Inc.: New York, 1994.

[3] Togni, A., Halterman, R.L. *Metallocenes - Synthesis. Reactivity. Applications*; Wiley-VCH: Weinheim; New York; Chichester; Brisbane; Singapore; Toronto, 1998; Vol. 2.

[4] Klipp, A., Hamelmann, F., Haindl, G., Hartwich, J., Kleineberg, U., Jutzi, P., Heinzmann, U. *Chem. Vap. Deposition* **2000**, *6*, 63.

[5] Beswick, M.A., Palmer, J.S., Wright, D.S. *Chem. Soc. Rev.* **1998**, *27*, 225.

[6] Klipp, A., Petri, S.H.A., Neumann, B., Stammler, H.G., Jutzi, P. *J. Organomet. Chem.* **2001**, *620*, 20.

[7] Mashima, K., Fujikawa, S., Tanaka, Y., Urata, H., Oshiki, T., Tanaka, E., Nakamura, A. *Organometallics* **1995**, *14*, 2633.

[8] Antinolo, A., Carrillo-Hermosilla, F., Fajardo, M., Fernandez-Baeza, J., Garcia-Yuste, S., Otero, A. *Coord. Chem. Rev.* **1999**, *195*, 43.

[9] Imanishi, Y., Naga, N. *Prog. Polym. Sci.* **2001**, *26*, 1147.

[10] Bitterwolf, T.E. et al. *J. Organomet. Chem.* **1998**, *557*, 77.

[11] Herrmann, W.A., Kalcher, W., Biersack, H., Bernal, I., Creswick, M. *Chem. Ber.-Recl.* **1981**, *114*, 3558.

[12] Tenhaeff, S.C., Tyler, D.R. *Organometallics* **1991**, *10*, 1116.

[13] Tenhaeff, S.C., Tyler, D.R. *Organometallics* **1991**, *10*, 473.

[14] Bechthold, H.C., Rehder, D. *J. Organomet. Chem.* **1981**, *206*, 305.

[15] Bitterwolf, T.E., Gallagher, S., Rheingold, A.L., Yap, G.P.A. *J. Organomet. Chem.* **1997**, *546*, 27.

[16] Herrmann, W.A., Biersack, H., Ziegler, M.L., Weidenhammer, K., Siegel, R., Rehder, D. *J. Am. Chem. Soc.* **1981**, *103*, 1692.

[17] Lichtenberger, D.L., Fan, H.J., Gruhn, N.E., Bitterwolf, T.E., Gallagher, S. *Organometallics* **2000**, *19*, 2012.

[18] Earp, J.C., Margolis, D.S., Tanjaroon, C., Bitterwolf, T.E., Kukolich, S.G. *J. Mol. Spectrosc.* **2002**, *211*, 82.

[19] Naumann, F., Rehder, D., Pank, V. *J. Organomet. Chem.* **1982**, *240*, 363.

[20] Gibson, V.C., Williams, D.N., Clegg, W., Hockless, D.C.R. *Polyhedron* **1989**, *8*, 1819.

[21] Williams, D.N. et al. *J. Chem. Soc.-Dalton Trans.* **1992**, 739.

[22] Fettinger, J.C., Keogh, D.W., Poli, R. *Inorg. Chem.* **1995**, *34*, 2343.

[23] Blaurock, S., Hey-Hawkins, E. *Z. Anorg. Allg. Chem.* **2002**, *628*, 2515.

[24] Rehder, D., Paulsen, K., Basler, W. *J. Magn. Reson.* **1983**, *53*, 500.

[25] Gobetto, R., Harris, R.K., Apperley, D.C. *J. Magn. Reson.* **1992**, *96*, 119.

[26] Gibson, V.C., Gobetto, R., Harris, R.K., Langdalebrown, C., Siemeling, U. *J. Organomet. Chem.* **1994**, *479*, 207.

[27] Hallock, K.J., Lee, D.K., Ramamoorthy, A. *Chem. Phys. Lett.* **1999**, *302*, 175.

[28] Sporer, C. et al. *Chem.-Eur. J.* **2004**, *10*, 1355.

[29] He, X., Lo, A.Y.H., Trudeau, M., Schurko, R.W., Antonelli, D. *Inorg. Chem.* **2003**, *42*, 335.

[30] Honnerscheid, A., van Wullen, L., Jansen, M., Rahmer, J., Mehring, M. *J. Chem. Phys.* **2001**, *115*, 7161.

[31] Heise, H., Kohler, F.H., Xie, X.L. *J. Magn. Reson.* **2001**, *150*, 198.

[32] Endregard, M., Nicholson, D.G., Stocker, M., Lamble, G.M. *J. Mater. Chem.* **1995**, *5*, 785.

[33] Uusitalo, A.M., Pakkanen, T.T., Iskola, E.I. *J. Mol. Catal. A-Chem.* **2002**, *177*, 179.

[34] Schnellbach, M., Kohler, F.H., Blumel, J. *J. Organomet. Chem.* **1996**, *520*, 227.

[35] Schurko, R.W., Hung, I., Schauff, S., Macdonald, C.L.B., Cowley, A.H. *J. Phys. Chem. A* **2002**, *106*, 10096.

[36] Willans, M.J., Schurko, R.W. *J. Phys. Chem. B* **2003**, *107*, 5144.

[37] Edwards, A.J., Burke, N.J., Dobson, C.M., Prout, K., Heyes, S.J. *J. Am. Chem. Soc.* **1995**, *117*, 4637.

[38] Schurko, R.W., Hung, I., Macdonald, C.L.B., Cowley, A.H. *J. Am. Chem. Soc.* **2002**, *124*, 13204.

[39] Iiskola, E.I., Timonen, S., Pakkanen, T.T., Harkki, O., Lehmus, P., Seppala, J.V. *Macromolecules* **1997**, *30*, 2853.

[40] Hung, I., Schurko, R.W. *Solid State Nucl. Magn. Reson.* **2003**, *24*, 78.

[41] Hung, I., Macdonald, C.L.B., Schurko, R.W. *Chem.-Eur. J.* **2004**, *10*, 5923.

[42] Hung, I., Schurko, R.W. *J. Phys. Chem. B* **2004**, *108*, 9060.

[43] Johnels, D., Boman, A., Edlund, U. *Magn. Reson. Chem.* **1998**, *36*, S151.

[44] Pietrass, T., Burkert, P.K. *Inorg. Chim. Acta* **1993**, *207*, 253.

[45] Pietrass, T., Burkert, P.K. *Z. Naturforsch., B: Chem. Sci.* **1993**, *48*, 1555.

[46] Janiak, C., Schumann, H., Stader, C., Wrackmeyer, B., Zuckerman, J.J. *Chem. Ber.-Recl.* **1988**, *121*, 1745.

[47] Wrackmeyer, B., Kupce, E., Kehr, G., Sebald, A. *Magn. Reson. Chem.* **1992**, *30*, 964.

[48] Armstrong, D.R. et al. *Organometallics* **1997**, *16*, 3340.

[49] Keates, J.M., Lawless, G.A. *Organometallics* **1997**, *16*, 2842.

[50] Spiess, H.W., Haas, H., Hartmann, H. *J. Chem. Phys.* **1969**, *50*, 3057.

[51] Pyykko, P. *Mol. Phys.* **2001**, *99*, 1617.

[52] Gabuda, S.P., Zil'berman, B.D., Goncharuk, V.K. *Zh. Strukt. Khim.* **1978**, 431.

[53] Ponce, A.L., Lin, X., Fripiat, J.J. *Solid State Ionics* **1996**, *84*, 213.

[54] Creel, R.B., Segel, S.L., Schoenberger, R.J., Barnes, R.G., Torgeson, D.R. *J. Chem. Phys.* **1974**, *60*, 2310.

[55] Barnes, R.G., Roenker, K.P., Brooker, H.R. *Ber. Bunsen-Ges. Phys. Chem. Chem. Phys.* **1976**, *80*, 875.

[56] Du, L.S., Schurko, R.W., Kim, N., Grey, C.P. *J. Phys. Chem. A* **2002**, *106*, 7876.

[57] Du, L.S., Schurko, R.W., Lim, K.H., Grey, C.P. *J. Phys. Chem. A* **2001**, *105*, 760.

[58] Ivanova, E.N., Yatsenko, A.V., Sergeev, N.A. *Solid State Nucl. Magn. Reson.* **1995**, *4*, 381.

[59] Blumel, J., Born, E., Metzger, T. *J. Phys. Chem. Solids* **1994**, *55*, 589.

[60] Bastow, T.J. *Z. Naturforsch., A: Phys. Sci.* **1994**, *49*, 320.

[61] Geselbracht, M.J., Stacy, A.M., Garcia, A.R., Silbernagel, B.G., Kwei, G.H. *J. Phys. Chem.* **1993**, *97*, 7102.

[62] Peterson, G.E., Bridenbaugh, P.M. *J. Chem. Phys.* **1968**, *48*, 3402.

[63] Kind, R., Graenicher, H., Derighetti, B., Waldner, F., Brun, E. *Solid State Commun.* **1968**, *6*, 439.

[64] Douglass, D.C., Peterson, G.E., McBrierty, V.J. *Phys. Rev. B* **1989**, *40*, 10694.

[65] Norcross, J.A., Ailion, D.C., Blinc, R., Dolinsek, J., Apih, T., Slak, J. *Phys. Rev. B* **1994**, *50*, 3625.

[66] Meadows, M.D., Smith, K.A., Kinsey, R.A., Rothgeb, T.M., Skarjune, R.P., Oldfield, E. *Proc. Natl. Acad. Sci. U. S. A.* **1982**, *79*, 1351.

[67] Cruz, L.P., Savariault, J.M., Rocha, J., Jumas, J.C., Pedrosa de Jesus, J.D. *J. Solid State Chem.* **2001**, *156*, 349.

[68] Fitzgerald, J.J., Prasad, S., Huang, J., Shore, J.S. *J. Am. Chem. Soc.* **2000**, *122*, 2556.

[69] Avogadro, A., Bonera, G., Borsa, F., Rigamonti, A. *Phys. Rev. B* **1974**, *9*, 3905.

[70] Wolf, F., Kline, D., Story, H.S. *J. Chem. Phys.* **1970**, *53*, 3538.

[71] Man, P.P., Theveneau, H., Papon, P. *J. Magn. Reson.* **1985**, *64*, 271.

[72] Ashbrook, S.E., Wimperis, S. *J. Magn. Reson.* **2002**, *156*, 269.

[73] Prasad, S., Zhao, P., Huang, J., Fitzgerald, J.J., Shore, J.S. *Solid State Nucl. Magn. Reson.* **1999**, *14*, 231.

[74] Prasad, S., Zhao, P., Huang, J., Fitzgerald, J.J., Shore, J.S. *Solid State Nucl. Magn. Reson.* **2001**, *19*, 45.

[75] Muntean, L., Ailion, D.C. *Phys. Rev. B* **2001**, *6301*.

[76] Zhou, D.H., Hoatson, G.L., Vold, R.L. *J. Magn. Reson.* **2004**, *167*, 242.

[77] Larsen, F.H., Jakobsen, H.J., Ellis, P.D., Nielsen, N.C. *J. Phys. Chem. A* **1997**, *101*, 8597.

[78] Larsen, F.H., Nielsen, N.C. *J. Phys. Chem. A* **1999**, *103*, 10825.

[79] Pangborn, A.B., Giardello, M.A., Grubbs, R.H., Rosen, R.K., Timmers, F.J. *Organometallics* **1996**, *15*, 1518.

[80] Jager, C., Mullerwarmuth, W., Mundus, C., Vanwullen, L. *J. Non-Cryst. Solids* **1992**, *149*, 209.

[81] Eichele, K., Wasylishen, R.E., v. 1.17.30, Tübingen, 2001.

[82] Bak, M., Rasmussen, J.T., Nielsen, N.C. *J. Magn. Reson.* **2000**, *147*, 296.

[83] Frisch, M.J.T., G. W.; Schlegel, H. B.; Scuseria, G. E.; Robb, M. A.; Cheeseman, J. R.; Zakrzewski, V. G.; Montgomery, Jr., J. A.; Stratmann, R. E.; Burant, J. C.; Dapprich, S.; Millam, J. M.; Daniels, A. D.; Kudin, K. N.; Strain, M. C.; Farkas, O.; Tomasi, J.; Barone, V.; Cossi, M.; Cammi, R.; Mennucci, B.; Pomelli, C.; Adamo, C.; Clifford, S.; Ochterski, J.; Petersson, G. A.; Ayala, P. Y.; Cui, Q.; Morokuma, K.; Malick, D. K.; Rabuck, A. D.; Raghavachari, K.; Foresman, J. B.; Cioslowski, J.; Ortiz, J. V.; Baboul, A. G.; Stefanov, B. B.; Liu, G.; Liashenko, A.; Piskorz, P.; Komaromi, I.; Gomperts, R.; Martin, R. L.; Fox, D. J.; Keith, T.; Al-Laham, M. A.; Peng, C. Y.; Nanayakkara, A.; Challacombe, M.; Gill, P. M. W.; Johnson, B.; Chen, W.; Wong, M. W.;

Andres, J. L.; Gonzalez, C.; Head-Gordon, M.; Replogle, E. S. and Pople, J. A., Revision A.9, Gaussian, Inc., Pittsburgh, PA, 1998.

[84] Frisch, M.J. et al., Rev. B.03, Gaussian, Inc., Pittsburgh, 2003.

[85] Huzinaga S., A.J. *Gaussian basis sets for molecular calculations*; Elsevier: New York, 1984.

[86] Coriani, S., Hattig, C., Jorgensen, P., Rizzo, A., Ruud, K. *J. Chem. Phys.* **1998,** *109*, 7176.

[87] Ditchfield, R. *Mol. Phys.* **1974**, *27*, 789.

[88] Wolinski, K., Hinton, J.F., Pulay, P. *J. Am. Chem. Soc.* **1990**, *112*, 8251.

[89] Shelyapina, M.G., Kasperovich, V.S., Shchegolev, B.F., Charnaya, E.V. *Phys. Status Solidi B-Basic Res.* **2001**, *225*, 171.

[90] Altomare, A. et al., CNR-IRMEC, Bari, 1997.

[91] Sheldrick, G.M., Universitat Gottingen, Gottingen, 1997.

[92] Wilson, A.J.C., Ed. *International Tables for X-ray Crystallography*; Kluwer Academic Press: Boston, 1992; Vol. C.

[93] Sheldrick, G.M., Bruker AXS Inc., Madison, WI, 2001.

[94] Kraus, W., Nolze, G., v. 2.4, Federal Institute for Materials Research and Testing, Berlin, Germany, 2000.

[95] Power, W.P., Wasylishen, R.E., Mooibroek, S., Pettitt, B.A., Danchura, W. *J. Phys. Chem.* **1990**, *94*, 591.

[96] Mason, J., Editor *Multinuclear NMR*; Plenum Publishing Corporation: New York, 1987.

[97] Schreckenbach, G. *J. Chem. Phys.* **1999**, *110*, 11936.

[98] Rehder, D., Bechthold, H.C., Kececi, A., Schmidt, H., Siewing, M. *Z. Naturforsch., B: Chem. Sci.* **1982**, *37*, 631.

[99] Pforr, I., Naeumann, F., Rehder, D. *J. Organomet. Chem.* **1983**, *258*, 189.

[100] Hoch, M., Rehder, D. *Z.Naturforsch.(B)* **1983**, *38B*, 446.

[101] Schmidt-Rohr, K., Spiess, H.W. *Multidimensional Solid-State NMR and Polymers*; Academic Press: Toronto, 1994.

[102] Massiot, D., Farnan, I., Gautier, N., Trumeau, D., Trokiner, A., Coutures, J.P. *Solid State Nucl. Magn. Reson.* **1995**, *4*, 241.

[103] Medek, A., Frydman, V., Frydman, L. *J. Phys. Chem. A* **1999**, *103*, 4830.

[104] Lipton, A.S., Wright, T.A., Bowman, M.K., Reger, D.L., Ellis, P.D. *J. Am. Chem. Soc.* **2002**, *124*, 5850.

[105] Alcalde, M.I., Delamata, J., Gomez, M., Royo, P., Pellinghelli, M.A., Tiripicchio, A. *Organometallics* **1994**, *13*, 462.

[106] Herzfeld, J., Berger, A.E. *J. Chem. Phys.* **1980**, *73*, 6021.

[107] Sayer, I. *J. Chem. Soc.-Chem. Commun.* **1988**, 227.

[108] Kentgens, A.P.M., Karrenbeld, H., Deboer, E., Schumann, H. *J. Organomet. Chem.* **1992**, *429*, 99.

[109] Orendt, A.M., Facelli, J.C., Jiang, Y.J., Grant, D.M. *J. Phys. Chem. A* **1998**, *102*, 7692.

[110] Gay, I.D., Young, G.B. *Organometallics* **1996**, *15*, 2264.

[111] Crosby, R.C., Haw, J.F., Lewis, D.H. *Anal. Chem.* **1988**, *60*, 2695.

[112] Harris, R.K., Olivieri, A.C. *Prog. Nucl. Magn. Reson. Spectrosc.* **1992**, *24*, 435.

[113] Wasylishen, R.E., Wright, K.C., Eichele, K., Cameron, T.S. *Inorg. Chem.* **1994**, *33*, 407.

[114] Kao, H.M., Lii, K.H. *Inorg. Chem.* **2002**, *41*, 5644.

[115] Lo, A.Y.H., Bitterwolf, T.E., Macdonald, C.L.B., Schurko, R.W. *J. Phys. Chem. A* **2005**, *109*, 7073.

[116] Enders, M., Rudolph, R., Pritzkow, H. *Chem. Ber.* **1996**, *129*, 459.

[117] Krutko, D.P., Borzov, M.V., Petrosyan, V.S., Kuzmina, L.G., Churakov, A.V. *Russ. Chem. Bull.* **1996**, *45*, 1740.

[118] Krutko, D.P., Borzov, M.V., Petrosyan, V.S., Kuzmina, L.G., Churakov, A.V. *Russ. Chem. Bull.* **1996**, *45*, 940.

[119] Lancaster, S.J., Thornton-Pett, M., Dawson, D.M., Bochmann, M. *Organometallics* **1998**, *17*, 3829.

[120] vanderZeijden, A.A.H., Mattheis, C., Frohlich, R. *Organometallics* **1997**, *16*, 2651.

[121] Wolff, S.K., Ziegler, T., van Lenthe, E., Baerends, E.J. *J. Chem. Phys.* **1999**, *110*, 7689.

[122] Bouten, R., Baerends, E.J., van Lenthe, E., Visscher, L., Schreckenbach, G., Ziegler, T. *J. Phys. Chem. A* **2000**, *104*, 5600.

[123] Ooms, K.J., Wasylishen, R.E. *J. Am. Chem. Soc.* **2004**, *126*, 10972.

Chapter 4

Multinuclear Solid-State NMR Characterization of Mesoporous Transition-Metal Oxide Composite Materials

4.1 Introduction

Porous materials are defined as solids possessing cavities, channels or interstices, and they are broadly classified into microporous, mesoporous and macroporous solids, based upon the average pore size. According to IUPAC definitions,[1] the pore sizes in microporous, mesoporous and macroporous solids is smaller than 2 nm, between 2 and 50 nm, and larger than 50 nm, respectively.

Periodic mesoporous silicates (MS41) were first synthesized by Mobil scientists in 1992.[2,3] In the family of MS41 mesoporous silicates, four sub-categories have been classified: MCM-41, MCM-48, MCM-50 and the surfactant-silica composites $(\mathrm{suf{\bullet}SiO_{2.5}})_8$.[4] The first two are thermally stable, while the last two phases are unstable.[5] MCM-41 features a hexagonal packing array with a unidimensional pore structure, while MCM-48 has cubic structural features with a three-dimensional pore architecture. MCM-41-type mesoporous materials are of great interest to scientists due to their unique physical properties such as large pore size/volume and surface area, etc. Such properties lead to a number of potential industrial and environmental applications such as heterogeneous catalysts, catalyst supports, selective absorption of heavy metal ions and many more.[4]

Antonelli and Ying introduced the syntheses of stable transition-metal oxide mesoporous materials (M-TMS1, where M is the transition metal), which were prepared based upon the ligand-assisted templating approach.[6,7] Mesoporous transition-metal oxide solids possess hexagonal packing array with long-range order, similar to MCM-41. However, M-TMS1 is distinct from MCM-41 in that the metal atoms in the wall of the mesostructure may assume a variety of oxidation states, leading to interesting magnetic, electronic and optical properties.[8] Such properties may extend the applicability of mesoporous materials to battery materials and hydrogen-storage devices.

Table 4.1. Identification of the mesoporous host-guest composites under study and the physical properties[a] of the host compounds.

Section	Host	BET surface area[b] ($m^2 g^{-1}$)	HK pore size[c] (Å)	Pore volume ($cm^3 g^{-1}$)	Guest
1	Ti oxide	785	24	0.479	bis(toluene)Ti
2	V-doped Nb oxides	457 to 721	23.2 to 25.7	0.331 to 0.412	0.1 and 0.7 equiv.[d] bis(benzene)Cr(0)
3	Ti oxide	723	20.6	0.479	0.2, 0.6 and 1.0 equiv. Li/Na naphthalenides
4	Ta oxide	483	22	not reported	Rb_3C_{60}, 0.5 and 1.0 equiv Rb naphthalenides

[a] All physical properties of the host compounds are obtained from reference [9-12]; [b] BET stands for (Brunauer, Emmett and Teller); [c] HK stands for Horvath-Kawazoe; [d] numbers in equivalents are calculated based on the %Nb, %Ti and %Ta in sections 2, 3 and 4, respectively.

In this thesis, a series of M-TMS1 materials, with M = Ti, mixed Nb-V and Ta, loaded with a variety of organometallic, organic and inorganic species are examined via a wide range of solid-state NMR experiments. The host-guest systems that are being investigated, along with some key physical properties of the host compounds, are summarized in Table 4.1. The chapter is divided into four sub-sections (Table 4.1), each of which are briefly introduced in the next few paragraphs.

4.2 Experimental

4.2.1 General Aspects

Materials. Syntheses and characterizations techniques including powder X-ray diffraction (XRD), nitrogen adsorption-desorption, electron paramagnetic resonance (EPR) experiments, IR and X-ray photoelectron spectroscopy (XPS), elemental and thermogravimetric analyses (TGA), as well as conductivity, magnetic susceptibility and charge-discharge cycle measurements, of all mesoporous transition-metal oxides composites are reported elsewhere.[9-12]

Solid-state NMR experiments. All solid-state NMR experiments were performed on a Varian Infinity Plus 9.4 T wide-bore NMR spectrometer, operating at ν_0 = 400.1 (^{1}H), 61.4 (^{2}H), 155.4 (^{7}Li), 100.5 (^{13}C), 40.5 (^{15}N), 105.7 (^{23}Na) and 130.8 (^{87}Rb) MHz.

4.2.2 Solid-State NMR Experiments on Ti-TMS1/Bis(toluene)Ti Composites

All of the samples were powdered and packed into 4 mm o.d. zirconium oxide rotors, which were sealed with specially constructed airtight Teflon caps. The spinning frequencies of both MAS and CP/MAS experiments were 5 kHz and a high-power broadband ^{1}H decoupling field of 62.5 kHz was applied. All ^{15}N NMR spectra were referenced with respect to liquid NH_3 (20 °C), δ_{iso} = 0.0 ppm, by setting the isotropic ammonium ^{15}N NMR peak of crystalline $^{15}NH_4{}^{15}NO_3$ to 23.8 ppm.[13,14] For the CP experiments, the optimized contact times ranged from 3 to 9 ms. The 90° pulse widths used in the ^{15}N NMR experiments ranged from 3.4 to 4.4 μs, with an applied rf field of ν_1 = 55 to 74 kHz. ^{15}N CP/MAS NMR spectra were acquired with ca. 200 to 2000 transients, and MAS NMR experiments with 200 to 1000 transients.

4.2.3 Solid-State NMR Experiments on V-Doped Nb-TMS1/Bis(benzene)Cr(0) Composites

Solid-state variable-temperature (VT) ^{2}H NMR experiments were conducted using Varian/Chemagnetics 5 mm wideline and 5 mm HXY MAS (in single-resonance ^{2}H mode) probes. For both stationary and spinning samples, a quadrupolar echo pulse sequence of the form $(\pi/2)_x$-τ-$(\pi/2)_y$-τ-acquire was applied.[15] A single set of rotor-synchronized quadrupolar echo magic-angle spinning (MAS) NMR experiments with spinning frequencies of 9.1 and 11.0 kHz were conducted on the mesoporous metal oxide loaded with 0.1 equiv. of bis(benzene)Cr(0). Sample temperatures were varied from -150 °C to +100 °C. Samples were carefully powdered and packed into 5 mm o.d. Teflon tubes or 5 mm o.d. zirconium oxide rotors and sealed with airtight caps. All ^{2}H NMR spectra were referenced with respect to TMS, $\delta_{iso}(^2H) = 0.0$ ppm, by using benzene-d_6 as a secondary reference with $\delta_{iso} = 7.3$ ppm. The 90° pulses ranged from 2.5 μs to 3.1 μs for experiments with the 5 mm static probe and 4.6 μs for MAS experiments, corresponding to rf fields ranging from ν_1 = 54.3 to 80.7 kHz. The inter-pulse delays in the quadrupolar echo sequence, τ, were 200 μs or 520 μs in the static experiments and $1/\nu_{rot}$ in the MAS experiments. The static NMR experiments on pure samples of bis(benzene)Cr(0) and bis(benzene)Cr(I) cation required the acquisition of ca. 200 to 2000 transients with pulse delays of 1 second and 0.5 seconds, respectively. Static experiments on the loaded mesoporous metal oxides required acquisition of ca. 4000 transients with a pulse delay of 0.5 s, while the MAS experiments required 368 scans.

Solid-state ^{1}H MAS NMR experiments were conducted on bis(benzene)Cr(I) cation, using a Varian/Chemagnetics 2.5 mm HX MAS probe, with a spinning frequency of 25 kHz. This sample was packed into a 2.5 mm o.d. zirconium oxide rotors and was referenced with respect to dichloromethane ($\delta_{\text{iso}}(^1\text{H}) = 5.3$ ppm). The 90° pulse width was 2.7 μs and $\nu_1 = 92.6$ kHz. The acquisition required 16 scans with 4 s recycle delay.

The NMR EFG tensor parameters, C_Q and η_Q, and δ_{iso} of most of the ^{2}H NMR spectra were obtained from spectral simulations using the WSOLIDS software package.[16] The effect of dynamic motion of the benzene rings on the solid-state ^{2}H spectra of bis(benzene)Cr(0) was simulated using the program MXQET[17] on a Dell Precision 420 workstation with dual 733 MHz Pentium III processor running Red Hat Linux 6.2.

4.2.4 Solid-State NMR Experiments on Ti-TMS1/Na- and Li-Naphthalenide Composites

A Varian/Chemagnetics 4 mm HX magic-angle spinning (MAS) probe was used in all solid-state ^{23}Na and ^{7}Li NMR experiments. All samples were carefully powdered under an inert atmosphere and were tightly packed into 4 mm o.d. ZrO rotors which were sealed with airtight Teflon spacer and caps at both ends. ^{23}Na NMR spectra were referenced with respect to a 1.0 M NaCl solution with $\delta_{iso}(^{23}\text{Na}) = 0.0$ ppm, and ^{7}Li NMR spectra were referenced with respect to a 1.0 M LiCl solution with $\delta_{iso}(^{7}\text{Li}) = 0.0$ ppm. In order to avoid baseline distortions which occur while using Bloch-decay experiments to acquire broad powder patterns, rotor-synchronized ^{23}Na and ^{7}Li MAS NMR experiments were conducted using a Hahn-echo pulse sequence of the form $(\pi/2)_x$-$(\pi)_y$-acquire, with spinning speeds of ca. $\nu_{rot} = 8.0$ kHz. The central-transition (CT) selective $\pi/2$ pulse width used in the ^{23}Na NMR experiments was 3.75 μs with an rf field of $\nu_1(^{23}\text{Na}) = 33.3$ kHz. For ^{7}Li NMR experiments, the CT selective $\pi/2$ pulse was 2.5 μs and $\nu_1(^{7}\text{Li}) = 50.0$ kHz. Between 16 and 64 transients were collected in each experiment, with calibrated recycle times of 7.0 s for ^{23}Na and 4.0 s for ^{7}Li. VT ^{23}Na MAS NMR experiments were also performed from +150 °C to -100 °C on the 1.0 equiv. sample.

Measurements of longitudinal (T_1) and transverse (T_2) relaxation time constants were conducted on the 1.0 equiv. sample from +100 °C to -70 °C. Saturation recovery experiments were conducted for the measurement of T_1 time constants, where ca. 100 $\pi/2$ pulses with 10 μs delays were applied to saturate the magnetization prior to detection. For T_2 relaxation measurements, Hahn-echo pulse sequences with linearly incremented inter-pulse delays were applied. Extractions of T_1 and T_2 time constants were accomplished by fitting the T_1 and T_2 curves, respectively, using the functions: $y(\tau) = A_f[1 - \exp(-\tau/T_{1f})] + A_s[1 - \exp(-\tau/T_{1s})]$, and $y(\tau) = B_f \exp(-\tau/T_{2f}) + B_s \exp(-\tau/T_{2s})$, where the subscripts "f" and "s" refer to fast and slow, respectively.

4.2.5 Solid-State NMR Experiments on Ta-TMS1/Rb_3C_{60} and Rb-naphthalenide Composites

A Varian/Chemagnetics 4 mm HX MAS probe (operating in single-resonance ^{87}Rb or double-resonance ^{1}H-^{13}C configurations) was used in all solid-state ^{87}Rb and ^{13}C NMR experiments. NMR experiments were conducted on pristine Rb_3C_{60}, as well as a series of composite materials including: mesoporous Ta oxide impregnated with Rb_3C_{60} (parent composite, $n = 1.0$), mesoporous Ta oxide reduced with rubidium naphthalenide only (1equiv.Rb-TaTMS1), and parent composite materials reduced to the oxidation states of $n = 3.0$ and $n = 4.0$, respectively. Samples were ground into fine powders under a nitrogen-containing atmosphere and tightly packed into 4 mm o.d. zirconium oxide rotors, which were sealed at both ends by air-tight Teflon caps and spacers.

Rubidium chemical shifts were referenced to 1.0 M $RbNO_3$ solution ($\delta_{iso}(^{87}Rb) = 0.0$ ppm). For both solid-state ^{87}Rb static and magic-angle spinning (MAS) NMR experiments, a spin-echo pulse sequence was applied. The CT selective $\pi/2$ pulse widths ranged from 1.45 μs to 4.0 μs, with rf fields (ν_1) ranging from 42.7 kHz to 85.9 kHz. Inter-pulse delays ranged from 35 μs to 100 μs for static echo experiments. For MAS experiments, samples were spun at $\nu_{rot} = 7$ kHz to 12.7 kHz, and spin-echo experiments were rotor-synchronized. Recycle delays times for all samples were optimized to 0.5 s or less, with a exception of the pure Rb_3C_{60} sample, for which a recycle delay times of 2 s was utilized. Between 20000 and 400000 transients were acquired for all static NMR experiments. The number of transients acquired for MAS NMR experiments ranged from ca. 320 to 17000, and ca.10900 to 22600 for SATRAS NMR experiments[18] in which the entire satellite transition manifold was acquired. VT NMR experiments were performed on $n = 3.0$ and $n = 4.0$ composites over a temperature range of -120 °C to 25 °C for the former and from -120 °C to 100 °C for the latter.

Carbon chemical shifts were referenced to TMS ($\delta_{iso}(^{13}C) = 0.0$ ppm) by setting the high-frequency resonance of adamantane to 38.57 ppm. Solid-state $^{13}C\{^1H\}$ MAS NMR experiments were conducted on all samples with high power continuous waves proton-decoupling ($\nu_2(^1H) = 35$ to 58 kHz) where appropriate. The $\pi/2$ pulse widths ranged from ca. 3.38 μs to 4 μs ($\nu_1(^{13}C) = 62.50$ kHz to 74.03 kHz). The recycle delays times were optimized between 9 s to 40 s, and the number of collected transients ranged from ca. 544 to 8400. ^1H-^{13}C VACP/MAS NMR experiments were performed only on samples $n = 1.0$, $n = 3.0$ and 1equiv.Rb-TaTMS1, using ^1H $\pi/2$ pulse widths of 4 μs ($\nu_1(^1H) = 58.14$ kHz), optimized pulse delays recycle times between 6 s to 10 s, optimized contact times from 2 ms to 4 ms and involved the collection of approximately 532 to 6500 transients.

4.3 Results and Discussion

4.3.1 Ti-TMS1/Bis(toluene)Ti Composites

Room-temperature cleavage of dinitrogen within the pores of mesoporous Nb oxide which is reacted with bis(toluene)Nb was previously demonstrated.[19] Reaction of mesoporous solid with the organometallic complex results in the deposition of a thin layer of low-valent niobium(II) over the surface of the wall of mesoporous Nb oxide, which is thought to result in the fixation of N_2 at the surface. While this is an unusual process which may represent the initial step of nitrogen reduction at the ambient conditions, another related study has been reported on the mesoporous Ta oxide/bis(toluene)Ti composites.[20] In this section, we discuss the application of solid-state NMR for the characterization of a composite system comprised of mesoporous titanium oxide loaded with bis(toluene) titanium, and then exposed to a ^{15}N-labelled N_2 atmosphere. The resulting product is rich in elemental nitrogen (as evidenced from elemental analysis);[9] solid-state ^{15}N NMR experiments are utilized to examine the nature of the nitrogen-containing species, which are very likely contained within the mesoporous channels.

Depicted in Figure 4.1A is the ^{15}N CP/MAS spectrum of the labelled nitrogen-containing material, clearly exhibiting a broad resonance at ca. 26 ppm relative to liquid ammonia, consistent with an aminoid sp^3 hybridized nitrogen.[7] The peak positions are similar to those reported previously for mesoporous niobium oxide reduced with bis(toluene) niobium under dinitrogen and differ substantially from those expected for a terminal nitride, which can appear as far downfield as +840 ppm relative to nitromethane (+1220 ppm relative to ammonia).[21] The activation of dinitrogen by a metal oxide is extremely difficult, though transition metal nitrides can be prepared with the application of microwave-generated nitrogen plasma.[22] We attribute the high reactivity of the composite material to low-valent, low-coordinate Ti centres on the surface of the material formed by the oxidative decomposition of bis(toluene) titanium on the surface of the material. Reductive cleavage of dinitrogen by transition metal complexes is rare; however, the cleavage of dinitrogen by sterically-shielded, low-coordinate d^3 Mo(III) centres

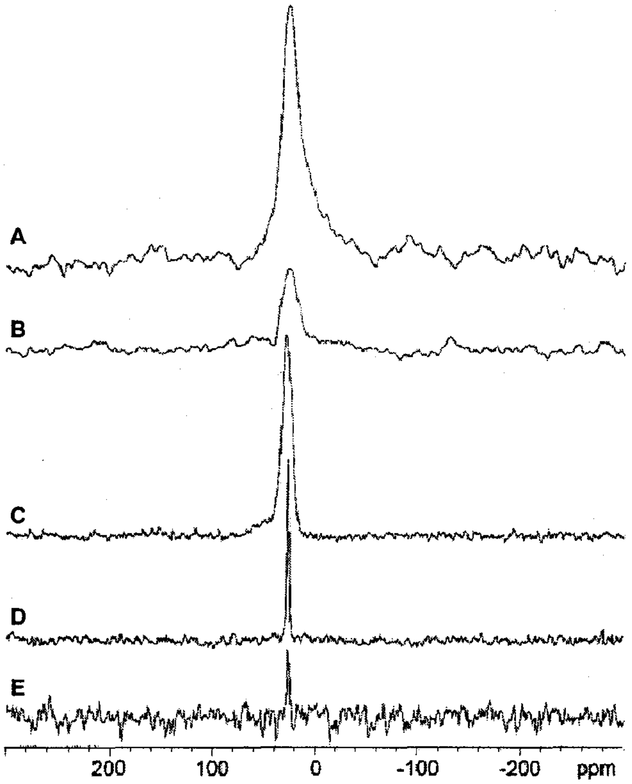

Figure 4.1. (A) ^1H-^{15}N CP/MAS NMR spectrum of mesoporous Ti oxide treated with bis(toluene)Ti in the presence of $^{15}N_2$. (B) $^{15}N\{^1H\}$ MAS NMR spectrum of the same sample. (C) ^1H-^{15}N CP/MAS NMR spectrum of the above sample exposed to air. (D) $^{15}N\{^1H\}$ MAS NMR spectrum of air-exposed sample treated with H_2O. (E) ^1H-^{15}N CP/MAS NMR spectrum of air-exposed sample treated with H_2O.

proceeds smoothly at room temperature.[21] Since Ti(II) does not have enough electrons to reduce dinitrogen, several adjacent Ti centres must be involved in this process. Many electropositive metals form a thin coating of nitride on the surface upon exposure to air, but these mesoporous materials are notoriously inert to have such nitride coatings.

To identify and characterize the structure and dynamics of the surface nitrogen species, a combination of $^{15}N\{^1H\}$ MAS and ^1H-^{15}N CP/MAS NMR experiments were conducted (spectra in Fig. 4.1A, B). In both cases, the NMR powder patterns are very broad (FWHH ranging from 500 to 700 Hz). Spectra acquired under conditions of cross polarization have higher S/N than comparable single pulse $^{15}N\{^{1}H\}$ MAS NMR spectra, by a factor of ca. 1.5 to 1.7. The isotropic chemical shifts in each spectrum are approximately 25.6(0.8) ppm with respect to liquid ammonia.[13,14] The chemical shift, broad line shape, and high proton CP efficiency suggest that the ^{15}N line shape arises from $^{15}NH_3$ groups that are anchored to the surface of the mesostructure. The chemical shift is very close to the shift of 23.8 ppm for the ammonium ion in NH_4NO_3, suggesting a tetrahedral nitrogen environment, as opposed to free N_2 ($\delta_{iso}(^{15}N) = 310$ ppm),[13,14] TiN ($\delta_{iso}(^{15}N) = 400$ ppm),[23] or other oxidized nitrogen species. The broad line shape arises from a distribution of chemical shifts due to the NH_3 on the disordered surface of the mesoporous titanium oxide, which may be chemisorbed or physisorbed. If the surface-bound ammonia has a strong binding interaction with a paramagnetic niobium atom, it is possible that there would be paramagnetic interactions resulting in a significant change in ^{15}N chemical shift or broadening from paramagnetic relaxation (inhomogeneous and/or homogeneous) of the ^{15}N NMR resonances. The observed resonances are not unusually shifted away from the typical range of ^{15}N chemical shifts for ammonia species, nor do they possess large spinning sideband manifolds; thus, if there is a contribution from unpaired electrons in the lattice to the ^{15}N NMR spectra, it is likely very small and difficult to distinguish from the inhomogeneous line broadening caused by a distribution of chemical shifts in the disordered sample. The fact that the NH_3 is anchored to the surface in this case results in ^{1}H-^{15}N CP/MAS NMR spectra that would not be observed if the NH_3 was isotropically tumbling away from the titania surface. Further, virtually identical NMR spectra have been reported for the absorption of NH_3 on the surface of TiO_2-supported V_2O_5 catalysts.[24]

NMR spectra of a $^{15}N_2$-treated sample exposed to varying degrees of air and moisture are compared in parts C to E of Figure 4.1. In the ^1H-^{15}N CP/MAS NMR spectrum (Figure 4.1C) of the sample exposed only to air, a familiar broad peak is centred at 26.5(1.0) ppm with a slightly reduced line width of 400 Hz compared to the original samples. There is also a broad tail on the peak in the high-frequency direction, suggesting perhaps that a minor reaction has taken place. Again, the high CP efficiency, chemical shift, and the broad line shape imply that the ammonia species remains adsorbed on the titania surface. $^{15}N\{^1H\}$ MAS NMR spectra (Figure 4.1D) of the sample treated with air, followed by excess moisture by vapour diffusion over several days, reveal a very sharp peak with $\delta_{iso}(^{15}N) = 27.1(0.2)$ ppm and a much reduced line width of ca. 80 Hz. ^1H-^{15}N CP/MAS NMR spectra (Figure 4.1E) acquired with various contact times and pulse delays have very poor S/N in comparison to corresponding MAS NMR spectra. This is further evidence that $^{15}NH_3$ has been produced at the titania surface after treatment with $^{15}N_2$, since surface $^{15}NH_3$ will react with water to form ammonium ions that are not physisorbed to the surface, and therefore not as amenable to cross polarization as surface-anchored NH_3. In addition, the loss of the broad line shape indicates that the nitrogen species are undergoing rapid isotropic motion.

To further prove our hypothesis regarding formation of surface NH_3 after treatment with N_2 and reaction with nascent protons, mesoporous titanium oxide materials were treated with isotopically enriched $^{15}NH_3$ and $^{15}NH_4NO_3$. The $^{15}N\{^1H\}$ MAS NMR

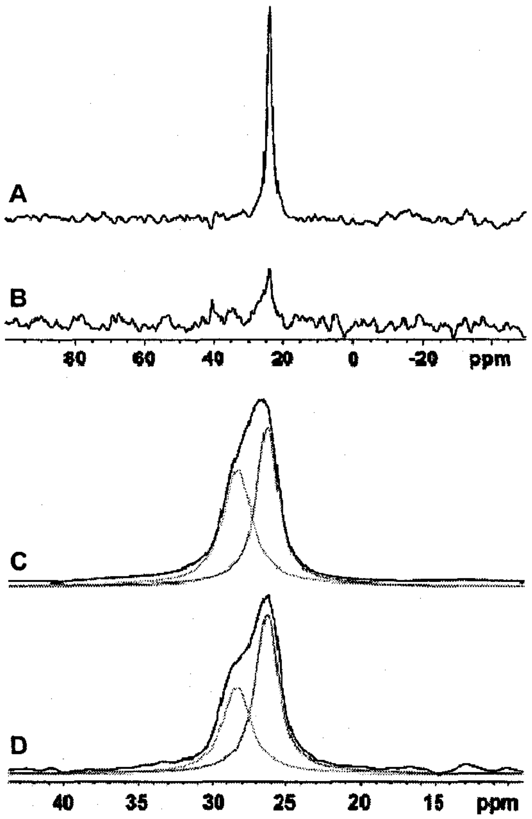

Figure 4.2. (A) $^{15}N\{^1H\}$ MAS and (B) ^1H-^{15}N CP/MAS NMR spectra of mesoporous Ti oxide treated with $^{15}NH_4NO_{3(aq)}$. (C) $^{15}N\{^1H\}$ MAS and (D) ^1H-^{15}N CP/MAS NMR spectra of mesoporous Ti oxide treated with NH_3. Peak deconvolution is shown for parts (C) and (D).

spectrum for titanium oxide treated with $^{15}NH_4NO_3$ (Figure 4.2A) has a single intense narrow peak (FWHH = 50 Hz) with $\delta_{iso}(^{15}N) = 22.4(0.2)$ ppm, suggesting the presence of free $^{15}NH_4^+$ ions. The corresponding ^1H-^{15}N CP/MAS NMR spectrum (Figure 4.2B) shows very poor CP efficiency, which is consistent with isotropic tumbling of the $^{15}NH_4^+$ ions. $^{15}N\{^1H\}$MAS and ^1H-^{15}N CP/MAS NMR spectra (Figure 4.2, parts C and D, respectively) of $^{15}NH_3$-treated titania both have broad peaks by comparison (ca. 110 to 130 Hz), with $\delta_{iso}(^{15}N) = 26.3(0.5)$ ppm. Compared to the sample treated with $^{15}NH_4NO_3$, the peaks are broadened by an inhomogeneous chemical shift distribution and increased

CP efficiency is observed in the ^{1}H-^{15}N CP/MAS NMR spectrum. However, the CP efficiency is less than observed for the original $^{15}N_2$-treated mesoporous titanium oxide samples (see Figure 4.1A,B). Deconvolution of the peaks in Figure 4.2, parts C and D, gives two peaks at 28.3 and 26.3 ppm in a 1:1 and 3:2 ratio, respectively, for the adsorption sites. The slightly different shift for the adsorption sites with respect to the sample loaded with $^{15}NH_4NO_3$ can possibly be accounted for by the different degrees of hydrogen bonding of the ammonia species expected in the two samples. These NMR studies unequivocally prove that surface ammonia species are present in the materials. The conversion of dinitrogen to ammonia in this system most likely occurs by cleavage of dinitrogen by low valent Ti centres on the surface of the mesostructure followed by reaction with water embedded beneath the surface, which slowly diffuses to the surface of the pore channels.

4.3.2 V-Doped Nb-TMS1/Bis(benzene)Cr(0) Composites

Solid-state ^{2}H NMR spectroscopy and relaxation measurements have long been used to study the dynamics of organic molecules in various host-guest systems, including perdeuterated *n*-hexane absorbed in microporous silicate[25] and deuterated n-C_6–n-C_{22} alkanes in zeolite 5A[26] by Stepanov and co-workers, benzene-d_6 in mesoporous silica by Buntkowsky et al.,[27] and pyridine-d_5 in cyclophosphazene by Villanueva-Garibay et al.,[28] etc.

Organometallic biscyclopentadienyl and bisarene complexes loaded into the M-TMS1 host, where M = Ti, Nb and Ta, have extensively been investigated by the research group of Antonelli.[29-34] For instance, bis(benzene)Cr(0) encapsulated in mesoporous niobium oxides has been studied previously.[29] The resulting material is semiconducting with the organometallic complex in the pores possessing mixed oxidation states. The amount of the oxidized bis(benzene)Cr species (i.e., bis(benzene)Cr(I) cations), however, is small due to the limited ability of the niobium oxide phase to accept electrons. When vanadium(V) is doped into the mesoporous niobium oxide, the oxidizing ability of the mesostructure increases, leading to the coexistence of bis(benzene)Cr(0) and bis(benzene)Cr(I) cations. In this section, mesoporous vanadium-doped niobium oxides loaded with various loading levels of neutral perdeuterated bis(benzene)Cr are investigated. While the coexistence of bis(benzene)Cr(0) and bis(benzene)Cr(I) cations is confirmed by solid-state ^{2}H NMR experiments, the dynamic behaviour of these organometallic species in the pores is also discussed.

Background. Before the discussion of NMR data, a brief background on solid-state ^{2}H NMR spectra is provided. Deuterium is a quadrupolar nucleus with a nuclear spin of 1 and very small nuclear quadrupole moment ($Q = 2.86 \times 10^{-31}$ m^2).[35] Solid-state NMR experiments on this integer spin typically yield Pake-like powder patterns which are dominated by the first-order quadrupolar interaction. The $+1 \leftrightarrow 0$ and $0 \leftrightarrow -1$ NMR transitions are observed in solid-state ^{2}H NMR spectra, which have overlapping anisotropic first-order patterns that usually span a range on the order of hundreds of kHz, depending upon the magnitude of the quadrupolar interaction. The ^{2}H NMR powder patterns can be easily measured with modern pulsed NMR experiments, due to the relatively small quadrupolar interactions. The great benefit of solid-state ^{2}H NMR is that

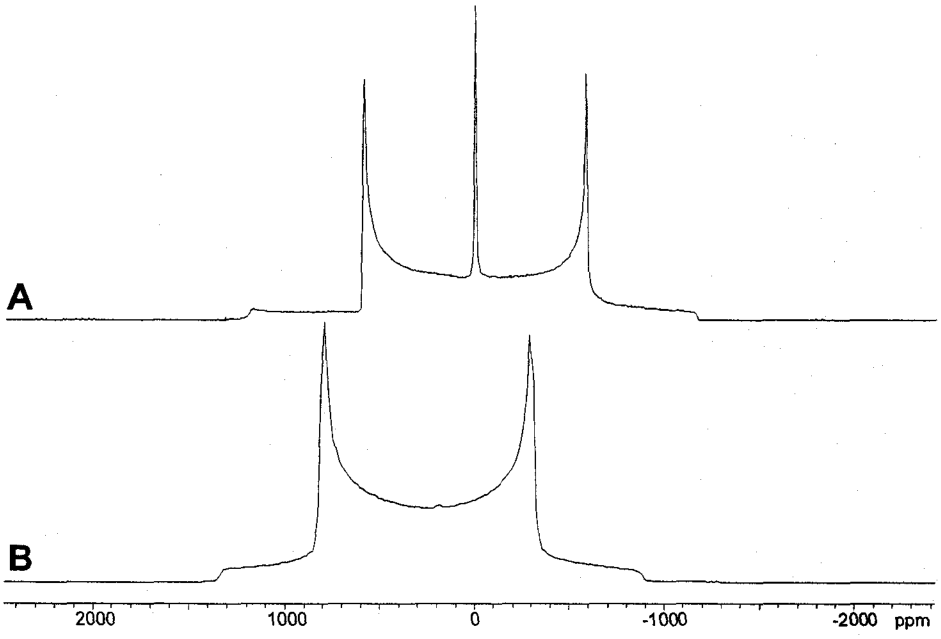

Figure 4.3. Static ^{2}H NMR spectra of (A) bis(benzene)Cr(0) and (B) bis(benzene)Cr(I) cation acquired at 9.4 T.

dynamic motion of deuterium atoms (and therefore the EFG tensors at the deuterium nuclei) can have a dramatic effect on the appearance of the static ^{2}H NMR spectrum. Dynamic simulations can be carried out in order to extract information on the quadrupolar interaction, molecular motion and activation energies for a variety of rotational, translational and diffusion processes.[17,36]

Characterization of organometallic samples. Solid-state static ^{2}H NMR spectra of pure bis(benzene)Cr(0) and the bis(benzene)Cr(I) cation are shown in Figure 4.3. Powder patterns corresponding to two distinct deuterium species are visible in Figure 4.3A: a large Pake doublet centred at 5.77 ppm and a sharp resonance centred at 7.27 ppm. The former corresponds to ^{2}H atoms on a rapidly rotating η^{6}-benzene rings in the bis(benzene)Cr(0) complex, and the latter to free benzene molecules (this peak is set to 7.27 ppm, and is useful as an internal ^{2}H chemical shift reference). The presence of free benzene molecules likely results from decomposition of the unstable bis(benzene)Cr(0) species. Similar ^{2}H NMR spectra identifying residual benzene have previously been observed for the analogous Mo(η-C_6D_6)$_2$ complex.[37] In Figure 4.3B, only a single ^{2}H Pake pattern is observed, which corresponds to the ^{2}H atoms of the bis(benzene)Cr(I) cation. The chemical shift of this pattern is measured to be 288 ppm. No benzene peak is observed, likely due to the fact that bis(benzene)Cr(I) is an air-stable compound and does not undergo decomposition as readily as bis(benzene)Cr(0). The isotropic chemical shift difference between the Cr(0) and Cr(I) complexes is attributed to the fact that the latter compound is paramagnetic, and some unpaired electron spin density is delocalized over the coordinated η^6-benzene rings, resulting in large high-frequency chemical shifts.[38,39] Simple analytical simulations of the ^{2}H Pake doublets of bis(benzene)Cr(0) and bis(benzene)Cr(I) yield values of $C_Q = 96$ kHz and $\eta_Q = 0$ and $C_Q = 90$ kHz and $\eta_Q = 0$, respectively. The values of C_Q obtained from analytical simulations are effective quadrupolar coupling constants,[40] which result from the averaging of quadrupolar interaction by dynamic motions, i.e., the rotation of the coordinated benzene ring about the C_6 axis. It should be noted that the effective C_Q of aromatic deuterons are very similar in many bisarene and metallocene complexes. For example, Overweg et al. studied the molecular motion of deuterated ferrocene and cobalt half-sandwich complexes in zeolites and found that values of $C_Q(^2H)$ around 97 kHz.[41]

Variable-temperature static ^{2}H NMR can be used to probe the rotational dynamics and temperature dependence of chemical shift of the various species identified in the room temperature spectra. Static ^{2}H NMR spectra for a sample of pure bis(benzene)Cr(0) with

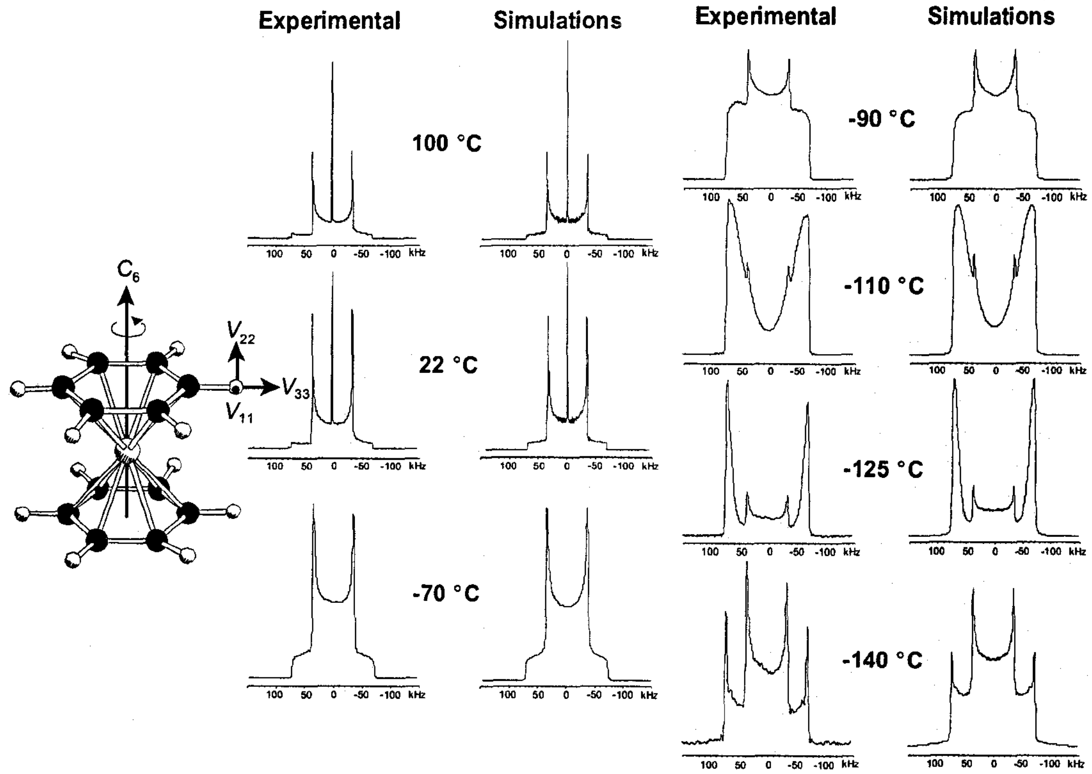

Figure 4.4. Variable-temperature static 2H NMR spectra and dynamic simulations of bis(benzene)Cr(0) acquired at 9.4 T.

residual benzene-d_6 are shown in Figure 4.4. At room temperature and higher, the Pake doublet for the bis(benzene)Cr(0) and a sharp resonance for isotropically reorienting benzene-d_6 are observed (isotropic reorientation averages the C_Q to zero, just like in the liquid phase). As the temperature is decreased to -70 °C, the sharp benzene resonance seems to disappear; however, what is actually occurring is that the benzene is no longer isotropically reorienting, but rather, behaving like a rigid rotor making rapid rotational jumps about the C_6 axis. This phenomenon is well documented for benzene loaded into microporous and mesoporous solids.[42,43] As the temperature is further decreased below -70 °C, the benzene ^{2}H powder pattern undergoes further dramatic changes, while the bis(benzene)Cr(0) powder pattern changes at a much slower rate.

A good estimate of the unaveraged "real" C_Q of bis(benzene)Cr(0) used in the dynamic simulations is approximately double the effective C_Q obtained from the analytical simulations,[42,44] whereas unaveraged C_Q of benzene-d_6 molecule has been determined from low-temperature ^{2}H NMR studies on solid benzene.[45-47] With C_Q = 191 to 195 kHz and $\eta_Q = 0$ for bis(benzene)Cr(0) and C_Q = 185-195 kHz and $\eta_Q = 0$ for benzene-d_6, the MXQET program[17] was applied to simulate all of the dynamic effects of rotational jumps about a C_6 axis on the first-order ^{2}H quadrupolar powder patterns, and to extract the relevant rate constants describing the reorientation of the rings. In order to perform such simulations, the orientation of the ^{2}H EFG tensor with respect to the molecular frame must be known, and the exchange matrix and angles describing the reorientation of the ^{2}H EFG tensors must be described. It is well known for many aromatic ^{2}H species that the largest component of the EFG tensor, V_{33}, points directly along the aromatic C-D bond, with the remaining components, V_{22} and V_{11} directed perpendicular and parallel to the plane of the aromatic ring, respectively.[37,43] In the case of an axially symmetric EFG tensor (i.e., $\eta_Q \approx 0$), the relative orientation of V_{11} and V_{22} are not crucial, and the only factors determining the appearance of the static ^{2}H powder pattern are the magnitude of V_{33}, the rate at which V_{33} reorients and the Euler angles determining the relative orientation of V_{33} at different sites. In the case of rotational jumps about the C_6 axis of benzene or benzene coordinated to chromium, the Euler angles can be set as $\varphi = 0°, 60°, 120°, 180°, 240°$ or $300°$, $\theta = 90°$ and $\rho = 90°$. The final result of applying these Euler angles is shown schematically in Figure 4.4, where the variable angle φ ensures that six different sites about an ideal hexagon are sampled, while θ tips V_{33} into the plane of the ring, and ρ orients V_{22} perpendicular to the ring plane. An Arrhenius plot, i.e., for $k = A\exp(-E_a/RT)$, of ln k vs. $1/T$, yields an activation energy for rotation of $E_a = 10.0$ kJ mol^{-1} and an activation parameter $A = 2.3 \times 10^{10}$ s^{-1} for bis(benzene)Cr(0) and $E_a = 30.5$ kJ mol^{-1} and $A = 4.0 \times 10^{15}$ s^{-1} for "free" benzene-d_6 trapped in the solid bis(benzene)Cr(0). The values for bis(benzene)Cr(0) are in reasonably good agreement with previously measured results of $E_a = 19.6$ kJ mol^{-1} for (η^6-C_6D_6)Cr(CO)$_3$,[46] 15.5 kJ mol^{-1} for bis(benzene)Cr(I) iodide,[48] and 18.8 kJ mol^{-1} in bis(benzene)Cr(0).[49] The E_a of the "free" benzene-d_6 molecule is higher than what was found in Buntkowsky et al. (16.8 kJ mol^{-1})[42] and Vold et al. (16.5 kJ mol^{-1}),[45] though our measurements were made upon residual benzene resulting from decomposition of bis(benzene)Cr(0) and their measurements were made upon pure solid benzene-d_6 over a larger temperature range.

Variable-temperature static ^{2}H powder patterns for bis(benzene)Cr(I) (Figure 4.5) change less dramatically than those for bis(benzene)Cr(0), since there is much less residual benzene due to the relatively higher stability of the bis(benzene)Cr(I) species. Only in the spectrum acquired at +100 °C is a small benzene-d_6 resonance detected at ca. 7.3 ppm. Since the bis(benzene)Cr(I) species is paramagnetic, there is a large temperature-dependent chemical shift: the ^{2}H resonance shifts to higher frequency as the temperature is lowered. At room temperature, the Pake doublet of bis(benzene)Cr(0) has an isotropic shift of ca. 5.8 ppm, while for that of bis(benzene)Cr(I), the isotropic shift at room temperature is 288 ppm. Graphing δ_{iso} as a function of $1/T$ yields a linear plot consistent with Curie-Weiss $1/T$ chemical shift dependence for paramagnetic species (Figure 4.6).

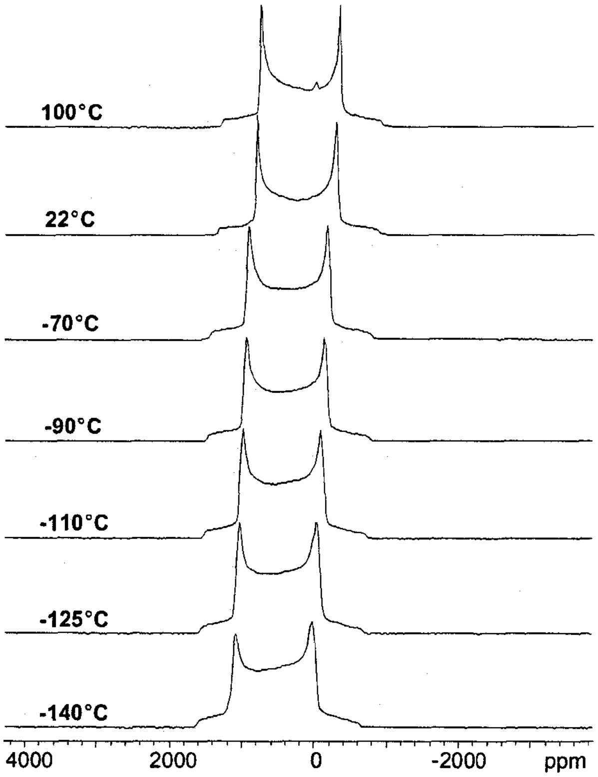

Figure 4.5. Variable-temperature static ^{2}H NMR spectra of bis(benzene)Cr(I) iodide acquired at 9.4 T.

Characterization of composite samples. Figure 4.7 shows the experimental VT ^{2}H NMR spectra of a mesoporous metal oxide loaded with 0.1 equivalents of bis(benzene)Cr(0), along with the corresponding analytical simulations. At room temperature, there appear to be two distinct powder patterns: a Pake doublet and a narrow powder pattern. The narrow pattern corresponds to the isotropically reorienting benzene-d_6 molecules at ca. 7.3 ppm. The intensity of this sharp benzene powder pattern decreases at lower temperatures and any contribution to the overall powder pattern intensity seems to disappear at -90 °C and lower. The absence of broad powder patterns for benzene-d_6 at lower temperatures likely indicate its low abundance in the loaded sample, and suggest that much of the bis(benzene)Cr(0) is rapidly converted to

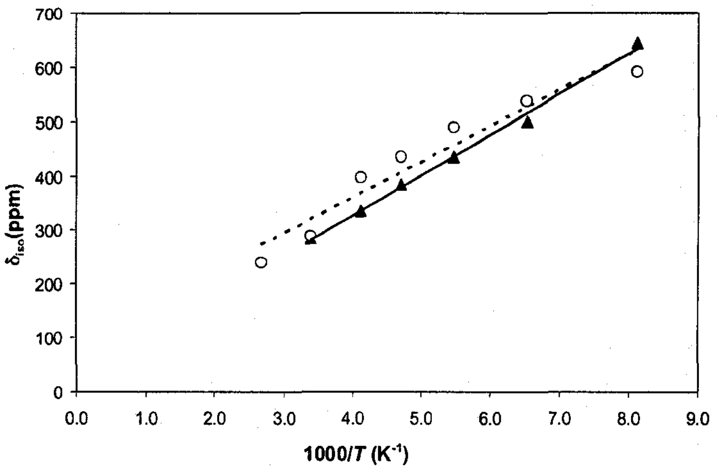

Figure 4.6. Temperature dependence of the paramagnetic deuterium chemical shift of bis(benzene)Cr(I) (○) and mesoporous metal oxides loaded with 0.1 equiv. of bis(benzene)Cr(0) (△).

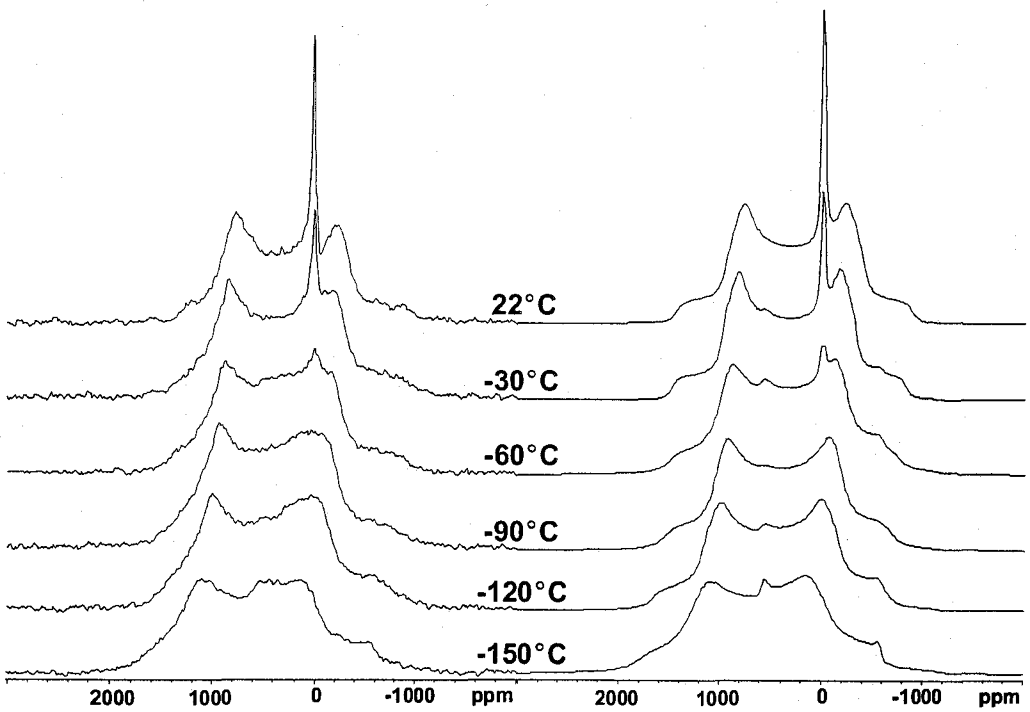

Figure 4.7. Experimental variable-temperature static ^{2}H NMR spectra (left) and analytical simulations (right) of mesoporous metal oxides loaded with 0.1 equiv. of bis(benzene)Cr(0). All NMR spectra were acquired at 9.4 T.

bis(benzene)Cr(I) upon loading. The Pake doublet corresponds to the bis(benzene)Cr(I) cation, and it shifts in the high frequency direction with decreasing temperature, from 285 ppm at room temperature to 645 ppm at -150 °C (C_Q varies from 92 to 95 kHz and η_Q varies from 0.1 to 0.15). This shift of the Pake doublet as the temperature decreases confirms the presence of bis(benzene)Cr(I). At -30 °C and lower, the presence of a new powder pattern is detected, centred at approximately 5 ppm, and with the shape of a Pake doublet that can be simulated with $C_Q = 94$ kHz and $\eta_Q = 0.01$. This powder pattern can be assigned to the bis(benzene)Cr(0) species which has not been oxidized to bis(benzene)Cr(I), since the powder pattern has identical NMR parameters to pure bis(benzene)Cr(0) and does not display the low-temperature powder patterns associated with benzene-d_6. The ^{2}H powder pattern of bis(benzene)Cr(0) is not apparent in the room temperature spectrum due to overlap of the Pake doublets of the Cr(0) and Cr(I) species and the fact that the ratio of bis(benzene)Cr(0) to bis(benzene)Cr(I) is about 1:10. ^{2}H MAS NMR experiments on this sample were relatively unsuccessful at resolving the individual species, though it is clear from the simulations of the static spectra shown in Figure 4.7 that the bis(benzene)Cr(0) species is present in low abundance. A VT plot of δ_{iso} of the loaded bis(benzene)Cr(I) species as a function of $1/T$ shows the same temperature dependence as for the pure bis(benzene)Cr(I) cation (Figure 4.6).

For a higher loading level of bis(benzene)Cr(0) (0.7 equiv.), ^{2}H NMR experiments reveal that the amount of bis(benzene)Cr(0) present in the metal oxide is much higher than the bis(benzene)Cr(I) cation, in contrast to the low loading sample. However, there is still evidence of the bis(benzene)Cr(I) cation resulting from oxidation of bis(benzene)Cr(0) (Figure 4.8). Three different ^{2}H species are resolved. The narrow resonance is assigned

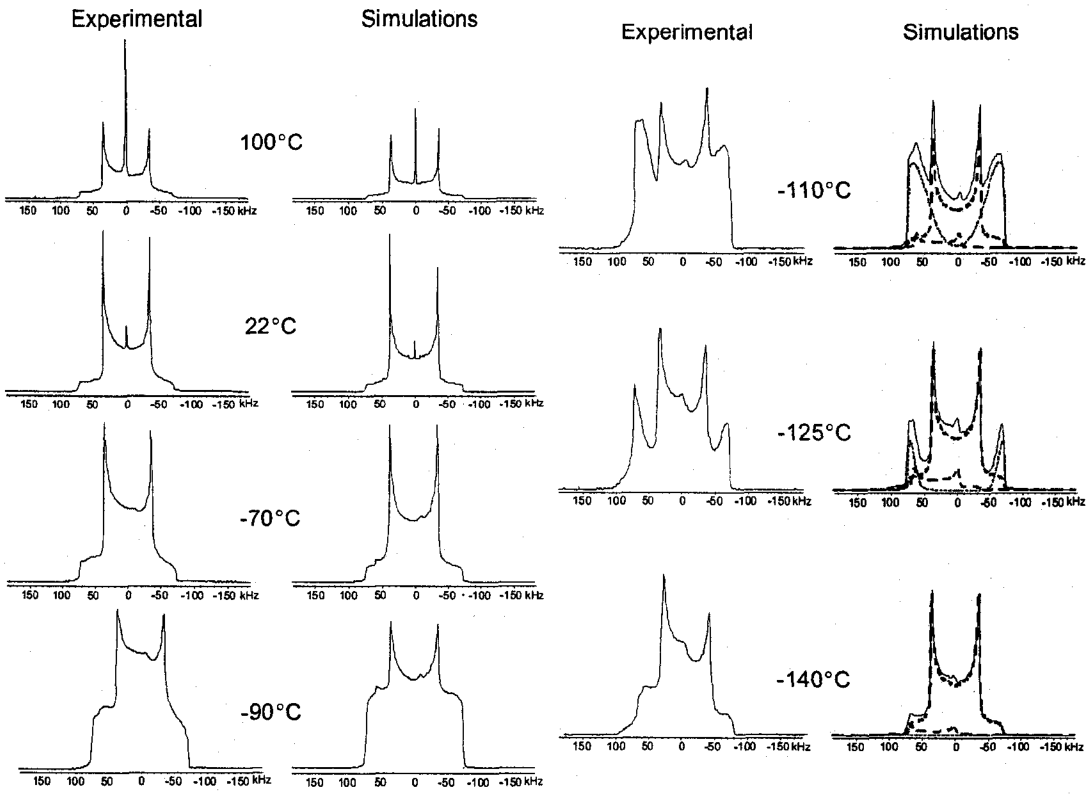

Figure 4.8. Variable-temperature static ^{2}H NMR spectra and simulations of mesoporous metal oxides loaded with 0.7 equiv. of bis(benzene)Cr(0). All NMR spectra were acquired at 9.4 T.

to benzene-d_6 with a chemical shift of ca. 7.3 ppm. The intense Pake doublet centred at ca. 6 ppm (C_Q = 96 - 97 kHz and η_Q = 0) corresponds to the bis(benzene)Cr(0) species and the smaller Pake doublet exhibiting the same temperature-dependent chemical shifts as the aforementioned examples has chemical shifts ranging from 240 to 591 ppm from +100 °C to -140 °C (C_Q = 90 - 91 kHz and η_Q = 0 - 0.06) and corresponds to the bis(benzene)Cr(I) cations. The narrow resonance again seems to disappear at lower temperatures, though benzene-d_6 is considerably more abundant than in the low loading species (notably apparent in the low-temperature spectra). Around -70 °C and lower, evidence of a small amount of the bis(benzene)Cr(I) cations can be detected shifting over a

350 ppm range from 100 °C to -140 °C. Though not strictly quantitative, the deconvolution of the low-temperature simulations reveal that the ratio of benzene-d_6:bis(benzene)Cr(0):bis(benzene)Cr(I) can be roughly estimated to be about 8:30:1.

This set of experiments indicates that loading with low and high levels of bis(benzene)Cr(0) into the mesoporous metal oxides produces a mixed-oxidation state composite material. In both cases, bis(benzene)Cr(I) cations are produced and both Cr(0) and Cr(I) species coexist. Low loading levels result in almost complete conversion of bis(benzene)Cr(0) to bis(benzene)Cr(I), whereas high loading levels contain a fair amount of unreacted bis(benzene)Cr(0) and residual benzene-d_6. The constancy of the ^{2}H Pake doublet patterns indicate that the bis(benzene) chromium species are not isotropically reorienting in this composite material; rather, the coordinated benzene rings undergo rapid reorientation about the C_6 axes and the molecules are fixed in position in a manner comparable to the pure compounds.

4.3.3 Ti-TMS1/Na- and Li-Naphthalenide Composites

Mesoporous main group sol-gel compounds with high surface areas have been proposed as alternatives to standard layered materials for Li^+ ion storage materials.[50,51] Mesoporous transition metal oxides, with their high surface areas and tunable metal oxidation states, are attractive candidates for Li^+ ions storage. It has been documented that mesoporous Ti, Nb and Ta oxides can act as electron acceptors with the presence of alkali metals, including Li, Na, K, Rb and Cs.[8,52,53] The authors have demonstrated that loading levels up to 1.0 equiv. (calculated relative to the % transition metal) of alkali metals do not result in the structural collapse of the mesostructure. Very little is known about the structure of the walls of the host materials, though a solid-state ^{17}O NMR study of mesoporous Nb oxide was recently reported.[54] The authors have demonstrated that the metal oxide framework is made up of distorted NbO_6 units, which are linked via corner-shared niobium-oxygen units. The metal oxide framework forms a three dimensional network which is terminated by Nb-OH groups. In this section, we discuss composite materials consisting of mesoporous titanium oxide intercalated with Na- or Li-naphthalenides. The coordination environments of the intercalated sodium and lithium cations are studied by solid-state ^{23}Na and ^{7}Li NMR experiments, in the hope that some insight is gained into the mesoporous Ti oxide structure. In addition, discussion of the mobility of sodium cations, examined by measurement of ^{23}Na longitudinal (T_1) and transverse (T_2) relaxation times at variable temperatures, is also presented.

Mesoporous Ti oxide synthesized using a dodecylamine template was previously characterized by extended X-ray absorption fine structure experiments (EXAFS), which suggested the presence of both 5- and 6-coordinate Ti in the walls;[55] however, there is clearly much more to learn about the wall structure in these materials. Solid-state ^{29}Si NMR is a powerful tool for the study of local structure in mesoporous silica;[56] however, the walls of the mesoporous metal oxides discussed herein do not contain a receptive spin-1/2 NMR nucleus that can be readily used as a structural probe. ^{47}Ti and ^{49}Ti are quadrupolar nuclei with relatively small quadrupole moments; ($Q(^{47}Ti) = 0.302 \times 10^{-28}$ m^2 and $Q(^{49}Ti) = 0.247 \times 10^{-28}$ m^2);[35] however, both titanium nuclides have very low NMR frequencies (near 22.5 MHz at 9.4 T) and low natural abundances, complicating the practical consideration of conducting experiments at standard magnetic field strengths. ^{17}O NMR studies are feasible, but require isotopic labelling, and are addressed in a separate study.[54] As a means of probing the structure of the walls indirectly, it is possible to conduct NMR experiments on the guest sodium and lithium cations. ^{23}Na and ^{7}Li are half-integer quadrupolar nuclei (both spin 3/2) and are extremely receptive NMR nuclides, possessing reasonably small nuclear quadrupole moments ($Q(^{23}\text{Na}) = 0.104 \times 10^{-28}$ m^2 and $Q(^{7}\text{Li}) = -0.0401 \times 10^{-28}$ m^2),[35] high natural abundances (100 % and 92.6 %, respectively) and high NMR frequencies. ^{23}Na and ^{7}Li NMR experiments have been applied in many instances to the study of microporous[57-60] and mesoporous solids,[61-64] and are applied in this work as useful probes of the coordination environment at the alkali metals in Na- or Li-reduced mesoporous Ti oxides.

Sodium-23 NMR. ^{23}Na MAS NMR spectra of mesoporous Ti oxide reduced with 0.2, 0.6 and 1.0 equiv. of Na-naphthalenides are shown in Figure 4.9. All of the spectra have a sharp resonance near 0 ppm with FWHH = 300 Hz, flanked by spinning sidebands which are indicative of a small quadrupolar interaction. At reduction levels of 0.6 and 1.0 equiv., broad peaks are observed which are centred at ca. -20 ppm and -15 ppm, with FWHH of 1200 Hz and 2350 Hz, respectively. Increasing the reduction level also results in a slight shift of the narrow resonance in the high frequency direction, from 0.37 ppm (0.2 equiv.) to 0.52 ppm (0.6 equiv.) to 0.71 ppm (1.0 equiv.). Deconvolution of the powder patterns, including all of the spinning sidebands associated with the narrow resonance, yields the following relative integrated areas of narrow and broad powder

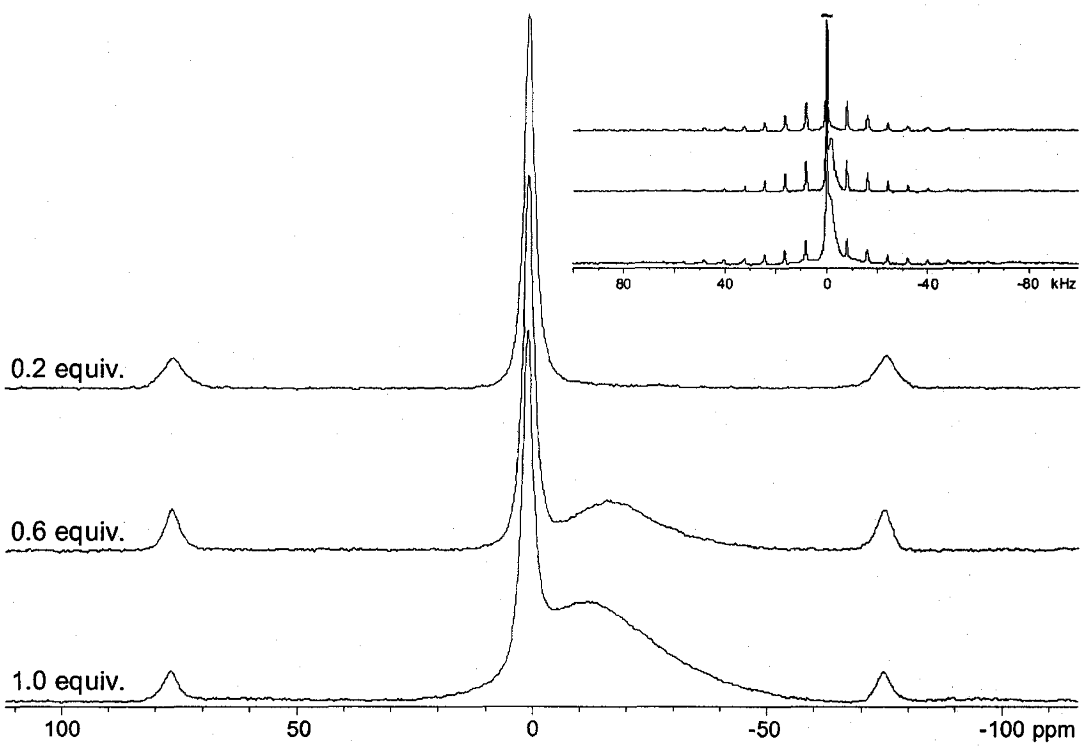

Figure 4.9. Solid-state ^{23}Na MAS NMR spectra (ν_{rot} = 8 kHz) of mesoporous Ti oxide composite materials reduced with Na-naphthalenides. Inset: vertical expansion of corresponding NMR spectra.

patterns at room temperature: 1:0.02, 1:0.59 and 1:0.91 reduced with 0.2, 0.6 and 1.0 equiv. Na-naphthalenides, respectively. In corresponding static ^{23}Na NMR experiments, the individual sites are not resolved, due to increased broadening resulting largely from non-averaged quadrupolar interactions.

Similar spectra have been reported for buried sodium sites in mesoporous aluminosilicates,[64] and for mesoporous metal oxides intercalated with sodium fullerides and reduced with Na-naphthalenides.[61] Based on these previous assignments, the sharp peaks near 0 ppm can be attributed to sodium cations which are contained within the mesoporous channels, whereas the broader resonances correspond to sodium cations which are confined within the walls of the metal oxide mesostructure. As the reduction level is increased, the augmented intensity of the broad resonance indicates that an increased number of sodium cations are becoming confined within the walls of the mesoporous framework. The broadening of this resonance can potentially result from several sources, including an increased quadrupolar interaction at the ^{23}Na nuclei, an inhomogeneous distribution of chemical shifts and quadrupolar coupling constants due to disorder, ^{23}Na-^{23}Na homonuclear dipolar coupling and/or homogeneous broadening which arises from environment-dependent T_2 time constants. Acquisition of spectra at a second magnetic field would be necessary to absolutely deconvolute the individual contributions from some of these mechanisms, but several factors point to a distribution of large quadrupolar interactions as the main source of peak broadening: (i) the sodium chemical shift range for diamagnetic compounds is relatively small (ca. 120 ppm) and a large distribution of shifts (spanning over ca. 2350 Hz) for chemically similar sites is very unlikely;[65] (ii) MAS speeds of 8 kHz would completely average all ^{23}Na-^{23}Na dipolar couplings, unless individual ^{23}Na nuclei are less than 1 Å apart (i.e., the dipolar coupling constant, $R_{DD}(^{23}\text{Na}, ^{23}\text{Na}) = 8.4$ kHz at 1.0 Å); and, (iii) long-range disorder and a variety of non-spherically symmetric sodium sites in the mesoporous walls are consistent with a distribution of large quadrupolar interactions (as well as the absence of spinning sidebands for the broad resonance). Issues of contributions to peak widths from relaxation phenomena are addressed later in this discussion.

Variable-temperature ^{23}Na MAS NMR experiments were conducted on the sample with highest reduction level (1.0 equiv. of Na-naphthalenide) to determine if temperature change has an effect on the relative populations of channel and framework sodium cations.

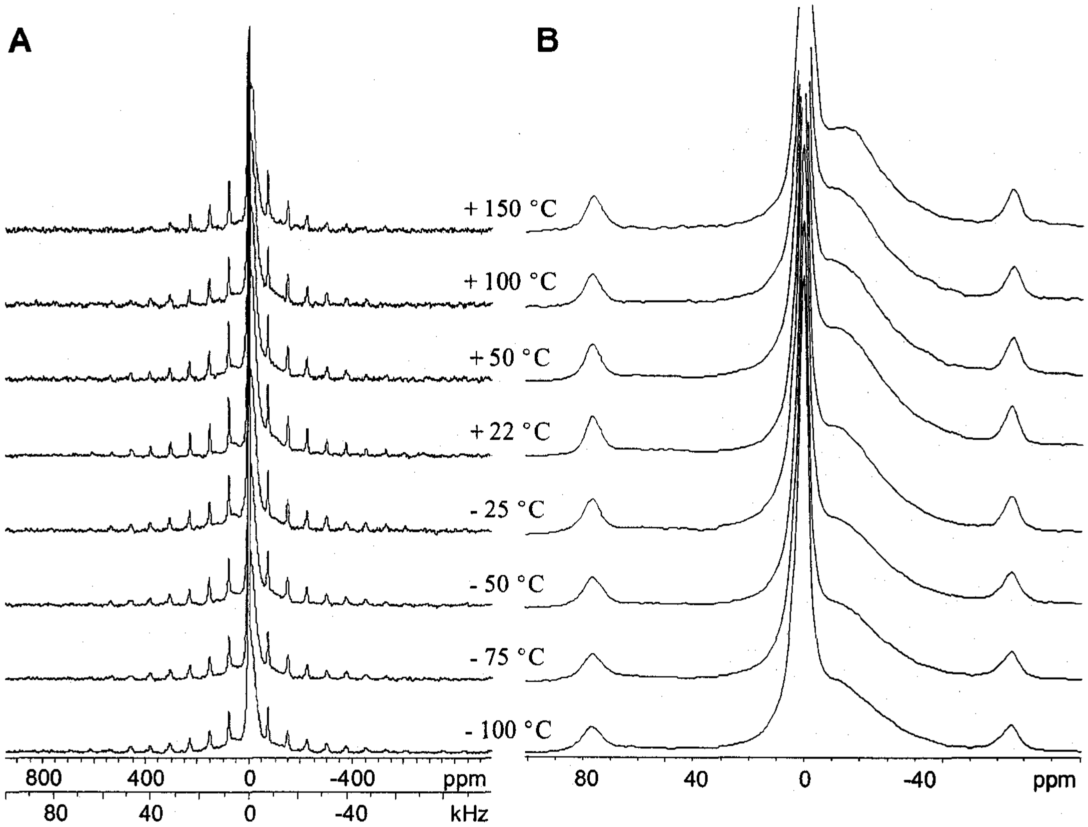

Figure 4.10. (A) Solid-state VT ^{23}Na MAS NMR spectra (ν_{rot} = 8 kHz) of mesoporous Ti oxide reduced with 1.0 equiv. of Na-naphthalenide. (B) High-resolution spectra of the isotropic regions.

The spinning sideband manifold does not change significantly with temperature, indicating a relatively constant quadrupolar interaction and therefore a relatively consistent local environment at the sodium cations (Figure 4.10). In addition, variation in temperature does not seem to have a noticeable effect on chemical shift of the narrow resonance. However, the centre of gravity of the broad resonance corresponding to framework sodium cations shifts very slightly from ca. -15.0 ppm at +150 °C to ca. -12.0 ppm at -100 °C. Furthermore, as the temperature changes, there does not seem to be a discernible trend in changing peak widths or integrated areas of both the narrow and broad powder patterns. Thus, the relative site populations appear to be solely determined by the reduction level, and hence site exchange is unlikely to happen. Temperature-dependent relaxation rates may influence the relative intensities of these peaks; however, calibrated spin-echo delays and relaxation times were determined in order to quantitatively acquire ^{23}Na MAS NMR spectra for the purposes of comparing relative site populations, effectively eliminating relaxation effects as a factor.[66,67]

Measurements of ^{23}Na T_1 and T_2 time constants were conducted from +100 °C to -70 °C, in order to (i) examine the dependence of relaxation times on temperature, (ii) gain insight into the temperature-dependent dynamics of the sodium cations and (iii) estimate contributions from transverse relaxation to the widths of the observed resonances. Relaxation measurements were only conducted on the sample with the highest reduction level with coarse steps in temperature, due to the relatively long experimental times associated with acquiring data at each temperature point. Relaxation curves at individual temperatures were fit using both mono-exponential and bi-exponential functions (Table 4.2). The bi-exponential fits involve two time constants, e.g., T_{1f} and T_{1s}, which represent "fast" and "slow" relaxation mechanisms, respectively. Contributions from multiple relaxation mechanisms are well known for a variety of NMR nuclei undergoing slow restricted motions in solid materials.[68] For instance, detailed measurements of ^{23}Na relaxation time constants of Na species in zeolites NaX and NaY have previously been reported, where relaxation data were fit with similar bi-exponential functions.[69,70] Generally speaking, better data fits are obtained herein for bi-exponential functions, especially for the narrow peak corresponding to the channel Na cations (Figure 4.11A and related materials).[11] Both mono- and bi-exponential fits

Table 4.2. ^{23}Na Longitudinal and Transverse (T_1 and T_2)[a,b] Relaxation Time Constants for Sodium Sites in Mesoporous Titanium Oxide Reduced with 1.0 equiv. of Na-Naphthalenide.

	monoexponential		biexponential				
T (°C)	A	T_1 (ms)	A_f	T_{1f} (ms)	A_s	T_{1s} (ms)	A_f/A_s[d]
			Channel Na Site				
100	2009 (30)[c]	988 (77)	557 (45)	96 (17)	1501 (43)	1693 (85)	0.37
22	5093 (64)	1176 (72)	1744 (202)	245 (44)	3499 (194)	2198 (163)	0.5
-35	3103 (46)	1813 (110)	1768 (96)	822 (51)	1506 (88)	5172 (414)	1.17
-70	1856 (31)	2026 (133)	1060 (58)	891 (59)	923 (51)	6252 (559)	1.15
			Framework Na Site				
100	842 (3)	26 (1)	N/A[e]	N/A	N/A	N/A	N/A
22	1858 (22)	54 (4)	922 (69)	18 (2)	965 (69)	162 (16)	0.96
-35	1135 (15)	157 (17)	683 (42)	64 (6)	477 (41)	577 (58)	1.43
-70	647 (9)	221 (24)	374 (23)	76 (7)	290 (22)	749 (76)	1.29
	monoexponential		biexponential				
T (°C)	B	T_2 (ms)	B_f	T_{2f} (ms)	B_s	T_{2s} (ms)	B_f/B_s[d]
			Channel Na Site				
100	3503 (241)	0.82	3417 (250)	0.28 (5)	1238 (197)	2.61 (42)	2.76
22	4166 (252)	1.19	3777 (251)	0.38 (6)	1608 (247)	3.32 (52)	2.35
-70	5484 (335)	1.55	5213 (212)	0.54 (5)	1705 (186)	6.06 (85)	3.06
			Framework Na Site				
100	1007 (59)	2.23	908 (30)	0.41 (3)	509 (23)	5.05 (29)	1.78
22	1575 (45)	3.74	837 (43)	0.98 (9)	958 (46)	6.51 (33)	0.87
-35	2138 (44)	7.37	724 (38)	1.42 (14)	1634 (42)	10.53 (32)	0.44

[a] Extraction of T_1 time constants was accomplished using the functions $A[1 - \exp(- \tau/T_1)]$ and $A_f[1 - \exp(-\tau/T_{1f})] + A_s[1 - \exp(-\tau/T_{1s})]$ for mono-exponential and bi-exponential fitting, respectively. The subscripts "f" and "s" refer to fast and slow, respectively; [b] extraction of T_2 time constants was accomplished using the functions $B \exp(-\tau/T_1)$ and $B_f \exp(-\tau/T_{2f}) + B_s \exp(-\tau/T_{2s})$ for mono-exponential and bi-exponential fitting, respectively; [c] all error bounds obtained from least-squares fitting are enclosed in parentheses; [d] A_f/A_s and B_f/B_s are the ratios of the weighted contributions of the "fast" and "slow" relaxation mechanisms; [e] bi-exponential fit not reported for this temperature point, due to lack of convergence in the least-squares fitting software.

follow similar trends with changes in temperature; thus, for simplicity, reference will be made to the constants from mono-exponential fits, unless otherwise noted.

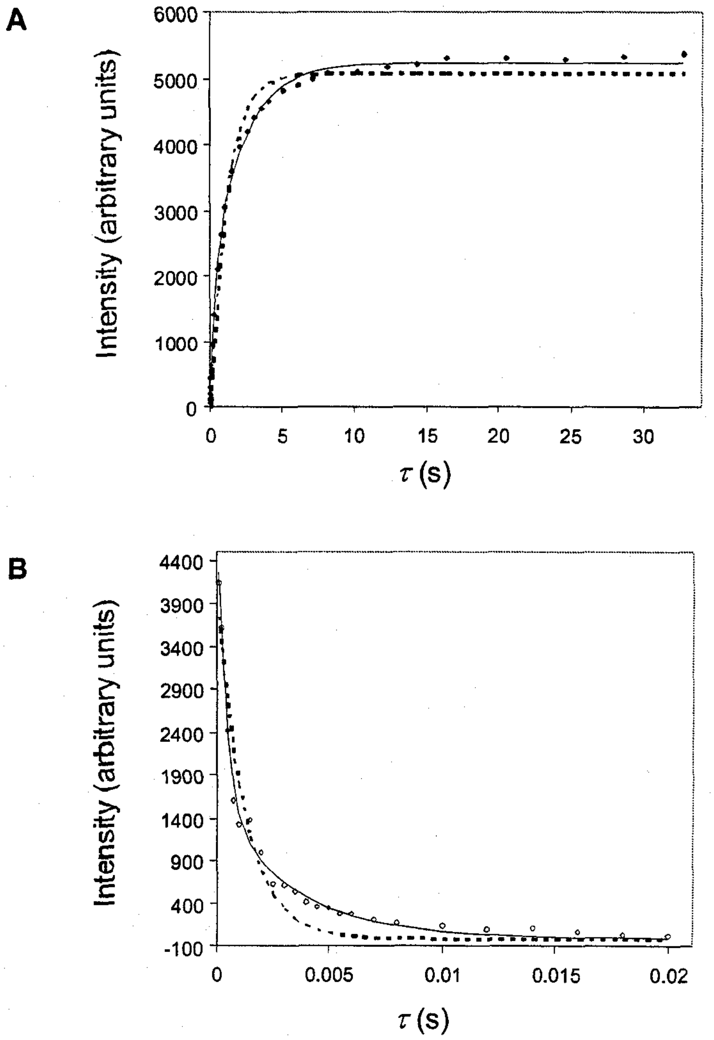

Figure 4.11. Comparison of monoexponential (dashed lines) and biexponential (solid lines) curve fits for ^{23}Na (A) T_1 and (B) T_2 relaxation data in mesoporous Ti oxides reduced with 1.0 equiv. of Na-naphthalenide at 22 °C. Errors in the echo intensities are less than 2%.

At all temperatures, the T_1 time constants of the channel species are on the order of one to two seconds, and are approximately one to two orders of magnitude larger than those of the framework species. If the quadrupolar relaxation mechanism is dominant, this supports the hypothesis that there are substantially larger quadrupolar interactions at the framework sodium sites. At 100 °C and 22 °C, the T_1 values do not change much for either site; however, as the temperature is dropped to -70 °C, the T_1 increases substantially at each site. The increase in T_1 with decreasing temperature at both sites is consistent with an increased correlation time and increasingly restricted motion, and does not arise from any significant changes in the magnitude of the quadrupolar interaction, as demonstrated in the VT NMR experiments above. This, and the fact that a bi-exponential function is necessary to accurately fit the data, implies that motion is not in the extreme narrowing limit, but on a timescale much slower than that of the ^{23}Na Larmor frequency. The bi-exponential fits for the channel sodium sites indicate an increased contribution from the "fast" relaxation mechanism as the temperature decreases (e.g., at 100 °C and -70 °C, the ratios of A_f/A_s are ca. 0.37 and 1.15, respectively); however, for the framework sites, the ratio of contributions from fast and slow mechanisms do not vary uni-directionally with decreasing temperature. Finally, the longer T_1 of the channel site, and smaller changes with decreasing temperature, intimates that the channel ions have a relatively high mobility (i.e., less restricted motion) in comparison to those constrained within the mesoporous metal oxide framework.

Measurements of T_2 constants confirm that motion is not in the extreme narrowing limit, but rather in the slow motion regime, where T_2's for channel and framework sites are much smaller than the T_1's: for instance, in the mono-exponential fits, they are on the order of 0.8 to 1.6 ms and 2.2 to 7.4 ms, respectively. Once again, bi-exponential fits provide better agreement with experiment than mono-exponential fits (Figure 4.11B and related materials),[11] though extracted time constants from both are similar. Interestingly, the fits for the channel ions indicate that fast and slow mechanisms make roughly the same contributions at all temperatures, with A_f/A_s between 2.4 and 3.0. However, for the framework ions, an increasing contribution from the "slow" relaxation mechanism is observed with decreasing temperature.

The effective transverse relaxation time constant, T_2*, can be estimated from $(\pi\Delta\nu_{1/2})^{-1}$, where $\Delta\nu_{1/2}$ is the FWHH obtained from deconvolution of the NMR powder patterns. At room temperature, $\Delta\nu_{1/2}$ = 300 Hz and T_2* = 1.06 ms for the channel ions, which is close to the value of 1.19(13) ms obtained mono-exponential fits. However, for the framework ions, $\Delta\nu_{1/2}$ = 2380 Hz and T_2* = 0.14 ms, which is substantially smaller than the measured T_2 of 3.74(21) ms. This suggests that for the channel sites, the peak broadening results almost solely from T_2 relaxation, while for the framework sites, the peak broadening results from sources other than transverse relaxation as proposed earlier, i.e., a distribution of ^{23}Na quadrupolar interactions.

The only puzzling feature of the transverse relaxation data is that the values of T_2 increase for both the channel and framework ions as the temperature is decreased. In the slow motion limit of mono-exponentially decaying transverse magnetization, one would normally anticipate a decrease in T_2 with decreasing temperature.[71,72] Bi-exponential fits do account for the observed behaviour, at least for the framework ions, where an increasing contribution from a slow relaxation mechanism is observed. The unusual T_2 constants and increased contribution from a slow relaxation mechanism at low temperatures may be the result of spin diffusion, since the framework Na sites are contained within a fairly flexible mesostructure, and may be capable of translational motion through the walls.[71,72]

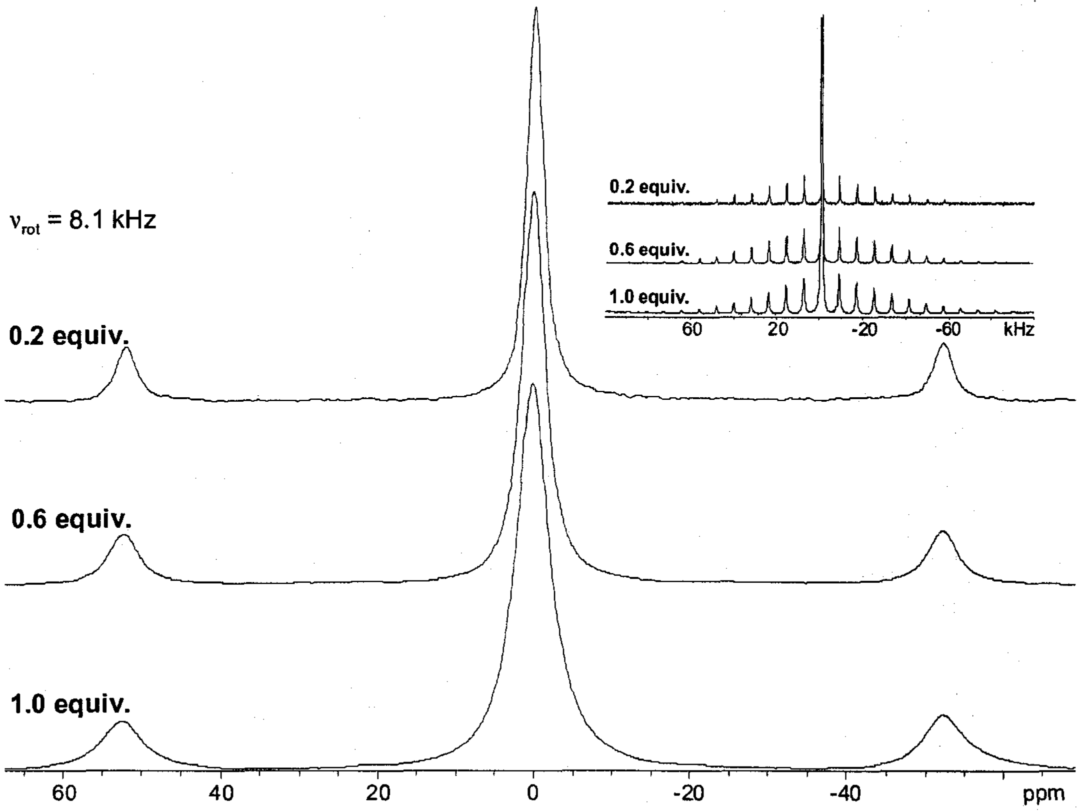

Figure 4.12. Solid-state ^{7}Li MAS NMR spectra of mesoporous Ti oxide reduced with Li-naphthalenides. Inset: full ^{7}Li MAS NMR spectra showing spinning sideband manifolds.

Lithium-7 NMR. A comparison of the ^{7}Li MAS NMR spectra of the three samples with different reduction levels is shown in Figure 4.12. As the reduction level increases from 0.2 equiv. to 1.0 equiv., the single ^{7}Li powder pattern becomes broadened and shifts very slightly in a positive direction (i.e., to high frequency direction), with FWHH of 280 Hz, 390 Hz and 650 Hz and centres of gravity at -0.30, -0.20 and +0.14 ppm, for the 0.2 equiv., 0.6 equiv. and 1.0 equiv. samples, respectively. Powder patterns corresponding to channel and framework alkali cations are not resolved in the ^{7}Li MAS NMR spectra as they are in the ^{23}Na MAS NMR spectra presented above, and all attempts to deconvolute these peaks into separate broad and narrow resonances were unsuccessful.

If there are magnetically distinct Li sites akin to those in the Na-reduced samples, they are likely not resolved since ^{7}Li has a much smaller nuclear quadrupole moment and a reduced chemical shift range (ca. 15 to 20 ppm) in comparison to ^{23}Na (ca. 40 to 50 ppm).[65] As a result, relaxation measurements were not conducted. The broadening in the MAS spectra does not arise from ^{7}Li-^{7}Li homonuclear dipolar coupling since the spinning rate of ca. 8 kHz is enough to average dipolar couplings in most lithium spin pairs, unless they separated by ca. 1.3 Å. However, substantial peak broadening is observed in the static ^{7}Li NMR spectra with increased reduction level (Figure B.4.1 in appendix B), indicating that there is some degree of homonuclear dipolar coupling.

The broadening observed in the MAS spectra likely indicates one of two possibilities: (i) the increasing presence of framework lithium ions or (ii) the gradual creation of a new phase at higher reduction levels. In the first case, the increasing presence of framework Li ions at higher reduction levels would give rise to slightly broader powder patterns, similar to those observed in the ^{23}Na NMR spectra of the Na-reduced samples. The lithium cations which are constrained within the mesoporous Ti oxide framework have a distribution of quadrupolar interactions and chemical shifts, and decreased transverse relaxation times, all of which contribute to broadening of the ^{7}Li resonances.[73] In the second case, the subtle chemical shift change from -0.30 to +0.14 ppm in the lithium-reduced mesoporous titanium oxide samples may be due to the presence of local anatase structure with no long-range order at low reduction levels, which is gradually converted to the titanate phase with no long-range order at higher reduction levels. Wagemaker et al. reported three separate lithium chemical shifts in their study of

TiO_2 anatase by ^7Li MAS NMR.[73] The first peak appearing at -0.85 ppm corresponds to Li intercalated into the anatase structure, the second peak at -2.8 ppm corresponds to Li interacting with the conduction band electrons, and the third peak at 0.7 ppm occurs at high Li reduction levels and corresponds to the formation of lithium titanate. In this study it was also shown that for increasing lithium concentrations, there is a strong preference for the lithium titanate structure over the anatase phase, which gradually disappears as more and more lithium is added to the host material. Herein, the subtle chemical shift change from -0.30 to +0.14 ppm in the lithium-reduced mesoporous titanium oxide samples may be due to the presence of local anatase structure with no long-range order at low reduction levels, which is gradually converted to the titanate phase with no long-range order at higher reduction levels. Alternatively, the change in the centre of gravity of the peak may simply arise from an increased presence of framework Li species possessing a marginally lower chemical shift, as in the case of the ^{23}Na NMR spectra. Unfortunately, the peak width is too broad to make any definitive assignments, and faster MAS speeds or MQMAS experiments are not helpful in obtaining resolving individual sites.

4.3.4 Ta-TMS1/Rb-Naphthalenide and Rb_3C_{60} Composites

The bulk alkali metal fullerides of the form A_3C_{60} (where A = Na, K, Rb and Cs) display superconducting properties at temperatures of 33 K or lower,[74-77] though they are predicted to Mott-Hubbard insulators because of their half-filled t_{1u} band.[78] On the hand, mesoporous transition-metal oxide hosts loaded with lithium fullerides are insulating,[62] while with K_nC_{60} (n ranging from 0.5 to 2.5, where n = the mean oxidation state of the fulleride as measured by Raman spectroscopy) and Na_nC_{60} are semiconductors. Both mesoporous transition-metal oxides/(K_nC_{60} and Na_nC_{60}) become insulators with n = 3.0 but are metals or semimetals when n approaches 4.[61,79] The metallic behaviour of potassium fulleride composites is not yet understood. Because ^{87}Rb is more receptive than ^{39}K (receptivities with respect to ^{13}C are $D^C(^{39}K) = 2.79$ and $D^C(^{87}Rb) = 2.90 \times 10^2$)[80] and has large chemical shift range, it can be used as a NMR probe to study mesoporous Ta oxide/(Rb_3C_{60}, Rb-naphthalenide) composite system.

In this final section, mesoporous tantalum oxide samples loaded with a variety of guest compounds are examined by solid-state ^{87}Rb and ^{13}C NMR spectroscopy. Both types of guest species act as reducing agents, meaning that they serve to reduce the Ta species within the mesoporous walls; however, the difference in the degree of reduction varies substantially between the guest species. The discussion has the following order: characterization of free Rb_3C_{60} using ^{87}Rb and ^{13}C NMR experiments is presented, followed by the discussion on mesoporous Ta oxide loaded with 1 equiv. of Rb-naphthalenide (hereafter abbreviated as 1eq.Rb-TaTMS1). Finally, results from solid-state ^{87}Rb and ^{13}C NMR experiments conducted on the mesoporous host reduced by Rb_3C_{60} (n = 1 sample), as well as the resulting materials loaded with additional equivalents of Rb-naphthalenide (n = 3 and n = 4 samples), are presented.

Solid-state ^{87}Rb and ^{13}C NMR studies. In a previously reported NMR investigation of mesoporous tantalum oxide sodium fulleride composites, it was found that it is possible to distinguish various types of sodium species via straightforward ^{23}Na MAS NMR experiments.[81] Three different types of sodium sites were differentiated, including free sodium ions in the mesoporous channels, sodium ions confined in the Ta oxide framework, and sodium ions that are associated with the different species of fullerides. ^{87}Rb, like ^{23}Na, is a half-integer quadrupolar nucleus (nuclear spin $I = 3/2$), and is very amenable to NMR experimentation due to its high receptivity and relatively small nuclear quadrupole moment ($Q = 0.1335 \times 10^{-28}$ m^2).[35] ^{85}Rb is the other NMR active isotope of rubidium and 0.15 times as receptive as ^{87}Rb, and also has a nuclear quadrupole moment which is roughly twice that of ^{87}Rb. ^{87}Rb NMR has proven to be an invaluable probe of the structure of alkali fullerides,[82,83] and has also been used to probe Rb ion environments in a variety of materials, including Rb salts intercalated into γ-alumina,[84] Rb ions in halide lattices,[85] Rb$^-$ ions in zeolite LiA,[86] rubidium cations in various sites in zeolites NH$_4$Y and LTA.[87,88] As for the sodium fullerides encapsulated into mesoporous metal oxides, or rubidium sites in microporous solids, the different chemical environments of the alkali metal species in mesoporous metal oxides should induce quadrupolar and chemical shielding interactions which can be employed to build an understanding of the molecular structure and dynamics in these composite materials. The rubidium chemical shift range is considerably larger than that of sodium,[65] so it is possible that additional species that could not be identified by ^{23}Na NMR experiments will be observed in the ^{87}Rb NMR spectra. Additionally, ^{13}C{^{1}H} MAS and ^{1}H-^{13}C VACP/MAS experiments were employed to identify the carbon-containing species in these composite materials, as well as to monitor changes in the oxidation states of the fullerene and fulleride species. Before proceeding with the discussion on NMR data of our composites it is prudent to review solid-state NMR data for pristine Rb$_3$C$_{60}$.

Solid-state ^{87}Rb and ^{13}C NMR of Rb_3C_{60}. Much effort has been expended on the structural characterization of alkali fullerides, due to the high-temperature superconductivity observed in alkali fullerides of the form A_3C_{60}, which has been surpassed only by high critical temperature of superconductivity (T_c) copper oxides.[89] Rb_3C_{60} has been the subject of numerous solid-state NMR investigations.[82,83] An initial paper on the synthesis and structural characterization of alkali fullerides proposed that Rb_3C_{60} may have a structure with tetrahedral (T) and octahedral (O) sites.[89] Tetrahedral and octahedral coordination sites in these alkali fullerides refer to alkali cations coordinated by four or six carbon atoms from the neighbouring fulleride species. Tycko et al. used ^{13}C NMR to investigate Rb_3C_{60} and other alkali fullerides.[90,91] Static ^{13}C NMR experiments at ambient temperature revealed a broad anisotropic pattern with a centre of gravity near 181 ppm,[90] whereas slow-spinning (3.5 kHz) MAS NMR spectra show an isotropic peak near 197 ppm, corresponding to the C_{60}^{3-} species, and a less intense resonance at 191 ppm, which is thought to arise from a Rb_4C_{60} impurity phase.[91] Pennington and Stenger claim to observe the isotropic peak for C_{60}^{3-} nearer to 182 ppm.[82] The broad peaks in the ^{13}C MAS NMR spectrum of Rb_3C_{60} are thought to arise from structural disorder which gives rise to an inhomogeneous distribution of chemical shifts.

^{87}Rb NMR spectra acquired at 440 K show that there are T and O rubidium sites in a 2:1 ratio.[92,93] As the temperature is dropped below 370 K, there is an additional resonance which is attributed to a second type of tetrahedral Rb site (T′). SEDOR NMR experiments imply that all three sites originate within the same phase.[92] It was suggested that the T′ site may arise from unique orientations or differential motion of the C_{60} molecules at lower temperatures (i.e., which deviate from the fcc structure of Rb_3C_{60}),[92,93] Jahn-Teller distortion of the C_{60}^{3-} molecules or even localization of excess charge density at the T′ sites, though most of these claims were disproved.[94] Later ^{87}Rb NMR studies by Zimmer et al. revealed fine structural detail in MAS NMR experiments not observed in previous static NMR experiments,[95] and 2D chemical exchange spectra showed no exchange between the various Rb sites.[96] The authors suggested that diffusion of Rb atoms between vacancies is a possible explanation for differentiation of the T and T′ sites in the ^{87}Rb spectra, though this was later shown not to be the case by Gorny et al.,[97] who suggested that the differences in the T and T′ sites likely arise from variations in the surroundings.

Our own ^{87}Rb static NMR experiments on Rb_3C_{60} reveal three relatively broad powder patterns centred at 80 ppm, -11 ppm and -135 ppm (Figure 4.13), in agreement with previously acquired NMR data.[92-94,98] The centres of gravity of these patterns are assigned to the Rb ions in T′, T and O sites, respectively. ^{87}Rb MAS NMR experiments serve to narrow the broad patterns substantially (Figure 4.13B), revealing some second-order structure in the two lower frequency patterns, with centres of gravity at 80 ppm, 2.2 ppm and -123 ppm. The corresponding $^{13}C\{^1H\}$ MAS NMR spectra (Figure 4.13C,D) have a sharp peak centred at 182.8 ppm as well as a broad non-uniform peak near 195 ppm. The former peak is assigned to the C_{60}^{3-} species,[82] while the latter peak may reflect a distribution of chemical shifts arising from some disorder in the sample, or from other non-stoichiometric rubidium fulleride species similar to that of observed in

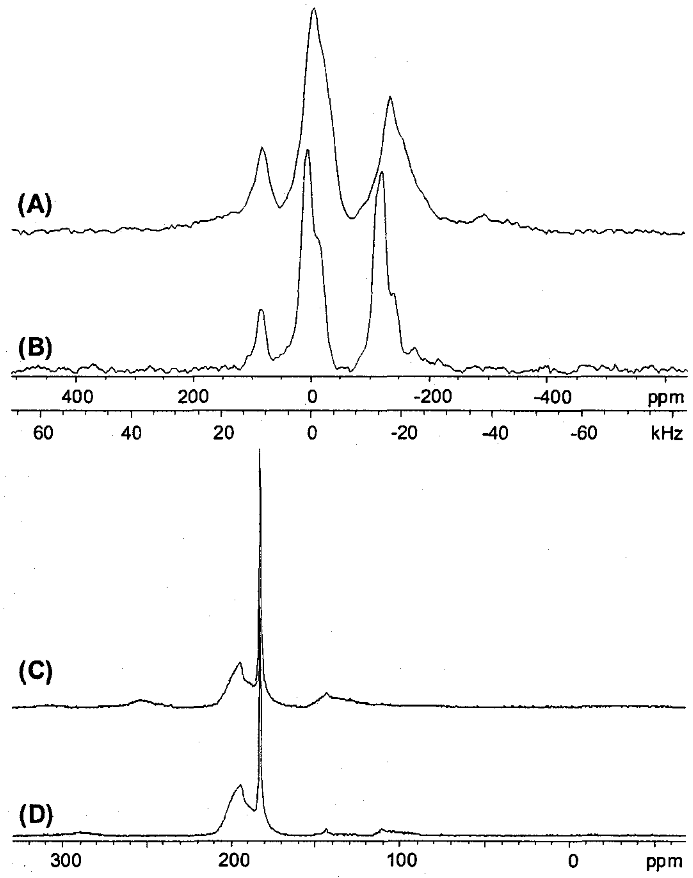

Figure 4.13. (A) Static ^{87}Rb NMR spectrum and (B) ^{87}Rb MAS NMR spectrum (ν_{rot} = 12 kHz) of Rb_3C_{60} at 9.4 T. ^{13}C MAS NMR spectra of Rb_3C_{60} at (C) ν_{rot} = 5.3 kHz and (D) ν_{rot} = 8.7 kHz.

Na_3C_{60} composites.[79] There are also some relatively weak signals at 144 ppm and 111 ppm, which are assigned to unreacted C_{60}[90] and Teflon contained within the sample spacers,[99] respectively.

Solid-state ^{87}Rb and ^{13}C NMR of Rb composites. In order to make more direct comparisons between the bulk phase of Rb_3C_{60} and mesoporous composite materials, and to elucidate the effect of coordination geometries of both the fulleride and rubidium species on the unusual electronic properties of the composite materials, solid-state ^{87}Rb and ^{13}C NMR measurements were employed for the samples with n = 1.0, n = 3.0 and n =

4.0, as well as for 1eq.Rb-TaTMS1, which is C_{60} "free".

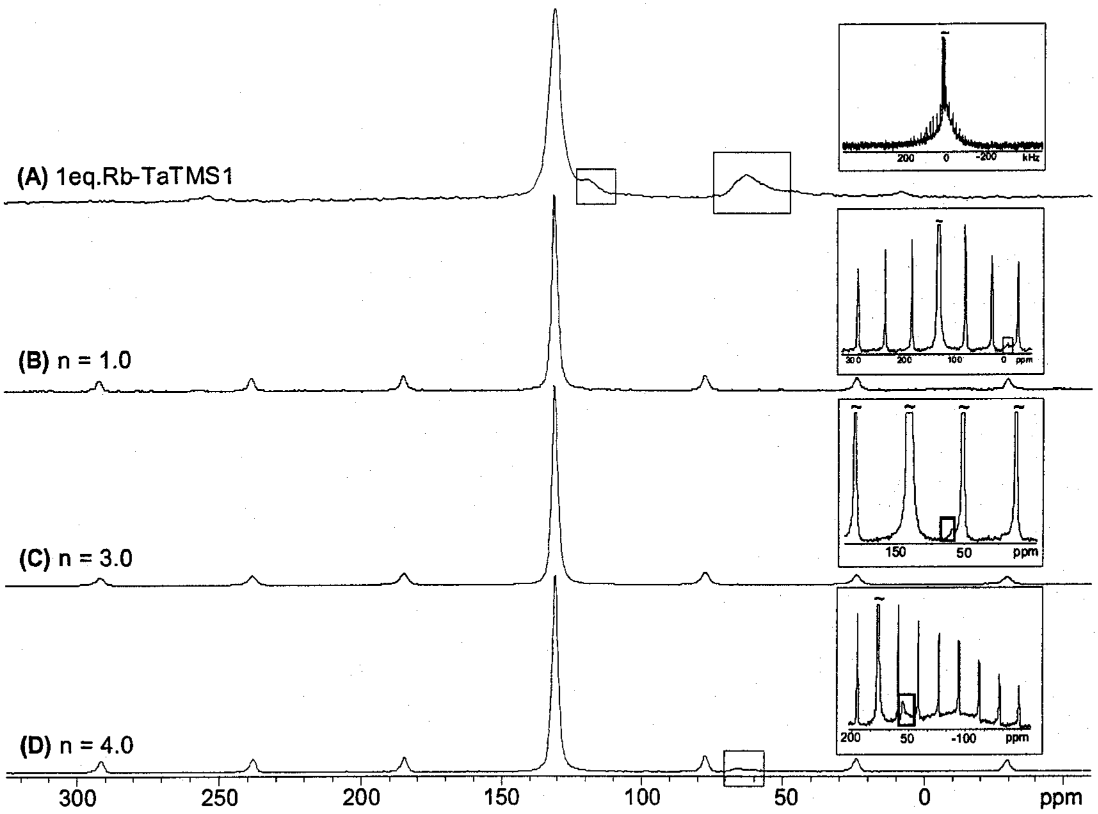

Figure 4.14. ^{87}Rb MAS NMR spectra of (A) mesoporous Ta oxide reduced with Rb-naphthalenide in the absence of C_{60}, (B) mesoporous Ta oxide Rb_3C_{60} composite (n = 1.0), and (C and D) mesoporous Ta oxide Rb_3C_{60} composite reduced to oxidation states of (C) n = 3.0 and (D) n = 4.0. Insets: vertical expansion of isotropic regions.

The room-temperature ^{87}Rb MAS NMR spectrum of 1eq.Rb-TaTMS1 (Figure 4.14A) possesses a major resonance at 130 ppm, as well as two other minor resonances at 119.1 ppm (sharp) and 65 ppm (broad). There is also an extremely broad powder pattern which spans ca. 350 kHz (see inset of Figure 4.14A), underlying the main peak and spinning sidebands. The major resonance at 130 ppm corresponds to free Rb ions in the channel of the mesostructure. The origin of peaks at 119 ppm and 0 ppm is not known for certain, but is likely related to unique Rb environments in the channels, or perhaps in smaller microporous channels. Peaks such as these were not observed in analogous ^{23}Na NMR experiments on tantalum oxide reduced with Na naphthalene,[81] either because the sites simply did not exist or were not resolved in the reduced sodium chemical shift range (i.e., sites may have had overlapping resonances). These peaks may also be due to formation of a rubidium tantalate phase due to slight overreduction of the framework, as they are not present in a sample of mesoporous Ta oxide reduced with only 0.5 equiv. of Rb-naphthalenide (Figure B.4.2). It was previously demonstrated by Antonelli et al. that treatment of mesoporous Ti oxide with more that 1.0 equiv. of Li-naphthalenide reagent led to destruction of the mesostructure and formation of numerous lithium titanate phases.[53]

The broad underlying pattern likely arises from the presence of Rb ions which are confined within the metal oxide framework (i.e., Rb ions which are strongly interacting with oxygen atoms at of the metal oxide framework and/or tightly bound surface species). Similar assignments have been made for ^{23}Na NMR spectra of Na ions resulting from the encapsulation of Na_3C_{60} into mesoporous Ta oxide,[81] as well as "surface" and "buried" sodium sites in sodium-doped mesoporous aluminosilicates.[64]

The static ^{87}Rb NMR spectra of 1eq.Rb-TaTMS1 (Figure 4.15A) displays two main powder patterns. The resonances, observed in the MAS NMR spectrum at 130 and 119.1 ppm, overlap and give rise to a single broad powder pattern with a centre of gravity at 133 ppm and a FWHH of ca. 2.2 kHz. The second powder pattern is centred at 65 ppm with a FWHH of ca. 6.3 kHz. The relative integrated areas of these powder patterns are 3:1 in favour of the higher frequency pattern. Thus, MAS and static ^{87}Rb NMR experiments

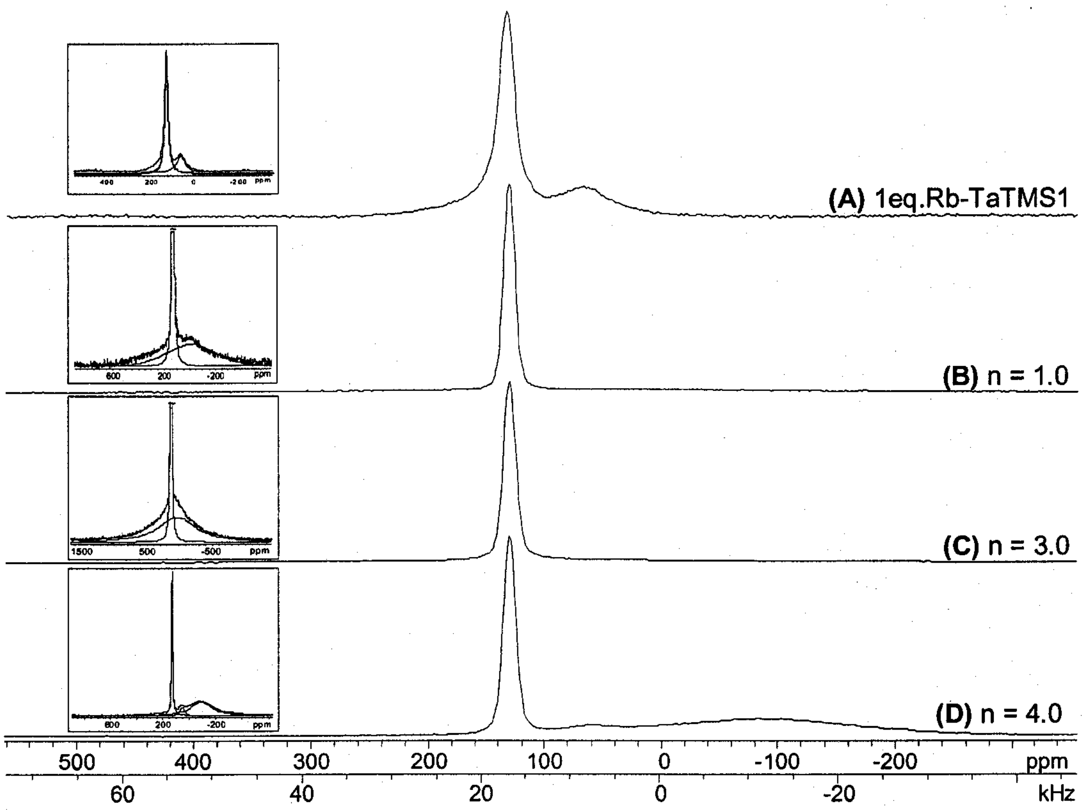

Figure 4. 15. Static ^{87}Rb NMR spectra of (A) mesoporous Ta oxide reduced with Rb-naphthalenide in the absence of C_{60}, (B) mesoporous Ta oxide Rb_3C_{60} composite (n = 1.0), and (C and D) mesoporous Ta oxide Rb_3C_{60} composite reduced to oxidation states of (C) n = 3.0 and (D) n = 4.0. Insets: vertical expansions and powder pattern deconvolution.

identify two major rubidium sites: "channel" Rb ions and framework Rb ions, which give rise to an intense sharp resonance at ca. 133 ppm and a broad overlapping resonance at ca. 65 ppm, respectively.

The ^{13}C MAS and VACP/MAS NMR spectra of 1eq.Rb-TaTMSl revealed a wide variety of different resonances, including benzene (129 ppm), Teflon from the spacers of the rotor (112 ppm), THF (68 and 26 ppm) and some residual TMS-chloride (near 0 ppm), as well as and some other carbon-containing species with resonances at 73 and 56 ppm which may arise from coordination of THF by Rb ions (Figure 4.16). The intense

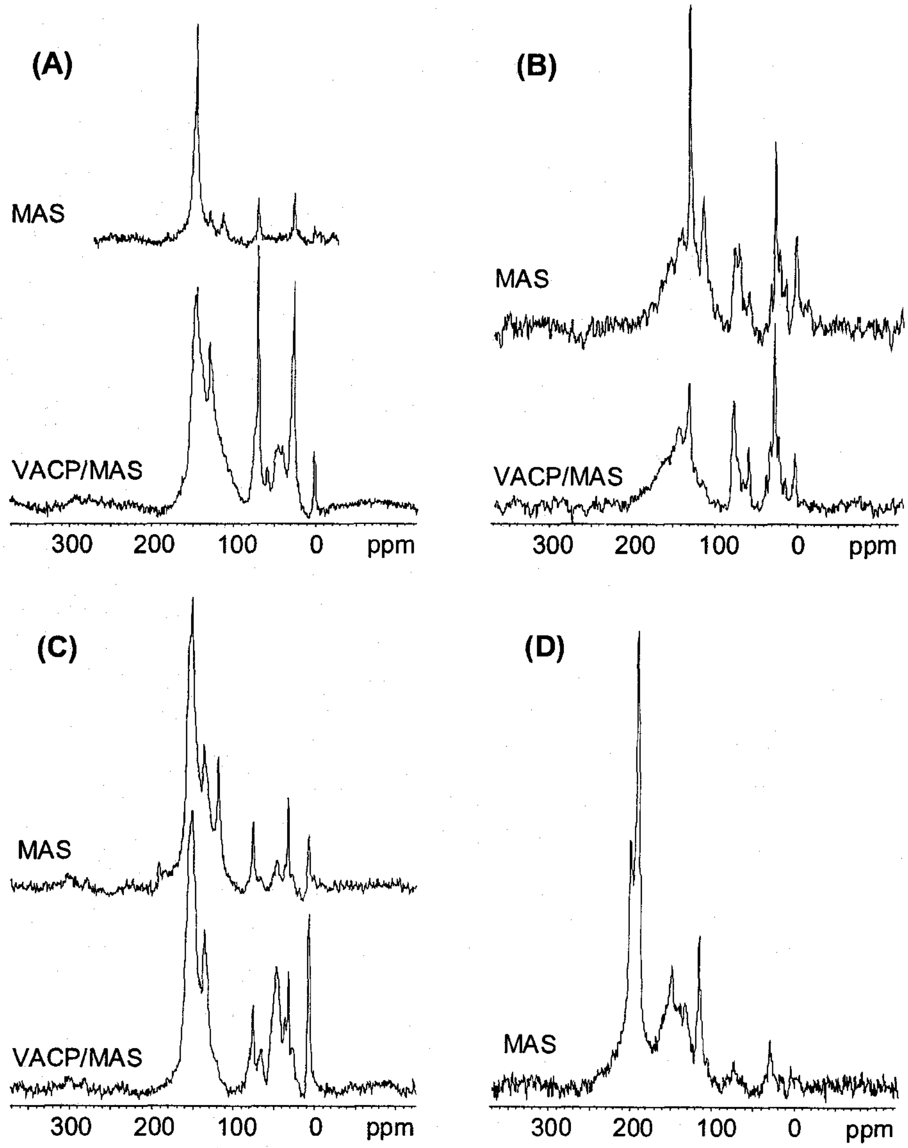

Figure 4.16. $^{13}C\{^{1}H\}$ MAS and ^{1}H-^{13}C VACP/MAS NMR spectra (ν_{rot} = 15 kHz) of (A) mesoporous Ta oxide reduced with Rb-naphthalenide in the absence of C_{60}, (B) mesoporous Ta oxide Rb_3C_{60} composite (n = 1.0), and (C and D) mesoporous Ta oxide Rb_3C_{60} composite reduced to oxidation states of (C) n = 3.0 and (D) n = 4.0.

peak centred at ca. 128.5 ppm in the ^{13}C MAS spectrum of 1eq.Rb-TaTMS1 arises from the overlap of benzene resonance (δ_{iso} = 128.5 ppm) with the naphthalene resonances (δ_{iso} = 126.1, 128.3 and 133.9 ppm).[100] There is a broad powder pattern that ranges from 100 to 200 ppm, which likely results from an inhomogeneous chemical shift distribution resulting from organic species interacting with the disordered mesoporous channels and a variety of different environments within the metal oxide framework.

The ^{87}Rb MAS NMR spectra of parent (n = 1.0) material is shown in Figure 4.14B. There is one major sharp peak at 131 ppm flanked by a manifold of spinning sidebands (SSBs), as well as a much smaller resonance at ca. -8 ppm. The SSBs indicate that there is a sizeable quadrupolar interaction, though not large enough to give rise to a second-order central transition powder pattern. Simulations of the isotropic resonance and SSBs using the SIMPSON simulation program[101] do not yield any precise quantitative information regarding the magnitude of the quadrupolar interaction (room-temperature ^{87}Rb SATRAS NMR spectrum not shown), since the SSBs taper off on each side of the central transition, probably as a result of long-range disorder in the solid. None of the ^{87}Rb NMR resonances observed for the pure phase Rb_3C_{60} are observed for this sample or for any of the other composite materials (*vide infra*). The small resonance at -8 ppm may correspond to Rb species associated with a fulleride species. Differing from the ^{87}Rb MAS NMR spectra of 1eq.Rb-TaTMSI, a broad underlying powder pattern is absent, implying less incorporation of Rb ions into the walls of the mesostructure in the parent material, which is consistent with the lower reduction level of the Ta framework.

In a vertical expansion of the ^{87}Rb static NMR spectrum of the n = 1.0, a broad underlying powder pattern centred at ca. -10 ± 10 ppm is observed (Figure 4.15B). The intense peak at 131 ppm corresponds to Rb cations in the channels of the mesoporous Ta oxide, whereas the latter broad peak near -10 ppm may arise from the presence of one or more Rb species associated with fulleride units. The absence of visible resonances at around ca. 65 ppm is not surprising as this quite weak resonance is most likely obscured by Rb fulleride species which are dominant in this case.

The ^{13}C MAS NMR spectra of the n = 1.0 sample (Figure 4.16B) has the same signature peaks as in the 1eq.Rb-TaTMS1 sample (i.e., benzene, Teflon, THF and TMS1) as well as additional C_{60} and $C_{60}{}^{n-}$ resonances. A sharp peak at 144 ppm and a neighbouring broader peak centred at 148 ppm are also evident. The narrow resonance at 144 ppm likely corresponds to pure C_{60}, while the latter resonance corresponds to a fulleride species in a distinct oxidation state, $C_{60}{}^{n-}$; however, the assignment of the exact oxidation state of this species is not possible at this time. Interestingly, no trace of $C_{60}{}^{3-}$ resonances are detected, further affirming that Rb_3C_{60} was oxidized by the channels of the metal oxide framework. In the ^{1}H-^{13}C VACP/MAS NMR spectra, the Teflon resonance completely disappears, the intensity of the C_{60} resonances becomes greatly reduced, and the benzene, THF and TMS1 peaks are enhanced, as anticipated. There are also broad unidentified peaks at ca. 59, 46 and 40 ppm.

The ^{87}Rb MAS NMR spectra of the n = 3.0 material (Figure 4.14C) is almost identical to the spectra of the parent material. The peaks correspond to Rb ions within the channel of parent and n = 3.0 materials have almost identical FWHH of ca. 320 Hz. The only noticeable differences are (i) a very subtle peak near 65 ppm and (ii) the absence of a very small peak near -8 ppm. The spinning sideband manifold extends a similar distance as compared to the spectra of the parent material, indicating that the quadrupolar interactions are similar (not shown). The peak at 65 ppm (Figure 4.14C, inset) likely corresponds to framework Rb ions consistent with the peak at the same position in 1eq.Rb-TaTMS1.

The static ^{87}Rb NMR spectrum of the n = 3.0 composite (Figure 4.15C) appears to be similar to that of the parent material. However, expansion of the vertical scale reveals a broad underlying pattern, distinct from that of the parent material, which extends in high- and low-frequency directions. This pattern undoubtedly arises from overlapping powder patterns corresponding to both framework Rb ions and Rb ions associated with the various fulleride species. The degree of Rb ion incorporation into the framework is higher than in the parent material, but clearly much lower than in the 1eq.Rb-TaTMS1 sample.

The ^{13}C MAS and VACP/MAS NMR spectra of the n = 3.0 composite (Figure 4.16C) are very similar to those of the parent composite (Figure 4.16B). However, the ^{13}C NMR spectra of the n = 3.0 material shows an increased amount of C_{60}^{n-} species and less C_{60} than in the parent material. In addition, there is a very small resonance at ca. 184 ppm which can be assigned to C_{60}^{3-}. These results are distinct from ^{13}C MAS NMR experiments previously conducted on mesoporous tantalum oxide impregnated with Na_3C_{60} and reduced with sodium naphthalene to the oxidation state of n = 3.0.[81] In these samples, the C_{60} species of the parent material were completely reduced to C_{60}^{3-} (i.e., a sharp peak at 187.3 ppm was the only indicator of fullerene/fulleride species) upon reduction, whereas in Rb samples reduced to the same oxidation state of n = 3.0 only a minute amount of C_{60}^{3-} is produced. The ^{87}Rb and ^{13}C NMR data therefore imply that n = 1.0 and n = 3.0 samples are very similar, with the exception of more confined Rb ions in the n = 3.0 material and the conversion of a small amount of C_{60} to C_{60}^{3-}.

The ^{87}Rb MAS NMR spectrum of the n = 4.0 material appears to combine elements of all of the other composites (Figure 4.14D). The usual sharp "channel" Rb site is present as evidenced by a peak at 130 ppm. There is a pronounced resonance at 65 ppm, similar to that observed in the 1eq.Rb-TaTMS1 and n = 3.0 samples which corresponds to confined Rb ions in the walls of mesostructure. Finally, there is also a very broad powder pattern centred at ca. -75 ppm. This pattern most likely corresponds to the Rb associated with one or more fulleride species.

The static ^{87}Rb NMR spectrum of the n = 4.0 composite (Figure 4.15D) is consistent with increased intercalation of Rb ions into the walls of the mesostructure relative to the n = 1.0 and n = 3.0 sample upon increased reduction to the n = 4.0 state. The resonance at -75 ppm, previously assigned to Rb associated with particular fulleride species, is also prominent. The relative integrated area of peaks assigned to channel (130 ppm) to confined (65 ppm) to fulleride related (-75 ppm) species is ca. 8:1:14, indicating the presence of the substantial amount of Rb ions associated with the new fulleride species in the channels identified in the ^{13}C NMR spectrum of this material.

Perhaps of equal interest is the ^{13}C MAS NMR spectrum of n = 4.0 material (Figure 4.16D). There are major resonances at 186 and 196 ppm, which can be assigned to C_{60}^{3-} and some other highly anionic C_{60}^{n-} species. The resonance near 144 ppm, is greatly diminished in intensity, indicating that the most of the C_{60} has been reduced to other fulleride species. This data further supports the assumption that the broad powder pattern centred at -75 ppm observed in ^{87}Rb MAS NMR is likely due to Rb ions coordinated to a fulleride species in the n = 4.0 sample, as compared to the n = 3.0 sample which has very little or no C_{60}^{3-} and showed less intense peak at -75 ppm in static ^{87}Rb NMR spectrum. As equally intriguing is that it was not possible to conduct ^{13}C MAS (with high-power decoupling) or ^{1}H-^{13}C VACP/MAS NMR experiments, since it was impossible to obtain a reasonable matching/tuning combination on the proton channel for this sample. The inability to tune or match on the narrow-banded proton channel indicates that the n = 4.0 material has a significant influence on the inductance of the sample coil, likely because of the strong magnetic properties which distinguish this sample from all of the other materials.

Variable-temperature ^{87}Rb NMR of Rb fulleride composites. Variable temperature solid-state NMR is a very useful analytical tool widely applied to probe temperature-dependant motion in solids. The change of structure with temperature is closely related to metal-insulator transitions in one-dimensional solids and for this reason VT studies of these materials may be useful in understanding their charge transport behaviour. To this end VT ^{87}Rb NMR experiments were conducted on the most insulating (n = 3.0) and the most conducting (n = 4.0) composite materials. The ^{87}Rb resonances which are assigned to channel Rb ions in n = 3.0 and n = 4.0 samples shifts to high frequency as the temperature is lowered (Figure 4.17). A similar temperature response is also observed for the smaller ^{87}Rb resonance near 65 ppm at room temperature of n = 4.0 sample (Figure 4.18). Interestingly, an analogous temperature-dependent shift was not observed for the channel Na ions in the ^{23}Na NMR spectra in Na/Ta system,[81] though the minor ^{23}Na resonance of Na ions closely associated with fulleride species did exhibit similar high frequency shifts with decreasing temperature. The broad powder pattern

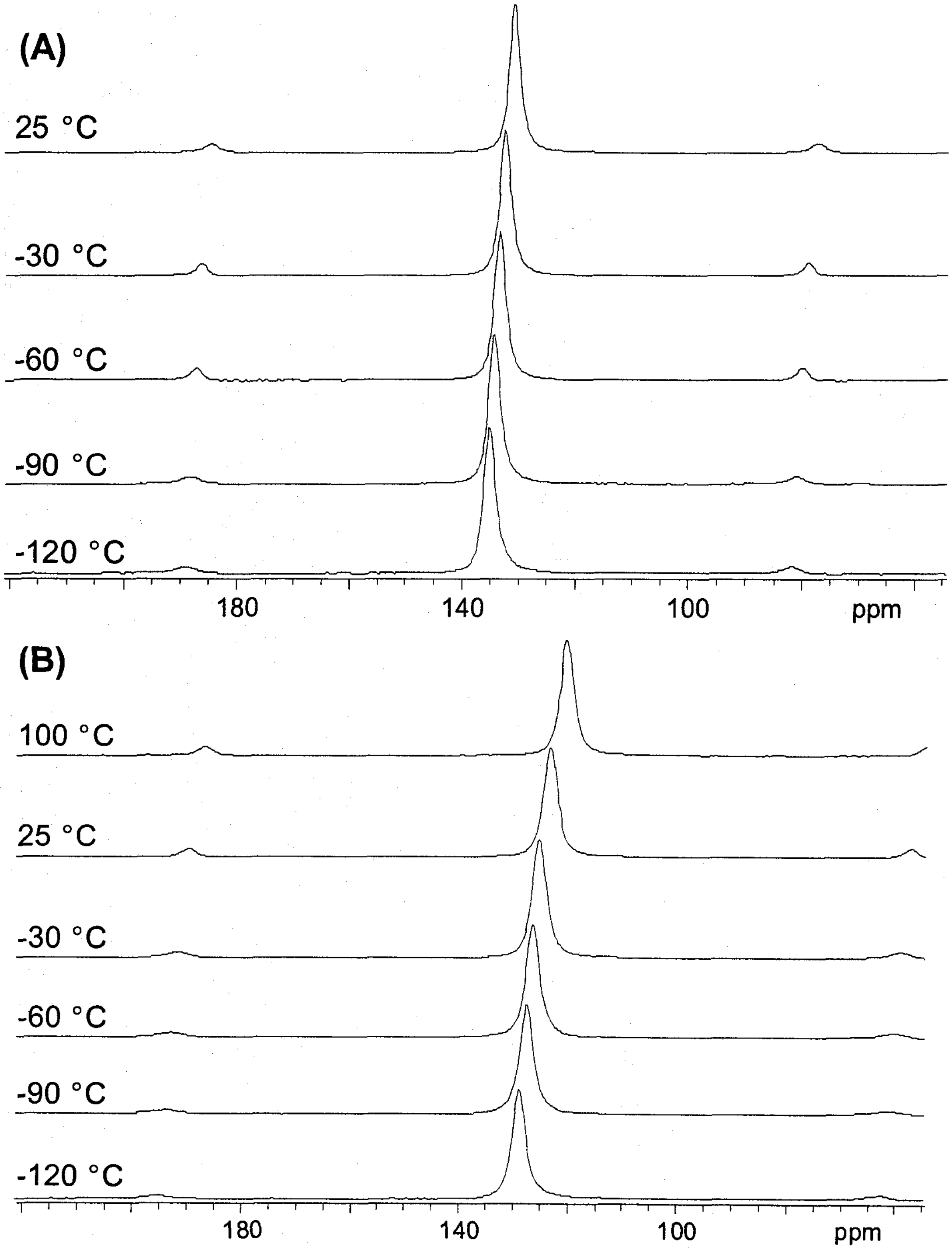

Figure 4.17. Variable-temperature ^{87}Rb MAS NMR spectra showing the expansion of isotropic regions for (A) n = 3.0 and (B) n = 4.0 composites.

centred at -60 ppm at +100 °C (Figure 4.18) shifts in the low frequency direction to -185

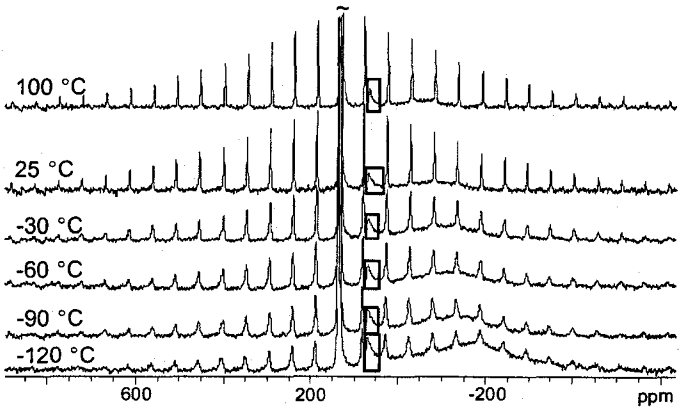

Figure 4. 18. Variable-temperature ^{87}Rb MAS NMR spectra of the entire spinning sideband manifold for the n = 4.0 composite sample.

ppm at -120 °C. It is known that at lower temperatures in solids the thermal motions in the solid are decreased, leading to a reduction in the motional averaging.[102,103] As a result, increases in the values of C_Q are typically observed with decreasing temperature, which results in a "quadrupolar induced shift" of the centre of gravity of the pattern in the low frequency direction. Rb sites associated with fulleride species which are extremely restricted in motion will be subject to such an effect, and should experience an increase in C_Q with decreasing temperature. It is also possible that a small temperature dependent chemical shift, perhaps opposite to that observed for the Rb species discussed above, may also contribute to the observed spectra. Such behaviour has been observed in ^{87}Rb NMR spectra of a variety of inorganic rubidium salts.[103] From these data it is not possible to determine whether the shifts in the resonances are related to 1D structural changes, or changes in paramagnetism arising from varying amounts of electrons in the conduction band of a metallic phase, as may be expected given the dramatic differences in conductivity between the n = 3.0 and n = 4.0 materials.

4.4 Conclusions

Mesoporous Ti, V-doped Nb and Ta oxides loaded with a series of guest molecules have been successfully characterized at the molecular level by multinuclear solid-state NMR spectroscopy. First, solid-state ^{1}H-^{15}N CP/MAS NMR and $^{15}N\{^{1}H\}$ MAS NMR experiments are used to demonstrate that NH_3 and NH_4^+ species, and not N_2 or nitride species as previously believed, were formed at the surface of the mesoporous Ti oxide/bis(toluene)Ti composites. Second, solid-state ^{2}H NMR spectroscopy confirms the coexistence of neutral bis(benzene)Cr(0) and cationic bis(benzene)Cr(I) organometallic complexes in the pores of a mesoporous V-doped Nb oxide host. While the Cr(0) is oxidized to Cr(I), the metal ions in the walls of the mesostructure are reduced at the same time. The amount of bis(benzene)Cr(I) cations produced depends on the loading level of the neutral species. The dynamic motions of both complexes are also examined with VT ^{2}H NMR spectroscopy and simulations of these spectra. It was found that the organometallic species are not isotropically tumbling, rather, a six-fold reorientation of the benzene ring about the molecular axis is observed. Third, loading of guest molecules such as Li-, Na- and Rb-naphthalenides result in reducing the metal ions in the wall of mesoporous Ti and Ta oxides. There are two main types of ions within the pores, designated as "channel" and "framework" ions. The former have high mobility while the latter are constrained within the mesoporous framework. Finally, both Rb-naphthalenide and rubidium fullerides can reduce the Ta in the wall of the mesoporous Ta oxide host. When Rb_3C_{60} is loaded into the mesoporous Ta oxide, most of the C_{60}^{3-} ions are oxidized to C_{60}, and rubidium cations are deposited in the channels and incorporated into the walls.

However, further addition of Rb-naphthalenide does not reduce the Ta in the wall of the mesostructure, rather, leading to the regeneration of some amount of rubidium fullerides, as evidenced by solid-state static ^{87}Rb and ^{87}Rb MAS NMR as well as ^{13}C{^{1}H} MAS and ^{1}H-^{13}C VACP/MAS NMR spectra.

Bibliography

[1] Rouquerol, J. et al. *Pure Appl. Chem.* **1994**, *66*, 1739.

[2] Kresge, C.T., Leonowicz, M.E., Roth, W.J., Vartuli, J.C., Beck, J.S. *Nature* **1992**, *359*, 710.

[3] Beck, J.S. et al. *J. Am. Chem. Soc.* **1992**, *114*, 10834.

[4] Selvam, P., Bhatia, S.K., Sonwane, C.G. *Ind. Eng. Chem. Res.* **2001**, *40*, 3237.

[5] Vartuli, J.C. et al. *Zeolites and Related Microporous Materials: State of Art*; Elsevier: Amsterdam, 1994.

[6] Antonelli, D.M., Nakahira, A., Ying, J.Y. *Inorg. Chem.* **1996**, *35*, 3126.

[7] Antonelli, D.M., Ying, J.Y. *Angew. Chem.-Int. Edit. Engl.* **1996**, *35*, 426.

[8] He, X., Antonelli, D. *Angew. Chem.-Int. Edit.* **2001**, *41*, 214.

[9] Vettraino, M., Trudeau, M., Lo, A.Y.H., Schurko, R.W., Antonelli, D. *J. Am. Chem. Soc.* **2002**, *124*, 9567.

[10] He, X., Lo, A.Y.H., Trudeau, M., Schurko, R.W., Antonelli, D. *Inorg. Chem.* **2003**, *42*, 335.

[11] Lo, A.Y.H., Schurko, R.W., Vettraino, M., Skadtchenko, B.O., Trudeau, M., Antonelli, D.M. *Inorg. Chem.* **2006**, *45*, 1828.

[12] Skadtchenko, B.O., Trudeau, M., Schurko, R.W., Lo, A.Y.H., Antonelli, D.M. *Chem. Mater.* **2005**, *17*, 1467.

[13] Hayashi, S., Hayamizu, K. *Bull. Chem. Soc. Jpn.* **1991**, *64*, 688.

[14] Witanowski, M., Stefaniak, L., Webb, G.A. *Annual Reports on NMR*

Spectroscopy **1993**, *25*, 1.

[15] Chandrakumar, N. *Spin-1 NMR*; Springer-Verlag: New York, 1996.

[16] Eichele, K., Wasylishen, R.E., v. 1.17.30, Tübingen, 2001.

[17] Greenfield, M.S., Ronemus, A.D., Vold, R.L., Vold, R.R., Ellis, P.D., Raidy, T.E. *J. Magn. Reson.* **1987**, *72*, 89.

[18] Jager, C., Mullerwarmuth, W., Mundus, C., Vanwullen, L. *J. Non-Cryst. Solids* **1992**, *149*, 209.

[19] Vettraino, M., He, X., Trudeau, M., Drake, J.E., Antonelli, D.M. *Adv. Funct. Mater.* **2002**, *12*, 174.

[20] Lezau, A., Skadtchenko, B., Trudeau, M., Antonelli, D. *Dalton Trans.* **2003**, 4115.

[21] Laplaza, C.E., Cummins, C.C. *Science* **1995**, *268*, 861.

[22] Niewa, R., DiSalvo, F.J. *Chem. Mater.* **1998**, *10*, 2733.

[23] MacKenzie, K.J.D., Meinhold, R.H., McGavin, D.G., Ripmeester, J.A., Moudrakovski, I. *Solid State Nucl. Magn. Reson.* **1995**, *4*, 193.

[24] Hu, S., Apple, T.M. *J. Catal.* **1996**, *158*, 199.

[25] Stepanov, A.G., Shubin, A.A., Luzgin, M.V., Shegai, T.O., Jobic, H. *J. Phys. Chem. B* **2003**, *107*, 7095.

[26] Kolokolov, D.I., Arzumanov, S.S., Stepanov, A.G., Jobic, H. *J. Phys. Chem. C* **2007**, *111*, 4393.

[27] Masierak, W., Emmler, T., Gedat, E., Schreiber, A., Findenegg, G.H., Buntkowsky, G. *J. Phys. Chem. B* **2004**, *108*, 18890.

[28] Villanueva-Garibay, J.A., Mueller, K. *Phys. Chem. Chem. Phys.* **2006**, *8*, 1394.

[29] He, X., Trudeau, M., Antonelli, D. *Adv. Mater.* **2000**, *12*, 1036.

[30] Murray, S., Trudeau, M., Antonelli, D.M. *Inorg. Chem.* **2000**, *39*, 5901.

[31] Murray, S., Trudeau, M., Antonelli, D.M. *Adv. Mater.* **2000**, *12*, 1339.

[32] He, X., Trudeau, M., Antonelli, D. *Chem. Mater.* **2001**, *13*, 4808.

[33] He, X., Trudeau, M., Antonelli, D. *Inorg. Chem.* **2001**, *40*, 6463.

[34] Vettraino, M., He, X., Trudeau, M., Antonelli, D.M. *J. Mater. Chem.* **2001**, *11*, 1755.

[35] Pyykko, P. *Mol. Phys.* **2001**, *99*, 1617.

[36] Duer, M.J. In *Annual Reports on NMR Spectroscopy*; Academic Press, 2001; Vol. 43, pp 1-58.

[37] O'Hare, D., Heyes, S.J., Barlow, S., Mason, S. *J. Chem. Soc., Dalton Trans.* **1996**, 2989.

[38] Blumel, J., Herker, M., Hiller, W., Kohler, F.H. *Organometallics* **1996**, *15*, 3474.

[39] Heise, H., Kohler, F.H., Xie, X.L. *J. Magn. Reson.* **2001**, *150*, 198.

[40] Penner, G.H., Chang, Y.C.P., Grandin, H.M. *Can. J. Chem.* **1999**, *77*, 1813.

[41] Overweg, A.R., Koller, H., de Haan, J.W., van de Ven, L.J.M., van der Kraan, A.M., van Santen, R.A. *J. Phys. Chem. B* **1999**, *103*, 4298.

[42] Gedat, E. et al. *J. Phys. Chem. B* **2002**, *106*, 1977.

[43] Xiong, J.C., Maciel, G.E. *J. Phys. Chem. B* **1999**, *103*, 5543.

[44] O'Brien, S., Tudor, J., O'Hare, D. *J. Mater. Chem.* **1999**, *9*, 1819.

[45] Ok, J.H., Vold, R.R., Vold, R.L., Etter, M.C. *J. Phys. Chem.* **1989**, *93*, 7618.

[46] Aliev, A.E., Harris, K.D.M., Guillaume, F. *J. Phys. Chem.* **1995**, *99*, 1156.

[47] Mantsch, H.H., Saito, H., Smith, I.C.P. *Prog. Nucl. Magn. Reson. Spectrosc.* **1977**, *11*, 211.

[48] Howard, J., Robson, K., Waddington, T.C. *J. Chem. Soc.-Dalton Trans.* **1982**, 977.

[49] Campbell, A.J., Fyfe, C.A., Haroldsmith, D., Jeffrey, K.R. *Molecular Crystals and Liquid Crystals* **1976**, *36*, 1.

[50] Miller, J.M., Dunn, B. *Langmuir* **1999**, *15*, 799.

[51] Rolison, D.R., Dunn, B. *J. Mater. Chem.* **2001**, *11*, 963.

[52] Vettraino, M., Trudeau, M.L., Antonelli, D.M. *Adv. Mater.* **2000**, *12*, 337.

[53] Vettraino, M., Trudeau, M., Antonelli, D.M. *Inorg. Chem.* **2001**, *40*, 2088.

[54] Skadtchenko, B.O. et al. *Angew. Chem.* **2007**, *119*, 2689

[55] Yoshitake, H., Sugihara, T., Tatsumi, T. *Chem. Mater.* **2002**, *14*, 1023.

[56] Simonutti, R., Comotti, A., Bracco, S., Sozzani, P. *Chem. Mater.* **2001**, *13*, 771.

[57] Grey, C.P., Poshni, F.I., Gualtieri, A.F., Norby, P., Hanson, J.C., Corbin, D.R. *J. Am. Chem. Soc.* **1997**, *119*, 1981.

[58] Lim, K.H., Grey, C.P. *J. Am. Chem. Soc.* **2000**, *122*, 9768.

[59] Engelhardt, G., Sieger, P., Felsche, J. *Anal. Chim. Acta* **1993**, *283*, 967.

[60] Feuerstein, M., Hunger, M., Engelhardt, G., Amoureux, J.P. *Solid State Nucl. Magn. Reson.* **1996**, *7*, 95.

[61] Skadtchenko, B., Trudeau, M., Schurko, R.W., Willans, M.J., Antonelli, D.M. *Adv. Funct. Mater.* **2003**, *13*, 671.

[62] Skadtchenko, B.O., Trudeau, M., Kwon, C.W., Dunn, B., Antonelli, D. *Chem. Mater.* **2004**, *16*, 2886.

[63] Kloetstra, K.R., vanLaren, M., vanBekkum, H. *J. Chem. Soc., Faraday Trans.* **1997**, *93*, 1211.

[64] Du, H.B., Terskikh, V.V., Ratcliffe, C.I., Ripmeester, J.A. *J. Am. Chem. Soc.* **2002**, *124*, 4216.

[65] Mason, J. *Multinuclear NMR*; Plenum Press: New York, 1987.

[66] Taulelle, F., Bessada, C., Massiot, D. *J. Chim. Phys.-Chim. Biol.* **1992**, *89*, 379.

[67] Engelhardt, G., Hunger, M., Koller, H., Weitkamp, J. *Stud. Surf. Sci. Catal.* **1994**, *84*, 421.

[68] Abragam, A. *Principles of Nuclear Magnetism*; Oxford University Press: Ely House, London W.1, 1961.

[69] Igarashi, M., Okubo, N., Hashimoto, S., Yoshizaki, R., Cha, D.J. *Z. Naturfors. Sect. A-J. Phys. Sci.* **1996**, *51*, 657.

[70] Igarashi, M., Okubo, N., Yoshizaki, R. *Z. Naturfors. Sect. A-J. Phys. Sci.* **1998**, *53*, 442.

[71] Norberg, R.E., Slichter, C.P. *Phys. Rev.* **1951**, *83*, 1074.

[72] Holcomb, D.F., Norberg, R.E. *Phys. Rev.* **1955**, *98*, 1074.

[73] Wagemaker, M., van de Krol, R., Kentgens, A.P.M., van Well, A.A., Mulder, F.M. *J. Am. Chem. Soc.* **2001**, *123*, 11454.

[74] Haddon, R.C. et al. *Nature* **1991**, *350*, 320.

[75] Hebard, A.F. In *China Center for Advanced Science and Technology (World*

Laboratory) Symposium/Workshop Proceedings, 1995; Vol. 11, pp. 339-354.

[76] Holczer, K., Klein, O., Huang, S.M., Kaner, R.B., Fu, K.J., Whetten, R.L., Diederich, F. *Science* **1991**, *252*, 1154.

[77] Tanigaki, K., Ebbesen, T.W., Saito, S., Mizuki, J., Tsai, J.S., Kubo, Y., Kuroshima, S. *Nature* **1991**, *352*, 222.

[78] Mott, N.F. *Metal-Insulator Transitions. 2nd Ed*; Maruzen Co., Ltd.: Tokyo, 1996.

[79] Ye, B., Trudeau, M., Antonelli, D. *Chem. Mater.* **2001**, *13*, 2730.

[80] Harris, R.K., Becker, E.D., Cabral De Menezes, S.M., Goodfellow, R., Granger, P. *Pure Appl. Chem.* **2001**, *73*, 1795.

[81] Skadtchenko, B.O., Trudeau, M., Schurko, R.W., Willans, M.J., Antonelli, D. *Adv. Funct. Mater.* **2003**, *13*, 671.

[82] Pennington, C.H., Stenger, V.A. *Rev. Mod. Phys.* **1996**, *68*, 855.

[83] Rosseinsky, M.J. *Chem. Mater.* **1998**, *10*, 2665.

[84] Cheng, J.T., Ellis, P.D. *J. Phys. Chem.* **1989**, *93*, 2549.

[85] de Dios, A.C., Walling, A., Cameron, I., Ratcliffe, C.I., Ripmeester, J.A. *J. Phys. Chem. A* **2000**, *104*, 908.

[86] Terskikh, V.V., Lapina, O.B., Bondareva, V.M. *Phys. Chem. Chem. Phys.* **2000**, *2*, 2441.

[87] Ciraolo, M.F., Hanson, J.C., Grey, C.P. *Microporous Mesoporous Mat.* **2001**, *49*, 111.

[88] Igarashi, M., Kodaira, T., Ikeda, T., Itoh, M., Shimizu, T., Goto, A., Nozue, Y. *Physica B* **2003**, *327*, 72.

[89] Murphy, D.W. et al. *J. Phys. Chem. Solids* **1992**, *53*, 1321.

[90] Tycko, R., Dabbagh, G., Rosseinsky, M.J., Murphy, D.W., Ramirez, A.P., Fleming, R.M. *Phys. Rev. Lett.* **1992**, *68*, 1912.

[91] Tycko, R. *J. Phys. Chem. Solids* **1993**, *54*, 1713.

[92] Walstedt, R.E., Murphy, D.W., Rosseinsky, M. *Nature* **1993**, *362*, 611.

[93] Buffinger, D.R., Ziebarth, R.P., Stenger, V.A., Recchia, C., Pennington, C.H. *J. Am. Chem. Soc.* **1993**, *115*, 9267.

[94] Pennington, C.H. et al. *Phys. Rev. B* **1996**, *54*, R6853.

[95] Zimmer, G., Thier, K.F., Mehring, M., Rachdi, F., Fischer, J.E. *Phys. Rev. B* **1996**, *53*, 5620.

[96] Zimmer, G., Mehring, M., Rachdi, F., Fischer, J.E. *Phys. Rev. B* **1996**, *54*, R3768.

[97] Gorny, K., Hahm, C., Martindale, J.A., Yu, S., Pennington, C.H., Buffinger, D.R., Ziebarth, R.P. *Phys. Rev. Lett.* **1997**, *79*, 5118.

[98] Stenger, V.A., Recchia, C., Vance, J., Pennington, C.H., Buffinger, D.R., Ziebarth, R.P. *Phys. Rev. B* **1993**, *48*, 9942.

[99] Liu, S.F., Schmidt-Rohr, K. *Macromolecules* **2001**, *34*, 8416.

[100] Gunther, H. *NMR Spectroscopy*; John Wiley & Sons: New York, 1980.

[101] Bak, M., Rasmussen, J.T., Nielsen, N.C. *J. Magn. Reson.* **2000**, *147*, 296.

[102] Das, T.P., Hahn, E.L. *Nuclear Quadrupole Resonance Spectroscopy*; Academic Press, Inc.: New York, 1958.

[103] Lucken, E.A.C. *Nuclear Quadrupole Coupling Constants*; Academic Press: New York, 1969.

Chapter 5

Multinuclear Solid-State NMR Spectroscopy of Doped Lanthanum Fluoride Nanoparticles

5.1 Introduction

Lanthanide(III)–doped nanoparticles (NPs) with inorganic cores and outer organic stabilizing ligands are of great interest due to their unique luminescent properties which have made them important in the manufacture of light–emitting diodes (LEDs),[1] liquid–crystal displays,[2] biological assays,[3] nanometre–scale optoelectronic devices,[4] and light sources in zero–threshold lasers.[5] NPs doped with different Ln^{3+} ions produce spectral emissions across the visible light (Eu^{3+} and Tb^{3+}) and near–infrared (NIR; Pr^{3+}, Nd^{3+}, Er^{3+} and Yb^{3+}) regions. NIR–emitting NPs are of particular interest because they are the luminescent elements in polymer–based telecommunication components, lasers, displays and polymer LEDs. Luminescence in Ln^{3+} ions arises from radiative relaxation after the parity–forbidden transitions within the partially filled 4*f* orbitals that are shielded by the filled 5*s* and 5*p* orbitals. Consequently, *f*–*f* transitions lead to low molar absorption coefficients and slow emission rates, resulting in long luminescent lifetimes.[6]

Polymeric materials are advantageous in the fabrication of optical components because they are easy to process by spin–coating and photolithography.[7] However, direct doping of the Ln^{3+} ions into polymeric materials is not practical because the largely spaced vibrational and/or electronic transitions present in polymers can often quench *f*–*f* transitions associated with the luminescent process. Initially, organic complexes as luminescent materials were studied, but lifetimes of NIR emitters are very short with low (<1%) quantum yields. A more promising strategy is to dope the luminescent Ln^{3+} ion into an inorganic matrix (low phonon matrices) and coat the surface with ligands to fine tune the processability through dispersion in organic solvents, since the latter have long luminescence lifetimes and high quantum efficiencies.[8-11] Thus, small amounts of the Ln^{3+} ions are doped into an inorganic framework to minimize the quenching process. In a recent publication, van Veggel et al. have shown that polymer-based optical amplifiers operating at 1.33 μm are possible based on Nd^{3+}-doped LaF_3 NPs.[12] A number of suitable inorganic frameworks such as $LaPO_4$,[13-15] LaF_3,[16,17] Y_2O_3,[18] YBO_3,[19] YVO_4,[20] etc., can be found in the literature. LaF_3 is of interest because it has low vibrational energies; hence, quenching of the luminescence from excited states of Ln^{3+} ions is minimized. A procedure for synthesizing LaF_3 NPs was originally reported by Dang et al.,[21] and then modified and optimized to yield luminescent, Ln^{3+}–doped NPs.[16]

In order to incorporate the Ln^{3+}–doped inorganic NPs into the organic polymer matrix, it is necessary to increase their solubility. This is accomplished by coating the NPs with surfactants or so–called "stabilizing ligands". These ligands are typically composed of a polar inorganic "head" which coordinates to the NP surface, and a nonpolar alkyl hydrocarbon "tail". In particular, ammonium di–*n*–octadectyldithiophosphate, $[NH_4][S_2P(OC_{18}H_{37})_2]$, was originally used to stabilize the Ln^{3+}–doped LaF_3 NPs in the organic matrix; however, other ligands have also been synthesized and attached to the NPs to improve solubility for different organic environments.[22] The ligands are used to (i) prevent aggregation of NPs, (ii) control the growth/size of the particles, and (iii) ensure the NPs are homogeneously distributed within the polymer matrix.

Ln^{3+}–doped LaF_3 NPs have been characterized by a number of techniques. Transmission electron microscopy (TEM) and powder X–ray diffraction (XRD) were used to determine the size and crystallinity, respectively, of the NPs. X–ray fluorescence (XRF) and elemental analysis are also routinely applied for analysis of composition. Emission/excitation and luminescence spectroscopies have been utilized to observe luminescent properties of particles with different Ln dopants.[16,17,22,23] Solution ^{1}H NMR spectroscopy has been applied for characterization of the di–*n*–octadectyldithiophosphate stabilizing ligand of the LaF_3 NPs.[17,22,23] To the best of our knowledge, there have not been any solid–state NMR experiments performed on this class of NPs. To date, statements about the molecular structure have been made only by inference, and no direct information on the ligand-NP surface interactions has been obtained.[16,17,22] Solid-state NMR spectroscopy is the ideal technique for characterization of such structural features.

In this work, we present a comprehensive multinuclear solid–state NMR characterization of pure and doped (Yb^{3+}, Y^{3+} and Sc^{3+}) LaF_3 NPs which are coordinated with di-*n*-octadectyldithiophosphate stabilizing ligands (Chart 5.1). To examine the structural order and crystallinity of the inorganic cores of the NPs, as well as the effects of doping with rare earth and lanthanide ions, solid–state ^{139}La and ^{19}F NMR experiments were conducted on bulk crystalline LaF_3, pristine LaF_3 NPs and doped LaF_3 NPs. Solid–state ^{89}Y and ^{45}Sc NMR experiments were used to attempt identification of

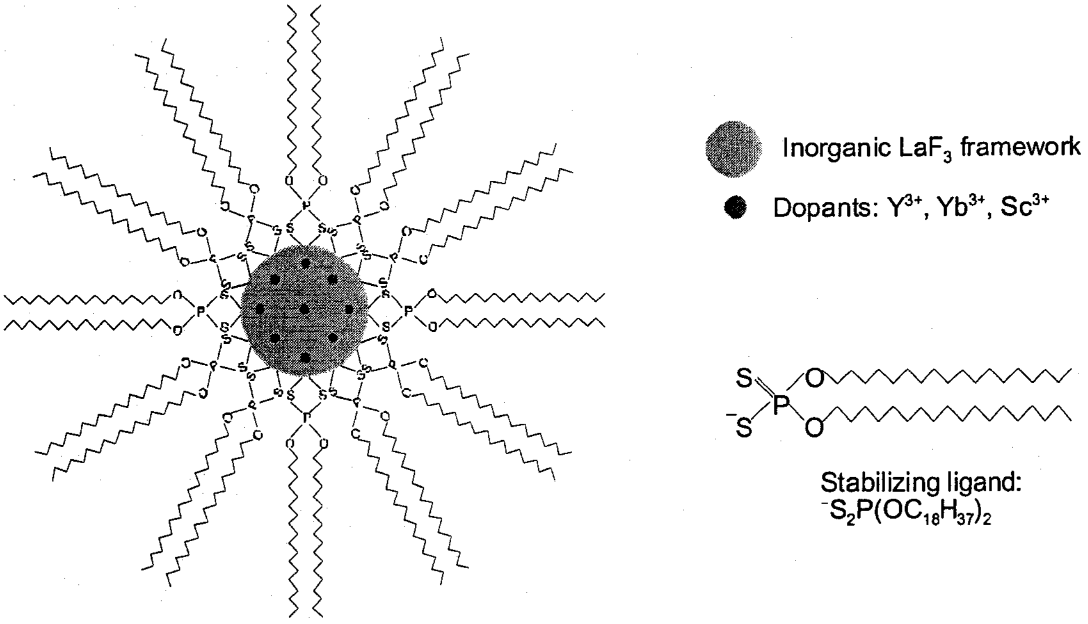

Chart 5.1. Schematic picture of a Ln^{3+}-doped LaF_3 nanoparticle stabilized by di-*n*-octadecyldithiophosphate ($^{-}S_2P(OC_{18}H_{37})_2$) ligands (Ln = Yb, Y, and Sc).

yttrium/scandium sites upon doping with Y^{3+}/Sc^{3+}. Solid–state ^1H and ^{31}P NMR experiments were carried out on selected samples to examine the nature of the stabilizing ligands and their interactions with the inorganic cores. Solid–state NMR spectroscopy is applied to investigate a number of facets of NP core and surface structure, as well as their interface, including the following: (i) the degree of disorder in the NP core, (ii) existence of Ln doping either in interstitial sites of the LaF_3 matrix or at crystallographic lanthanum sites, (iii) structural changes in the inorganic core resulting from doping, (iv) chemical changes in the stabilizing ligands over time, and (v) nature of the interactions between the stabilizing ligands and inorganic cores.

5.2 Experimental

Sample preparation and handling. Crystalline, anhydrous LaF_3, YF_3, and ScF_3

were purchased from Strem and used without further purification, with the exception of YF_3 which was dried under a vacuum at ca. 120 °C for over 8 h. Pure LaF_3 NPs and those doped with Yb^{3+}, Y^{3+}, and Sc^{3+} were synthesized according to literature procedures.[16,17] All samples were packed into zirconia rotors for NMR experiments.

Solid–state NMR. Most solid-state NMR experiments were conducted on a Varian Infinity Plus NMR spectrometer with a 9.4 T wide–bore Oxford magnet, operating at $\nu_0(^{139}La) = 56.46$ MHz, $\nu_0(^{45}Sc) = 97.10$ MHz, $\nu_0(^{19}F) = 376.06$ MHz, $\nu_0(^{89}Y) = 19.59$ MHz, $\nu_0(^{1}H) = 399.73$ MHz, and $\nu_0(^{31}P) = 161.81$ MHz. Typical ^1H and ^{19}F decoupling with rf fields ranging from 60 to 123 kHz were applied where appropriate. Varian/Chemagnetics 2.5 mm HX, 4 mm HX, and 5 mm HXY magic–angle spinning (MAS) probes were utilized for all experiments. Tuning and matching for low–frequency (i.e., 19.59 MHz) experiments were accomplished with a Varian/Chemagnetics low–gamma tuning box. Hahn–echo pulse sequences of the form $[(\pi/2)_x–\tau_1–(\pi)_y–\tau_2–\text{acquire}]$ (where τ_1 and τ_2 are the interpulse delays) were applied in most of the solid–state NMR experiments, since standard Bloch–decay acquisitions of broad NMR spectra resulted in the loss of points at the beginning of the FID, giving rise to spectral artifacts and baseline distortions. Additional solid–state ^{45}Sc MAS NMR experiments were conducted on a 900 MHz Bruker AVANCE–II NMR spectrometer, operating at $\nu_0(^{45}Sc) = 218.68$ MHz. Further details concerning experimental parameters can be found elsewhere.[24]

Lanthanum chemical shifts were referenced to a 1.0 M aqueous $LaCl_3$ solution ($\delta_{iso}(^{139}La) = 0.0$ ppm). The central–transition (CT) selective $\pi/2$ pulse widths (i.e., real

$\pi/2$ pulse scaled by $(I + ½)^{-1}$) ranged from 0.76 μs to 1.1 μs (rf fields ranged from 60 to 80 kHz). For rotor-synchronized MAS NMR experiments, a Rotor–Assisted Population Transfer (RAPT) pulse scheme[25] was applied prior to the Hahn–echo sequence for signal enhancement. For both MAS and static NMR experiments, calibrated recycle delays were 1.0 s or less, and between 30000 and 330000 transients were acquired.

Fluorine chemical shifts were referenced to neat $CFCl_3$ liquid ($\delta_{iso}(^{19}F) = 0.0$ ppm). For all MAS experiments, $\pi/2$ pulse widths were ca. 2.0 μs. Calibrated recycle delays ranged from 8 to 300 s, and between 384 and 7624 transients were collected. Proton chemical shifts were referenced to TMS ($\delta_{iso}(^{1}H) = 0.0$ ppm) by using solid adamantane as a secondary reference, setting the ^{1}H NMR resonance to 1.85 ppm. $\pi/2$ pulse widths between 2.0 μs and 4.1 μs were applied to all ^{1}H Bloch–decay MAS NMR experiments. Recycle delays were from 1 to 4 s and four transients were collected for each experiment. Phosphorous chemical shifts were referenced to an 85% H_3PO_4 solution ($\delta_{iso}(^{31}P) = 0.0$ ppm). Solid-state $^{31}P\{^{1}H\}$ MAS NMR experiments involved $\pi/2$ pulse widths of 4.7 μs ($\nu_1(^{31}P) = 25$ kHz), optimized recycle delays between 5 and 40 s, and the acquisition of 528 to 4288 transients. ^{1}H–^{31}P and ^{19}F–^{31}P variable-amplitude cross-polarization MAS (VACP/MAS) NMR experiments involved rf powers of 90 to 123 kHz in the Hartmann–Hahn match for both $^{1}H/^{19}F$ and ^{31}P channels. Contact times varied from 2 to 12 ms, and the longest recycle delay of 60 s was utilized. Yttrium chemical shifts were referenced to a 1.0 M YCl_3 aqueous solution ($\delta_{iso}(^{89}Y) = 0.0$ ppm) by setting the NMR resonance in solid $Y(NO_3)_3•6H_2O$ (as a secondary reference) to –53.0 ppm.[26]

Bloch–decay ^{89}Y{^{19}F} MAS NMR experiments involved a $\pi/2$ pulse of 20.0 μs ($\nu_1(^{89}\text{Y})$ = 11.1 kHz), a 300 s recycle delay, and an acquisition of 500 scans. ^{19}F–^{89}Y VACP/MAS NMR experiments utilized a pulse width of 2.8 μs, a Hartmann–Hahn matching rf field of 13 to 18 kHz, 30 to 60 s calibrated recycle delays, 30 to 40 ms contact times, and involved the collection of 880 to 1452 transients. Scandium chemical shifts were referenced to a 0.11 M $ScCl_3$ solution in 0.05 M HCl ($\delta_{\text{iso}}(^{45}\text{Sc})$ = 0.0 ppm).[27,28] In ^{45}Sc MAS NMR experiments, 0.43 μs $\pi/2$ pulses and 5 s recycle delays were utilized, and 9031 scans were collected.

Room–temperature ^{139}La longitudinal (T_1) and transverse (T_2) relaxation measurements were conducted on bulk LaF_3, as well as pure and Yb^{3+}–doped LaF_3 NPs. T_1 constants were determined using saturation recovery.[29] The quadrupolar Carr–Purcell Meiboom–Gill (QCPMG) pulse sequence[30] was applied to stationary samples for the measurement of T_2 time constants. Extraction of T_1 time constants was accomplished from the functions $y(\tau) = A[1 - \exp(-\tau/T_1)]$ and $y(\tau) = A_f[1 - \exp(-\tau/T_{1f})] + A_s[1 - \exp(-\tau/T_{1s})]$ for mono– and bi–exponential curve fits, respectively, while for T_2 time constants, functions such as $y(\tau) = B \exp(-\tau/T_2)$ and $y(\tau) = B_f \exp(-\tau/T_{2f}) + B_s \exp(-\tau/T_{2s})$ were utilized. The subscripts “f” and “s” in the above functions indicate the “fast” and “slow” contributions to relaxation (*vide infra*).

Spectral simulations. The EFG tensor parameters of ^{139}La static and MAS NMR spectra of bulk LaF_3 were obtained from analytical and numerical simulations using the WSOLIDS[31] and SIMPSON[32] simulation packages, respectively. The latter is installed on a Dell Precision 420 workstation with a dual 3.6 GHz Xenon Precision 670n workstation running Red Hat Linux 9.0. SIMPSON simulations were carried out by the *direct* method with powder averaging using the *zcw4180* crystal file, which is provided with the package. I_{1z} was set as the start detect operator, while I_{1p} or I_{1c} (with and without consideration of satellite transitions (STs), respectively) was set as the detect operator. The number of gamma angles was set to 63 and 18 for ν_{rot} = 16 and 28 kHz, respectively.

Powder X–ray Diffraction. Powder X–ray diffraction (XRD) experiments were conducted on samples loaded into 1.0 mm o.d. capillary tubes using a Bruker AXS D8 DISCOVER powder X-ray diffractometer, which utilizes a Cu Kα_2 (λ = 1.54056 Å) radiation source with a Bruker AXS HI-STAR area detector. Simulations of powder XRD patterns from known crystal structures[33-39] were performed using PowderCell software.[40]

5.3 Results and Discussion

This section is organized as follows: NMR characterization of bulk crystalline LaF_3 (**1**) is presented, followed by a comparison with the undoped parent LaF_3 NPs (**2**). The NMR spectra of the LaF_3 NPs doped with 5 and 10 mol % paramagnetic Yb^{3+} ions (**3** and **4**, respectively; dopant concentrations are calculated relative to the number of moles of Ln^{3+}) are compared with those of **2**. ^{139}La spin–lattice (T_1) and spin–spin (T_2) relaxation data for **1**, **2**, and **4**, as well as NMR data for LaF_3 NPs doped with diamagnetic Y^{3+} (5 and 10 mol %) and Sc^{3+} (10 mol %) ions (samples **5**, **6**, and **7**, respectively) are discussed.

Solid–state ^{89}Y and ^{45}Sc NMR spectra of bulk YF_3 (**8**) and ScF_3 (**9**) are used for comparison with diamagnetically doped samples. Finally, the stabilizing ligands, which are expected to be coordinated to the surface of NPs, are examined by ^{1}H MAS, ^{31}P{^{1}H} MAS, ^{1}H–^{31}P variable-amplitude cross-polarization MAS (VACP/MAS), and ^{19}F–^{31}P VACP/MAS NMR experiments.

Bulk crystalline lanthanum trifluoride, 1. LaF_3 has been well characterized by a number of techniques, including single–crystal X–ray[41-47] and neutron[48] diffraction, solid–state ^{19}F NMR[49-55] and ^{139}La NMR,[55,56] as well as variable–temperature ^{139}La nuclear quadrupole resonance (NQR) experiments.[57,58] Numerous structures of LaF_3 have been reported involving different space groups, cell dimensions, and atomic positions (see above references). The currently accepted structure is found in a combined X–ray and neutron–diffraction study on a single–crystal of LaF_3 by Maximov et al.[47] They reported a single lanthanum site and three distinct fluorine sites (denoted as F1, F2, and F3); however, the fluoride ions are known to undergo dynamic exchange, which may be largely responsible for the ionic conduction in LaF_3.[51-54,59] The local structure centred at the La site is depicted in Chart 5.2A. The La atom is 11-coordinate and has C_2 symmetry, with eight F1, two F2, and one F3 positions. The rotational axis lies along the lone La–F3 bond which is also parallel to the crystallographic *a*–axis (Chart 5.2A,B). The ratio of F1/F2/F3 sites in the unit cell is 6:2:1. Each of the F1 atoms is shared between four different La atoms in a tetrahedral arrangement, while each of the F2 and F3 atom is shared by three La atoms in trigonal pyramidal and trigonal planar coordination

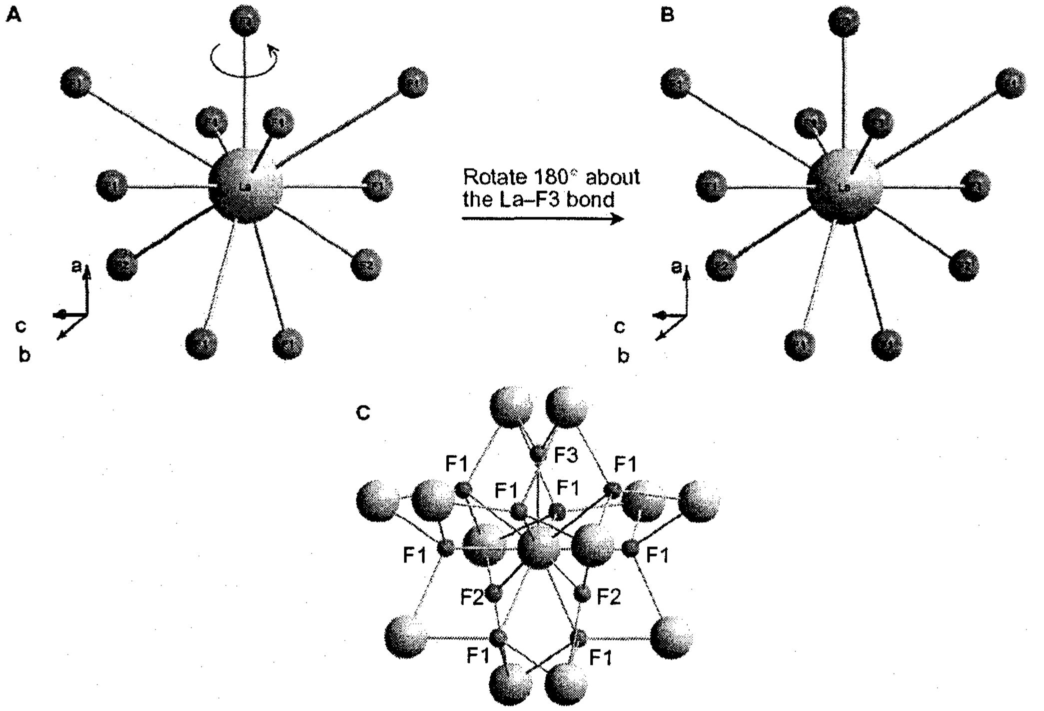

Chart 5.2. (A and B) Rotation of a LaF_{11} unit about the La-F3 Bond (parallel to a-axis of the unit cell) by 180° illustrating a local C_2 symmetry in **1** and (C) extended structure of **1**.

environments, respectively (Chart 5.2C). Our room–temperature ^{19}F MAS NMR spectrum of crystalline LaF_3 (Figure 5.1A) shows three distinct ^{19}F resonances centred at -23.5, 24.9 and 17.3 ppm, which are assigned to F1, F2, and F3, respectively (Figure 5.1A, inset). Deconvolution of the entire NMR powder pattern (i.e., including all spinning sidebands) reveals an F1/F2/F3 ratio of 13.2(2):3.6(4):2.0(4), in good agreement with the previously reported X–ray[47] and NMR[54] data.

^{139}La NMR experiments were also conducted on **1**. Lanthanum has two NMR active isotopes, ^{138}La and ^{139}La, which have spins $I = 5$ and 7/2, respectively. The latter is more favourable for NMR experimentation due to its high natural abundance (99.91%) and smaller nuclear quadrupole moment ($Q(^{139}La) = 0.20 \times 10^{-28}$ m^2 and

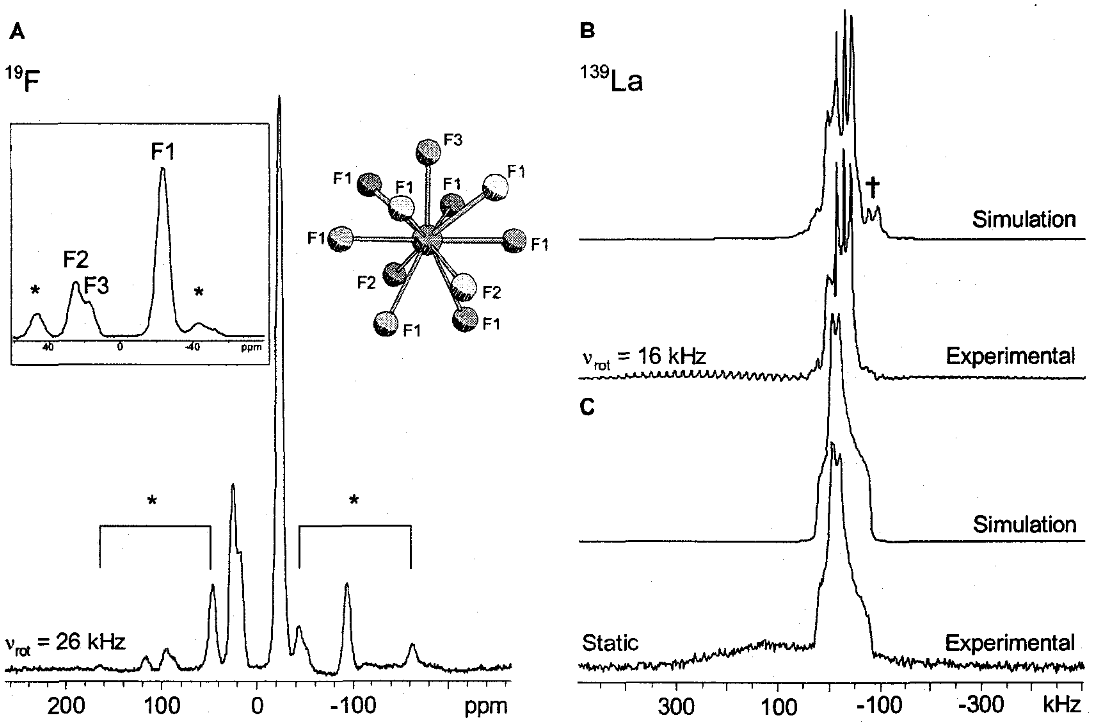

Figure 5.1. (A) ^{19}F MAS, (B) ^{139}La MAS and (C) static ^{139}La NMR spectra of **1** acquired at 9.4 T, along with the coordination environment of the La atom in a LaF_{11} unit for reference. Inset of (A): Expansion of the isotropic region, with "*" denoting the spinning sidebands. In (B), the symbol "†" in the numerical simulation indicates a spinning sideband of the central transition, and is not observed in the experimental powder pattern due to overlapping satellite transitions (see Figure B.5.2).

$Q(^{138}La) = 0.45 \times 10^{-28}$ m^2).[60] Solid–state ^{139}La NMR spectroscopy has been applied to study a variety of systems, including LaF_3 single crystals,[55] $La_{1-x}A_xMO_3$ (where A = Sr, Ca and M = Mn, Cr and Co),[61-64] $LaMn(O_{1-x}F_x)_3$,[65] as well as for studying cation exchange processes in lanthanum–containing Y zeolites.[66-69] Solid–state ^{139}La NMR experiments have also been conducted on La_2O_3,[70] lanthanum halides (LaX_3 with X = F, Cl, Br, and I),[56] and a variety of complexes,[71,72] to investigate the ^{139}La electric field gradient (EFG) tensors, as well as to test pulse sequences such as quadrupolar phase–adjusted spinning sidebands (QPASS)[73] and fast amplitude modulation (FAM) with a receptive spin-7/2 nucleus.[74]

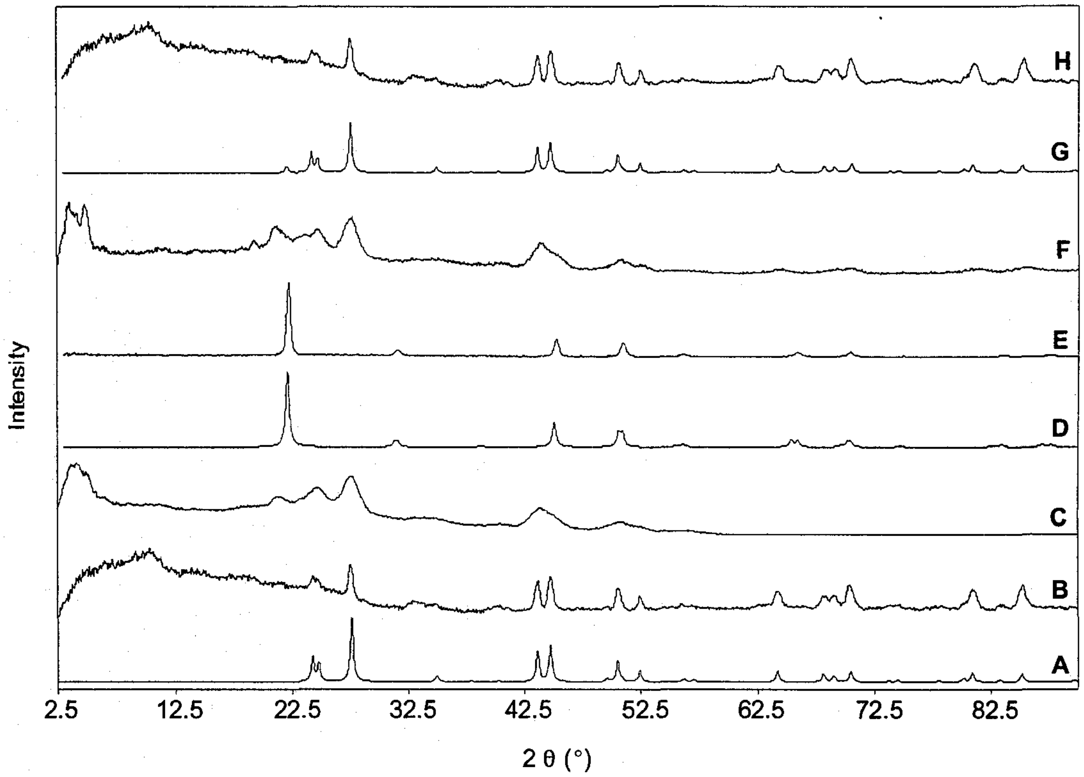

Figure 5.2. Powder X–ray diffraction patterns of (A) simulation and (B) experimental of **1**, (C) experimental of **2**, (D) simulation and (E) experimental of **9**, and (F) experimental of **7**. (G) and (H) are the calculated and experimental, respectively, powder XRD patterns composed of 90 % of **1** and 10 % of **9**.

The ^{139}La MAS NMR spectrum of **1** is presented in Figure 5.1B. The complexity of the NMR powder pattern may stem from either (i) overlapping of the central transition (CT) and satellite transitions (STs) or (ii) the presence of multiple lanthanum sites. Comparison of the powder XRD pattern of bulk LaF_3 to a simulated pattern (Figure 5.2A,B) confirms that there is a single unique La site. In addition, numerical simulation of the MAS NMR pattern utilizing a single La site, with δ_{iso} = -130 ppm, C_Q = 16.0 MHz, and η_Q = 0.81, also confirms this. The ^{139}La static NMR spectrum (Figure 5.1C) can be simulated with parameters matching that of the ^{139}La MAS NMR data discussed above (the effect of lanthanum chemical shielding anisotropy (CSA) is negligible at 9.4 T; see Figure B.5.1A,B in appendix B). The relatively weak underlying pattern results from partial excitation of the STs (Figure B.5.1C to E), since the STs are very intense near the CT for high-spin quadrupolar nuclei (e.g., 7/2 or 9/2) with η_Q close to 1. Both MAS and static NMR data provide quadrupolar and chemical shift parameters which are in excellent agreement with previously reported values.[55,56]

Pure LaF_3 NPs, 2. Pure and Eu^{3+}–doped LaF_3 NPs have previously been characterized by powder XRD experiments,[23,75] which demonstrate that the cores are crystalline. In addition, the broadening of the diffraction peaks was used to estimate the size of the NPs, which range from 8 to 10 nm. Qin and co–workers utilized powder XRD, TEM, and electron diffraction experiments to probe the structure of Yb^{3+}/Er^{3+}-doped LaF_3 NPs. XRD data revealed that the NPs are highly crystalline with a hexagonal structure (unit cell dimensions of a = 0.716 nm and c = 0.733 nm, space group $P6_322$), and TEM images showed hexagonal morphology with average edge length of ca. 15 nm.[76] The XRD pattern of pure LaF_3 NPs presented herein (Figure 5.2C) is consistent with previous data, confirming the presence of a crystalline LaF_3 phase with a distribution of environments resulting from the small NP size. The diffraction peak at $2\theta \approx 5°$ is indicative of some degree of NP organization or packing.

Solid–state ^{19}F and ^{139}La NMR spectra are shown in Figures 5.3 to 5.5. A comparison between the ^{19}F NMR spectra of **1** and **2** (Figure 5.3A,B) reveals that resonances with chemical shifts and integrated intensities corresponding to the F1 and F(2,3) fluorine sites are still observed for the NPs. There is significant broadening and a

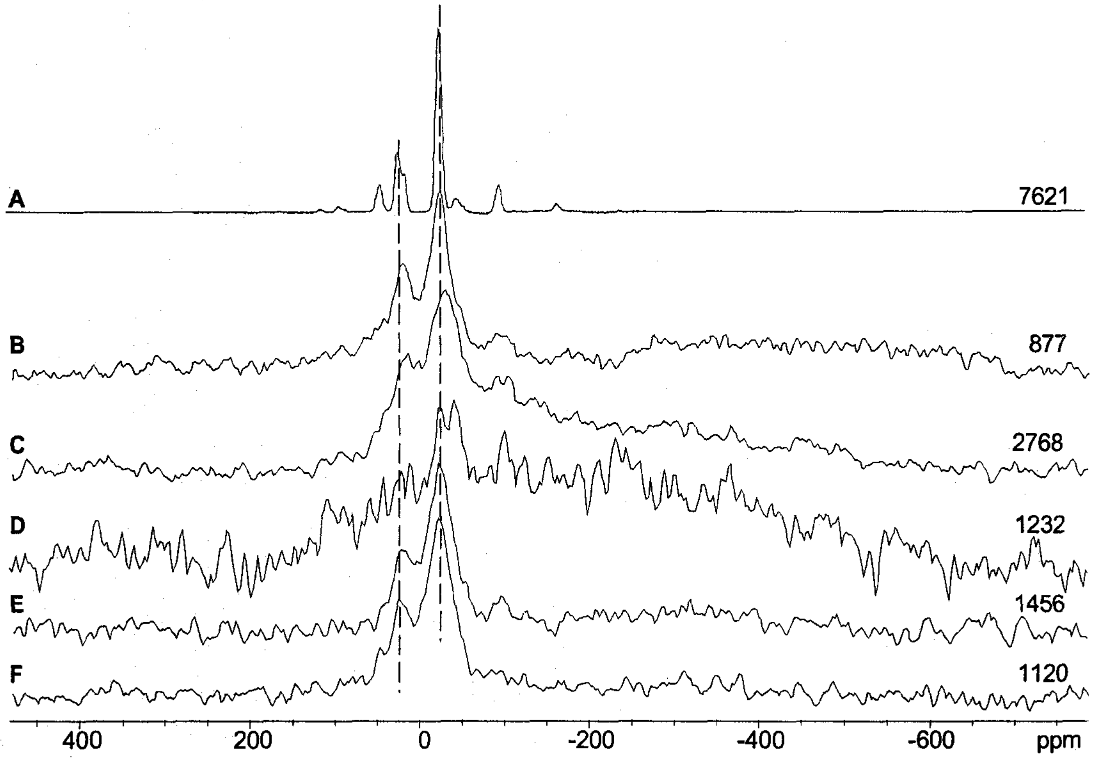

Figure 5.3. ^{19}F MAS NMR spectra of (A) **1**, (B) **2**, (C) **3**, (D) **4**, (E) **5** and (F) **6** acquired at 9.4 T. Numbers of scans for each NMR spectrum are indicated on the right. Spinning frequencies of all NMR spectra range from 26 to 27 kHz. Dashed lines indicate the positions of F1 and F(2,3) sites in **1**.

reduced signal-to-noise (S/N) ratio in the spectrum of **2**, such that the F2 and F3 resonances cannot be distinguished, and spinning sidebands are not observed. The chemical shift values corresponding to F1 and F(2,3) resonances are -23.1 and 22.0 ppm and have full widths at half height (FWHH or $\Delta\nu_{1/2}$) of 9.8 and 11.0 kHz, respectively, compared to FWHH values of F1, F2, and F3 resonances of 2.9, 2.5, and 2.5 kHz, respectively, in the spectrum of **1**. The broadening of the NMR pattern is consistent with the small NP size and long-range disorder arising from differentiation of fluorine sites in the core and near the surface (i.e., size effects), as suggested by the powder XRD data. Broadening does not arise from ^{19}F–^{19}F dipolar couplings, since the applied spinning speeds far exceeded the magnitudes of such couplings (^{19}F–^{19}F dipolar coupling constant is on the order of 5.5 kHz based on the shortest F–F distance in the crystal structure of **1**). In the spectrum of **2**, the broad, weak powder pattern observed in the low-frequency direction (ca. -200 to -650 ppm) arises from the background ^{19}F signal from the probe and sample spacers (Figure B.5.3). This background signal is observed in all ^{19}F NMR spectra of NPs since S/N is limited by the low mol % of ^{19}F nuclei (due to the stabilizing ligands) and extremely long ^{19}F longitudinal relaxation time constants (reduced number of total acquisitions).

The ^{139}La MAS NMR spectra of **1** and **2** (Figure 5.4A,B) have the same centres of gravity and similar distributions of CT spinning sidebands, and no new resonances are observed, indicating that the La sites are similar in both the bulk material and NPs. The fine detail in the spectrum of **1** which arises from the second-order quadrupolar interaction, and the sharp spinning sidebands, are not observed in that of **2** due to inhomogeneous broadening, which is again consistent with long-range disorder and small NP size. A similar observation is made for the static Hahn-echo ^{139}La NMR spectra of **1** and **2** (Figure 5.5A,B). As in the case of the ^{19}F NMR data, there are not expected to be significant contributions to line broadening from ^{139}La-^{19}F dipolar couplings in either the MAS or static spectra, since they are completely averaged by fast MAS in the former and make negligible contributions to the broad powder pattern in the latter (^{139}La-^{19}F dipolar coupling constants are calculated from known bond lengths to be on the order of 1 kHz).[56]

The combination of XRD and NMR data confirms that the local LaF_3 structure in

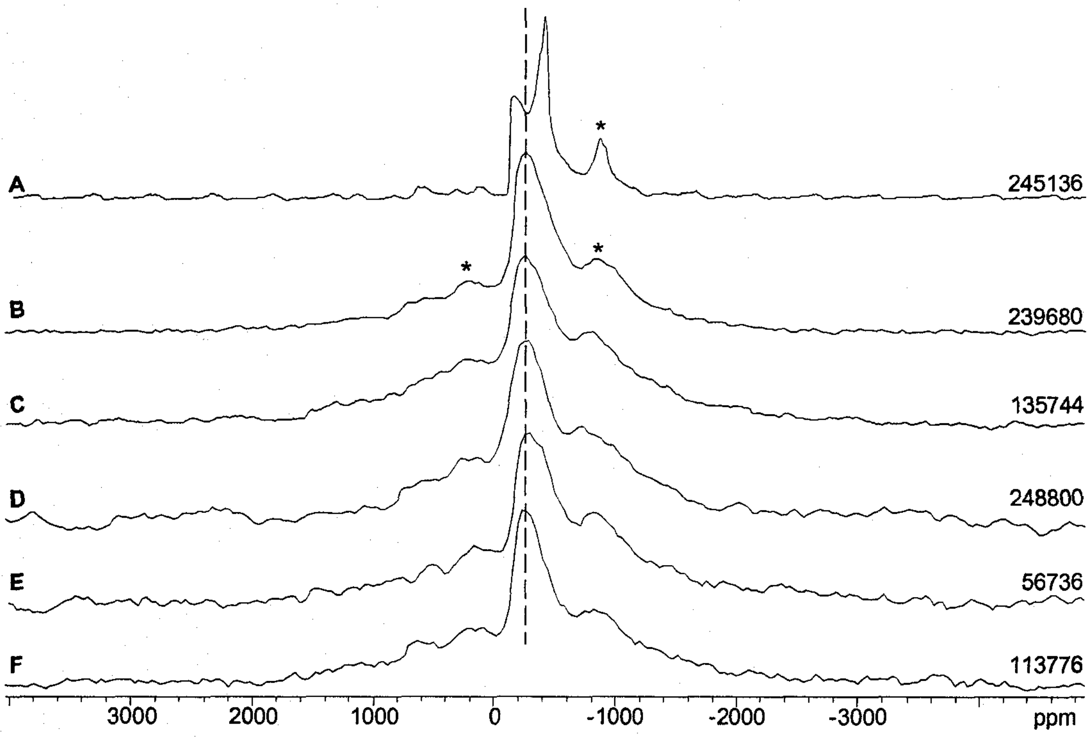

Figure 5.4. ^{139}La MAS NMR spectra of (A) **1**, (B) **2**, (C) **3**, (D) **4**, (E) **5** and (F) **6** acquired at 9.4 T. The symbol "*" denotes a spinning sideband. Numbers of scans of each NMR spectrum are shown on the right. Spinning frequencies of all NMR spectra range from 28 to 30 kHz. The dashed line indicates that there is no paramagnetic shift in (C) and (D).

the NPs is similar to that in the bulk phase. The ^{19}F and ^{139}La NMR powder patterns are inhomogeneously broadened due to a distribution of ^{19}F and ^{139}La chemical shifts and ^{139}La quadrupolar interactions. This results from both the small sizes of the NPs and the presence of surface-bound ligands, since the ^{19}F and ^{139}La nuclei in the core of the NP exist within different electronic environments and, hence, experience different magnetic interactions than those near the NP surface. The net broadening is the result of a continuum of slightly different environments from the core to the surface. The NMR interactions in the NPs therefore largely resemble that of the pristine LaF_3, and unique, unusual resonances are not observed. Such broadening effects in NMR powder patterns

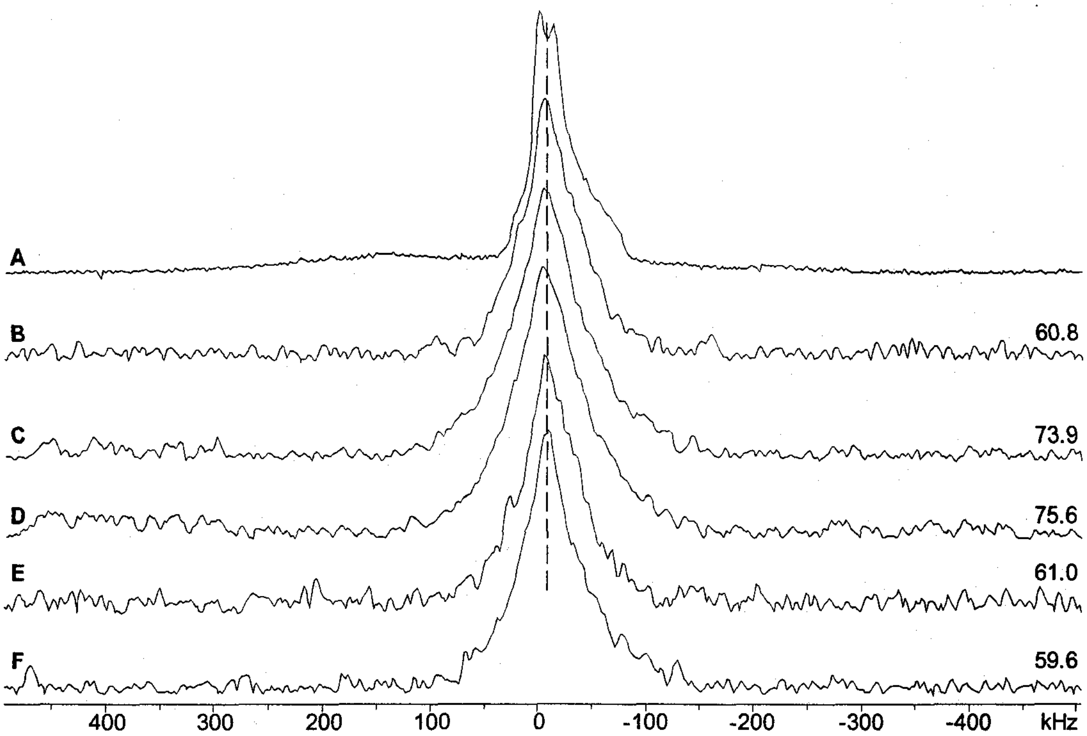

Figure 5.5. Static ^{139}La NMR spectra of (A) **1**, (B) **2**, (C) **3**, (D) **4**, (E) **5**, and (F) **6** acquired at 9.4 T. Numbers on the right indicate the FWHH (in kHz) of corresponding static spectra, and the dashed line marks the centre of gravity of the pattern.

of NPs are well-known.[77-81] For instance, Douglass et al. observed similar line broadening effects in solid–state ^{77}Se NMR experiments on a series of CdSe samples with different molecular sizes. A single, high S/N ^{77}Se peak is observed for the bulk CdSe, but line broadening and/or an increase of the number of ^{77}Se resonances is observed as the size of the NP decreases.[77]

LaF$_3$ NPs doped with paramagnetic Yb^{3+} ions, 3 and 4. ^{171}Yb NMR experiments conducted on Yb^{3+}–doped NPs (5 and 10 mol % relative to La in Ln–doped LaF$_3$ NPs) do not yield observable signals, since Yb^{3+} is paramagnetic. However, ^{19}F and ^{139}La NMR experiments may provide insight into whether and how the paramagnetic ions are incorporated into the NP core. The ^{19}F MAS NMR spectra of **3** and **4** are shown in

Figure 5.3C,D, respectively. In comparison to the spectra of **2**, the 5 mol % Yb^{3+} doping of **3** shifts the ^{19}F resonances to low frequency very slightly, but broadens them significantly. The increased 10 mol % doping of **4** broadens the resonances further, such that the F1 resonance is barely detectable and the F(2,3) resonance disappears completely. The S/N in the spectrum of **4** is quite low due to the paramagnetic broadening and long ^{19}F T_1 constants (a recycle delay of 60 s was applied). The S/N of the F1 resonance is considerably reduced, and the centre of gravity shifted to -34 ppm (compared to -23.1 ppm in the spectrum of **2**). The increased broadening of the powder patterns with higher sample doping arises predominantly from paramagnetic relaxation induced by unpaired electrons and possibly anisotropic broadening resulting from dipolar coupling with the unpaired spin density on the Yb atom.[82,83] The extreme broadening makes it impossible to accurately measure the isotropic chemical shift; however, the apparent negative shift may result from a pseudo-contact interaction with the unpaired electron.[50] The most important feature of the ^{19}F NMR spectra of **3** and **4** is the absence of intense, unshifted, and unbroadened resonances, indicating that the Yb^{3+} dopants are homogeneously distributed throughout the LaF_3 NP cores. This is consistent with both powder XRD data and luminescence decay measurements from Eu^{3+} emission spectra in previous works.[16,17,22]

The ^{139}La MAS NMR spectra of **3** and **4** (Figure 5.4C,D, respectively) are very similar to those of **2**, as are the corresponding static ^{139}La NMR spectra (Figure 5.5C,D). The centres of gravity of the MAS and static powder patterns are not influenced by a paramagnetic shift, likely because the paramagnetic dopants are not in the first coordination sphere of the La sites. However, the FWHH of the static ^{139}La NMR spectra increases from 61(2) to 76(2) kHz as the doping level increases from **2** to **4** (Figure 5.5B to D). Possible origins of this broadening include increased paramagnetic relaxation efficiency due to unpaired electrons (as in the case of the ^{19}F NMR spectra) and/or a wider distribution of chemical shifts and/or quadrupolar interactions due to local structural variations from doping.[84] To confirm the origin of this broadening, a series of ^{139}La relaxation measurements was conducted.

Table 5.1. ^{139}La T_1 and T_2 Relaxation Data Extracted from Mono– and Bi–exponential Functions for Bulk LaF$_3$ (1), Pure (2) and 10 mol % Yb^{3+}–doped LaF$_3$ NPs (4).

	Monoexponential[a]		Biexponential					
	A	T_1 (ms)	X^{2b}	A_f	T_{1f} (ms)	A_s	T_{1s} (ms)	X^2
1	0.96(1)	146.39(560)	0.15	0.17(1)	13.44(303)	0.80(1)	234.71(1051)	0.03
2	0.72(3)	1.04(16)	1.15	0.36(5)	0.19(6)	0.44(5)	6.67(202)	0.61
4	0.89(2)	0.70(11)	1.05	0.28(7)	0.04(3)	0.61(7)	1.85(58)	0.59
	B	T_2 (μs)	X^2	B_f	T_{2f} (μs)	B_s	T_{2s} (μs)	X^2
1	0.69(5)	490(50)	0.53	0.61(42)	20(10)	0.42(1)	890(30)	0.02
2	0.97(9)	70(10)	0.86	0.74(30)	20(3)	0.30(2)	330(30)	0.01
4	0.98(6)	40(6)	0.42	0.77(23)	20(2)	0.23(2)	190(20)	0.01

[a] Mono- and biexponential functions used in relaxation–curve fittings are defined in the Experimental section.; [b] X^2 values (in %) are calculated by an equation of the form $<x_{exp} - x_{cal}>^2$, where x_{exp} and x_{cal} represent experimental and calculated data points.

^{139}La relaxation measurements. ^{139}La T_1 and T_2 time constants were measured for **1**, **2**, and **4** at room temperature (Table 5.1). Unfortunately, due to the extremely long recycle delays and low S/N inherent in the ^{19}F NMR experiments, ^{19}F relaxation measurements are not reported for these systems. ^{139}La relaxation data for each sample were fitted using both mono– and biexponential functions. The latter involves two components which represent “fast” and “slow” mechanisms in the relaxation process and are denoted as T_{1f} (or T_{2f}) and T_{1s} (or T_{2s}). The existence of multiple relaxation mechanisms for NMR nuclei undergoing slow motions in a variety of solid materials is well known.[85] The biexponential curve fits are in better agreement with experimental data, as indicated by smaller X^2 values (best fits are found in the supporting information, Figures B.5.4 and B.5.5). The T_{1s} components are the dominant components for longitudinal relaxation (slightly to much higher weighting than T_{1f}). For transverse relaxation, the T_{2f} components are more heavily weighted but, interestingly, vary little between samples; however, the T_{2s} constants are quite disparate. Similar trends in relaxation behaviour are predicted for samples **1**, **2**, and **4** in both mono– and biexponential curve fits; accordingly, reference is made to the former in the ensuing discussion for simplicity.

The longitudinal relaxation rates are significantly increased (i.e., values of T_1 time constants decrease) in the NPs compared to the bulk. The T_1 of **2** is approximately 2 orders of magnitude smaller than that of **1**; however, the T_1 in **4** is only slightly smaller than that in **2**. Similar behaviour is observed for the transverse relaxation, where the T_2 decreases from 490 (**1**) to 70 (**2**) to 40 (**4**) μs. The large decrease of T_1 and T_2 in **2** and **4** compared to **1** may at first seem puzzling, since quadrupolar relaxation is expected to be the dominant mechanism in these samples and the ^{139}La quadrupolar interaction does not vary significantly between samples. The reduction in relaxation time constants in the NPs with respect to the bulk material could result from the presence of a dipolar relaxation mechanism (i.e., from the abundant mobile protons in the surface ligands)[86] or possibly the presence of some paramagnetic impurities introduced during synthesis.[87] The latter is unlikely, since there is a very modest decrease in T_1 and T_2 constants from **2** to **4** resulting from paramagnetic relaxation. Another possibility is that the relaxation time is greatly enhanced by some sort of quantum size effect, though such effects are only well understood and defined for metal NPs.[88] A temperature-dependent relaxation study of NPs of various sizes and modelling of these data is beyond the current scope of this paper.

The effective spin–spin relaxation time constant, T_2*, is related to the line width of the powder pattern: $(\pi\Delta\nu_{1/2})^{-1} = T_2^*$. Though this relationship holds strictly for Lorentzian lineshapes, a rough approximation of T_2* for **2** and **4** can be estimated from their static ^{139}La NMR patterns. The FWHH values of **2** and **4** are 61 and 76 kHz, respectively (Figure 5.5B,D), corresponding to T_2* values of ca. 4.19 and 5.21 μs, which are much smaller than their corresponding T_2 time constants (40 and 70 μs, respectively). Obviously, the breadths and shapes of the patterns largely result from a distribution of second-order quadrupolar interactions; but interestingly, the inverse of the difference in powder pattern widths, 21.2 μs, approximately equals the difference in their T_2 constants (30 μs). Hence, the difference in broadening of the ^{139}La NMR patterns of **2** and **4** arises chiefly from T_2 relaxation, and not from the presence of distinct La environments in these samples.

LaF_3 NPs doped with diamagnetic Y^{3+} ions, 5 and 6, and bulk crystalline YF_3, 8. Neither the ^{19}F MAS nor the ^{139}La MAS and static NMR spectra of **5** and **6** (parts E and F in Figures 5.3, 5.4, and 5.5, respectively) are significantly different from those of **2**. The breadths of the static ^{139}La NMR powder patterns of **2**, **5**, and **6** are almost identical (ranging from 60(2) to 61(2) kHz, Figure 5.5). The similarity of the NMR spectra of the Y^{3+}–doped and pure LaF_3 NPs strongly indicates that there are no major structural changes upon doping and the local LaF_3 structure remains largely the same. This confirms similar conclusions drawn above from the NMR spectra of paramagnetic-doped NPs, where the spectra are substantially different in appearance from those of the pure NPs, but only because of the presence of unpaired electrons at the Yb^{3+} sites.

In order to explore the nature of the metal dopant environments, solid-state ^{89}Y NMR experiments were conducted upon the 10 mol % Y^{3+}–doped NPs (**6**) and bulk YF_3 (**8**). While it was possible to acquire high S/N ^{19}F-^{89}Y CP/MAS NMR spectra for **8** (Figure B.5.6), signals corresponding to Y^{3+} sites in the NP were not observed; rather, two narrow ^{89}Y resonances were observed which may correspond to unreacted $Y(NO_3)_3{\bullet}6H_2O$ embedded in the LaF_3 matrix ($\delta_{iso}(^{89}Y)$ of $Y(NO_3)_3{\bullet}6H_2O$ = -53 ppm).[89] ^{89}Y is a 100% naturally abundant spin–1/2 nucleus and subject only to anisotropic chemical shielding and heteronuclear dipolar interactions; however it is extremely unreceptive due to its low gyromagnetic ratio, $\gamma(^{89}Y) = -1.3163 \times 10^7$ rad T^{-1} s^{-1}, which results in low S/N NMR signals, acoustic probe ringing which obliterates FIDs, and large longitudinal relaxation time constants. In addition to this, since the number of Y^{3+} sites are considerably dilute (i.e., Y^{3+} doping is 10 mol %), it is not surprising that broad ^{89}Y NP resonances corresponding to Y located in La sites in the LaF_3 matrix were not observed.

LaF_3 NPs doped with 10 mol % diamagnetic Sc^{3+} ions, 7 and bulk ScF_3, 9. Since ^{89}Y signals could not be observed, ^{45}Sc NMR experiments were conducted to examine the Sc environments in Sc^{3+}–doped NPs and bulk ScF_3. ^{45}Sc ($I = 7/2$) is an extremely receptive NMR nucleus, being 100% naturally abundant and possessing a high magnetogyric ratio (6.5088×10^7 rad T^{-1} s^{-1}). It has a moderately sized quadrupole moment ($Q(^{45}Sc) = -0.22 \times 10^{-28}$ m^2),[60] so the second-order quadrupolar lineshapes should not broaden and reduce the signal beyond detection limits, which is significant given the low doping level.

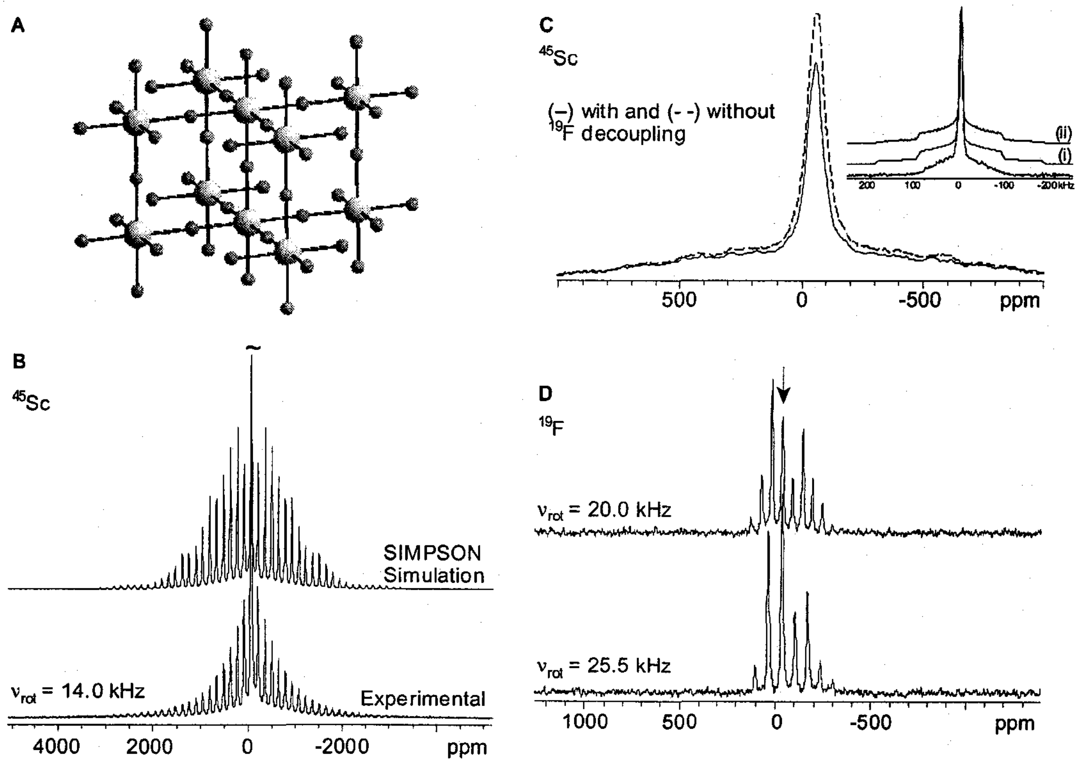

Figure 5.6. (A) Extended X-ray structure of ScF_3. (B) SATRAS and (C) static ^{45}Sc, and (D) ^{19}F MAS NMR spectra at 9.4 T of **9** (with the arrow indicates isotropic ^{19}F resonance). Inset of (C): full spectrum of the ^{19}F-decoupled static ^{45}Sc powder pattern of ScF_3 along with the (i) analytical (perfect excitation) and (ii) numerical (imperfect excitation) simulation, showing partial excitation of the STs.

The X-ray structure of ScF_3 (**9**) predicts single Sc and F sites in the unit cell,[37-39] and the powder XRD pattern presented herein (Figure 5.2E) confirms the crystallinity and purity of the sample. The Sc atom is coordinated by six F atoms in an almost perfectly octahedral arrangement, which bond to neighbouring Sc atoms to comprise an extended ScF_6 three–dimensional lattice (Figure 5.6A). While it is not expected that the Sc^{3+} sites in the NPs will be octahedral, the ^{45}Sc NMR of the bulk ScF_3 provides spectroscopic data for a reasonably comparable Sc environment (no other similar data are currently available in the literature). The ^{45}Sc{^{19}F} SATRAS and static ^{45}Sc NMR spectra of ScF_3 are displayed in Figure 5.6B,C, respectively. There is a small degree of long-range disorder in the sample, as indicated by the sloping spinning sideband manifolds; nevertheless, the scandium chemical shift is precisely measured at $\delta_{iso} = -52$ ppm and the $C_Q(^{45}Sc)$ is estimated to be ca. 1.3(2) MHz. The small value of $C_Q(^{45}Sc)$ is consistent with the high spherical symmetry around the ^{45}Sc. The partially excited inner satellite transitions can be seen flanking the central transition in the static spectrum (Figure 5.6C). Interestingly, comparison of ^{45}Sc and ^{45}Sc{^{19}F} NMR spectra reveal that the effects of ^{45}Sc–^{19}F dipolar coupling are very small, with the former spectrum only ca. 1 kHz wider than the latter. Given the proximity of the ^{45}Sc nucleus to the surrounding ^{19}F nuclei, and their large gyromagnetic ratios, this is somewhat surprising (Sc–F bond distance = 2.011 Å, giving rise to a ^{45}Sc–^{19}F dipolar coupling constant of ca. 3.4 kHz); however, it is possible that the dynamic motion of the fluorine atoms may partially average the dipolar interactions.[90] The ^{19}F MAS spectra of **9** (Figure 5.6D) reveal an isotropic chemical shift of -35.9 ppm, in good agreement with previously reported results.[91] The spinning sideband manifold arises largely from fluorine CSA, with a span of ca. 305 ppm and skew of 0.53 from Herzfeld–Berger analysis.[92]

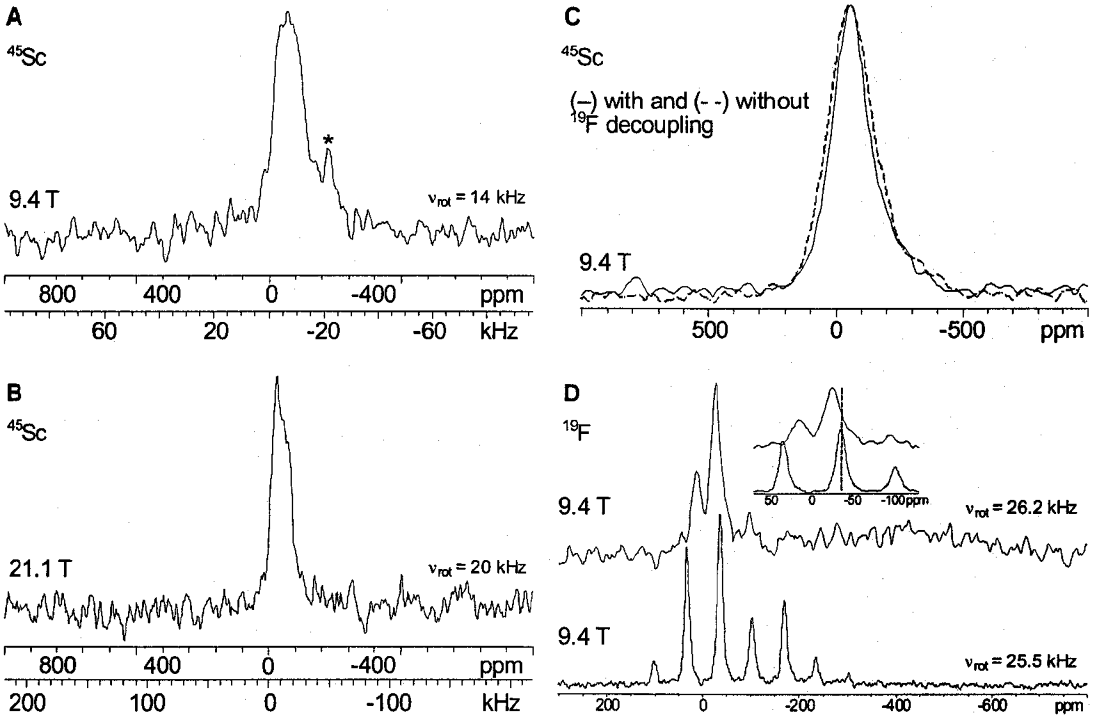

Figure 5.7. (A and B) ^{45}Sc MAS NMR spectra of 7 at multiple fields. (C) Static ^{45}Sc NMR spectra of 7. (D) ^{19}F MAS NMR spectra of **7** (top) and **9** (bottom). Isotropic peaks in **7** and **9** are not at the same frequency. The symbol "*" denotes a spinning sideband in (A).

The powder XRD and NMR data seem to indicate that the Sc^{3+} atoms are uniformly doped into La^{3+} positions and that pure ScF_3 is not observed. The powder XRD pattern of **7** (Figure 5.2F) resembles that of **2** (Figure 5.2C), except some higher angle peaks are observed which match positions in the mixed bulk LaF_3 and ScF_3 (Figure 5.2G,H). Once again, the broadened peaks are indicative of NP structure, and the low-angle peaks indicate some NP organization or packing. The ^{45}Sc MAS NMR spectra of **7** acquired at 9.4 and 21.1 T (Figure 5.7A,B) have an FWHH of ca. 11 kHz, significantly broader than that of **9** (FWHH of 3.4 kHz). The broadening prevents the accurate measurement of C_Q and δ_{iso} directly from the NMR spectra. The broadened powder patterns and absence of sharp spinning sideband manifolds are suggestive of both local disorder of the Sc sites (i.e., distribution of quadrupolar coupling constants and chemical shifts) and a significantly increased C_Q in comparison to that of the bulk material (which indicates the Sc^{3+} ions are not in octahedral environments). The centres of gravity of the NMR patterns at 9.4 and 21.1 T are at -75.8 ppm and -45 ppm, respectively. The differences in the centres of gravity result from the reduction of second-order quadrupolar induced shifts upon moving to higher field, indicating that there is a significantly larger C_Q for **7** than in the case of **9**. The $\delta_{iso}(^{45}Sc)$ and the quadrupolar product, $P_Q = C_Q(1 + \eta_Q^2/3)^{1/2}$,[93] can be calculated by measuring the centres of gravity of the ^{45}Sc powder patterns obtained at two different magnetic fields, and then solving two equations in two unknowns.[94] A unique solution of δ_{iso} = -37(5) ppm and $P_Q(^{45}Sc)$ = 12 MHz is calculated. The δ_{iso} is similar to that measured for **9**, but clearly indicates a distinct chemical shift environment. The P_Q indicates a potential range of C_Q between 12 and 14 MHz (depending upon the magnitude of η_Q), clearly indicating that the Sc nuclei are in spherically asymmetric environments. In addition, there is no unreacted $Sc(NO_3)_3$ present in these NPs, as this would yield an intense signal near δ_{iso} = -18.5 ppm with a moderate $C_Q(^{45}Sc)$ around 6.2 MHz.[28] As in the case of the bulk sample, ^{19}F decoupling has little effect on the static ^{45}Sc NMR spectrum of **7** (Figure 5.7C). Further, the ^{19}F MAS NMR spectrum of **7** (Figure 5.7D) is similar to those of **2**, **5**, and **6**, the only difference being a slightly reduced S/N ratio in the spectrum of **7** (Figure B.5.7). This and the absence of an isotropic peak corresponding to ScF_3 (Figure 5.7D, inset) support the retention of the local LaF_3 structure upon doping and that Sc^{3+} ions are occupying La positions in the LaF_3

core (i.e., the Sc atoms are not in octahedral environments).

Structure of the Inorganic NP Core – Summary. The combination of powder XRD and solid-state NMR data on bulk and NP samples allows for a number of conclusions to be made regarding the structure of the NP core. First, the inorganic core is crystalline, and the local structures of the La and F atoms are similar to that of the bulk material. Due to the small sizes of the NPs and presence of surface ligands, the local environments gradually change from the centre to the surface of the NP giving rise to broad XRD peaks. This is confirmed by the inhomogeneously broadened NMR powder patterns arising from distributions of NMR interactions. Second, it is clear from both ^{19}F and ^{139}La NMR experiments that the low doping levels of early transition metal or lanthanide ions do not give rise to significant changes in the local structure of LaF_3 or the long-range structure in the NPs. Third, doping with paramagnetic Yb^{3+} ions leads to severe broadening of ^{19}F powder patterns and only moderate broadening of ^{139}La powder patterns, while no significant paramagnetically induced shifts are observed. This indicates that the paramagnetic ions are uniformly distributed throughout the NP and are located in the La positions in the extended LaF_3 structure (i.e., Yb^{3+} ions are more proximate to ^{19}F nuclei than ^{139}La nuclei). Finally, the ^{45}Sc NMR data show the complete incorporation of the Sc^{3+} ions into the extended LaF_3 structure and confirm that dopant ions occupy La^{3+} sites. This is direct evidence for positions of dopant lanthanide ions proposed in earlier papers.[16]

Characterization of stabilizing ligands by ^{1}H and ^{31}P NMR spectroscopy. Solid-state ^{1}H and ^{31}P NMR experiments were applied to probe the nature of the

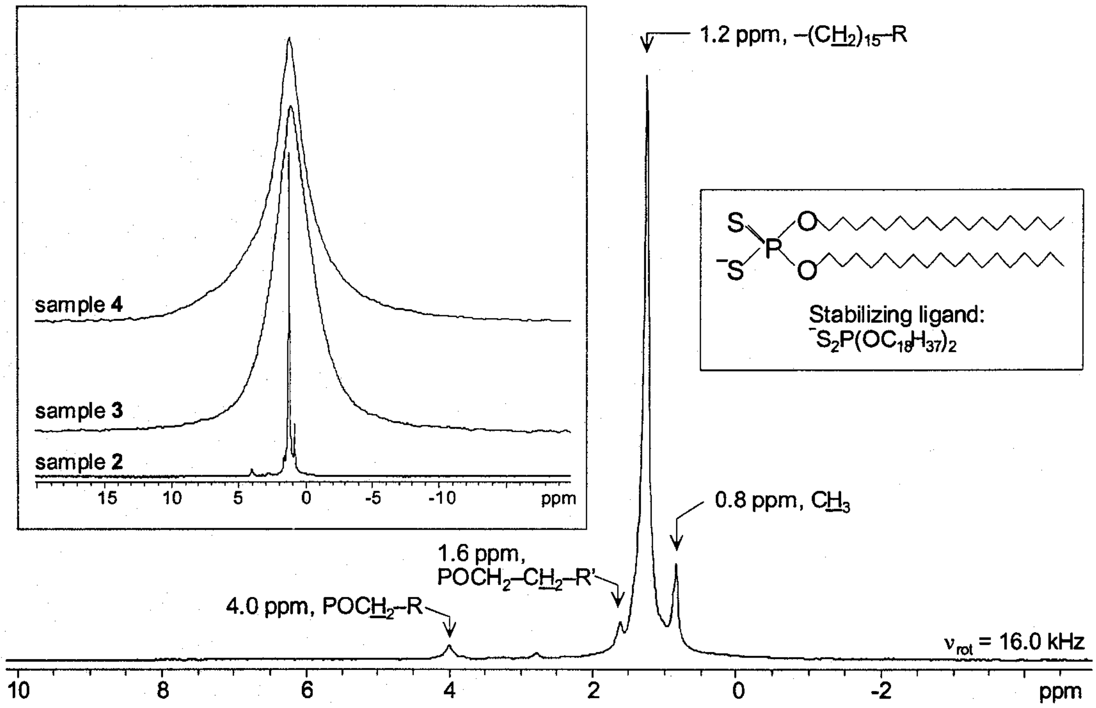

Figure 5.8. ^{1}H MAS NMR spectrum of **2** at 9.4 T. Inset on the left: a comparison between ^{1}H MAS NMR spectra of **2**, **3** and **4** acquired at 9.4 T; inset on the right: a schematic picture of the di–*n*–octadecyldithiophosphate stabilizing ligand.

stabilizing ligands (i.e., the di–*n*–octadecyldithiophosphate anion ($^-S_2P(OC_{18}H_{37})_2$, Chart 5.1) on the surface of the NPs. Solid–state ^{1}H MAS NMR spectra of **2**, **3**, and **4** are shown in Figure 5.8. For **2**, a spinning speed of 16.0 kHz is enough to average the ^{1}H–^{1}H dipolar interactions almost completely, producing a solution-like spectrum. Peaks at 4.0 and 1.6 ppm are assigned to ethylene protons that are the closest and the next closest to the dithiophosphate group, respectively. The peak at 0.8 ppm is assigned to the terminal methyl protons, while the intense, broadened ^{1}H resonance at 1.2 ppm corresponds to the remaining ethylene protons. All peak assignments are in excellent agreement with solution NMR data.[17,22] In the ^{1}H MAS NMR spectra of **3** and **4** (inset of Figure 5.8), the fine structure of NMR spectrum disappears completely, despite the higher spinning speeds.

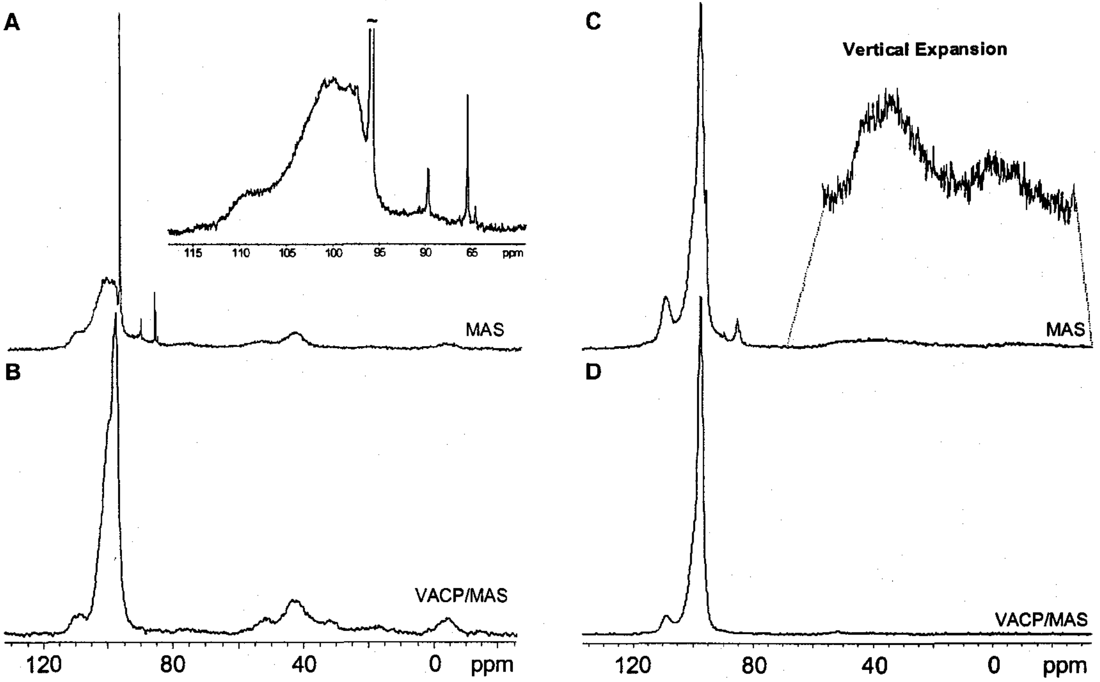

Figure 5.9. (A) $^{31}P\{^1H\}$ MAS and (B) ^1H–^{31}P VACP/MAS NMR spectra of **2**. (C) $^{31}P\{^1H\}$ MAS and (D) ^1H–^{31}P VACP/MAS NMR spectra of **4**. All NMR spectra were acquired at 9.4 T with rotational frequency of 25 kHz. Insets: expansion of (A) showing sharp ^{31}P resonances, and vertical expansion of (C) about the thiophosphate and phosphate regions.

The powder pattern of **4** is considerably broader than that of **3**, undoubtedly due to the increased paramagnetic doping in the former. This is direct evidence for attachment of the ligands to the NP surface, since ^1H NMR signals of nuclei in the side chain are being broadened by unpaired electrons localized within the inorganic core of the NP.

^{31}P MAS and ^1H-^{31}P VACP/MAS NMR spectra of **2** (Figure 5.9A,B) are somewhat similar, with the exception of four sharp ^{31}P peaks positioned at 84.5, 85.4, 89.7, and 95.8 ppm in the former. There are three main ^{31}P resonances with centres of gravity at ca. 100, 40, and -4 ppm, which are inhomogeneously broadened from the distribution of distinct environments on the NP surface. The resonance centred at 100 ppm is assigned as a dithiophosphate resonance ($(RO)_2P(S)S^-$),[95] while the peaks at 40

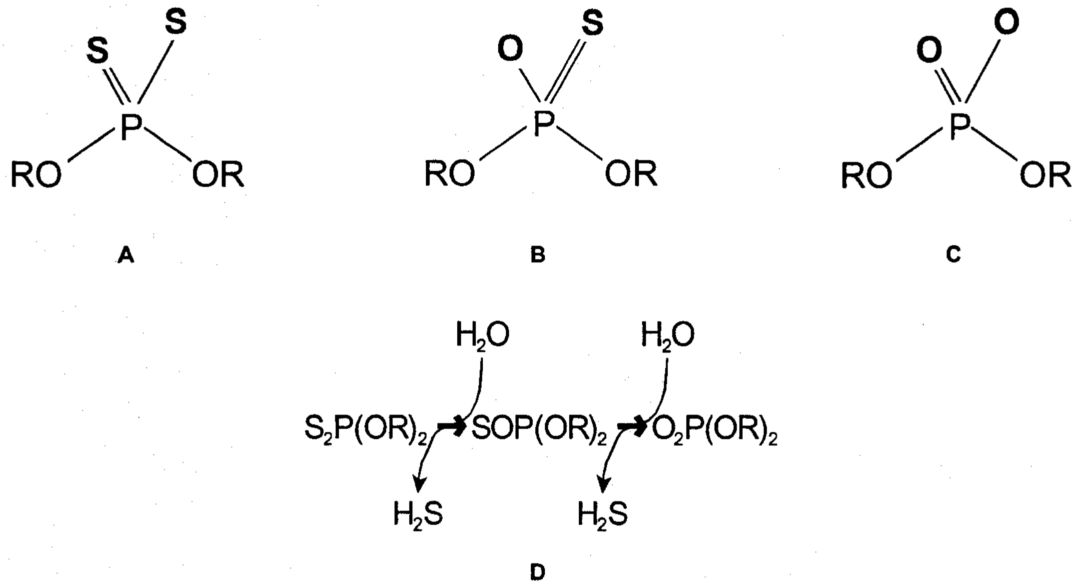

Chart 5.3. Functional groups of stabilizing ligands: (A) dithiophosphate, (B) thiophosphate and (C) phosphate heads, with R = $C_{18}H_{37}$. (D) Proposed hydrolysis process of the dithiophosphate groups in the stabilizing ligands.

ppm and -4 ppm correspond to thiophosphate ($(RO)_2P(S)O^-$)[96-98] and phosphate ($(RO)_2P(O)O^-$) functional groups, respectively (Chart 5.3A to C).[97,99,100] The presence of thiophosphate and phosphate species is unexpected, though they may be formed by hydrolysis reactions during NP formation (Chart 5.3D).[101] The ^{31}P chemical shifts of the remaining four sharp minor peaks (Figure 5.9A, inset) fall into a range corresponding to a variety of forms of neutral[102] and anionic[103] phosphorous sulfides, such as P_4S_7 (81.9 to 112.8 ppm), α-P_4S_3 (84.5 and 91.0 ppm), PS_4^{3-} (88.5 and 103.3 ppm), $P_2S_7^{4-}$ (90.0 to 111.8 ppm), and $P_2S_6^{4-}$ (91.3 to 109.4 ppm). A ^{31}P MAS NMR experiment conducted on **4** after three months in a sample vial reveals almost no change in the thiophosphate and phosphate resonances; however, the intensity of the dithiophosphate powder pattern decreases, while an unassigned peak centred at ca. 86 ppm increases dramatically (Figure B.5.8). Interestingly, phosphorous chemical shifts which correspond to starting material in the synthesis of stabilizing ligand are absent (i.e., P_2S_5 or P_4S_{10} [16,17,22] have shifts of 49.7 and 51.6 ppm, respectively).[102]

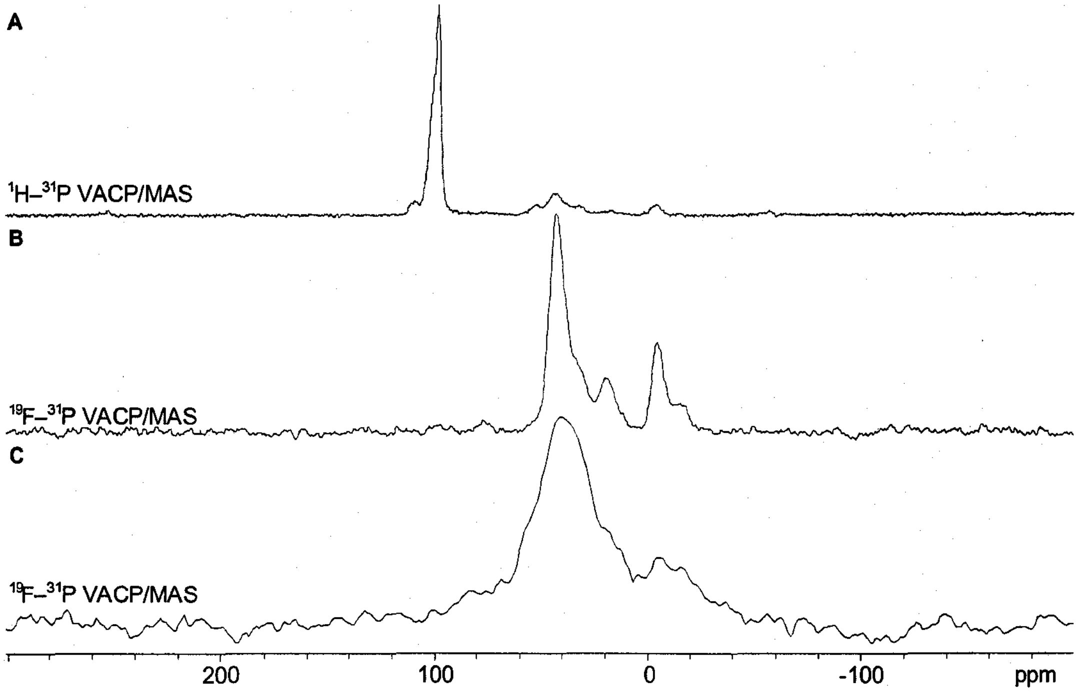

Figure 5.10. (A) ^{1}H–^{31}P MAS and (B) ^{19}F–^{31}P VACP/MAS NMR spectra of **2**. (C) ^{19}F–^{31}P VACP/MAS NMR spectra of **4**. All NMR spectra were acquired at 9.4 T with rotational frequency of 25 kHz.

^{31}P MAS and ^{1}H–^{31}P VACP/MAS NMR spectra of **4** (Figure 5.9C,D) appear to have only the resonance corresponding to the dithiophosphate species; however, vertical expansion of the thiophosphate and phosphate regions reveals broadened resonances (similar spectra are observed for **3**). It is possible that the two latter peaks are broadened due to relaxation by unpaired electrons at the Yb^{3+} ions in the NP cores or that partial hydrolysis has not occurred in this NP, thereby reducing the intensity of these peaks. To investigate this further, ^{19}F–^{31}P VACP/MAS NMR experiments were conducted on **2** and **4** (Figure 5.10). In the ^{19}F–^{31}P spectra of the pure and doped NP, large signal enhancements are obtained for the thiophosphate and phosphate resonances, while the dithiophosphate resonance is essentially absent. This could be due to the ^{31}P nucleus in the dithiophosphate group being further from the NP surface than ^{31}P nuclei in the thiophosphate, and phosphate species (the signal for the phosphate species has the highest ^{19}F CP enhancement). Since the ^{19}F spin polarization originates from the NP, this is consistent with the paramagnetic relaxation of the ^{31}P resonances: the ^{31}P nuclei of the dithiophosphate species are distant enough from the NP surface that CP is very inefficient; conversely, the ^{31}P nuclei in the thiophosphate and phosphate species are proximate enough that CP efficiency is high.

Structure of the NP Surface - Summary. At the NP surface, di-*n*-octadecyldithiophosphate ligands are identified by both ^{1}H and ^{31}P NMR experiments. Broadening of the ^{1}H and ^{31}P NMR resonances in the Yb^{3+}–doped samples suggests that stabilizing ligands are indeed coordinated to the NP surface. In addition, ^{31}P NMR data also identify a coexistence of dithiophosphate, thiophosphate and phosphate species in the samples, though the dithiophosphate is predominant. The thiophosphate and phosphate species may be generated by hydrolysis reactions. ^{19}F–^{31}P VACP/MAS experiments reveal that the distances between the NP surface and the aforementioned functional groups vary, in the order of dithiophosphate > thiophosphate > phosphate, which suggests that La^{3+} surface sites interact with the O-containing head groups more strongly.

5.4 Conclusion

Multinuclear solid-state NMR data, in combination with powder X-ray diffraction measurements, have been used to gain insight into the local atomic and molecular structure in LaF_3 NPs. ^{19}F and ^{139}La NMR experiments give insight into the molecular structure of the core and effects of paramagnetic doping and, in combination with ^{45}Sc experiments, into the dopant ion environments. The LaF_3 core of the NPs is relatively unperturbed compared to the bulk, but inhomogeneously broadened powder patterns indicate distributions of La and F sites from the core of the NP to its surface. Comparison of powder pattern shapes and relaxation time constants adds new insights into the differences between the structures of NPs and bulk parent materials. ^{1}H and ^{31}P NMR experiments identify an interesting surface chemistry, and the combination of paramagnetically doped samples and ^{19}F-^{31}P VACP/MAS experiments reveal the interface between the LaF_3 core and the dithiophosphate surface ligands. We anticipate that this study will encourage future solid-state NMR investigations on this important class of NPs.

Bibliography

[1] Dabbousi, B.O., Bawendi, M.G., Onitsuka, O., Rubner, M.F. *Appl. Phys. Lett.* **1995**, *66*, 1316.

[2] Justel, T., Nikol, H., Ronda, C. *Angew. Chem.-Int. Edit.* **1998**, *37*, 3085.

[3] Dahan, M., Laurence, T., Pinaud, F., Chemla, D.S., Alivisatos, A.P., Sauer, M., Weiss, S. *Opt. Lett.* **2001**, *26*, 825.

[4] Gonsalves, K.E., Carlson, G., Rangarajan, S.P., Benaissa, M., JoseYacaman, M. *J. Mater. Chem.* **1996**, *6*, 1451.

[5] Klimov, V.I. et al. *Science* **2000**, *290*, 314.

[6] Maas, H., Currao, A., Calzaferri, G. *Angew. Chem.-Int. Edit.* **2002**, *41*, 2495.

[7] Slooff, L.H. et al. *J. Appl. Phys.* **2002**, *91*, 3955.

[8] Hebbink, G.A., Reinhoudt, D.N., van Veggel, F. *Eur. J. Org. Chem.* **2001**, 4101.

[9] Klink, S.I., Hebbink, G.A., Grave, L., Peters, F.G.A., van Veggel, F., Reinhoudt, D.N., Hofstraat, J.W. *Eur. J. Org. Chem.* **2000**, 1923.

[10] Wolbers, M.P.O., van Veggel, F.C.J.M., SnellinkRuel, B.H.M., Hofstraat, J.W., Geurts, F.A.J., Reinhoudt, D.N. *J. Am. Chem. Soc.* **1997**, *119*, 138.

[11] Slooff, L.H. et al. *Opt. Mater.* **2000**, *14*, 101.

[12] Dekker, R. et al. *Appl. Phys. Lett.* **2004**, *85*, 6104.

[13] Hebbink, G.A., Stouwdam, J.W., Reinhoudt, D.N., Van Veggel, F.C.J.M. *Adv. Mater.* **2002**, *14*, 1147.

[14] Riwotzki, K., Meyssamy, H., Kornowski, A., Haase, M. *J. Phys. Chem. B* **2000**, *104*, 2824.

[15] Riwotzki, K., Meyssamy, H., Schnablegger, H., Kornowski, A., Haase, M. *Angew. Chem., Int. Ed.* **2001**, *40*, 573.

[16] Stouwdam, J.W., van Veggel, F.C.J.M. *Nano Lett.* **2002**, *2*, 733.

[17] Stouwdam, J.W., Hebbink, G.A., Huskens, J., van Veggel, F.C.J.M. *Chem. Mat.* **2003**, *15*, 4604.

[18] Zhang, W.-W., Xu, M., Zhang, W.-P., Yin, M., Qi, Z.-M., Xia, S.-D., Garapon, C. *Chem. Phys. Lett.* **2003**, *376*, 318.

[19] Jiang, X.-C., Yan, C.-H., Sun, L.-D., Wei, Z.-G., Liao, C.-S. *J. Solid State Chem.* **2003**, *175*, 245.

[20] Yan, C.-H., Sun, L.-D., Liao, C.-S., Zhang, Y.-X., Lu, Y.-Q., Huang, S.-H., Lu, S.-Z. *Appl. Phys. Lett.* **2003**, *82*, 3511.

[21] Zhou, J.F., Wu, Z.S., Zhang, Z.J., Liu, W.M., Dang, H.X. *Wear* **2001**, *249*, 333.

[22] Stouwdam, J.W., van Veggel, F.C.J.M. *Langmuir* **2004**, *20*, 11763.

[23] Sudarsan, V., van Veggel, F.C.J.M., Herring, R.A., Raudsepp, M. *J. Mater. Chem.* **2005**, *15*, 1332.

[24] Lo, A.Y.H., Sudarsan, V., Sivakumar, S., van Veggel, F., Schurko, R.W. *J. Am. Chem. Soc.* **2007**, *129*, 4687.

[25] Yao, Z., Kwak, H.T., Sakellariou, D., Emsley, L., Grandinetti, P.J. *Chem. Phys. Lett.* **2000**, *327*, 85.

[26] Merwin, L.H., Sebald, A. *J. Magn. Reson.* **1990**, *88*, 167.

[27] Haid, E. et al. *Z. Naturforsch., A: Phys. Sci.* **1983**, *38A*, 317.

[28] Rossini, A.J., Schurko, R.W. *J. Am. Chem. Soc.* **2006**, *128*, 10391.

[29] Markley, J.L., Horsley, W.J., Klein, M.P. *J. Chem. Phys.* **1971**, *55*, 3604.

[30] Larsen, F.H., Jakobsen, H.J., Ellis, P.D., Nielsen, N.C. *J. Phys. Chem. A* **1997**, *101*, 8597.

[31] Eichele, K., Wasylishen, R.E., v. 1.17.30, Tübingen, 2001.

[32] Bak, M., Rasmussen, J.T., Nielsen, N.C. *J. Magn. Reson.* **2000**, *147*, 296.

[33] Zalkin, A., Templeton, D.H. *J. Am. Chem. Soc.* **1953**, *75*, 2453.

[34] Cheetham, A.K., Norman, N. *Acta Chem. Scand.* **1974**, *28*, 55.

[35] Rotereau, K., Gesland, J.Y., Daniel, P., Bulou, A. *Mater. Res. Bull.* **1993**, *28*, 813.

[36] Nowacki, W. *Naturwissenschaften* **1938**, *26*, 801.

[37] Nowacki, W. *Z. Kristallogr. Kristallgeom. Kristallphys. Kristallchem.* **1939**, *101*, 273.

[38] Ippolitov, E.G., Maklachkov, A.G. *Zhurnal Neorg. Khimii* **1970**, *15*, 1466.

[39] Loesch, R., Hebecker, C., Ranft, Z. *Z. Anorg. Allg. Chem.* **1982**, *491*, 199.

[40] Kraus, W., Nolze, G., v. 2.4, Federal Institute for Materials Research and Testing, Berlin, Germany, 2000.

[41] Schlyter, K. *Ark. Kemi* **1952**, *5*, 73.

[42] Wyckoff, R.W.G. *Crystal Structures*; Interscience Publishers: New York, 1963; Vol. 2.

[43] Mansmann, M. *Z. Anorg. Allg. Chem.* **1964**, *331*, 98.

[44] Mansmann, M. *Z. Kristallogr. Kristallgeom. Kristallphys. Kristallchem.* **1966**,

122, 375.

[45] Zalkin, A., Templeton, D.H., Hopkins, T.E. *Inorg. Chem.* **1966**, *5*, 1466.

[46] de Rango, C., Tsoucaris, G., Zelwer, C. *C. R. Seances Acad. Sci. C* **1966**, *263*, 64.

[47] Maximov, B., Schulz, H. *Acta Crystallogr., Sect. B: Struct. Sci.* **1985**, *41*, 88.

[48] Gregson, D., Catlow, C.R.A., Chadwick, A.V., Lander, G.H., Cormack, A.N., Fender, B.E.F. *Acta Crystallogr., Sect. B: Struct. Sci.* **1983**, *39*, 687.

[49] Saraswati, V., Vijayaraghavan, R. *Phys. Lett.* **1966**, *21*, 363.

[50] Saraswati, V., Vijayaraghavan, R. *J. Phys. Chem. Solids* **1967**, *28*, 2111.

[51] Jaroszkiewicz, G.A., Strange, J.H. *J. Phys. C: Solid State Phys.* **1985**, *18*, 2331.

[52] Aalders, A.F., Arts, A.F.M., De Wijn, H.W. *Phys. Rev. B* **1985**, *32*, 5412.

[53] Privalov, A.F., Cenian, A., Fujara, F., Gabriel, H., Murin, I.V., Vieth, H.M. *J. Phys.: Condens. Matter* **1997**, *9*, 9275.

[54] Wang, F., Grey, C.P. *Chem. Mat.* **1997**, *9*, 1068.

[55] Andersson, L.O., Proctor, W.G. *Z. Kristallogr.* **1968**, *127*, 366.

[56] Ooms, K.J., Feindel, K.W., Willans, M.J., Wasylishen, R.E., Hanna, J.V., Pike, K.J., Smith, M.E. *Solid State Nucl. Magn. Reson.* **2005**, *28*, 125.

[57] Lee, K., Sher, A., Andersson, L.O., Proctor, W.G. *Phys. Rev.* **1966**, *150*, 168.

[58] Nakamura, N., Chihara, H. *J. Phys. Chem. Solids* **1987**, *48*, 833.

[59] Goldman, M., Shen, L. *Phys. Rev.* **1966**, *144*, 321.

[60] Pyykko, P. *Mol. Phys.* **2001**, *99*, 1617.

[61] Savosta, M.M., Doroshev, V.D., Kamenev, V.I., Borodin, V.A., Tarasenko, T.N., Mazur, A.S., Marysko, M. *J. Exp. Theor. Phys.* **2003**, *97*, 573.

[62] Papavassiliou, G. et al. *Phys. Rev. B* **1998**, *58*, 12237.

[63] Bastow, T.J. *Solid State Nucl. Magn. Reson.* **1994**, *3*, 17.

[64] Hoch, M.J.R., Kuhns, P.L., Moulton, W.G., Reyes, A.P., Lu, J., Wu, J., Leighton, C. *Phys. Rev. B* **2004**, *70*, 174443/1.

[65] Mikhalev, K.N., Lekomtsev, S.A., Gerashchenko, A.P., Yakubovskii, A.Y., Kaul, A.R. *JETP Lett.* **2003**, *77*, 401.

[66] Hunger, M., Engelhardt, G., Weitkamp, J. *Stud. Surf. Sci. Catal.* **1994**, *84*, 725.

[67] Engelhardt, G., Hunger, M., Koller, H., Weitkamp, J. *Stud. Surf. Sci. Catal.* **1994**, *84*, 421.

[68] Hunger, M., Engelhardt, G., Weitkamp, J. *Microporous Mater.* **1995**, *3*, 497.

[69] Herreros, B., Man, P.P., Manoli, J.M., Fraissard, J. *J. Chem. Soc., Chem. Commun.* **1992**, 464.

[70] Bastow, T.J. *Z. Naturforsch., A: Phys. Sci.* **1994**, *49*, 320.

[71] Willans, M.J., Feindel, K.W., Ooms, K.J., Wasylishen, R.E. *Chem.-Eur. J.* **2005**, *12*, 159.

[72] Hamaed, H., Lo, A.Y.H., Lee, D.S., Evans, W.J., Schurko, R.W. *J. Am. Chem. Soc.* **2006**, *128*, 12638.

[73] Aurentz, D.J., Vogt, F.G., Mueller, K.T., Benesi, A.J. *J. Magn. Reson.* **1999**, *138*, 320.

[74] Madhu, P.K., Johannessen, O.G., Pike, K.J., Dupree, R., Smith, M.E., Levitt, M.H. *J. Magn. Reson.* **2003**, *163*, 310.

[75] Tao, X.-j., Zhou, J.-f., Zhang, Z.-j., Dang, H.-x. *Huaxue Yanjiu* **2000**, *11*, 8.

[76] De, G., Qin, W., Zhang, J., Zhao, D., Zhang, J. *Chem. Lett.* **2005**, *34*, 914.

[77] Thayer, A.M., Steigerwald, M.L., Duncan, T.M., Douglass, D.C. *Phys. Rev. Lett.* **1988**, *60*, 2673.

[78] Tomaselli, M., Yarger, J.L., Bruchez, M., Jr., Havlin, R.H., deGraw, D., Pines, A., Alivisatos, A.P. *J. Chem. Phys.* **1999**, *110*, 8861.

[79] Ladizhansky, V., Vega, S. *J. Phys. Chem. B* **2000**, *104*, 5237.

[80] Mikulec, F.V., Kuno, M., Bennati, M., Hall, D.A., Griffin, R.G., Bawendi, M.G. *J. Am. Chem. Soc.* **2000**, *122*, 2532.

[81] Berrettini, M.G., Braun, G., Hu, J.G., Strouse, G.F. *J. Am. Chem. Soc.* **2004**, *126*, 7063.

[82] Mustafa, M.R., Jones, W.E., McGarvey, B.R., Greenblatt, M., Banks, E. *J. Chem. Phys.* **1975**, *62*, 2700.

[83] McGarvey, B.R. *J. Chem. Phys.* **1976**, *65*, 955.

[84] Matsushita, M., Kato, T. *Chem. Phys. Lett.* **1997**, *273*, 291.

[85] Abragam, A. *Principles of Nuclear Magnetism*; Oxford University Press: Ely House, London W.1, 1961.

[86] Ladizhansky, V., Hodes, G., Vega, S. *J. Phys. Chem. B* **1998**, *102*, 8505.

[87] Shames, A.I. et al. *J. Phys. Chem. Solids* **2002**, *63*, 1993.

[88] van der Klink, J.J., Brom, H.B. *Prog. Nucl. Magn. Reson. Spectrosc.* **2000**, *36*, 89.

[89] Wu, J.J., Boyle, T.J., Shreeve, J.L., Ziller, J.W., Evans, W.J. *Inorg. Chem.* **1993**, *32*, 1130.

[90] Du, L.S., Schurko, R.W., Lim, K.H., Grey, C.P. *J. Phys. Chem. A* **2001**, *105*, 760.

[91] Avkhutskii, L.M., Gagarinskii, Y.V., Polishchuk, S.A., Gabuda, S.P. *Spectrosc. Lett.* **1969**, *2*, 75.

[92] Herzfeld, J., Berger, A.E. *J. Chem. Phys.* **1980**, *73*, 6021.

[93] Mueller, K.T., Baltisberger, J.H., Wooten, E.W., Pines, A. *J. Phys. Chem.* **1992**, *96*, 7001.

[94] Freude, D. In *Encyclopedia of Analytical Chemistry*; Meyers, R.A., Ed.; John Wiley & Sons Ltd, 2000, pp 1 - 37.

[95] McCleverty, J.A., Kowalski, R.S.Z., Bailey, N.A., Mulvaney, R., Ocleirigh, D.A. *J. Chem. Soc.-Dalton Trans.* **1983**, 627.

[96] Bruzik, K., Stec, W.J. *J. Org. Chem.* **1981**, *46*, 1625.

[97] Kudelska, W., Michalska, M. *Tetrahedron* **1981**, *37*, 2989.

[98] Chojnowski, J., Cypryk, M., Fortuniak, W., Michalski, J. *Synthesis* **1977**, 683.

[99] Satterthwait, A.C., Westheimer, F.H. *J. Am. Chem. Soc.* **1980**, *102*, 4464.

[100] Jacob, L., Julia, M., Pfeiffer, B., Rolando, C. *Synthesis* **1983**, 451.

[101] Corbridge, D.E.C. In *Studies in Inorganic Chemistry, Vol.2: Phosphorus: An Outline of its Chemistry, Biochemistry and Technology.*; 2nd ed.; Elsevier Scientific Publishing Company: New York, 1980; Vol. 2, p 357.

[102] Eckert, H., Liang, C.S., Stucky, G.D. *J. Phys. Chem.* **1989**, *93*, 452.

[103] Schmedt auf der Gunne, J., Eckert, H. *Chem.-Eur. J.* **1998**, *4*, 1762.

Chapter 6

Multinuclear Solid-State NMR Spectroscopy of Bulk CdSe and CdSe Nanoparticle Aerogels and Xerogels

6.1 Introduction

Inorganic nano-scaled materials have recently attracted much attention in the literature, since it has been demonstrated that variation of particle size and shape, as well as tuning of nanoparticle (NP) composition and structure at the molecular level, is crucial for their rational design. For instance, the unique luminescent properties of CdSe quantum dots (QDs) have made them important in manufacture and design of light-emitting/optical devices,[1-3] as well as in a variety of biotechnological applications,[4,5] due to their size-tunable optical absorption and sharp band-edge luminescent properties[2,6] and dimensional similarities with biological macromolecules. Among the novel materials comprised of elemental combinations from groups 12-16 and 14-16, CdS and CdSe NPs are relatively easy to synthesize which has lead to a number of investigations of their applications including nonlinear optical devices,[7] biological labelling and diagnostics,[8] electro-luminescent[1,9] or photovoltaic devices,[10-12] and sensors.[13-15] Such NPs are often coated or capped with organic ligands for better dispersability and solubility, leading to different chemical environments near and/or at the surface than the core of NPs due to the interactions with the surface ligands.[2,16,17]

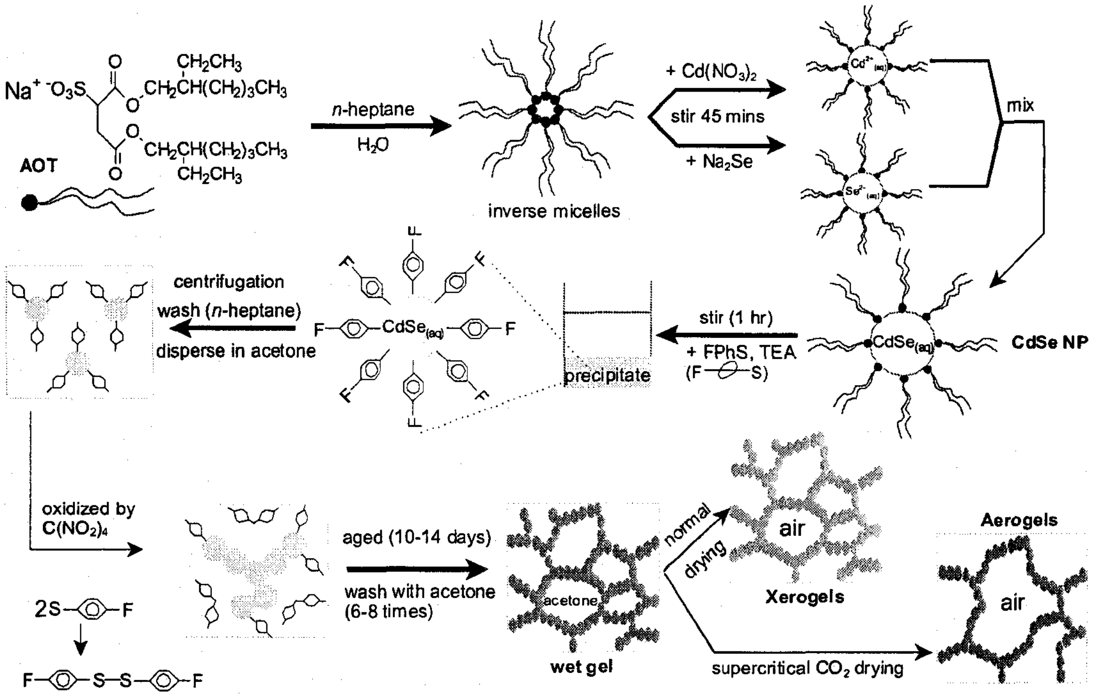

Figure 6.1. Synthetic scheme for CdSe aerogels and xerogels. 4-Fluorobenzenethiol (FPhS) is the capping ligand. Triethylamine (TEA) is used to alter the pH of the solution, so that the FPhS ligands are more readily capped onto the surface. Normal drying during the formation of xerogels means that the wet gels are dried under ambient conditions.

Mesoporous chalcogenide materials synthesized from CdS or CdSe NP building blocks have recently been reported.[18-20] The synthesis (Figure 6.1) involves the generation of CdS or CdSe NPs using the inverse-micelle strategy. The surfactants (sodium bis(2-ethylhexyl)sulfosuccinate or AOT) are exchanged with 4-fluorobenzenethiol (FPhS), which are then oxidized and removed from the surface of the NPs, leading to the gelation of the naked NPs. The resulting gels are wet due to the presence of a significant amount of acetone (which is used to wash away the dimeric FPhS ligands), and must be dried. Two distinct drying processes are used: drying under a stream of supercritical CO_2 at fixed pressure and temperature leads to the formation of low density aerogels, whereas

Table 6.1. Physical Properties of CdSe Aerogels and Xerogels.[a]

Property	Xerogels	Aerogels
elemental composition (%)	Cd/Se/S, 47.3 : 43.5 : 9.2	Cd/Se/S, 46.2 : 43.6 : 10.2
crystallite size (nm)[b]	2.2	2.7
BET surface area (m^2/g)	41 to 65	128 to 161
average pore diameter (nm)	4 to 5	16 to 29
cumulative pore volume (cm^3/g)	0.05 to 0.07	0.53 to 0.98
density relative to bulk CdSe (%)	30 to 50	ca. 1.5

[a] Data are obtained from the literature;[19,20] [b] crystallite size was calculated based upon PXRD data.

conventional drying produces higher density xerogels (Table 6.1). Both materials have mesoporous architectures, but of the two, the aerogels are considerably more porous and have sample densities only 8.5% that of water. The unique physical properties of the aerogel materials open up a wide variety of potential applications such as catalytic supports, sensors, thermal insulators, cosmic dust collectors and electrochemical device components.[21,22] Traditionally, the uses of aerogels have been very limited since they are often synthesized from metal oxides, which are either insulators or large band-gap semiconductors (e.g., SiO_2, Al_2O_3 and TiO_2); hence, non-metal oxide materials such as CdSe aerogels are of great interest due to their electro-optical properties, high surface area and high-porosity architectures.

Solid-state NMR spectroscopy has proven to be a powerful tool for characterization of molecular structure and dynamics in a variety of systems, including an assortment of amorphous solids[23] and sol-gel materials.[24-33] Several solution and solid-state NMR studies have been reported for CdS or CdSe molecular clusters and NPs. For instance, Thayer et al.[34] studied the size effect of CdSe molecular clusters on the appearance of solid-state ^{77}Se NMR spectra, which are inhomogeneously broadened as the cluster size decreases. The structure of the NP surface and dopant positions of the NPs were investigated in various NMR studies including solid-state ^{113}Cd NMR of CdS NPs,[35] Co-doped CdS NPs,[36] and Mn-doped CdSe NPs with and without TOP/TOPO capping ligands;[37,38] solid-state ^{31}P NMR of TOP/TOPO-capped CdSe NPs,[39] and solution ^{1}H NMR of CdS NPs with surface-bound H_2O.[17] A number of NMR studies have reported the structural characterization of surface ligands and NPs, as well as adamantanoid-cage complexes. They include 1D and 2D solution ^{1}H NMR of 2-ethylhexanoate-capped CdS NPs,[40] multinuclear solid-state NMR of TOP/TOPO-capped[41] and hexadecylamine- (HDA-) capped CdSe NPs and nano-scaled CdSeTe alloys,[42] and solution ^{113}Cd and ^{77}Se NMR of CdS and CdSe adamantanoid-cage complexes.[43] However, to the best of our knowledge, there have not been any reported NMR investigations of CdSe aerogels and xerogels to date, though they have been characterized by UV-visible and luminescence spectroscopy, powder X-ray diffraction (PXRD), nitrogen adsorption/desorption and scanning and transmission electron microscopy.[18-20]

Although the microscopic structure of the CdSe sol-gel materials is well established, there is very little known about their structures at the molecular level. In this chapter, we discuss a multinuclear solid-state NMR study of the CdSe aerogel and xerogel samples. Solid-state ^{111}Cd and ^{77}Se NMR and powder X-ray diffraction experiments were conducted on the aerogel and xerogel samples, as well as bulk crystalline CdSe, in order to compare structural differences between the microcrystalline and nanoscale materials. Solid-state ^{19}F, ^{13}C and ^{1}H MAS and variable-amplitude cross-polarization magic-angle spinning (VACP/MAS) NMR experiments are utilized for the identification of surface ligands and/or other organic agents that were used in the syntheses of the NPs. Solid-state NMR experiments are also used to examine NP-surface ligand interactions and the potential role these plays in stabilizing the long-range porous structure. Finally, the connectivities between organic species and metal sites at the surface of the NP core are also investigated by ^{1}H-^{111}Cd/^{77}Se and ^{19}F-^{111}Cd VACP/MAS NMR experiments.

6.2 Experimental

Sample preparation and handling. Crystalline CdSe was purchased from Aldrich and used without further purification. Cubic-phase CdSe nanoparticle (NP) xerogels[19] and aerogels[20] were synthesized according to literature procedures employing the inverse-micelle strategy. AOT was purchased from Acros and used as received.

Solid–state NMR. All samples were packed into 2.5 mm or 4.0 mm o.d. zirconia rotors under a nitrogen atmosphere. All solid-state NMR experiments were conducted on a Varian Infinity Plus NMR spectrometer with a 9.4 T wide–bore Oxford magnet, operating at $\nu_0(^{111}\text{Cd}) = 84.80$ MHz, $\nu_0(^{77}\text{Se}) = 76.20$ MHz, $\nu_0(^{19}\text{F}) = 376.08$ MHz, $\nu_0(^{13}\text{C}) = 100.52$ MHz and $\nu_0(^{1}\text{H}) = 399.73$ MHz. Varian/Chemagnetics 2.5 mm HX and 4 mm HX magic–angle spinning (MAS) probes were utilized for all experiments. For cadmium, ^{113}Cd is the generally preferred isotope due to its slightly higher NMR frequency; however, interference from a local FM radio station hindered the acquisition of high signal-to-noise (S/N) ^{113}Cd NMR spectra at 9.4 T (ν_0 = 89.18 MHz). Hence, solid-state ^{111}Cd NMR experiments were utilized instead. Since standard Bloch-decay acquisitions result in the loss of data points at the beginning of the free induction decay (FID) for broad NMR spectra, some solid-state NMR spectra were acquired using Hahn–echo pulse sequences of the form $[(\pi/2)_x - \tau_1 - (\pi)_y - \tau_2$–acquire] (where τ_1 and τ_2 are the inter–pulse delays). All MAS experiments employing the Hahn-echo pulse sequence were rotor synchronized. The spinning frequencies for all MAS and VACP/MAS NMR experiments were 21 to 23 kHz for ^{19}F, and 15 kHz or less for all other nuclei. ^{1}H and ^{19}F decoupling fields ranging from 31 to 76 kHz were applied where appropriate.

Cadmium chemical shifts were referenced to a 0.1 M $Cd(ClO_4)_2$ aqueous solution ($\delta_{iso}(^{111}Cd) = 0.0$ ppm) by setting the NMR resonance of solid $Cd(NO_3)_2$ to $\delta_{iso}(^{111}Cd) =$ -100 ppm. The calibrated $\pi/2$ pulse width was 2.6 μs. Selenium chemical shifts were referenced to neat $Se(CH_3)_2$ liquid ($\delta_{iso}(^{77}Se) = 0.0$ ppm) by setting the NMR resonance of solid $(NH_4)_2SeO_4$ to $\delta_{iso}(^{77}Se) = +1040$ ppm. The calibrated $\pi/2$ pulse width was 1.8 μs. Fluorine chemical shifts were referenced to neat $CFCl_3$ liquid ($\delta_{iso}(^{19}F) = 0.0$ ppm). For all ^{19}F MAS NMR experiments, the $\pi/2$ pulse widths were 3.1 μs. Carbon chemical shifts were referenced to TMS ($\delta_{iso}(^{13}C) = 0.0$ ppm) by setting the high-frequency NMR resonance of solid adamantane to 38.57 ppm. A $\pi/2$ pulse width of 3.0 μs with optimized recycle delays ranging from 10 to 300 s were applied in all $^{13}C\{^1H\}$ MAS NMR experiments. Proton chemical shifts were referenced to TMS ($\delta_{iso}(^1H) = 0.0$ ppm) by setting the NMR resonance of solid adamantane to 1.85 ppm. A $\pi/2$ pulse width of 1.6 μs was applied for all ^{1}H MAS NMR experiments. Recycle delays of either 1 or 6 s were used and 16 transients were collected for each experiment. ^{111}Cd, ^{77}Se and ^{19}F NMR experiments conducted on the aerogel, xerogel and bulk CdSe samples utilized calibrated recycle delays of 40 to 420, 600 and 20 s, respectively.

VACP/MAS NMR experiments. Solid-state ^{1}H/^{19}F-X (where X is the observe nucleus) VACP/MAS NMR experiments were run under optimized Hartmann-Hahn matching conditions, using rf fields during the contact time ranging from 78.1 to 87.6 kHz for ^{111}Cd, 57.9 to 67.0 kHz for ^{77}Se, and 39.6 to 87.6 kHz for ^{13}C. The initial ^{1}H/^{19}F $\pi/2$ pulse widths were between 1.6 to 2.0 μs for all VACP/MAS experiments. Optimized contact times varied from 4 to 20 ms and 1 to 3 ms for ^{111}Cd/^{77}Se and ^{13}C NMR experiments, respectively. Optimized recycle delays were determined from arrays of ^{1}H or ^{19}F Bloch-decay NMR experiments.

Spectral simulations. The cadmium and selenium chemical shielding (CS) tensor parameters of bulk CdSe were extracted from analytical simulations using WSOLIDS.[44]

Theoretical calculations. Restricted Hartree-Fock (RHF) and B3LYP hybrid density functional theory (Becke's three-parameter hybrid density functional[45,46] with the Lee, Yang and Parr correlation functional)[47] calculations were performed using the Gaussian 03 software package[48] on a dual-3.6 Xenon Dell Precision 670n workstation running Red Hat Linux 9.0. Cadmium and selenium CS tensors were calculated using the gauge-including atomic orbitals (GIAO) method.[49,50] Structural parameters of bulk hexagonal CdSe were obtained from previously reported X-ray study.[51] Basis sets that were utilized in all calculations are all-electron basis sets, which were either obtained from

EMSL Gaussian Basis Set Order Form via the Internet[52] or the basis set reference book by Huzinaga.[53] For Cd, DGauss DZVP polarized DFT orbitals basis sets (hereafter denoted as DZVP)[54] were used; while the Huzinaga with 4333/433/4 (for s/p/d orbitals) contraction,[53] Schafer, Horn and Ahlrichs VDZ[55] and TZV[56] basis sets (denoted as A-VDZ and A-TZV, respectively), as well as the correlation consistent polarized valence double zeta (cc-pVDZ), triple zeta (cc-pVTZ) and quadruple zeta (cc-pVQZ)[57-61] basis sets were applied for Se atoms. The absolute shielding of the Cd and Se nuclei were converted to the chemical shift scale, using $Cd(OH_2)_6^{2+}$ and $Se(CH_3)_2$, respectively (with both were set to $\delta_{iso} = 0.0$ ppm), as the primary references. The absolute shieldings of the reference compounds were obtained from a full geometry-optimized $Cd(OH_2)_6^{2+}$ ion and $Se(CH_3)_2$ molecule, at all previously mentioned levels of theory and basis sets. Theoretical isotropic Cd and Se chemical shifts can be obtained from $\delta_{iso} \approx \sigma_{ref} - \sigma_{sample}$.

Powder X–ray Diffraction. Powder X–ray diffraction (XRD) experiments were conducted on samples loaded into 0.7 mm o.d. capillary tubes using a Bruker AXS D8 DISCOVER powder X-ray diffractometer, which utilizes a Cu-Kα_2 ($\lambda = 1.54056$ Å) radiation source with a Bruker AXS HI-STAR area detector. Simulation of powder XRD patterns from known crystal structure[51] were performed using PowderCell software.[62]

6.3 Results and Discussion

Bulk CdSe. At room temperature, CdSe occurs in hexagonal[51] and cubic[63] phases, which have wurtzite and zinc blende structural types, respectively (Figure 6.2A). Both phases have single crystallographic Cd and Se sites which are four coordinate. However, in the hexagonal phase there are three identical (2.633 Å) and one distinct (2.629 Å; parallel with the *c*-axis) Cd-Se bond lengths, while in the cubic phase the Cd and Se atoms are at the centre of perfect tetrahedra (i.e., all four Cd-Se bond lengths = 2.631 Å). Comparison of the experimental PXRD pattern of bulk CdSe simulated patterns of hexagonal and cubic phases (Figure 6.2B) demonstrates that the bulk CdSe sample is clearly in hexagonal phase.

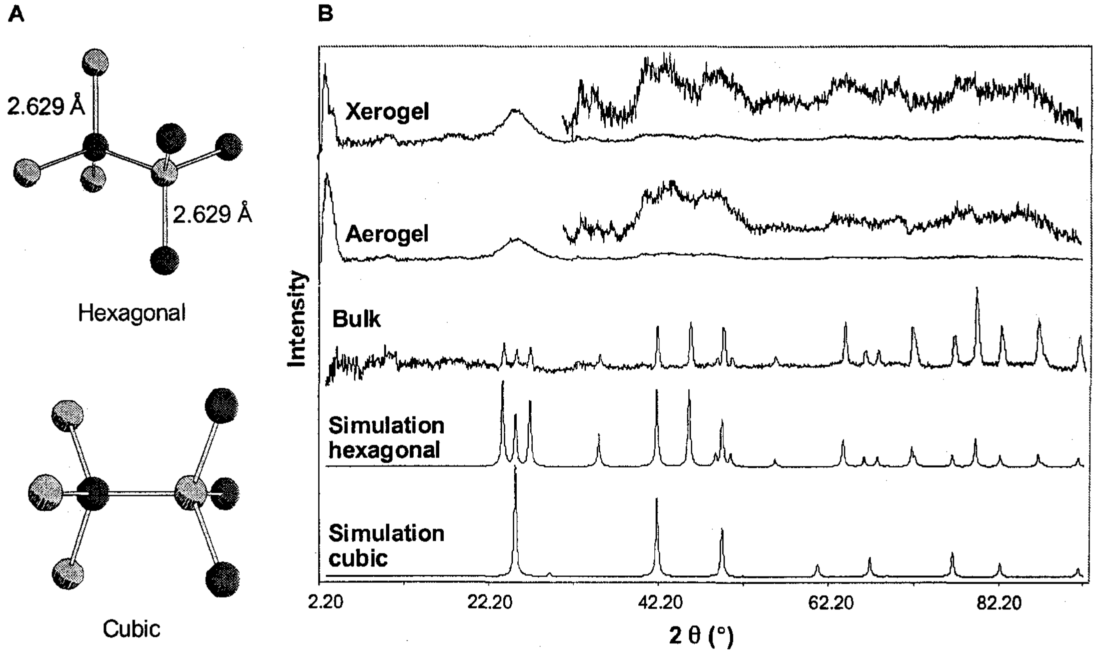

Figure 6.2. (A) Four-coordinate environments of the Cd (grey) and Se (red) atoms in hexagonal- and cubic-phase CdSe. (B) Experimental (room temperature) and simulated powder X-ray diffraction patterns of various CdSe-containing samples. Inset: vertical expansion of powder X-ray diffraction patterns of aerogel and xerogel samples in the $30.5° \leq 2\theta \leq 90°$ region.

Solid-state ^{111}Cd and ^{77}Se NMR spectra and their corresponding analytical simulations are pictured in Figure 6.3A,B. The CS tensor parameters (see Table 6.2 for

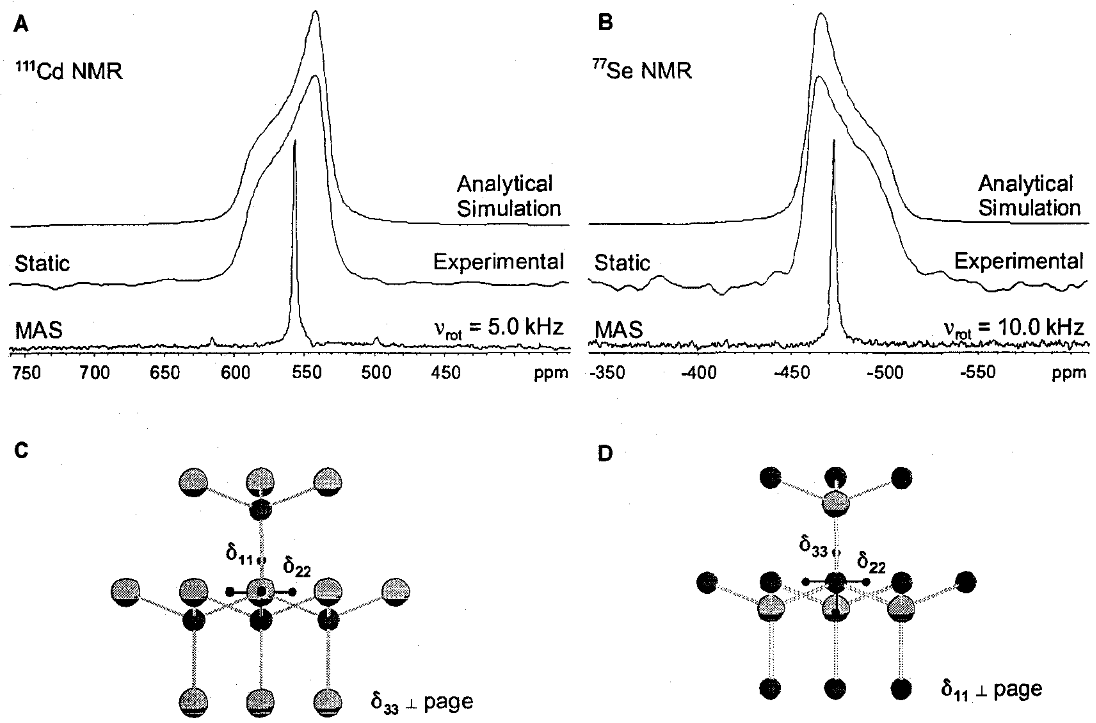

Figure 6.3. (A) ^{111}Cd and (B) ^{77}Se solid-state NMR spectra of bulk hexagonal CdSe. Calculated orientations of the (C) Cd and (D) Se CS tensors.

definition) are δ_{iso} = +557(1) ppm, Ω = 61(2) ppm and κ = -0.75(10) for cadmium, and δ_{iso} = -476(1) ppm, Ω = 44(2) ppm and κ = +1.00(10) for selenium, and are in reasonably good agreement with previously reported data.[41,64,65] The sizable chemical shielding anisotropies (CSA) further confirm that the bulk CdSe is in the hexagonal phase, since a CSA near zero would be expected for both tetrahedral Cd and Se sites in cubic CdSe (Tables A.6.1 and A.6.2 in appendix A). The cadmium CS tensor is near axial symmetry with a negative skew, indicating that δ_{11} is the distinct component of the CS tensor. On the other hand, the selenium CS tensor is of perfect axial symmetry, with δ_{33} as the unique component. Undoubtedly, the distinct CS tensor components must be oriented along the direction of the unique Cd-S bond of the hexagonal structure; however, in order to understand why the skews are of opposite signs, as well as the relationships between the

CS tensors and molecular structure, a set of theoretical calculations of the Cd and Se CS tensors has been performed.

Table 6.2. Experimental and Theoretical Cd CS Tensors Parameters of Bulk CdSe.

Source[a]	δ_{11}[b]	δ_{22}	δ_{33}	δ_{iso} (ppm)[c]	Ω (ppm)	κ
Experiment	**595**	**542**	**534**	**557(1)**	**61(2)**	**-0.75(10)**
RHF/Huzinaga[d]	995	984	984	987	11	-1.00
RHF/A-VDZ	939	921	921	972	18	-1.00
RHF/A-TZV	987	977	977	981	10	-1.00
RHF/cc-pVDZ	977	958	958	964	19	-1.00
RHF/cc-pVTZ	938	923	923	928	15	-1.00
RHF/cc-pVQZ	933	933	923	929	10	+1.00
B3LYP/Huzinaga	1073	1057	1056	1062	17	-0.84
B3LYP/A-VDZ	1040	1012	1011	1021	29	-0.92
B3LYP/A-TZV	1092	1073	1072	1079	20	-0.90
B3LYP/cc-pVDZ	1073	1043	1042	1053	30	-0.92
B3LYP/cc-pVTZ	1024	1001	999	1008	26	-0.83
B3LYP/cc-pVQZ	1007	1005	999	1004	9	0.36

[a] Calculations are conducted on large $Cd_{13}Se_4^{18+}$ clusters which involve the second-coordination sphere about the central Cd atom, with an all-electron DZVP basis set is applied on Cd atoms in all cases; [b] δ_{ii} (in ppm) are the principal components of the Cd/Se CS tensors such that $\delta_{11} \geq \delta_{22} \geq \delta_{33}$; [c] δ_{iso}, Ω and κ are defined as $(\delta_{11} + \delta_{22} + \delta_{33})/3$, $\delta_{11} - \delta_{33}$ and $3(\delta_{22} - \delta_{iso})/\Omega$, respectively; [d] basis sets that are applied on Se atoms.

The calculated Cd and Se CS tensor parameters are summarized in Tables 6.2 and 6.3, respectively. Initial calculations, which were conducted on small clusters involving only the first coordination sphere (i.e., $CdSe_4^{6-}$ and Cd_4Se^{6+} clusters), are in poor agreement with experimental values (Tables A.6.1 and A.6.2). Better agreement with experimental data was obtained from calculations on larger clusters with additional Cd and Se atoms in the second coordination sphere, i.e., the $Cd_4Se_{13}^{18-}$ and $Cd_{13}Se_4^{18+}$ clusters (Figure 6.3C,D). Interestingly, not only is the correct skew predicted, but improvement in

Table 6.3. Experimental and Theoretical Se CS Tensors Parameters of Bulk CdSe.

Source[a]	δ_{11}[b]	δ_{22}	δ_{33}	δ_{iso} (ppm)[c]	Ω (ppm)	κ
Experiment	**-461**	**-461**	**-505**	**-476(1)**	**44(2)**	**1.00(10)**
RHF/Huzinaga[d]	-1013	-1013	-1123	-1050	110	1.00
RHF/A-VDZ	-796	-796	-841	-811	45	1.00
RHF/A-TZV	-911	-911	-932	-918	21	1.00
RHF/cc-pVDZ	-767	-767	-813	-782	46	1.00
RHF/cc-pVTZ	-784	-784	-795	-788	11	1.00
RHF/cc-pVQZ	-943	-943	-946	-944	3	1.00
B3LYP/Huzinaga	-1044	-1054	-1175	-1091	132	0.85
B3LYP/A-VDZ	-739	-742	-795	-759	56	0.89
B3LYP/A-TZV	-955	-957	-964	-959	8	0.54
B3LYP/cc-pVDZ	-703	-706	-757	-722	54	0.90
B3LYP/cc-pVTZ	-834	-851	-857	-847	23	-0.47
B3LYP/cc-pVQZ	-1065	-1067	-1078	-1070	13	0.67

[a] Calculations are conducted on large $Cd_4Se_{13}^{18-}$ clusters, which involve the second-coordination sphere about the central Se atom, with an all-electron DZVP basis set is applied on Cd atoms in all cases; [b] δ_{ii} (in ppm) are the principal components of the Cd/Se CS tensors such that $\delta_{11} \geq \delta_{22} \geq \delta_{33}$; [c] δ_{iso}, Ω and κ are defined as $(\delta_{11} + \delta_{22} + \delta_{33})/3$, $\delta_{11} - \delta_{33}$ and $3(\delta_{22} - \delta_{iso})/\Omega$, respectively; [d] basis sets that are applied on Se atoms.

agreement with the experimental span is also obtained (though it is still underestimated in most cases). The discrepancy between experimental and ab initio results may originate from cluster calculations failing to accurately account for the effects of the extended lattice on chemical shielding Nevertheless, all of the calculations predict similar tensor orientations (Figure 6.3C,D). As expected, the unique components δ_{11} and δ_{33} of the Cd and Se CS tensors, respectively, are oriented along the unique Cd-Se bond and parallel to the unique axis (*c*-axis) of the crystal system, in agreement with our predictions from experimental data.

CdSe NP aerogels and xerogels. A comparison of the PXRD patterns of the CdSe aerogel and xerogel samples to that of bulk CdSe reveals that the molecular structure of the NPs is similar to the bulk material (Figure 6.2), suggesting the hexagonal CdSe structure is retained. The broad diffraction peaks of the xerogel and aerogel samples indicate there is some degree of disorder with respect to the bulk CdSe; however, the peak positions are consistent from sample to sample, suggesting an ordered crystalline NP core. The longer-range disorder originates from a range of subtly different chemical environments from the core to surface of the NP, consistent with previous observation for CdSe NPs/QDs.[42,66] The structure of the NP core is similar to that of the bulk sample, while the NP surface is influenced by interactions with surface ligands and perhaps even neighbouring NPs. The degree of broadening of the diffraction peaks prevents a definite conclusion as to whether the sol-gel samples are in the hexagonal or cubic phase; however, the set of high-angle diffraction peaks indicate the samples are likely in the hexagonal phase, though low-temperature syntheses resulting in cubic CdSe have been reported.[19,20,67,68] In addition, there are low-angle peaks at ca. 3° for both the aerogel and xerogel samples, which indicate some sort of long-range NP organization or packing.

The powder patterns in the ^{111}Cd{^{1}H} and ^{77}Se{^{1}H} NMR spectra of the aerogel sample are considerably broader than the sharp peaks of the bulk samples (Figure 6.4A to 6.4D), with full widths at half height (FWHH) for the aerogel and bulk samples of 8 kHz and 250 Hz (^{111}Cd) and 11 kHz and 200 Hz (^{77}Se). The centres of gravity of the main powder patterns are at $\delta(^{111}\text{Cd}) = 582$ ppm and $\delta(^{77}\text{Se}) = -571$ ppm, and occur to high and

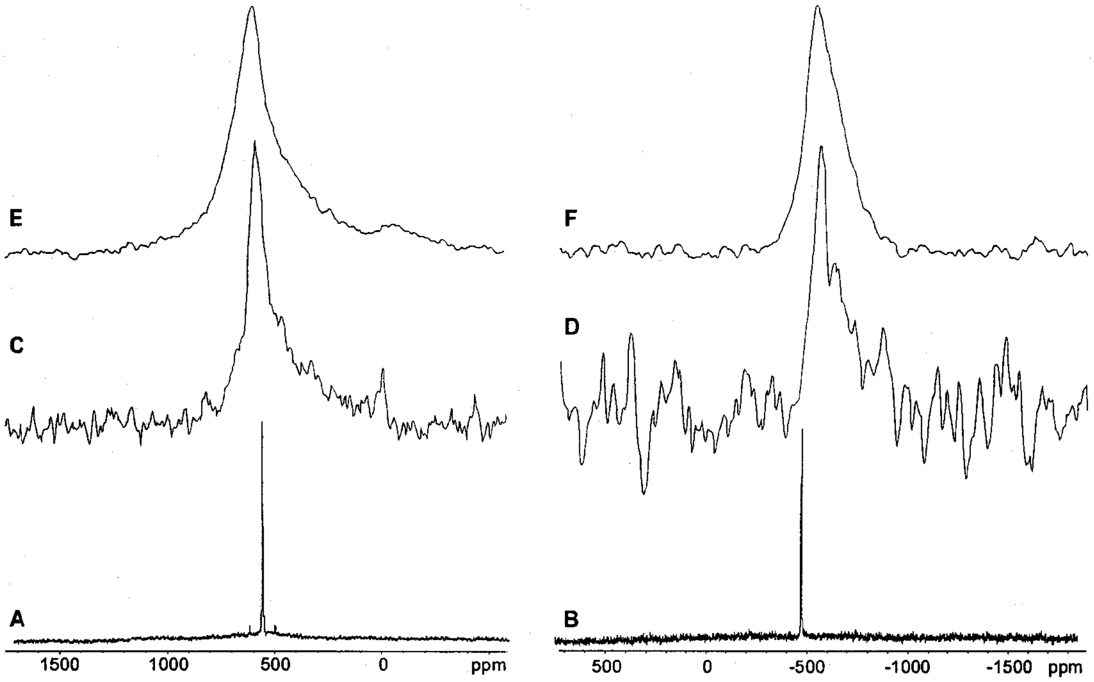

Figure 6.4. (A) ^{111}Cd and (B) ^{77}Se MAS NMR spectra of bulk hexagonal CdSe. (C) ^{111}Cd{^{1}H} and (D) ^{77}Se{^{1}H} MAS NMR spectra, and (E) ^{1}H-^{111}Cd and (F) ^{1}H-^{77}Se VACP/MAS NMR spectra, of CdSe aerogels. The number of transients collected in (C) to (F) were 352, 144, 10844 and 11724, respectively. All NMR spectra were acquired at spinning frequencies between 4.2 and 15.0 kHz.

low frequency of the corresponding resonances for the bulk CdSe sample, respectively. This indicates that on average, the ^{111}Cd and ^{77}Se nuclei in the aerogel sample are less and more shielded, respectively, than those in the bulk CdSe. The spectral broadening is undoubtedly the result of Cd/Se chemical shift distributions, which arise from the gradual change of Cd/Se environments from the NP core to its surface (Figures 6.5 and 6.6). The gradual change of Cd and Se chemical environments are consistent with previous observations on CdSe nanocrystals[42] and quantum dots.[66] The broadened ^{111}Cd and ^{77}Se powder patterns may also be indicative for surface Cd/Se sites which are at the interface between NPs. Interestingly, there seems to be correspondence between the preferential high and low frequency shifts of the ^{111}Cd and ^{77}Se patterns and the distinct

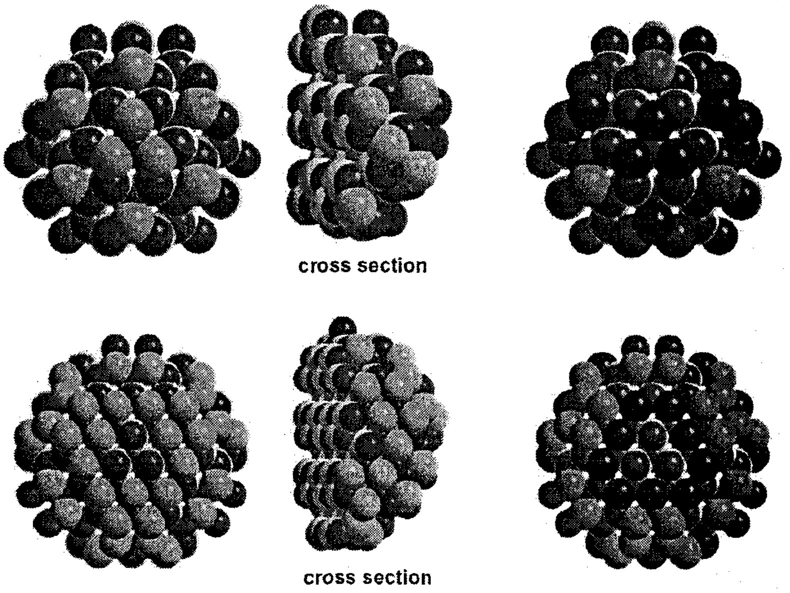

Figure 6.5. Diamond representation of long-range structure of hexagonal CdSe with diameters of (top) 2.2 and (bottom) 2.8 nm, which are used to model the xerogel and aerogel samples. All Se atoms are red. Surface Cd sites are denoted in cyan (left and middle), while Cd atoms in different coordination spheres are differentiated by colour: 2-(green), 3-(blue) and 4-coordinate (grey) (right).

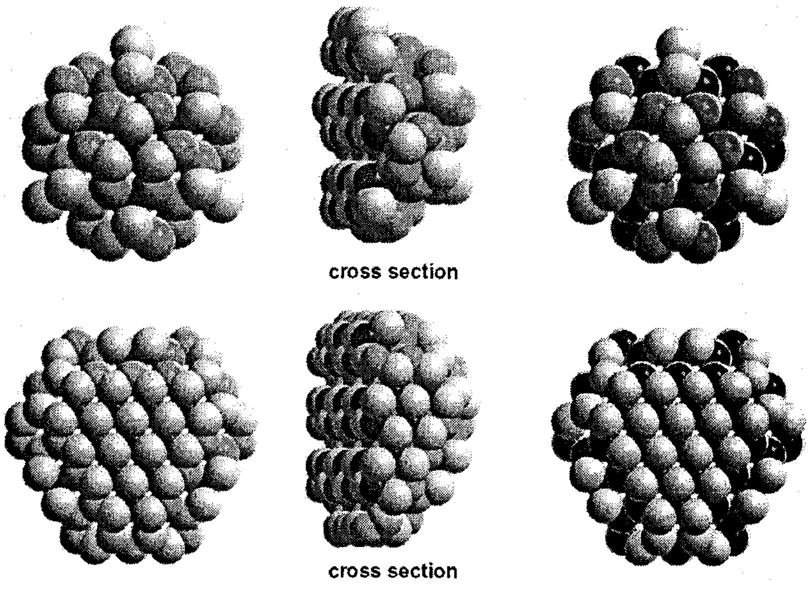

Figure 6.6. Diamond representation of long-range structure of hexagonal CdSe with diameters of (top) 2.2 and (bottom) 2.8 nm, which are used to model the xerogel and aerogel samples. All Cd atoms are grey. Surface Se sites are denoted in cyan (left and middle), while Se atoms in different coordination spheres are differentiated by colour: 2-(green), 3-(blue) and 4-coordinate (red) (right).

components of the cadmium and selenium shift tensors; that is, $\delta_{11}(^{111}Cd)$ and $\delta_{33}(^{77}Se)$, which are directed along or near the unique Cd-Se bonds and the *c*-axis of the unit cell. Finally, in the $^{111}Cd\{^1H\}$ MAS NMR spectra of the CdSe aerogel sample, two other NMR resonances of relatively low intensity are also observed (-20 and -440 ppm in Figure 6.4C), which may correspond to Cd sites that are either coordinated to surface ligands or perhaps involved in weak interactions with ligands from neighbouring NPs. Similar resonances are not observed in the corresponding $^{77}Se\{^1H\}$ NMR spectra, either due to low S/N or the absence of such sites.

Solid-state ^{1}H, ^{13}C and ^{19}F NMR Spectroscopy of Organic Species. During the synthesis of aerogel and xerogel samples, it was thought that most of the surface ligands and other organic species were removed during washing with acetone (Figure 6.1). However, NMR experiments show otherwise. In fact, the amount of "residual" surface ligands is quite significant, as evidenced by the intense peaks in the ^{1}H MAS NMR spectra of aerogel and xerogel samples (Figure 6.7), which required only 16 scans for the acquisition of high S/N spectra. In the ^{1}H MAS NMR spectra of both samples, proton peaks at 6.9(2) and 7.4(2) ppm correspond to the aromatic protons of FPhS (Figure 6.7, inset), consistent with solution NMR data.[69] There are no free FPhSH species, as evidenced by the absence of a sharp resonance in the vicinity of 3.5 ppm, which would correspond to thiol protons (FPh-S$\underline{H}$).[69-71] An interesting and important feature of these spectra is the presence of chemical shifts ranging from 0 to 4 ppm (Figure 6.7, inset) which correspond to aliphatic protons. Although some of the peaks in the aliphatic region are narrow in both NMR spectra, there is a significant degree of broadening, further

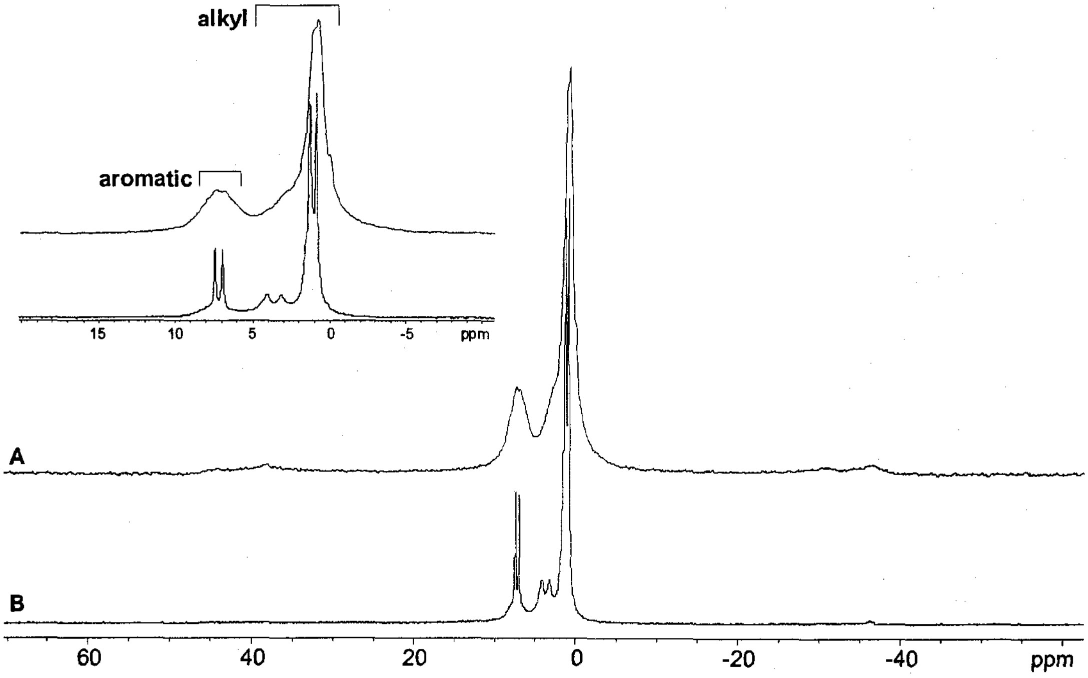

Figure 6.7. ^{1}H MAS NMR spectra of (A) CdSe aerogels and (B) xerogels. Both spectra were acquired at a spinning frequency of 15 kHz. Inset: horizontal expansion showing ^{1}H NMR resonances which correspond to aromatic and alkyl protons.

suggesting that there are no isotropically reorienting organic ligands. These spectra indicate that there are a number of other organic compounds coordinated to the NP surface, including AOT, triethylamine (TEA), *n*-heptane and acetone, all of which were employed in the NP synthesis (Figure 6.1). Identification of other organic compounds within the CdSe mesostructure is further discussed in the ^{13}C NMR section.

Comparison of the ^{1}H MAS NMR spectrum of the aerogel (Figure 6.7A) and xerogel (Figure 6.7B) samples reveal that the powder patterns in the former are more broadened. Spectral broadening in each case arises from both inhomogeneous and homogeneous contributions. Inhomogeneous broadening arises from the interaction between surface ligands and the amorphous NP surface, resulting in a distribution of proton chemical shifts, while homogeneous broadening arises from both different ^{1}H transverse relaxations time constants (T_2) and strong homonuclear dipolar coupling that is not completely averaged by MAS. The difference in peak widths between the two samples largely arises due to differences in homogeneous broadening contributions, for the following reasons. The longitudinal relaxation time (T_1) is shorter in the xerogels than in the aerogels, as evidenced by the optimized recycle delays utilized for spectra acquisition (recycle times = 1 s and 6 s for xerogel and aerogel samples, respectively). The ^{1}H T_2 relaxation times are likely much longer in the xerogel than in the aerogel. The shorter T_1 and longer T_2 in the xerogel sample indicates the surface ligands are more mobile than in the aerogel samples. This is consistent with reduced broadening from homonuclear dipolar couplings and sharper peak widths in the xerogel spectrum. A variable-temperature relaxation study would certainly shed more light on this aspect of the surface ligands, but is beyond the scope of the present study.

The ^{1}H-^{13}C VACP/MAS NMR spectra of the xerogel and aerogel are presented in Figure 6.8. Both NMR spectra confirm the presence of FPhS ligands in both samples, with the ^{13}C NMR resonances ranging from 115 to 170 ppm in both spectra are assigned to the ortho, meta and para carbons (ca. 115, 130 and 162 ppm, respectively). The peak assignments are confirmed by a comparison to the ^{19}F-^{13}C VACP/MAS NMR spectrum of the xerogel sample (Figure 6.8C), and are in good agreement with the literature.[72] Depicted in Figure 6.8E is the ^{1}H-^{13}C VACP/MAS NMR spectrum of free AOT. This NMR spectrum is in excellent agreement with previously reported solution ^{13}C NMR data.[73-75] Comparison of the ^{13}C NMR spectrum of free AOT to the ^{13}C NMR spectra of xerogel and aerogel samples reveals the presence of a significant amount of AOT

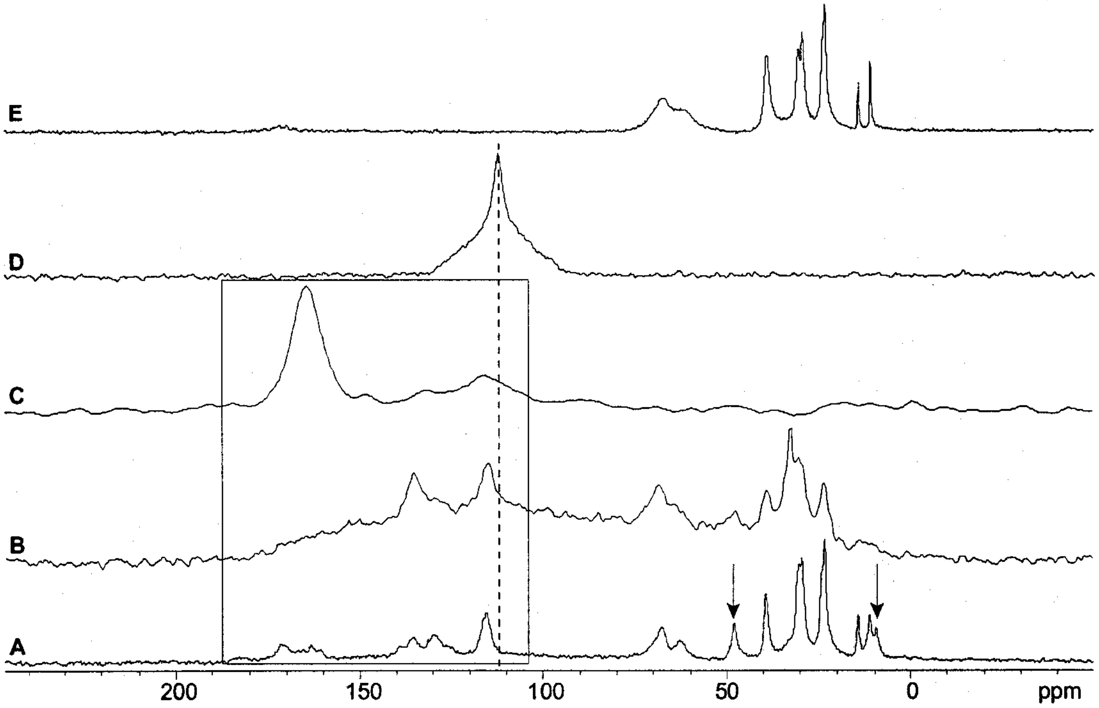

Figure 6.8. ^{1}H-^{13}C VACP/MAS NMR spectra of the CdSe (A) xerogel, (B) aerogel and (E) free AOT samples. The ^{19}F-^{13}C VACP/MAS NMR spectrum of CdSe xerogels is shown in (C), while the ^{19}F-^{13}C CP/MAS NMR spectrum of Teflon rotor spacers is depicted in (D). All NMR spectra were acquired at spinning frequencies between 4 to 14 kHz. Arrows in (A) indicate NMR resonances corresponding to TEA. The NMR resonances corresponding to FPhS ligands are surrounded by a box. The vertical line indicates no ^{19}F peak corresponding to Teflon is observed in (A) to (C).

ligands in the latter. The coexistence of both AOT and FPhS ligands is also consistent with the ^{1}H NMR data (Figure 6.7). Finally, two ^{13}C peaks with low intensity, which correspond to the ethyl and methyl carbons of TEA,[76] are resolved in the ^{1}H-^{13}C VACP/MAS NMR spectrum of the xerogel sample (Figure 6.8A).

The peaks in both ^{1}H-^{13}C VACP/MAS and $^{13}C\{^{1}H\}$MAS NMR spectra of the xerogel sample are narrower than those in the ^{13}C NMR spectra of aerogels (Figure 6.9), similar to the observations from the ^{1}H NMR data. This is again suggestive of higher ligand mobility for both AOT and FPhS ligands in the xerogel sample. Again, it is

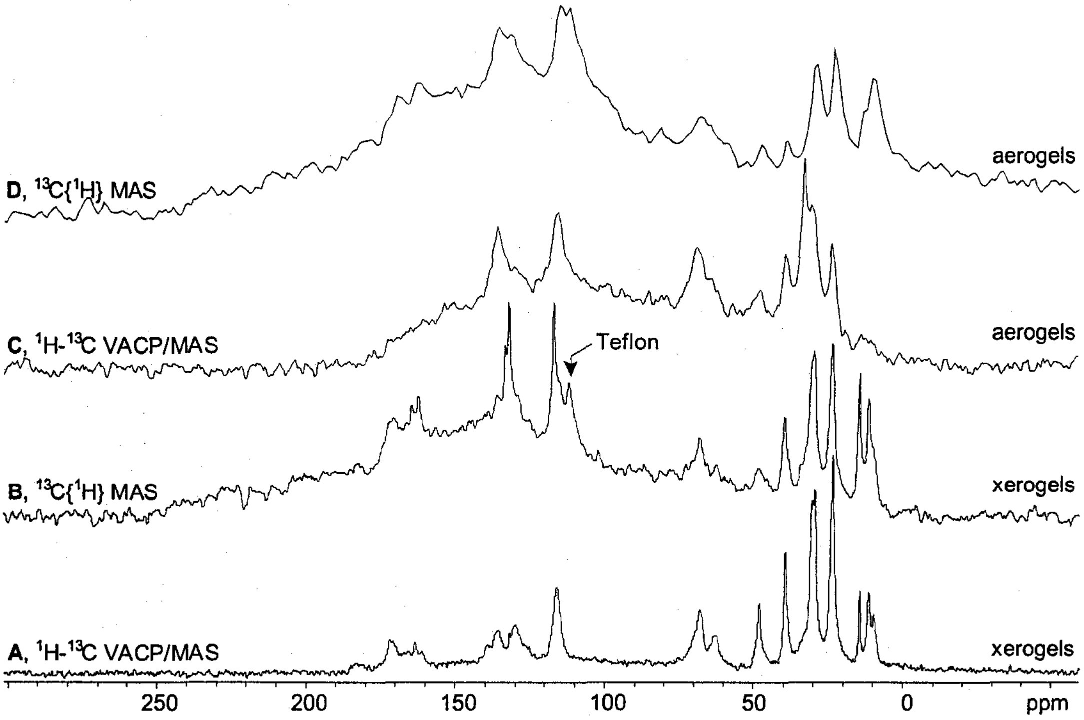

Figure 6.9. ^{1}H-^{13}C VACP/MAS and ^{13}C{^{1}H} MAS NMR spectra of CdSe (A,B) xerogels and (C,D) aerogels. All NMR spectra were acquired at spinning frequencies ranging 13.1 to 15.0 kHz.

important to note that none of the surface ligands are freely tumbling, as evidenced by the generally broad NMR resonances, the success of the VACP/MAS NMR experiments, and the absence of sharp resonances in Bloch decay ^{13}C{^{1}H} MAS NMR spectra which would indicate such species (Figure 6.9).

The presence of AOT is somewhat surprising, since it should have been removed by repeated washing with *n*-heptane (Figure 6.1). According to descriptions of the syntheses of the xerogel and aerogel samples,[19,20] this step is crucial, since successful removal of the AOT ligands or exchange of these ligands with FPhS is important for efficient gelation of CdSe NPs. Inefficient removal/exchange would clearly reduce the porosity of the sol-gel materials. It is possible that different pH conditions should be considered in the AOT-FPhS exchange step during synthesis.

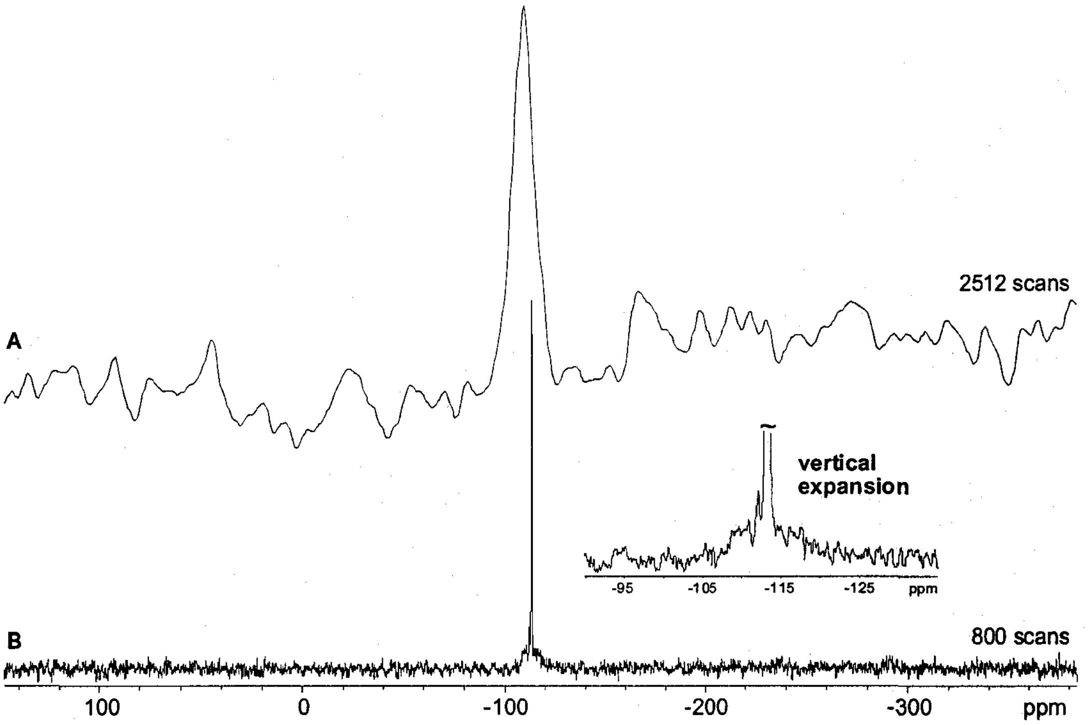

Figure 6.10. ^{19}F MAS NMR spectra of (A) the CdSe aerogel and (B) xerogel samples, which were acquired at spinning frequencies of 21 and 23 kHz, respectively. The number of transients collected for each spectrum is indicated on the right. Inset: vertical expansion around the isotropic region of (B).

The powder patterns in ^{19}F MAS NMR spectra of the aerogel and xerogel sample confirm that residual FPhS remains in both samples (Figure 6.10). For the aerogel sample, a broad ^{19}F powder pattern is centred at -109(2) ppm with a FWHH = 5.0(2) kHz. The experiment was conducted at a rotational frequency of 21 kHz, which is high enough to average the ^{19}F-^{19}F dipole-dipole interactions (a dipolar coupling constant of ca. 4 kHz is calculated for a ^{19}F-^{19}F spin pair with the internuclear distance of 3 Å, which is much shorter than any expected intermolecular ^{19}F-^{19}F contacts). The centre of gravity of the broad fluorine pattern is consistent with the chemical shift value of free FPhS molecules.[77] The ^{19}F MAS NMR spectrum of the xerogel sample consists of a single, sharp NMR peak, with a broad, low-intensity pattern underneath (Figure 6.10B and inset). The sharp peak has an isotropic chemical shift of -113(1) ppm with a FWHH of 140(10) Hz. The broad pattern in the ^{19}F NMR spectrum of aerogels stems from a distribution of fluorine chemical shifts and/or short ^{19}F T_2 relaxation times. The former would arise from a variety of interaction of the FPhS ligands with the amorphous NP surface, while the latter would result from the reduced mobility FPhS ligands. The extremely sharp line in the NMR spectrum of xerogel sample suggests that there is probably not a significant chemical shift distribution, and that there is a much longer ^{19}F T_2 relaxation time in the xerogel, confirming that the FPhS ligands on the xerogel surface have increased mobility. The broad underlying pattern corresponds to a small fraction of less mobile FPhS ligands.

Surface ligands-NP connectivity. In order to probe the connectivity between CdSe NP surface and the organic ligands, ^{1}H-^{111}Cd and ^{1}H-^{77}Se VACP/MAS NMR experiments were conducted on the aerogel sample (Figure 6.4E,F). The ^{111}Cd and ^{77}Se NMR powder patterns in these spectra are of higher S/N and much broader (FWHH = 17 and 14 kHz for ^{111}Cd and ^{77}Se NMR powder patterns, respectively) than their non-CP counterparts. The ^{1}H-^{111}Cd VACP/MAS spectrum of the aerogel sample consists of an intense powder pattern (ca. 600 ppm) and a broad low intensity pattern (ca. -30 ppm); however, no NMR resonance is observed in the -440 ppm region. The powder pattern in ^{1}H-^{77}Se VACP/MAS NMR spectrum resembles that obtained from the Bloch-decay MAS experiment; however, no resonance other than the one corresponding to core Se sites is observed. The ^{1}H-^{111}Cd/^{77}Se VACP/MAS NMR experiments required much shorter experimental times (by typically 40%) and yielded higher S/N (4×) than standard MAS experiments. The higher S/N and broader patterns indicate that the CP experiments are successful at enhancing both ^{111}Cd and ^{77}Se NMR signals arising from nuclei close to the NP surface and therefore proximate to the proton-rich surface ligands. The distinct powder pattern near -30 ppm very likely corresponds to Cd sites interacting with oxygen-donor ligands.[78]

Ligand-NP interactions at the NP surface. The efficiency of CP/MAS experiments relies upon internuclear dipolar interactions between abundant and dilute spins, the magnitude of which diminish as the inverse cube of the internuclear separation. Hence, it may be possible to determine which portions of the powder pattern correspond to core and surface Cd/Se sites by varying the contact time during spin cross polarization. Since the CP/MAS NMR spectra are of high intensity, and there are no paramagnetic impurities in these samples, the experimental behaviour can be said to operating in the fast CP regime.[79] Therefore, during the contact time of CP/MAS experiments, the rate of magnetization build up for the dilute spins (^{111}Cd) depends upon the cross-relaxation time constant (T_{CdH}) and the longitudinal relaxation time constant of protons in the rotating frame ($T_{1\rho\mathrm{H}}$).[80,81] T_{CdH} depends upon the internuclear distances between the ^{1}H and ^{111}Cd spins, with increasing CP efficiency (increased CP rate) as the internuclear distance decreases. If the dipolar interaction is averaged by molecular motions, this CP efficiency can decrease. $T_{1\rho\mathrm{H}}$ is largely influenced by relaxation resulting from dipolar interactions among the protons themselves; hence, strong fluctuating dipolar couplings will serve to limit the length of the applied contact time.

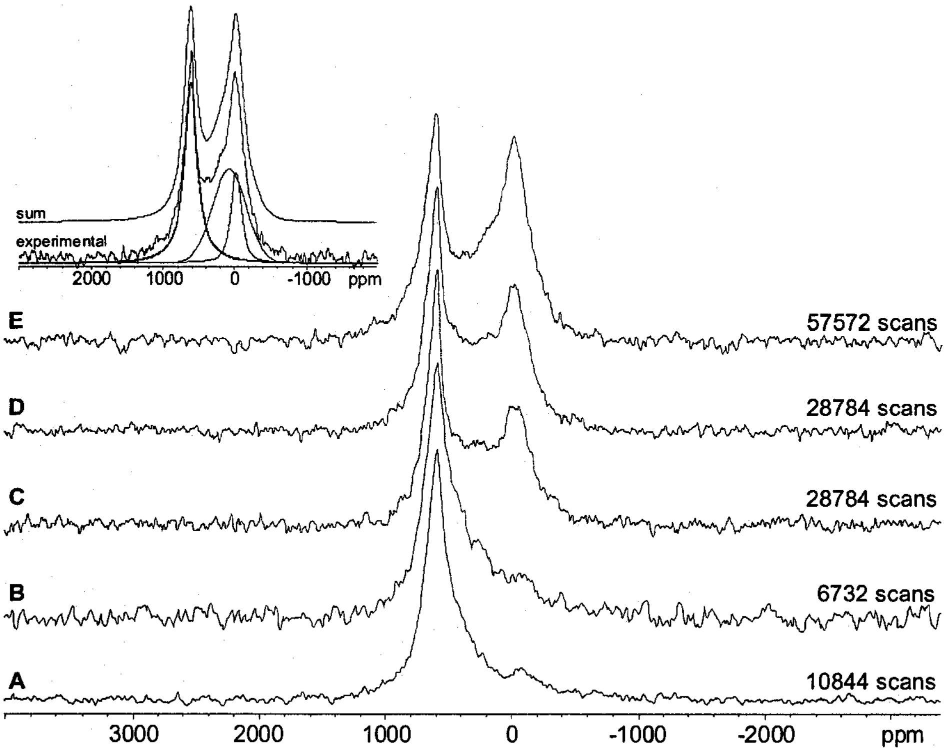

Figure 6.11. Variable contact time ^{1}H-^{111}Cd VACP/MAS NMR spectra of CdSe (A) and (B) aerogels, and (C) to (E) xerogels. The contact times of each spectrum were (A) 12, (B) 4, (C) 16, (D) 10 and (E) 4 ms. The number of transients collected for each spectrum is shown on the right. All NMR spectra were acquired at spinning frequency of 5.0 kHz. Inset: deconvolution of (E) reveals core, intermediate and surface Cd sites.

Variation of the contact time in ^{1}H-^{111}Cd CP/MAS NMR experiments on the aerogel samples results in no measurable change in intensities for resonances at 600 and -30 ppm (Figure 6.11A,B). However, for the xerogel sample, signal enhancement is observed in powder patterns corresponding to Cd surface species (ca. -30 ppm), when NMR experiments employing shorter contact times (16 to 10 to 4 ms; Figure 6.11C to 6.11E) are applied. The short contact times that were used to achieve optimal signal intensity for resonances corresponding to the surface Cd sites are consistent with the surface species being close to the proximate ^{1}H spins of the ligands (i.e., a strong dipolar interaction between ^{111}Cd and ^{1}H). Similar observations have been reported for ^{1}H-^{29}Si CP/MAS NMR study of sol-gel microporous silica,[29] multiple ^{1}H-^{13}C CP/MAS NMR studies of Delrin,[82] coal,[83] wood and wood pulping,[84] as well as ^{1}H-^{15}N CP/MAS study of pyridine-absorbed silica-alumina.[85] Relatively efficient $T_{1\rho H}$ relaxation arising from dipolar interactions among the protons in the mobile surface ligands of the xerogel gradually causes a decrease in CP efficiency. This is not observed for the aerogel, consistent with the reduced mobility of these surface ligands and corresponding decrease in $T_{1\rho H}$ efficiency. Regardless of the contact time applied in ^{1}H-^{111}Cd VACP/MAS experiments on the xerogel sample, the powder patterns at ca. -30 ppm are much more intense than those in the NMR spectra of the aerogel sample. This suggests that either (i) there are more AOT ligands interacting with Cd sites at the NP surface of the xerogels in comparison to aerogels, and/or (ii) the surface/bulk ratio is much higher in the xerogel sample (surface/bulk Cd sites = 0.64:1.0 for xerogel and 0.56:1.0 for aerogel, which are determined from the 2.2 and 2.8 nm CdSe crystallites depicted in Figure 6.6).

The shape of all NMR powder patterns for the xerogel sample reveal the presence of at least three types of Cd environments, corresponding to core, intermediate and surface. The inset of Figure 6.11 illustrates the Gaussian deconvolution and the weight contributed from the three species with their centres of gravity at 622(5), 74 (10) and -23(5) ppm originating from core, intermediate and surface Cd sites, respectively. The ratios of areas of the powder patterns corresponding to core, intermediate and surface sites are 10:14:4 (ct = 4 ms), 10:16:2 (ct = 10 ms), and 10:15:2 (ct = 16 ms). Comparison of the three Cd powder patterns reveals that ^{111}Cd nuclei close to the NP surface are more shielded, which is consistent with both decreased Se coordination and increased O and/or S coordination.[38,42,86,87] In addition, there may be some vacant Se surface sites where the ligands may bind (as observed by Strouse et al. in their study of discrete HDA-capped CdSe NPs).[42] In both the xerogel and aerogel, S atoms (of FPhS ligands) or the O atoms (of AOT) can interact with tetrahedral Cd environments at these sites, which would lead to high- and low-frequency shifts of the ^{111}Cd NMR resonances, respectively.[78] Therefore, the resonances near -30 ppm are assigned to surface Cd sites that are coordinated to one or more oxygen atoms of the AOT ligands.

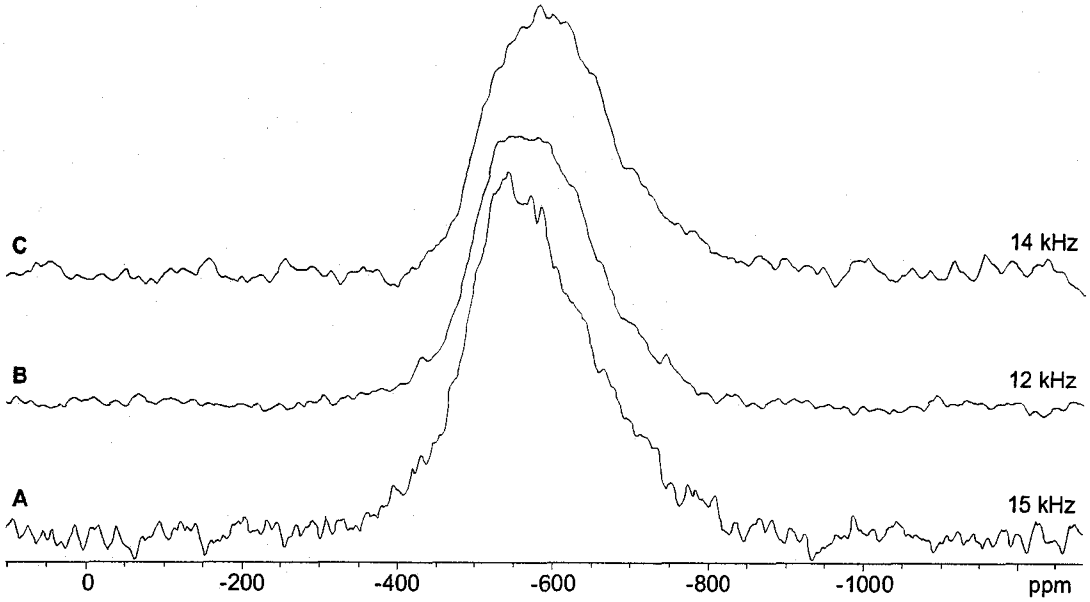

Figure 6.12. ^{1}H-^{77}Se VACP/MAS NMR spectra of CdSe (A) aerogels (ct = 20 ms), and (B),(C) xerogels (ct = 20 and 4 ms, respectively). All NMR spectra were acquired at spinning frequencies between 4.2 and 5.0 kHz. FWHH in kHz of the NMR powder patterns are indicated on the right.

Unlike the ^{1}H-^{111}Cd VACP/MAS NMR experiments, variable-contact-time ^{1}H-^{77}Se VACP/MAS NMR spectra of the aerogel and xerogel samples are less informative, and vary little between samples (Figure 6.12). All NMR spectra consist of a broad powder pattern, which cannot be deconvoluted, with similar FWHH of 15(2), 12(2) and 14(2) kHz for the aerogel (ct = 20 ms) and xerogel samples (ct = 20 and 4 ms), respectively. The centres of gravity of the powder patterns are slightly different from each other (-565(10), -574(10) and -597(10) ppm, respectively). Given that the chemical shift range of Se is ca. 3300 ppm[88] and the gyromagnetic ratio of Se (5.1214×10^7 rad T^{-1} s^{-1}) is similar to that of Cd (-5.7046×10^7 rad T^{-1} s^{-1}), it is expected that if there are ligands coordinated to surface Se sites, that distinct resonances would be observed in the ^{1}H-^{77}Se VACP/MAS NMR spectra. The similarity of variable contact time ^{1}H-^{77}Se VACP/MAS NMR spectra of both aerogel and xerogel samples indicate that while CP from the ^{1}H nuclei of the surface ligands to sites with ^{77}Se nuclei, that they are further separated than ^{1}H-^{111}Cd spin pairs. This strongly infers that both FPhS and AOT ligands are directly interacting with the surface Cd sites, and interactions with surface Se sites are absent or limited.

Surface ligand mobilities in the aerogel and xerogel are related to the interactions between FPhS/AOT ligands and the NP surface (i.e., the coordination between the S/O and Cd atoms). A number of studies of CdS molecular cages and clusters have demonstrated that the S atoms of thiophenolate ligands can be terminally bound to Cd or doubly/triply bridging over multiple Cd sites.[89-92] For CdS nanocrystals, it was observed via solution ^{1}H and ^{13}C NMR experiments that the thiophenolate ligands are terminally bound to the surface.[93,94] For the CdSe aerogel and xerogel samples, careful inspection of the surface Cd sites of a nearly spherical NP with a diameter of approximately 2 nm, which was generated from the known crystal structure of hexagonal CdSe (Figure 6.13), may provide insights into the bonding motifs. The terminal bonding

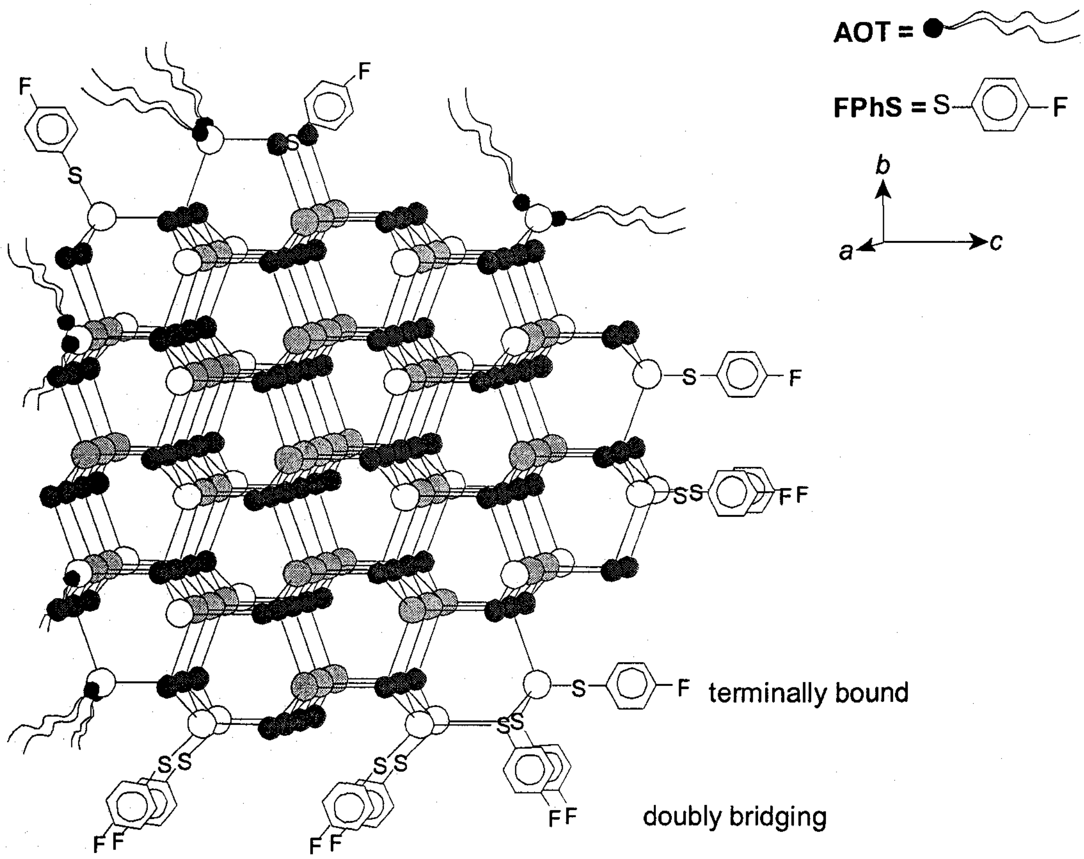

Figure 6.13. A schematic picture showing some of the bridging and terminal interactions between FPhS/AOT ligands and the Cd surface sites (white) of a 2.2 nm hexagonal CdSe crystallite (xerogel). 4-coordinate Cd and Se atoms are in light and dark grey colouration, respectively.

motif allows rotation about the Cd-S axis, which would allow some degree of mobility, giving rise to the narrow ^{19}F NMR peak for the xerogel (Figure 6.10B). On the other hand, the broad, low-intensity pattern in same ^{19}F MAS NMR spectrum could correspond to ^{19}F nuclei in the FPhS ligands which have bridging interactions with Cd sites at the NP surface (Figure 6.13). For the ^{19}F NMR spectrum of the aerogel sample, the broad powder pattern and the absence of a sharp resonance result from FPhS ligands with restricted mobility, possibly from bridging bonding motifs. The presence of (mainly) terminally bound FPhS in the xerogel and bridging FPhS in the aerogel supports the hypothesis of higher organic surface coverage in the former.

^{19}F-^{111}Cd VACP/MAS NMR experiments, with a recycle time of 20 s (optimized in the ^{19}F MAS NMR experiments on the xerogel sample), and broad ranges of CP mixing powers and contact times, did not yield an observable ^{111}Cd NMR signal for either sample. The failure of ^{19}F-^{111}Cd CP/MAS NMR experiments to produce observable signals arises from (i) the limited number of FPhS ligands on the NP surface, (ii) the relatively long internuclear distances between ^{19}F and ^{111}Cd (e.g., a ^{19}F-^{111}Cd internuclear distance of 6 Å results in a dipolar coupling constant of 111 Hz), and (iii) rotation about the Cd-S axis which may wholly/partially average ^{19}F-^{111}Cd dipole-dipole interaction. The oxygen atoms of the AOT ligand can also form terminal or bridging bonds with Cd sites at the NP surface. In the same manner as FPhS, it is possible that the sharper ^{1}H and ^{13}C NMR resonances in the xerogel spectra stem from increased mobility of the AOT ligands due to a higher number of terminally bound AOT surface ligands. However, the AOT ligand is relatively bulky in comparison to FPhS, and will generally have more restricted mobility; hence the differences between the ^{1}H and ^{13}C NMR spectra of the aerogel and xerogel are not as dramatic as in the case of the ^{19}F NMR spectra.

6.4 Conclusion

Solid-state NMR and PXRD experiments were utilized to examine CdSe aerogel and xerogel NP samples. Spectral broadening of ^{111}Cd and ^{77}Se resonances in ^{111}Cd{^{1}H} and ^{77}Se{^{1}H} MAS NMR spectra, as well as peaks in the PXRD patterns, indicate that there is some degree of structural disorder (i.e., a size effect), which arises from gradual differentiation of sites from the core to the surface of the NP. At the NP surface, the presence of AOT, TEA and FPhS ligands is verified by ^{1}H and ^{13}C NMR experiments (as well as ^{19}F NMR experiments for FPhS). The presence of broad NMR powder patterns, the generally high efficiency of CP/MAS experiments and the absence of sharp isotropic peaks in Bloch decay MAS NMR experiments indicate that the organic species are constrained at the NP surfaces. The generally narrow NMR resonances for the xerogel and the broader powder patterns in the NMR spectra of aerogel indicate high and low ligand mobilities, respectively.

Surface ligand-NP connectivity is studied via ^{1}H-^{111}Cd and ^{1}H-^{77}Se CP/MAS experiments. For the former, powder patterns corresponding to core and surface Cd sites are enhanced via ^{1}H polarization transfer. ^{1}H-^{111}Cd VACP/MAS NMR experiments reveal core, intermediate and surface Cd sites, with surface resonances enhanced at shorter contact times. However, ^{1}H-^{77}Se VACP/MAS experiments yield broad spectra but give no indication of surface Se sites. These experiments suggest that surface ligands interact almost exclusively with the Cd atoms at the NP surface. Inspection of the ratio of surface to bulk Cd sites in the 2.2 nm and 2.8 nm NPs reveals that there are many more surface Cd sites present in the former. Both terminal and bridging interactions between the Cd sites at the NP surface and FPhS/AOT ligands are possible, with the former allowing for increased mobility of the surface ligands.

While this study has elucidated some fascinating elements of molecular structure and dynamics in these systems, further studies including (i) CASTEP plane wave calculations on the bulk CdSe to improve agreement between theoretical Cd/Se CS tensors parameters and experiments, (ii) measurements of ^{1}H, ^{13}C and ^{19}F T_1, T_2 and $T_{1\rho}$ relaxation time constants, and (iii) ^{1}H-^{111}Cd HETCOR experiments will provide key pieces of information that will undoubtedly confirm our current structural model. The major piece of information is regarding inter-nanoparticle interactions which are responsible for holding the sol-gel matrices together; as of yet, these interactions have not definitively revealed themselves in our NMR experiments.

Bibliography

[1] Dabbousi, B.O., Bawendi, M.G., Onitsuka, O., Rubner, M.F. *Appl. Phys. Lett.* **1995**, *66*, 1316.

[2] Alivisatos, A.P. *Science* **1996**, *271*, 933.

[3] Klimov, V.I. et al. *Science* **2000**, *290*, 314.

[4] Dahan, M., Laurence, T., Pinaud, F., Chemla, D.S., Alivisatos, A.P., Sauer, M., Weiss, S. *Opt. Lett.* **2001**, *26*, 825.

[5] Chan, W.C.W., Maxwell, D.J., Gao, X., Bailey, R.E., Han, M., Nie, S. *Current Opinion in Biotechnology* **2002**, *13*, 40.

[6] Wang, Y., Herron, N. *J. Phys. Chem.* **1991**, *95*, 525.

[7] D'Amore, F. et al. *Phys. Stat. Sol. C* **2004**, *1*, 1001.

[8] Michalet, X. et al. *Science* **2005**, *307*, 538.

[9] Colvin, V.L., Schlamp, M.C., Alivisatos, A.P. *Nature* **1994**, *370*, 354.

[10] Huynh, W.U., Dittmer, J.J., Alivisatos, A.P. *Science* **2002**, *295*, 2425.

[11] Sun, B.Q., Marx, E., Greenham, N.C. *Nano Lett.* **2003**, *3*, 961.

[12] Liu, J.S., Tanaka, T., Sivula, K., Alivisatos, A.P., Frechet, J.M.J. *J. Am. Chem. Soc.* **2004**, *126*, 6550.

[13] Meeker, K., Ellis, A.B. *J. Phys. Chem. B* **1999**, *103*, 995.

[14] Ivanisevic, A., Reynolds, M.F., Burstyn, J.N., Ellis, A.B. *J. Am. Chem. Soc.* **2000**, *122*, 3731.

[15] Nazzal, A.Y., Qu, L.H., Peng, X.G., Xiao, M. *Nano Lett.* **2003**, *3*, 819.

[16] Scolan, E., Magnenet, C., Massiot, D., Sanchez, C. *J. Mater. Chem.* **1999**, *9*, 2467.

[17] Ladizhansky, V., Hodes, G., Vega, S. *J. Phys. Chem. B* **2000**, *104*, 1939.

[18] Mohanan, J.L., Arachchige, I.U., Brock, S.L. *Science* **2005**, *307*, 397.

[19] Arachchige, I.U., Mohanan, J.L., Brock, S.L. *Chem. Mat.* **2005**, *17*, 6644.

[20] Arachchige, I.U., Brock, S.L. *J. Am. Chem. Soc.* **2006**, *128*, 7964.

[21] Rolison, D.R., Dunn, B. *J. Mater. Chem.* **2001**, *11*, 963.

[22] Husing, N., Schubert, U. *Angew. Chem.-Int. Edit.* **1998**, *37*, 22.

[23] Eckert, H. *Curr. Opin. Solid State Mat. Sci.* **1996**, *1*, 465.

[24] Heinrich, T., Raether, F., Marsmann, H. *J. Non-Cryst. Solids* **1994**, *168*, 14.

[25] Scharf, U., Schneider, M., Baiker, A., Wokaun, A. *J. Catal.* **1994**, *149*, 344.

[26] Komarneni, S., Rutiser, C. *J. European Ceram. Soc.* **1996**, *16*, 143.

[27] Stallworth, P.E., Johnson, F.S., Greenbaum, S.G., Passerini, S., Flowers, J., Smyrl, W. *J. Appl. Phys.* **2002**, *92*, 3839.

[28] Husing, N., Bauer, J., Kalss, G., Garnweitner, G., Kickelbick, G. *J. Sol-Gel Sci. Technol.* **2003**, *26*, 73.

[29] Cannas, C., Casu, M., Musinu, A., Piccaluga, G. *J. Non-Cryst. Solids* **2004**, *351*, 3476.

[30] Marzouk, S., Rachdi, F., Fourati, M., Bouaziz, J. *Colloid Surf. A-Physicochem. Eng. Asp.* **2004**, *234*, 109.

[31] Baumann, T.F., Gash, A.E., Chinn, S.C., Sawvel, A.M., Maxwell, R.S., Satcher, J.H. *Chem. Mat.* **2005**, *17*, 395.

[32] Moudrakovski, I.L., Ratcliffe, C.I., Ripmeester, J.A., Wang, L.Q., Exarhos, G.J., Baumann, T.F., Satcher, J.H. *J. Phys. Chem. B* **2005**, *109*, 11215.

[33] Ma, Z.R., Dunn, B.C., Turpin, G.C., Eyring, E.M., Ernst, R.D., Pugmire, R.J. *Fuel Process. Technol.* **2007**, *88*, 29.

[34] Thayer, A.M., Steigerwald, M.L., Duncan, T.M., Douglass, D.C. *Phys. Rev. Lett.* **1988**, *60*, 2673.

[35] Elbaum, R., Vega, S., Hodes, G. *Chem. Mat.* **2001**, *13*, 2272.

[36] Ladizhansky, V., Vega, S. *J. Phys. Chem. B* **2000**, *104*, 5237.

[37] Mikulec, F.V., Kuno, M., Bennati, M., Hall, D.A., Griffin, R.G., Bawendi, M.G. *J. Am. Chem. Soc.* **2000**, *122*, 2532.

[38] Ladizhansky, V., Hodes, G., Vega, S. *J. Phys. Chem. B* **1998**, *102*, 8505.

[39] Becerra, L.R., Murray, C.B., Griffin, R.G., Bawendi, M.G. *J. Chem. Phys.* **1994**, *100*, 3297.

[40] Diaz, D. et al. *J. Phys. Chem. B* **1999**, *103*, 9854.

[41] Ratcliffe, C.I., Yu, K., Ripmeester, J.A., Zaman, M.B., Badarau, C., Singh, S. *Phys. Chem. Chem. Phys.* **2006**, *Advance Article.*

[42] Berrettini, M.G., Braun, G., Hu, J.G., Strouse, G.F. *J. Am. Chem. Soc.* **2004**, *126*, 7063.

[43] Dean, P.A.W., Vittal, J.J., Payne, N.C. *Inorg. Chem.* **1987**, *26*, 1683.

[44] Eichele, K., Wasylishen, R.E., v. 1.17.30, Tübingen, 2001.

[45] Becke, A.D. *Phys. Rev. A: At., Mol., Opt. Phys.* **1988**, *38*, 3098.

[46] Becke, A.D. *J. Chem. Phys.* **1993**, *98*, 5648.

[47] Lee, C., Yang, W., Parr, R.G. *Phys. Rev. B* **1988**, *37*, 785.

[48] Frisch, M.J.e.a., Rev. B.03, Gaussian, Inc., Pittsburgh, 2003.

[49] Ditchfield, R. *Mol. Phys.* **1974**, *27*, 789.

[50] Wolinski, K., Hinton, J.F., Pulay, P. *J. Am. Chem. Soc.* **1990**, *112*, 8251.

[51] Zachariasen, W. *Z. physik. Chem.* **1926**, *124*, 436.

[52] Basis sets were obtained from the Extensible Computational Chemistry Environment Basis Set Database, Version 02/02/06, as developed and distributed by the Molecular Science Computing Facility, Environmental and Molecular Sciences Laboratory which is part of the Pacific Northwest Laboratory, P.O. Box 999, Richland, Washington 99352, USA, and funded by the U.S. Department of Energy. The Pacific Northwest Laboratory is a multi-program laboratory operated by Battelle Memorial Institute for the U.S. Department of Energy under contract DE-AC06-76RLO 1830. Contact Karen Schuchardt for further information.

[53] Huzinaga, S., Andzelm, J. In *Gaussian basis sets for molecular calculations*; Elsevier: New York, 1984, pp 213 - 215.

[54] Godbout, N., Salahub, D.R., Andzelm, J., Wimmer, E. *Can. J. Chem.* **1992**, *70*, 560.

[55] Schaefer, A., Horn, H., Ahlrichs, R. *J. Chem. Phys.* **1992**, *97*, 2571.

[56] Schaefer, A., Huber, C., Ahlrichs, R. *J. Chem. Phys.* **1994**, *100*, 5829.

[57] Dunning, T.H., Jr. *J. Chem. Phys.* **1989**, *90*, 1007.

[58] Woon, D.E., Dunning, T.H., Jr. *J. Chem. Phys.* **1993**, *98*, 1358.

[59] Woon, D.E., Dunning, T.H., Jr. *J. Chem. Phys.* **1994**, *100*, 2975.

[60] Koput, J., Peterson, K.A. *J. Phys. Chem. A* **2002**, *106*, 9595.

[61] Wilson, A.K., Woon, D.E., Peterson, K.A., Dunning, T.H., Jr. *J. Chem. Phys.* **1999**, *110*, 7667.

[62] Kraus, W., Nolze, G., v. 2.4, Federal Institute for Materials Research and Testing, Berlin, Germany, 2000.

[63] West, A.R. *Basic Solid State Chemistry*, 1996.

[64] Nolle, A. *Z. Naturforsch., A* **1978**, *33A*, 666.

[65] Koch, W., Lutz, O., Nolle, A. *Z. Phys. A: At. Nucl.* **1978**, *289*, 17.

[66] Jose, R., Zhanpeisov, N.U., Fukumura, H., Baba, Y., Ishikawa, M. *J. Am. Chem. Soc.* **2006**, *128*, 629.

[67] Bandaranayake, R.J., Wen, G.W., Lin, J.Y., Jiang, H.X., Sorensen, C.M. *Appl. Phys. Lett.* **1995**, *67*, 831.

[68] Kale, R.B., Lokhande, C.D. *J. Phys. Chem. B* **2005**, *109*, 20288.

[69] Marcus, S.H., Miller, S.I. *J. Phys. Chem.* **1964**, *68*, 331.

[70] D'Souza, V.T., Nanjundiah, R., Baeza H, J., Szmant, H.H. *J. Org. Chem.* **1987**, *52*, 1720.

[71] SDBSWeb : http://www.aist.go.jp/RIODB/SDBS/ (National Institute of Advanced Industrial Science and Technology)

[72] Sengar, R.S., Nemykin, V.N., Basu, P. *New J. Chem.* **2003**, *27*, 1115.

[73] Yoshino, A., Okabayashi, H., Yoshida, T., Kushida, K. *J. Phys. Chem.* **1996**, *100*, 9592.

[74] Heatley, F. *J. Chem. Soc., Faraday Trans.* **1987**, *83*, 517.

[75] Martin, C.A., Magid, L.J. *J. Phys. Chem.* **1981**, *85*, 3938.

[76] Eggert, H., Djerassi, C. *J. Am. Chem. Soc.* **1973**, *95*, 3710.

[77] Evans, B.J., Doi, J.T., Musker, W.K. *J. Org. Chem.* **1990**, *55*, 2337.

[78] Summers, M.F. *Coord. Chem. Rev.* **1988**, *86*, 43.

[79] Fyfe, C.A., Brouwer, D.H., Tekely, P. *J. Phys. Chem. A* **2005**, *109*, 6187.

[80] Mehring, M. In *Principles of High Resolution NMR in Solids*; 2 ed.; Springer-Verlag: Berlin, 1983, pp 143-168.

[81] Duer, M.J. In *Introduction to Solid-State NMR Spectroscopy*; Blackwell Science Ltd.: Oxford, 2004, pp 96-106.

[82] Zhang, M., Maciel, G.E. *Anal. Chem.* **1989**, *61*, 2579.

[83] Jurkiewicz, A., Maciel, G.E. *Fuel* **1994**, *73*, 828.

[84] Haw, J.F., Maciel, G.E., Schroeder, H.A. *Anal. Chem.* **1984**, *56*, 1323.

[85] Maciel, G.E., Haw, J.F., Chuang, I.S., Hawkins, B.L., Early, T.A., McKay, D.R., Petrakis, L. *J. Am. Chem. Soc.* **1983**, *105*, 5529.

[86] Helm, M.L., Hill, L.L., Lee, J.P., Van Derveer, D.G., Grant, G.J. *Dalton Trans.* **2006**, 3534.

[87] Yu, M., Fernando, G.W., Li, R., Papadimitrakopoulos, F., Shi, N., Ramprasad, R. *Appl. Phys. Lett.* **2006**, *88*, 231910/1.

[88] Duddeck, H. *Prog. Nucl. Magn. Reson. Spectrosc.* **1995**, *27*, 1.

[89] Hagen, K.S., Stephan, D.W., Holm, R.H. *Inorg. Chem.* **1982**, *21*, 3928.

[90] Dance, I.G., Choy, A., Scudder, M.L. *J. Am. Chem. Soc.* **1984**, *106*, 6285.

[91] Craig, D., Dance, I.G., Garbutt, R. *Angew. Chem.-Int. Edit. Engl.* **1986**, *25*, 165.

[92] Herron, N., Calabrese, J.C., Farneth, W.E., Wang, Y. *Science* **1993**, *259*, 1426.

[93] Sachleben, J.R., Wooten, E.W., Emsley, L., Pines, A., Colvin, V.L., Alivisatos, A.P. *Chem. Phys. Lett.* **1992**, *198*, 431.

[94] Sachleben, J.R., Colvin, V., Emsley, L., Wooten, E.W., Alivisatos, A.P. *J. Phys. Chem. B* **1998**, *102*, 10117.

Chapter 7

Future Research Directions

Solid-state NMR spectroscopy, in combination with ab initio calculations and X-ray diffraction experiments, have been demonstrated to be extremely useful for the study of molecular structures and dynamic motion in a variety of crystalline and disordered materials. A particular theme in this thesis is the use of NMR spectroscopy of metal nuclei. It has been shown herein that characterization of fundamental, well-understood model systems by solid-state NMR of both metal nuclei and standard nuclei such as ^{1}H, ^{2}H, ^{13}C, ^{15}N, etc., is crucial in allowing for the application of solid-state NMR to understanding complicated materials at the molecular level.

A computational study of ^{51}V EFG tensors in a series of crystalline pyrovanadates and metavanadates is presented in Chapter 2. ^{51}V EFG tensors in such systems are challenging to calculate using either ab initio or plane wave methods. Since the EFG tensors are affected by both local bonding and long-range electrostatic interactions, suitable basis sets or pseudo-potential functions for ab initio and plane wave calculations, respectively, are needed for the vanadium atoms. Our work focussed upon using RHF and B3LYP calculations to find the appropriate cluster size, basis sets and cluster termination to obtain the best agreement with experimentally determined EFG tensor components. Embedded cluster MO calculations were also attempted, to gauge the dependence of EFG tensors on long-range electrostatic interactions in various vanadate systems. From these systematic trial and error investigations, a sound methodology for fast, accurate computation of ^{51}V EFG tensors is suggested. ^{51}V EFG tensor components and orientations were also interpreted in terms of general structural types and symmetry, which will undoubtedly aid in future interpretations of EFG tensor parameters in vanadium oxide systems with unknown structures, including vanadates and/or vanadia with amorphous/disordered natures, such as glasses, supports for heterogeneous catalysis, etc.

For instance, the experimentally measured vanadium chemical shifts provide information about the number of oxygen atoms that are coordinated to the vanadium centre; hence, reducing the number of possible structures.[1] Increasing availability of inexpensive computer clusters and software capable of ab initio computations on parallel processors will permit rapid, iterative calculations of EFG and CS tensors for a variety of structural types. By using either commercial computer programs such as Cerius^2[2] or handwritten routines, it is possible to carry out a large series of calculations for vanadium-oxygen units with slightly different bond lengths and bond angles, which will be useful in isolating the ^{51}V NMR tensor parameters for a variety of VO_x structures. Comparison of these parameters with those extracted/estimated from solid-state ^{51}V NMR data for known VO_x environments will permit further structural refinement. Currently, no other experimental techniques are available for this sort of detailed structural investigation of amorphous materials.

In Chapter 3, we demonstrated that the rapid acquisition of solid-state ^{93}Nb NMR spectra of a series of Nb(I) metallocenes is useful for detecting subtle changes in the molecular structure, even well beyond the first coordination sphere of the niobium centre.

The ^{93}Nb EFG tensor is also extremely sensitive to the Nb oxidation state: C_Q is very small and quite large for the Nb(I) and Nb(V) oxidation states, respectively. Computation of the ^{93}Nb EFG tensor components and orientations also lends insight into the variation of ^{93}Nb NMR parameters upon coordination of solvate to the metal centre.

Since the catalytic processes often occur at the metal centres of metallocene complexes, rapid acquisition of solid-state NMR spectra of the metal nuclei is essential for probing any structural changes before, during, and after the catalytic process. With the aid of ab initio calculations, and complimentary techniques such as IR and/or Raman spectroscopy, insights into the nature of chemisorption or physisorption onto a support material, as well as actual catalytic mechanisms, may also be obtained. For example, half-sandwich metallocenes which possess a carboxylate methyl functional group on the Cp ring can graft on the surface of mesoporous MCM-41 and MCM-48 solids.[3] Since the composite materials are disordered, single-crystal XRD experiments do not provide much information about the chemistry in these systems. Powder XRD and nitrogen adsorption/desorption experiments have been primarily used to characterize the composite materials; however, very little is known regarding the nature of the grafting and orientations of the metallocenes with respect to the surface, both of which are essential in rational design of heterogeneous catalysts. For example, one of the piano-stool Nb(I) metallocenes discussed in Chapter 3 possesses a carboxylate methyl functional group. When it is loaded onto the mesoporous solid, the rapid acquisition of solid-state ^{93}Nb NMR spectra allows the "instant detection" of any changes of the niobium environment. From that, one can easily determine if the niobocenes are grafted on the surface or not, by contrasting the NMR spectra between the composite material and bulk samples.

Solid-state NMR spectroscopy of guest species in mesoporous Ti/Ta/mixed V-Nb oxides is presented in Chapter 4. Owing to amorphous nature of the hosts, structural characterization by XRD techniques provides very limited information. Solid-state NMR spectroscopy is one of the best candidates for studying molecular structures of amorphous systems; however, there is limited information available in these systems from NMR spectroscopy of the metal nuclei which comprise the framework. The $^{47/49}$Ti and ^{181}Ta quadrupolar nuclei are very unreceptive. Although the receptivity of these quadrupolar nuclei are comparable to ^{13}C ($D^{C}(^{47/49}\text{Ti}) \approx 1.0$ and $D^{C}(^{181}\text{Ta}) \approx 200$),[4] the spectral broadening due to the large nuclear quadrupole moments[4] prevents the acquisition of high S/N NMR spectra. On the other hand, solid-state ^{93}Nb NMR experiments on mesoporous Nb oxide are possible; however, little can be learnt from the poorly defined powder patterns (Figure 7.1).

Solid-state ^{17}O NMR experiments on ^{17}O-labelled samples are feasible at high magnetic field strengths. Further insights regarding the metal-oxide network may be obtained from ^{17}O NMR spectra of isotopically labelled mesoporous titanium, niobium, and tantalum oxides. For example, in the solid-state ^{17}O NMR studies of mesoporous niobia reported by Smith and co-workers,[5] distorted NbO_6 octahedra, which are linked by corner-shared oxygen atoms, are determined. In addition, high-temperature solid-state ^{17}O NMR experiments on heated samples reveal structural changes of the corner-shard ONb_2 sites, forming two similar, but nonequivalent, ONb_2 sites. Regular microporous channels in the walls running between the 3D array of distorted octahedra were suggested, allowing the dislocations and twisting of NbO_6 units.

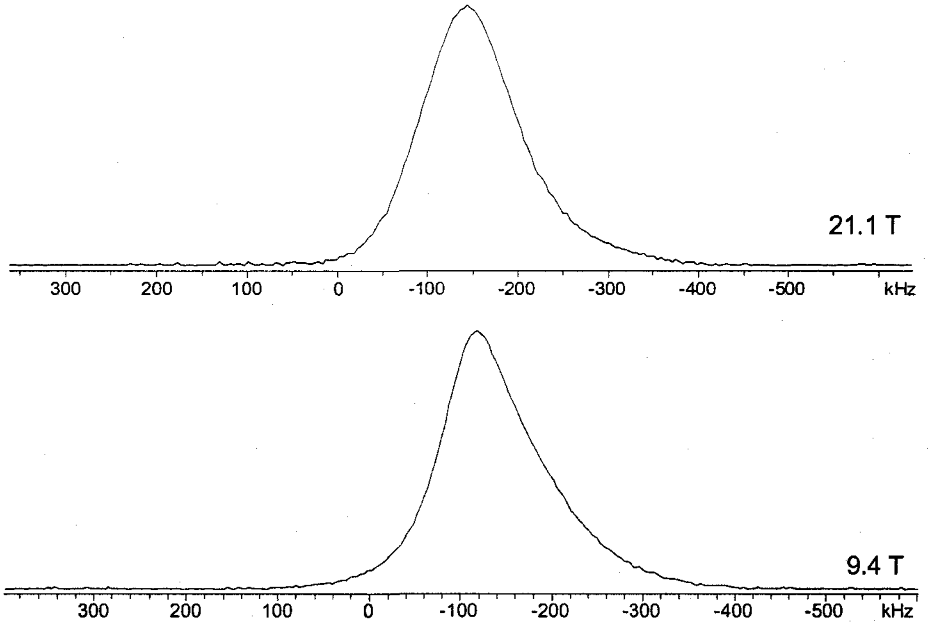

Figure 7.1. Static ^{93}Nb NMR spectra of pure mesoporous Nb oxide.

Alternatively, solid-state NMR spectroscopy of guest molecules provides insights into the structures of the host materials. For instance, for the Ti-TMS1/bis(toluene)Ti composites, it was initially believed that layers of dinitrogen molecules were coated onto the surface of the mesoporous walls. This however, was disproved by solid-state ^{15}N NMR experiments, which showed that ammonia molecules are on the surface. The mechanism of formation of NH_3 inside the mesoporous channels is not clear at the present time, though it was suggested that the cleavage of atmospheric dinitrogen is accomplished by the low-valent, low coordinate Ti centres in the wall of the mesostructure. The nitrogen react with the moisture and/or the Lewis acid sites on the walls to form NH_3 molecules which are anchored on the surface.[6]

Solid-state NMR data presented herein have also provided a deeper understanding of the origin of the electrochemical properties of these host-guest systems. For example, the V-doped Nb-TMS1/bis(arene)Cr(0) composites have different conductivities varying loading levels of the organometallic species. It was also found that higher Cr(0)/Cr(I) ratios are correlated to higher conductivity, whereas the conductivity of the composite materials decreases with increased vanadium doping levels. It was proposed that the vanadium atoms act as spin traps which prevent electron transfer.[7]

The orientation and motion of the guest organometallic species are also extremely important in determining the electronic properties of these materials. Solid-state ^{2}H NMR experiments prove that the organometallic species are not isotropically tumbling in the channels, but rather, have their rotational axes aligned along the direction of channel propagation. Solid-state ^{53}Cr NMR experiments would undoubtedly contribute more to our understanding of molecular orientation and motion in the channels; however, such experiments on these systems are not feasible at this time since ^{53}Cr is extremely unreceptive (n.a. = 9.5 %, $Q(^{53}\mathrm{Cr}) = -0.15 \times 10^{-28}$ m^2, and $D^{C} = 0.51$), and the guest species are relatively dilute in these systems. It may be possible to apply ^{59}Co NMR for the characterization of an analogous system featuring Cp_2Co/Cp_2Co^+ loaded into mesoporous Nb oxide.[8] The cationic organometallic complex is diamagnetic, so it is possible to directly probe the molecular structure and orientations within the mesoporous channels via solid-state ^{59}Co NMR experiments. A preliminary solid-state ^{59}Co NMR spectrum of the bulk Cp_2Co^+ ion is depicted in Figure 7.2. The CT powder pattern is very broad (ca. 5 MHz wide), and must be acquired in a piecewise fashion at standard field strengths, though substantial spectral narrowing can be obtained at higher fields.[9] For

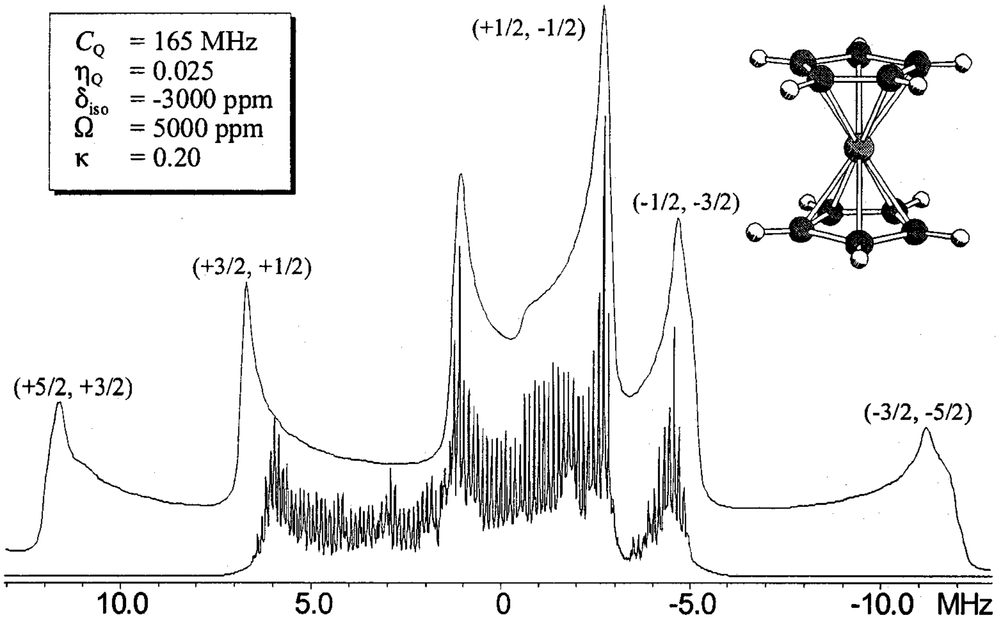

Figure 7.2. Solid-state static ^{59}Co NMR spectrum of bulk Cp_2Co^+ at 9.4 T.

the Cp_2Co^+ complex in the mesoporous Nb oxide, since there is limited amount of Co(III) present from the partial oxidation of Co(II) which is paramagnetic, the acquisition of NMR spectra may be difficult, though ^{59}Co is 100 % naturally abundant. For the composite materials, when the organometallic complexes posses dynamic motions in the wall of the mesostructure, the ^{59}Co EFG tensor will be partially averaged; consequently, a reduced "effective" quadrupolar interaction is observed (i.e., the breadth of the powder pattern will be reduced). With this, and the solid-state ^{2}H NMR data of deuterated Cp_2Co^+ guest molecules, a complete picture of how they are oriented with respect to the surface can be obtained. Further, very-fast MAS (VFMAS) ^{1}H and ^{13}C NMR spectroscopy[10-13] of the paramagnetic species would also likely be very informative, providing additional probes of both structure and dynamics.

In Chapters 5 and 6, multinuclear solid-state NMR studies of nanoparticle composite materials are presented. Often, the characterization of the structures of NPs is accomplished using various types of microscopy (e.g., AFM, SEM, TEM), powder XRD, elemental analyses, and X-ray fluorescence (XRF), while solution ^{1}H NMR experiments are used to characterize the surface ligands when applicable.[14-24] In this thesis, we have demonstrated that solid-state NMR experiments can be used to characterize the core and surface ligands, as well as their connectivities. However, what is missing in the study of mesoporous CdSe aerogel and xerogel (Chapter 6) is the information about the NP-NP connectivity. Future aspects of this project will include 2D solid-state ^{1}H-^{111}Cd heteronuclear correlation (HETCOR) experiments which should provide information on binding of surface ligands at various Cd sites, high-field ^{111}Cd and ^{77}Se NMR experiments for chemical shift dispersion, and measurements of relaxation parameters which will aid in understanding the dynamics of the surface ligands. Solid-state NMR studies can be extended to the characterization of increasingly complex systems such as core-shell NPs.[19,21,24,25] One example is the silica-coated lanthanide-doped LaF_3 NPs which have recently been synthesized by van Veggel et al.[23] Little is known about these NPs, aside from their fascinating luminescent properties. It has been proposed that the Ln^{3+}-doped LaF_3 core is coated by silica, which in turn is coated by organic ligands which are functionalized to allow for bioconjugation to proteins (e.g. avidin). Since the luminescent properties of the materials are closely related to the core structure, it is important to have information on dopant positions, dispersability of the dopants and structural stability upon doping and spin coating. Based upon the experimental approach presented in Chapter 5, we believe multinuclear solid-state NMR experiments and relaxation measurements will elucidate much about the NP structure at the molecular level. High-field ^{139}La NMR experiments should be able to differentiate core and surface La sites due to their different electronic environments. A thorough understanding of the binding of the organic ligands to the NP surface and the functional groups to the protein is crucial for the interaction with targeted biomolecules.

All of the studies reported herein should serve as useful characterization models for NMR spectroscopists, as well as for inorganic chemists and materials scientists who wish to obtain a deeper understanding of the relations between molecular structure and bulk properties of increasingly complex materials.

Bibliography

[1] Lapina, O.B., Mastikhin, V.M., Shubin, A.A., Krasilnikov, V.N., Zamaraev, K.I. *Prog. Nucl. Magn. Reson. Spectrosc.* **1992**, *24*, 457.

[2] Accelrys Software Inc., San Diego, CA, 1999.

[3] Sakthivel, A., Abrantes, M., Chiang, A.S.T., Kuehn, F.E. *J. Organomet. Chem.* **2006**, *691*, 1007.

[4] Harris, R.K., Becker, E.D., Cabral De Menezes, S.M., Goodfellow, R., Granger, P. *Pure Appl. Chem.* **2001**, *73*, 1795.

[5] Skadtchenko, B.O. et al. *Angew. Chem.* **2007**, *119*, 2689

[6] Vettraino, M., Trudeau, M., Lo, A.Y.H., Schurko, R.W., Antonelli, D. *J. Am. Chem. Soc.* **2002**, *124*, 9567.

[7] He, X., Lo, A.Y.H., Trudeau, M., Schurko, R.W., Antonelli, D. *Inorg. Chem.* **2003**, *42*, 335.

[8] Murray, S., Trudeau, M., Antonelli, D.M. *Adv. Mater.* **2000**, *12*, 1339.

[9] Ooms, K.J., Terskikh, V.V., Wasylishen, R.E. *J. Am. Chem. Soc.* **2007**, *129*, 6704.

[10] Ishii, Y., Wickramasinghe, N.P., Chimon, S. *J. Am. Chem. Soc.* **2003**, *125*, 3438.

[11] Wickramasinghe, N.P., Shaibat, M., Ishii, Y. *J. Am. Chem. Soc.* **2005**, *127*, 5796.

[12] Ouyang, L., Aguiar, P.M., Batchelor, R.J., Kroeker, S., Leznoff, D.B. *Chem. Commun.* **2006**, 744.

[13] Wickramasinghe, N.P., Ishii, Y. *J. Magn. Reson.* **2006**, *181*, 233.

[14] Hebbink, G.A., Stouwdam, J.W., Reinhoudt, D.N., Van Veggel, F.C.J.M. *Adv.*

Mater. **2002**, *14*, 1147.

[15] Slooff, L.H. et al. *J. Appl. Phys.* **2002**, *91*, 3955.

[16] Stouwdam, J.W., van Veggel, F.C.J.M. *Nano Lett.* **2002**, *2*, 733.

[17] Stouwdam, J.W., Hebbink, G.A., Huskens, J., van Veggel, F.C.J.M. *Chem. Mat.* **2003**, *15*, 4604.

[18] Dekker, R. et al. *Appl. Phys. Lett.* **2004**, *85*, 6104.

[19] Stouwdam, J.W., van Veggel, F.C.J.M. *Langmuir* **2004**, *20*, 11763.

[20] Arachchige, I.U., Mohanan, J.L., Brock, S.L. *Chem. Mat.* **2005**, *17*, 6644.

[21] Sudarsan, V., van Veggel, F.C.J.M., Herring, R.A., Raudsepp, M. *J. Mater. Chem.* **2005**, *15*, 1332.

[22] Arachchige, I.U., Brock, S.L. *J. Am. Chem. Soc.* **2006**, *128*, 7964.

[23] Sivakumar, S., Diamente, P.R., van Veggel, F.C.J.M. *Chem.-Eur. J.* **2006**, *12*, 5878.

[24] Arachchige, I.U., Brock, S.L. *J. Am. Chem. Soc.* **2007**, ACS ASAP.

[25] Lifshitz, E., Fradkin, L., Glozman, A., Langof, L. *Annu. Rev. Phys. Chem.* **2004**, *55*, 509.

Appendix A – Supplementary Tables

Table A.2.1. All calculated ^{51}V EFG tensor parameters of α-$Zn_2V_2O_7$ pyrovanadate.

Cluster[a]	Level of Theory[b]	V_{11} (a.u.)[c]	V_{22} (a.u.)	V_{33} (a.u.)	$\|C_Q\|$[d]	η_Q[e]
–	**Experimental**[f]	–	–	–	**3.86**	**0.56**
$V_2O_7^{4-}$	iR41	0.0347	0.2523	-0.2870	3.51	0.76
$V_2O_7^{4-}$	iR411	0.0282	0.2362	-0.2644	3.23	0.79
$V_2O_7^{4-}$	iR411+	0.0066	0.2220	-0.2285	2.79	0.94
$V_2O_7^{4-}$	iR61	0.0125	0.2950	-0.3076	3.76	0.92
$V_2O_7^{4-}$	iR611	-0.0006	-0.2530	0.2536	3.10	1.00
$V_2O_7^{4-}$	iR611+	-0.0183	-0.2184	0.2367	2.89	0.85
$V_2O_7^{4-}$	iB41	0.0728	0.2382	-0.3110	3.80	0.53
$V_2O_7^{4-}$	iB411	0.0707	0.2544	-0.3251	3.97	0.57
$V_2O_7^{4-}$	iB411+	0.0439	0.2349	-0.2788	3.41	0.69
$V_2O_7^{4-}$	iB61	0.0538	0.2826	-0.3363	4.11	0.68
$V_2O_7^{4-}$	iB611	0.0469	0.2756	-0.3225	3.94	0.71
$V_2O_7^{4-}$	iB611+	0.0224	0.2537	-0.2761	3.37	0.84
$V_2O_7^{4-}$	eR41	0.1139	0.3607	-0.4747	5.80	0.52
$V_2O_7^{4-}$	eR411	0.1043	0.3592	-0.4635	5.66	0.55
$V_2O_7^{4-}$	eR411+	0.2007	0.2714	-0.4721	5.77	0.15
$V_2O_7^{4-}$	eR61	0.0965	0.4371	-0.5335	6.52	0.64
$V_2O_7^{4-}$	eR611	0.0948	0.4068	-0.5016	6.13	0.62
$V_2O_7^{4-}$	eR611+	0.1520	0.2931	-0.4452	5.44	0.32
$V_2O_7^{4-}$	eB41	0.1482	0.3345	-0.4827	5.90	0.39
$V_2O_7^{4-}$	eB411	0.1721	0.3158	-0.4879	5.96	0.29
$V_2O_7^{4-}$	eB411+	0.2290	0.2854	-0.5144	6.28	0.11
$V_2O_7^{4-}$	eB61	0.1443	0.3659	-0.5102	6.23	0.43
$V_2O_7^{4-}$	eB611	0.1426	0.3822	-0.5248	6.41	0.46
$V_2O_7^{4-}$	eB611+	0.2130	0.3183	-0.5313	6.49	0.20
VO_4^{3-}	iB411+	0.0297	0.2340	-0.2638	3.22	0.77
VO_4^{3-}	eB411+	-0.0627	-0.6380	0.7006	-8.56	0.82

[a] Cluster sizes utilized in calculations; [b] isolated (i) or embedded (e) cluster calculation with in the form methods/basis sets for V/basis sets for other atoms (6-31G**, 6-311G**, 6-311+G**, 6-311++G**). For instances, iR411+ = RHF/4F/6-311+G** calculation upon an isolated cluster, and eB611 = B3LYP/6D/6-311G** calculation upon an embedded cluster; [c] principal components of the EFG tensor with $|V_{11}| \leq |V_{22}| \leq |V_{33}|$ in atomic units; [d] absolute values of quadrupolar coupling constant ($C_Q = eQV_{zz}/h$) of ^{51}V EFG tensor in MHz, and were obtained from multiplying the V_{33} in a.u. by 9.7177 × 10^{21} V·m^{-2} × eQ/h; [e] asymmetric parameters of ^{51}V EFG tensor, $\eta_Q = (V_{11} - V_{22})/V_{33}$; [f] obtained from reference [1].

Table A.2.2. All calculated ^{51}V EFG tensor parameters of $Cd_2V_2O_7$ pyrovanadate.

Cluster[a]	Level of Theory[b]	V_{11} (a.u.)[c]	V_{22} (a.u.)	V_{33} (a.u.)	$\|C_Q\|$[d]	η_Q[e]
–	**Experimental[f]**	–	–	–	**6.00**	**0.41**
$V_2O_7^{4-}$	iR41	0.1707	0.3422	-0.5129	6.27	0.33
$V_2O_7^{4-}$	iR411	0.1585	0.3166	-0.4752	5.81	0.33
$V_2O_7^{4-}$	iR411+	0.1225	0.2893	-0.4118	5.03	0.41
$V_2O_7^{4-}$	iR61	0.1509	0.3712	-0.5220	6.38	0.42
$V_2O_7^{4-}$	iR611	0.1283	0.3206	-0.4489	5.48	0.43
$V_2O_7^{4-}$	iR611+	0.1032	0.2993	-0.4025	4.92	0.49
$V_2O_7^{4-}$	iB41	0.1929	0.3274	-0.5202	6.36	0.26
$V_2O_7^{4-}$	iB411	0.1915	0.3383	-0.5298	6.47	0.28
$V_2O_7^{4-}$	iB411+	0.1419	0.2988	-0.4407	5.38	0.36
$V_2O_7^{4-}$	iB61	0.1791	0.3599	-0.5391	6.59	0.34
$V_2O_7^{4-}$	iB611	0.1688	0.3470	-0.5158	6.30	0.35
$V_2O_7^{4-}$	iB611+	0.1305	0.3131	-0.4437	5.42	0.41
$V_2O_7^{4-}$	eR41	0.1346	0.4567	-0.5913	7.22	0.54
$V_2O_7^{4-}$	eR411	0.1306	0.4316	-0.5622	6.87	0.54
$V_2O_7^{4-}$	eR411+	0.0634	0.4582	-0.5216	6.37	0.76
$V_2O_7^{4-}$	eR61	0.1161	0.4979	-0.6140	7.50	0.62
$V_2O_7^{4-}$	eR611	0.0817	0.4538	-0.5355	6.54	0.69
$V_2O_7^{4-}$	eR611+	0.0476	0.4969	-0.5445	6.65	0.83
$V_2O_7^{4-}$	eB41	0.1190	0.4742	-0.5932	7.25	0.60
$V_2O_7^{4-}$	eB411	0.1204	0.4937	-0.6141	7.50	0.61
$V_2O_7^{4-}$	eB411+	0.0129	0.5757	-0.5886	7.19	0.96
$V_2O_7^{4-}$	eB61	0.1296	0.5162	-0.6458	7.89	0.60
$V_2O_7^{4-}$	eB611	0.1124	0.5183	-0.6307	7.71	0.64
$V_2O_7^{4-}$	eB611+	0.0370	0.6009	-0.6379	7.79	0.88

[a-f] See footnotes of Table A.2.1.

Table A.2.3. All calculated ^{51}V EFG tensor parameters of β-$Mg_2V_2O_7$ pyrovanadate.

Cluster[a]	Site	Level of Theory[b]	V_{11} (a.u.)[c]	V_{22} (a.u.)	V_{33} (a.u.)	$\|C_Q\|$[d]	η_Q[e]
–	**a**	**Experimental[f]**	–	–	–	**4.80**	**0.39**
	b		–	–	–	**10.10**	**0.44**
$V_2O_7^{4-}$	a	iR41	0.1697	0.2867	-0.4564	5.58	0.26
	b		0.2393	0.9146	-1.1538	14.10	0.59
$V_2O_7^{4-}$	a	iR411	0.1606	0.2663	-0.4268	5.22	0.25
	b		0.2289	0.8540	-1.0829	13.23	0.58
$V_2O_7^{4-}$	a	iR411+	0.1487	0.2033	-0.3521	4.30	0.16
	b		0.1826	0.7524	-0.9350	11.43	0.61
$V_2O_7^{4-}$	a	iR61	0.2124	0.2994	-0.5118	6.25	0.17
	b		0.2649	0.9988	-1.2637	15.44	0.58
$V_2O_7^{4-}$	a	iR611	0.1731	0.2625	-0.4355	5.32	0.21

	b		0.2378	0.9112	-1.1490	14.04	0.59
$V_2O_7^{4-}$	a	iR611+	0.1496	0.2020	-0.3517	4.30	0.15
	b		0.1929	0.8203	-1.0133	12.38	0.62
$V_2O_7^{4-}$	a	iB41	0.1688	0.2820	-0.4508	5.51	0.25
	b		0.2290	0.7973	-1.0263	12.54	0.55
$V_2O_7^{4-}$	a	iB411	0.1965	0.2856	-0.4820	5.89	0.18
	b		0.2414	0.7914	-1.0328	12.62	0.53
$V_2O_7^{4-}$	a	iB411+	0.1868	0.2184	-0.4052	4.95	0.08
	b		0.2017	0.6684	-0.8701	10.63	0.54
$V_2O_7^{4-}$	a	iB61	0.2125	0.2991	-0.5115	6.25	0.17
	b		0.2651	0.8947	-1.1598	14.17	0.54
$V_2O_7^{4-}$	a	iB611	0.2116	0.2893	-0.5009	6.12	0.16
	b		0.2616	0.8629	-1.1245	13.74	0.53
$V_2O_7^{4-}$	a	iB611+	0.1875	0.2232	-0.4107	5.02	0.09
	b		0.2212	0.7504	-0.9716	11.87	0.54
$V_2O_7^{4-}$	a	eR41	0.1684	0.3032	-0.4716	5.76	0.29
	b		0.3298	0.8494	-1.1792	14.41	0.44
$V_2O_7^{4-}$	a	eR411	0.1284	0.3096	-0.4380	5.35	0.41
	b		0.3339	0.7822	-1.1162	13.64	0.40
$V_2O_7^{4-}$	a	eR411+	0.0345	0.3804	-0.4148	5.07	0.83
	b		0.3755	0.6254	-1.0009	12.23	0.25
$V_2O_7^{4-}$	a	eR61	0.1919	0.3484	-0.5403	6.60	0.29
	b		0.3319	0.9799	-1.3118	16.03	0.49
$V_2O_7^{4-}$	a	eR611	0.0870	0.3443	-0.4313	5.27	0.60
	b		0.3266	0.8510	-1.1776	14.39	0.45
$V_2O_7^{4-}$	a	eR611+	0.0013	0.4043	-0.4057	4.96	0.99
	b		0.3794	0.6953	-1.0747	13.13	0.29
$V_2O_7^{4-}$	a	eB41	0.1805	0.3339	-0.5143	6.28	0.30
	b		0.3705	0.7345	-1.1051	13.50	0.33
$V_2O_7^{4-}$	a	eB411	0.1835	0.3659	-0.5493	6.71	0.33
	b		0.3852	0.7368	-1.1220	13.71	0.31
$V_2O_7^{4-}$	a	eB411+	0.1046	0.4591	-0.5637	6.89	0.63
	b		0.4664	0.5048	-0.9712	11.87	0.04
$V_2O_7^{4-}$	a	eB61	0.2302	0.3596	-0.5898	7.21	0.22
	b		0.3918	0.8558	-1.2476	15.24	0.37
$V_2O_7^{4-}$	a	eB611	0.2232	0.3659	-0.5891	7.20	0.24
	b		0.3902	0.8342	-1.2245	14.96	0.36
$V_2O_7^{4-}$	a	eB611+	0.1324	0.4501	-0.5825	7.12	0.55
	b		0.4692	0.5895	-1.0587	12.94	0.11

$^{a-f}$ See footnotes of Table A.2.1.

Table A.2.4. All calculated ^{51}V EFG tensor parameters of BaCaV$_2$O$_7$ pyrovanadate.

Cluster[a]	Site	Level of Theory[b]	V_{11} (a.u.)[c]	V_{22} (a.u.)	V_{33} (a.u.)	$\|C_Q\|$[d]	η_Q[e]
–	**a**	**Experimental**[f]	–	–	–	**2.57**	**0.32**
	b		–	–	–	**3.20**	**0.85**
$V_2O_7^{4-}$	a	iR41	-0.1214	-0.1330	0.2544	3.11	0.05
	b		-0.0506	-0.3442	0.3948	4.82	0.74
$V_2O_7^{4-}$	a	iR411	-0.1071	-0.1290	0.2360	2.88	0.09
	b		-0.0452	-0.3172	0.3624	4.43	0.75
$V_2O_7^{4-}$	a	iR411+	-0.0725	-0.1292	0.2017	2.46	0.28
	b		-0.0484	-0.2646	0.3129	3.82	0.69
$V_2O_7^{4-}$	a	iR61	-0.1235	-0.1748	0.2983	3.65	0.17
	b		-0.0806	-0.3928	0.4734	5.78	0.66
$V_2O_7^{4-}$	a	iR611	-0.1222	-0.1460	0.2681	3.28	0.09
	b		-0.0479	-0.3662	0.4141	5.06	0.77
$V_2O_7^{4-}$	a	iR611+	-0.0864	-0.1414	0.2278	2.78	0.24
	b		-0.0452	-0.3062	0.3514	4.29	0.74
$V_2O_7^{4-}$	a	iB41	-0.0556	-0.1548	0.2104	2.57	0.47
	b		-0.0977	-0.2349	0.3326	4.06	0.41
$V_2O_7^{4-}$	a	iB411	-0.0411	-0.1805	0.2216	2.71	0.63
	b		-0.1196	-0.2310	0.3506	4.28	0.32
$V_2O_7^{4-}$	a	iB411+	-0.0097	-0.1821	0.1917	2.34	0.90
	b		-0.1211	-0.1867	0.3078	3.76	0.21
$V_2O_7^{4-}$	a	iB61	-0.0578	-0.1950	0.2528	3.09	0.54
	b		-0.1269	-0.2821	0.4089	5.00	0.38
$V_2O_7^{4-}$	a	iB611	-0.0520	-0.1986	0.2506	3.06	0.59
	b		-0.1263	-0.2741	0.4004	4.89	0.37
$V_2O_7^{4-}$	a	iB611+	-0.0213	-0.1914	0.2127	2.60	0.80
	b		-0.1207	-0.2236	0.3443	4.21	0.30
$V_2O_7^{4-}$	a	eR41	0.0098	0.3444	-0.3542	4.33	0.94
	b		0.1260	0.4393	-0.5653	6.91	0.55
$V_2O_7^{4-}$	a	eR411	0.0117	0.3768	-0.3885	4.75	0.94
	b		0.1348	0.3342	-0.4690	5.73	0.43
$V_2O_7^{4-}$	a	eR411+	0.1875	0.5629	-0.7505	9.17	0.50
	b		-0.0852	-0.3550	0.4402	5.38	0.61
$V_2O_7^{4-}$	a	eR61	0.0175	0.3286	-0.3461	4.23	0.90
	b		-0.0057	-0.4575	0.4632	5.66	0.98
$V_2O_7^{4-}$	a	eR611	-0.0063	-0.3196	0.3259	3.98	0.96
	b		-0.0202	-0.4786	0.4987	6.09	0.92
$V_2O_7^{4-}$	a	eR611+	0.0309	0.8845	-0.9155	11.19	0.93
	b		-0.0942	-0.3774	0.4716	5.76	0.60
$V_2O_7^{4-}$	a	eB41	-0.0732	-0.1252	0.1984	2.42	0.26

	b		-0.0236	-0.3390	0.3625	4.43	0.87
$V_2O_7^{4-}$	a	eB411	-0.0649	-0.2154	0.2802	3.42	0.54
	b		-0.0944	-0.4572	0.5516	6.74	0.66
$V_2O_7^{4-}$	a	eB411+	-0.0115	-0.2865	0.2980	3.64	0.92
	b		-0.1317	-0.3428	0.4745	5.80	0.44
$V_2O_7^{4-}$	a	eB61	-0.0448	-0.1580	0.2028	2.48	0.56
	b		-0.1427	-0.3124	0.4551	5.56	0.37
$V_2O_7^{4-}$	a	eB611	-0.0496	-0.1597	0.2093	2.56	0.53
	b		-0.1483	-0.3124	0.4607	5.63	0.36
$V_2O_7^{4-}$	a	eB611+	-0.0135	-0.3022	0.3157	3.86	0.91
	b		-0.1329	-0.3428	0.4757	5.81	0.44

[a-f] See footnotes of Table A.2.1.

Table A.2.5. All calculated ^{51}V EFG tensor parameters of LiVO$_3$ metavanadate.

Cluster[a]	Level of Theory[b]	V_{11} (a.u.)[c]	V_{22} (a.u.)	V_{33} (a.u.)	$\lvert C_Q \rvert$[d]	η_Q[e]
–	**Experimental[f]**	–	–	–	**3.25**	**0.88**
$H_2VO_4^-$	iR41	-0.0463	-0.2891	0.3354	4.10	0.72
$H_2VO_4^-$	iR411	-0.0721	-0.2614	0.3336	4.08	0.57
$H_2VO_4^-$	iR411+	-0.0797	-0.2467	0.3264	3.99	0.51
$H_2VO_4^-$	iR411++	-0.0749	-0.2485	0.3234	3.95	0.54
$H_2VO_4^-$	iR61	-0.0795	-0.3160	0.3955	4.83	0.60
$H_2VO_4^-$	iR611	-0.0864	-0.2582	0.3447	4.21	0.50
$H_2VO_4^-$	iR611+	-0.0858	-0.2512	0.3370	4.12	0.49
$H_2VO_4^-$	iR611++	-0.0823	-0.2505	0.3328	4.07	0.51
$H_2VO_4^-$	iB41	-0.0878	-0.2969	0.3847	4.70	0.54
$H_2VO_4^-$	iB411	-0.1262	-0.3032	0.4294	5.25	0.41
$H_2VO_4^-$	iB411+	-0.1376	-0.2804	0.4180	5.11	0.34
$H_2VO_4^-$	iB411++	-0.1367	-0.2814	0.4182	5.11	0.35
$H_2VO_4^-$	iB61	-0.0960	-0.3278	0.4238	5.18	0.55
$H_2VO_4^-$	iB611	-0.1173	-0.3045	0.4218	5.15	0.44
$H_2VO_4^-$	iB611+	-0.1205	-0.2927	0.4131	5.05	0.42
$H_2VO_4^-$	iB611++	-0.1189	-0.2931	0.4120	5.03	0.42
$H_2VO_4^-$	eR41	-0.0054	-0.3854	0.3908	4.77	0.97
$H_2VO_4^-$	eR411	-0.0058	-0.3678	0.3735	4.56	0.97
$H_2VO_4^-$	eR411+	-0.0216	-0.3220	0.3436	4.20	0.87
$H_2VO_4^-$	eR411++	-0.0215	-0.3223	0.3437	4.20	0.87
$H_2VO_4^-$	eR61	-0.0269	-0.4724	0.4993	6.10	0.89
$H_2VO_4^-$	eR611	-0.0169	-0.4187	0.4356	5.32	0.92
$H_2VO_4^-$	eR611+	-0.0266	-0.3738	0.4004	4.89	0.87
$H_2VO_4^-$	eR611++	-0.0268	-0.3731	0.3999	4.89	0.87
$H_2VO_4^-$	eB41	0.0414	0.3003	-0.3419	4.18	0.76

$H_2VO_4^-$	eB411	0.0370	0.3302	-0.3672	4.49	0.80
$H_2VO_4^-$	eB411+	-0.0163	-0.3017	0.3180	3.89	0.90
$H_2VO_4^-$	eB411++	-0.0163	-0.3019	0.3182	3.89	0.90
$H_2VO_4^-$	eB61	0.0278	0.4141	-0.4419	5.40	0.87
$H_2VO_4^-$	eB611	0.0252	0.4140	-0.4392	5.37	0.89
$H_2VO_4^-$	eB611+	-0.0142	-0.3770	0.3912	4.78	0.93
$H_2VO_4^-$	eB611++	-0.0141	-0.3757	0.3898	4.76	0.93
VO_4^{3-}	iR41	-0.0099	-0.4270	0.4369	5.34	0.95
VO_4^{3-}	iR411	-0.0172	-0.3950	0.4121	5.04	0.92
VO_4^{3-}	iR411+	-0.0068	-0.3786	0.3854	4.71	0.96
VO_4^{3-}	iR61	-0.0278	-0.5200	0.5478	6.69	0.90
VO_4^{3-}	iR611	-0.0324	-0.4587	0.4910	6.00	0.87
VO_4^{3-}	iR611+	-0.0164	-0.4395	0.4558	5.57	0.93
VO_4^{3-}	iB41	0.0122	0.3394	-0.3516	4.30	0.93
VO_4^{3-}	iB411	-0.0015	-0.3694	0.3708	4.53	0.99
VO_4^{3-}	iB411+	-0.0052	-0.3455	0.3507	4.29	0.97
VO_4^{3-}	iB61	-0.0018	-0.4423	0.4442	5.43	0.99
VO_4^{3-}	iB611	-0.0143	-0.4336	0.4480	5.47	0.94
VO_4^{3-}	iB611+	-0.0109	-0.4085	0.4194	5.12	0.95
VO_4^{3-}	eR41	0.0127	0.3780	-0.3908	4.77	0.93
VO_4^{3-}	eR411	0.0055	0.3501	-0.3556	4.34	0.97
VO_4^{3-}	eR411+	-0.0491	-0.3514	0.4015	4.91	0.76
VO_4^{3-}	eR61	-0.0076	-0.4789	0.4865	5.94	0.97
VO_4^{3-}	eR611	-0.0061	-0.4284	0.4345	5.31	0.97
VO_4^{3-}	eR611+	-0.0436	-0.3995	0.4431	5.41	0.80
VO_4^{3-}	eB41	0.0562	0.3382	-0.3944	4.82	0.71
VO_4^{3-}	eB411	0.0491	0.3737	-0.4228	5.17	0.77
VO_4^{3-}	eB411+	-0.0584	-0.4145	0.4729	5.78	0.75
VO_4^{3-}	eB61	0.0510	0.4501	-0.5012	6.12	0.80
VO_4^{3-}	eB611	0.0448	0.4617	-0.5065	6.19	0.82
VO_4^{3-}	eB611+	0.0189	0.4675	-0.4864	5.94	0.92

[a-f] See footnotes of Table A.2.1.

Table A.2.6. All calculated ^{51}V EFG tensor parameters of α-$NaVO_3$ metavanadate.

Cluster[a]	Level of Theory[b]	V_{11} (a.u.)[c]	V_{22} (a.u.)	V_{33} (a.u.)	$\lvert C_Q \rvert$[d]	η_Q[e]
–	**Experimental[f]**	–	–	–	**3.77**	**0.49**
$H_2VO_4^-$	iR41	-0.0540	-0.3661	0.4201	5.13	0.74
$H_2VO_4^-$	iR411	-0.0589	-0.3435	0.4024	4.92	0.71
$H_2VO_4^-$	iR411+	-0.0721	-0.3172	0.3893	4.76	0.63
$H_2VO_4^-$	iR411++	-0.0701	-0.3181	0.3883	4.74	0.64
$H_2VO_4^-$	iR61	-0.0623	-0.4052	0.4675	5.71	0.73
$H_2VO_4^-$	iR611	-0.0501	-0.3394	0.3895	4.76	0.74
$H_2VO_4^-$	iR611+	-0.0577	-0.3205	0.3782	4.62	0.69
$H_2VO_4^-$	iR611++	-0.0550	-0.3207	0.3757	4.59	0.71
$H_2VO_4^-$	iB41	-0.1149	-0.3648	0.4797	5.86	0.52
$H_2VO_4^-$	iB411	-0.1368	-0.3872	0.5240	6.40	0.48
$H_2VO_4^-$	iB411+	-0.1486	-0.3523	0.5009	6.12	0.41
$H_2VO_4^-$	iB411++	-0.1482	-0.3527	0.5010	6.12	0.41
$H_2VO_4^-$	iB61	-0.0995	-0.4118	0.5113	6.25	0.61
$H_2VO_4^-$	iB611	-0.1003	-0.3957	0.4960	6.06	0.60
$H_2VO_4^-$	iB611+	-0.1085	-0.3684	0.4769	5.83	0.54
$H_2VO_4^-$	iB611++	-0.1078	-0.3688	0.4765	5.82	0.55
$H_2VO_4^-$	eR41	0.0083	0.4387	-0.4496	5.46	0.96
$H_2VO_4^-$	eR411	0.0095	0.4093	-0.4188	5.12	0.95
$H_2VO_4^-$	eR411+	0.0063	0.3870	-0.3933	4.81	0.97
$H_2VO_4^-$	eR411++	0.0059	0.3875	-0.3933	4.81	0.97
$H_2VO_4^-$	eR61	-0.0064	-0.5395	0.5460	6.67	0.98
$H_2VO_4^-$	eR611	-0.0033	-0.4740	0.4773	5.83	0.99
$H_2VO_4^-$	eR611+	-0.0106	-0.4376	0.4482	5.48	0.95
$H_2VO_4^-$	eR611++	-0.0106	-0.4373	0.4480	5.47	0.95
$H_2VO_4^-$	eB41	0.0479	0.3167	-0.3646	4.45	0.74
$H_2VO_4^-$	eB411	0.0439	0.3494	-0.3933	4.81	0.78
$H_2VO_4^-$	eB411+	-0.0101	-0.3199	0.3300	4.03	0.94
$H_2VO_4^-$	eB411++	-0.0101	-0.3199	0.3300	4.03	0.94
$H_2VO_4^-$	eB61	0.0391	0.4351	-0.4742	5.79	0.84
$H_2VO_4^-$	eB611	0.0345	0.4343	-0.4688	5.73	0.85
$H_2VO_4^-$	eB611+	-0.0104	-0.3900	0.4004	4.89	0.95
$H_2VO_4^-$	eB611++	-0.0102	-0.3894	0.3996	4.88	0.95
VO_4^{3-}	iR41	0.0249	0.4406	-0.4655	5.69	0.89
VO_4^{3-}	iR411	0.0172	0.4131	-0.4303	5.26	0.92
VO_4^{3-}	iR411+	0.0189	0.3970	-0.4160	5.08	0.91
VO_4^{3-}	iR61	0.0162	0.5621	-0.5783	7.07	0.94
VO_4^{3-}	iR611	0.0104	0.4987	-0.5091	6.22	0.96
VO_4^{3-}	iR611+	0.0157	0.4711	-0.4868	5.95	0.94

VO_4^{3-}	iB41	0.0409	0.3372	-0.3781	4.62	0.78
VO_4^{3-}	iB411	0.0290	0.3741	-0.4030	4.92	0.86
VO_4^{3-}	iB411+	0.0203	0.3630	-0.3832	4.68	0.89
VO_4^{3-}	iB61	0.0340	0.4538	-0.4878	5.96	0.86
VO_4^{3-}	iB611	0.0234	0.4569	-0.4804	5.87	0.90
VO_4^{3-}	iB611+	0.0195	0.4345	-0.4540	5.55	0.91
VO_4^{3-}	eR41	-0.0750	-0.2164	0.2913	3.56	0.49
VO_4^{3-}	eR411	-0.1232	-0.1630	0.2862	3.50	0.14
VO_4^{3-}	eR411+	0.3901	0.8115	-1.2016	14.68	0.35
VO_4^{3-}	eR61	-0.1006	-0.2604	0.3610	4.41	0.44
VO_4^{3-}	eR611	-0.1591	-0.1660	0.3251	3.97	0.02
VO_4^{3-}	eR611+	0.0445	0.2396	-0.2841	3.47	0.69
VO_4^{3-}	eB41	-0.1362	-0.2724	0.4086	4.99	0.33
VO_4^{3-}	eB411	-0.1836	-0.2390	0.4226	5.16	0.13
VO_4^{3-}	eB411+	0.0489	0.4502	-0.4992	6.10	0.80
VO_4^{3-}	eB61	-0.1362	-0.3476	0.4838	5.91	0.44
VO_4^{3-}	eB611	-0.1940	-0.2777	0.4717	5.76	0.18
VO_4^{3-}	eB611+	-0.0059	-0.4009	0.4067	4.97	0.97

[a-f] See footnotes of Table A.2.1.

Table A2.7. All calculated ^{51}V EFG tensor parameters of KVO_3 metavanadate.

Cluster[a]	Level of Theory[b]	V_{11} (a.u.)[c]	V_{22} (a.u.)	V_{33} (a.u.)	$\|C_Q\|$[d]	η_Q[e]
–	**Experimental[f]**	–	–	–	**4.15**	**0.85**
$H_2VO_4^-$	iR41	0.0008	0.4708	-0.4717	5.76	1.00
$H_2VO_4^-$	iR411	-0.0010	-0.4400	0.4410	5.39	1.00
$H_2VO_4^-$	iR411+	-0.0227	-0.3892	0.4119	5.03	0.89
$H_2VO_4^-$	iR411++	-0.0213	-0.3894	0.4107	5.02	0.90
$H_2VO_4^-$	iR61	0.0281	0.4923	-0.5204	6.36	0.89
$H_2VO_4^-$	iR611	0.0417	0.3927	-0.4345	5.31	0.81
$H_2VO_4^-$	iR611+	0.0218	0.3702	-0.3920	4.79	0.89
$H_2VO_4^-$	iR611++	0.0241	0.3683	-0.3924	4.79	0.88
$H_2VO_4^-$	iB41	-0.0874	-0.4545	0.5419	6.62	0.68
$H_2VO_4^-$	iB411	-0.1030	-0.4758	0.5788	7.07	0.64
$H_2VO_4^-$	iB411+	-0.1141	-0.4205	0.5345	6.53	0.57
$H_2VO_4^-$	iB411++	-0.1136	-0.4206	0.5342	6.53	0.57
$H_2VO_4^-$	iB61	-0.0400	-0.5190	0.5590	6.83	0.86
$H_2VO_4^-$	iB611	-0.0328	-0.4965	0.5293	6.47	0.88
$H_2VO_4^-$	iB611+	-0.0467	-0.4462	0.4929	6.02	0.81
$H_2VO_4^-$	iB611++	-0.0461	-0.4464	0.4926	6.02	0.81
$H_2VO_4^-$	eR41	0.0604	0.3002	-0.3606	4.41	0.66
$H_2VO_4^-$	eR411	0.0756	0.2778	-0.3534	4.32	0.57

$H_2VO_4^-$	eR411+	0.1210	0.2761	-0.3971	4.85	0.39
$H_2VO_4^-$	eR411++	0.1201	0.2755	-0.3956	4.83	0.39
$H_2VO_4^-$	eR61	0.0762	0.5737	-0.6500	7.94	0.77
$H_2VO_4^-$	eR611	0.0593	0.5083	-0.5676	6.94	0.79
$H_2VO_4^-$	eR611+	-0.1823	-0.3931	0.5755	7.03	0.37
$H_2VO_4^-$	eR611++	-0.1810	-0.3951	0.5760	7.04	0.37
$H_2VO_4^-$	eB41	0.1210	0.2487	-0.3696	4.52	0.35
$H_2VO_4^-$	eB411	0.1386	0.2692	-0.4078	4.98	0.32
$H_2VO_4^-$	eB411+	0.1612	0.2076	-0.3689	4.51	0.13
$H_2VO_4^-$	eB411++	0.1613	0.2076	-0.3689	4.51	0.13
$H_2VO_4^-$	eB61	0.1313	0.4145	-0.5458	6.67	0.52
$H_2VO_4^-$	eB611	0.1197	0.4340	-0.5537	6.77	0.57
$H_2VO_4^-$	eB611+	0.1662	0.3062	-0.4724	5.77	0.30
$H_2VO_4^-$	eB611++	0.1680	0.3057	-0.4737	5.79	0.29
VO_4^{3-}	iR41	0.1838	0.4070	-0.5908	7.22	0.38
VO_4^{3-}	iR411	0.1677	0.3815	-0.5492	6.71	0.39
VO_4^{3-}	iR411+	0.1492	0.3618	-0.5110	6.24	0.42
VO_4^{3-}	iR61	0.2018	0.5184	-0.7202	8.80	0.44
VO_4^{3-}	iR611	0.1830	0.4596	-0.6426	7.85	0.43
VO_4^{3-}	iR611+	0.1677	0.4285	-0.5961	7.28	0.44
VO_4^{3-}	iB41	0.1653	0.3119	-0.4772	5.83	0.31
VO_4^{3-}	iB411	0.1568	0.3468	-0.5036	6.15	0.38
VO_4^{3-}	iB411+	0.1333	0.3278	-0.4612	5.63	0.42
VO_4^{3-}	iB61	0.1865	0.4191	-0.6057	7.40	0.38
VO_4^{3-}	iB611	0.1741	0.4224	-0.5965	7.29	0.42
VO_4^{3-}	iB611+	0.1531	0.3939	-0.5470	6.68	0.44
VO_4^{3-}	eR41	0.1267	0.2658	-0.3925	4.80	0.35
VO_4^{3-}	eR411	0.0869	0.2835	-0.3704	4.53	0.53
VO_4^{3-}	eR411+	-0.3904	-0.5046	0.8951	10.94	0.13
VO_4^{3-}	eR61	0.1389	0.3125	-0.4515	5.52	0.38
VO_4^{3-}	eR611	0.1150	0.2653	-0.3803	4.65	0.40
VO_4^{3-}	eR611+	0.0061	0.7524	-0.7585	9.27	0.98
VO_4^{3-}	eB41	0.0537	0.3250	-0.3787	4.63	0.72
VO_4^{3-}	eB411	0.0324	0.3370	-0.3694	4.51	0.82
VO_4^{3-}	eB411+	-0.0504	-0.3665	0.4169	5.09	0.76
VO_4^{3-}	eB61	0.0863	0.3792	-0.4656	5.69	0.63
VO_4^{3-}	eB611	0.0612	0.3576	-0.4189	5.12	0.71
VO_4^{3-}	eB611+	-0.1830	-0.3047	0.4877	5.96	0.25

$^{a-e}$ See footnotes of Table A.2.1; ^{f} obtained from reference [2].

Table A.2.8. All calculated ^{51}V EFG tensor parameters of ZnV_2O_6 metavanadate.

Cluster[a]	Level of Theory[b]	V_{11} (a.u.)[c]	V_{22} (a.u.)	V_{33} (a.u.)	$\|C_Q\|$[d]	η_Q[e]
–	**Experimental[f]**	–	–	–	**6.86**	**0.4**
$H_2VO_4^-$	iR41	0.1163	0.4353	-0.5516	6.74	0.58
$H_2VO_4^-$	iR411	0.1251	0.4378	-0.5629	6.88	0.56
$H_2VO_4^-$	iR411+	0.1527	0.4035	-0.5562	6.80	0.45
$H_2VO_4^-$	iR411++	0.1483	0.4027	-0.5510	6.73	0.46
$H_2VO_4^-$	iR61	0.1918	0.5292	-0.7210	8.81	0.47
$H_2VO_4^-$	iR611	0.1079	0.5949	-0.7028	8.59	0.69
$H_2VO_4^-$	iR611+	0.0992	0.5494	-0.6486	7.92	0.69
$H_2VO_4^-$	iR611++	0.0966	0.5543	-0.6509	7.95	0.70
$H_2VO_4^-$	iB41	0.1974	0.3357	-0.5331	6.51	0.26
$H_2VO_4^-$	iB411	0.2810	0.3151	-0.5961	7.28	0.10
$H_2VO_4^-$	iB411+	0.2975	0.3256	-0.6231	7.61	0.10
$H_2VO_4^-$	iB411++	0.2960	0.3252	-0.6212	7.59	0.10
$H_2VO_4^-$	iB61	0.2321	0.4364	-0.6685	8.17	0.31
$H_2VO_4^-$	iB611	0.2311	0.4679	-0.6990	8.54	0.34
$H_2VO_4^-$	iB611+	0.2399	0.4309	-0.6707	8.20	0.28
$H_2VO_4^-$	iB611++	0.2393	0.4327	-0.6720	8.21	0.29
$H_2VO_4^-$	eR41	0.2438	0.7726	-1.0164	12.42	0.52
$H_2VO_4^-$	eR411	0.2212	0.7815	-1.0027	12.25	0.56
$H_2VO_4^-$	eR411+	0.0500	0.7666	-0.8166	9.98	0.88
$H_2VO_4^-$	eR411++	0.0477	0.7663	-0.8140	9.95	0.88
$H_2VO_4^-$	eR61	0.4421	0.7578	-1.1999	14.66	0.26
$H_2VO_4^-$	eR611	0.3980	0.7844	-1.1823	14.45	0.33
$H_2VO_4^-$	eR611+	not converge				
$H_2VO_4^-$	eR611++	not converge				
$H_2VO_4^-$	eB41	0.1218	0.7873	-0.9091	11.11	0.73
$H_2VO_4^-$	eB411	0.2145	0.7267	-0.9412	11.5	0.54
$H_2VO_4^-$	eB411+	-0.0883	-0.4548	0.5431	6.64	0.67
$H_2VO_4^-$	eB411++	-0.0855	-0.4553	0.5409	6.61	0.68
$H_2VO_4^-$	eB61	0.1942	0.7673	-0.9615	11.75	0.60
$H_2VO_4^-$	eB611	0.2531	0.7467	-0.9999	12.22	0.49
$H_2VO_4^-$	eB611+	not converge				
$H_2VO_4^-$	eB611++	not converge				
VO_6^{7-}	iR41	-0.0403	-0.5046	0.5449	6.66	0.85
VO_6^{7-}	iR411	-0.0051	-0.5276	0.5326	6.51	0.98
VO_6^{7-}	iR411+	not converge				
VO_6^{7-}	iR61	-0.0861	-0.5447	0.6308	7.71	0.73
VO_6^{7-}	iR611	-0.0191	-0.5764	0.5956	7.28	0.94
VO_6^{7-}	iR611+	0.0323	0.4067	-0.4391	5.37	0.85

VO_6^{7-}	iB41	-0.0935	-0.3338	0.4274	5.22	0.56
VO_6^{7-}	iB411	-0.0918	-0.3357	0.4275	5.22	0.57
VO_6^{7-}	iB411+	not converge				
VO_6^{7-}	iB61	-0.0444	-0.4412	0.4856	5.93	0.82
VO_6^{7-}	iB611	-0.0064	-0.4639	0.4703	5.75	0.97
VO_6^{7-}	iB611+	0.0167	0.3180	-0.3347	4.09	0.90
VO_6^{7-}	eR41	0.0978	0.5017	-0.5994	7.32	0.67
VO_6^{7-}	eR411	0.1472	0.4761	-0.6234	7.62	0.53
VO_6^{7-}	eR411+	not converge				
VO_6^{7-}	eR61	0.0994	0.5732	-0.6726	8.22	0.70
VO_6^{7-}	eR611	0.1725	0.5342	-0.7068	8.64	0.51
VO_6^{7-}	eR611+	0.1890	0.2234	-0.4124	5.04	0.10
VO_6^{7-}	eB41	0.0879	0.4397	-0.5276	6.45	0.67
VO_6^{7-}	eB411	0.0724	0.4578	-0.5302	6.48	0.73
VO_6^{7-}	eB411+	not converge				
VO_6^{7-}	eB61	-0.0851	-0.3301	0.4151	5.07	0.59
VO_6^{7-}	eB611	-0.0875	-0.3501	0.4377	5.35	0.60
VO_6^{7-}	eB611+	-0.1078	-0.4370	0.5448	6.66	0.60

[a-f] See footnotes of Table A.2.1.

Table A.2.9. All calculated ^{51}V EFG tensor parameters of MgV_2O_6 metavanadate.

Cluster[a]	Level of Theory[b]	V_{11} (a.u.)[c]	V_{22} (a.u.)	V_{33} (a.u.)	$\|C_Q\|$[d]	η_Q[e]
–	**Experimental[f]**	–	–	–	**7.5**	**0.34**
$H_2VO_4^-$	iR41	0.1323	0.4553	-0.5877	7.18	0.55
$H_2VO_4^-$	iR411	0.1415	0.4515	-0.5930	7.25	0.52
$H_2VO_4^-$	iR411+	0.1660	0.4186	-0.5846	7.14	0.43
$H_2VO_4^-$	iR411++	0.1612	0.4176	-0.5789	7.07	0.44
$H_2VO_4^-$	iR61	0.2074	0.5472	-0.7546	9.22	0.45
$H_2VO_4^-$	iR611	0.1268	0.6000	-0.7268	8.88	0.65
$H_2VO_4^-$	iR611+	0.1169	0.5579	-0.6748	8.25	0.65
$H_2VO_4^-$	iR611++	0.1140	0.5629	-0.6769	8.27	0.66
$H_2VO_4^-$	iB41	0.2110	0.3577	-0.5687	6.95	0.26
$H_2VO_4^-$	iB411	0.2923	0.3372	-0.6295	7.69	0.10
$H_2VO_4^-$	iB411+	0.3163	0.3331	-0.6494	7.94	0.00
$H_2VO_4^-$	iB411++	0.3149	0.3327	-0.6476	7.91	0.00
$H_2VO_4^-$	iB61	0.2472	0.4552	-0.7024	8.58	0.30
$H_2VO_4^-$	iB611	0.2465	0.4796	-0.7261	8.87	0.32
$H_2VO_4^-$	iB611+	0.2531	0.4420	-0.6951	8.49	0.27
$H_2VO_4^-$	iB611++	0.2524	0.4438	-0.6962	8.51	0.27
$H_2VO_4^-$	eR41	0.0720	0.5894	-0.6614	8.08	0.78
$H_2VO_4^-$	eR411	0.0777	0.5980	-0.6758	8.26	0.77
$H_2VO_4^-$	eR411+	0.2203	0.4183	-0.6386	7.80	0.31
$H_2VO_4^-$	eR411++	0.2170	0.4178	-0.6348	7.76	0.32
$H_2VO_4^-$	eR61	0.1865	0.6324	-0.8189	10.01	0.54
$H_2VO_4^-$	eR611	0.1445	0.6727	-0.8172	9.99	0.65
$H_2VO_4^-$	eR611+	0.1875	0.5341	-0.7216	8.82	0.48
$H_2VO_4^-$	eR611++	0.1899	0.5349	-0.7248	8.86	0.48
$H_2VO_4^-$	eB41	0.0323	0.5529	-0.5852	7.15	0.89
$H_2VO_4^-$	eB411	0.0841	0.5362	-0.6203	7.58	0.73
$H_2VO_4^-$	eB411+	0.2326	0.3926	-0.6253	7.64	0.26
$H_2VO_4^-$	eB411++	0.231	0.3936	-0.6247	7.63	0.26
$H_2VO_4^-$	eB61	0.1078	0.5798	-0.6876	8.40	0.69
$H_2VO_4^-$	eB611	0.1348	0.5842	-0.7189	8.78	0.63
$H_2VO_4^-$	eB611+	0.193	0.4838	-0.6767	8.27	0.43
$H_2VO_4^-$	eB611++	0.1965	0.4816	-0.6781	8.29	0.42
VO_6^{7-}	iR41	0.0353	0.5772	-0.6125	7.48	0.88
VO_6^{7-}	iR411	0.0668	0.5593	-0.6260	7.65	0.79
VO_6^{7-}	iR411+	not converge				
VO_6^{7-}	iR61	-0.0077	-0.6649	0.6726	8.22	0.98
VO_6^{7-}	iR611	0.0554	0.6284	-0.6838	8.35	0.84
VO_6^{7-}	iR611+	0.1830	0.2084	-0.3914	4.78	0.10
VO_6^{7-}	iB41	-0.0239	-0.4337	0.4576	5.59	0.90
VO_6^{7-}	iB411	-0.0229	-0.4359	0.4588	5.61	0.90
VO_6^{7-}	iB411+	not converge				
VO_6^{7-}	iB61	0.0220	0.5169	-0.5389	6.59	0.92

VO$_6^{7-}$	iB611	0.0603	0.4982	-0.5585	6.82	0.78
VO$_6^{7-}$	iB611+	0.0614	0.3178	-0.3792	4.63	0.68
VO$_6^{7-}$	eR41	-0.0642	-0.4623	0.5265	6.43	0.76
VO$_6^{7-}$	eR411	-0.0212	-0.6268	0.6480	7.92	0.93
VO$_6^{7-}$	eR411+	not converge				
VO$_6^{7-}$	eR61	0.5884	0.8619	-1.4502	17.72	0.19
VO$_6^{7-}$	eR611	0.1686	0.7863	-0.9549	11.67	0.65
VO$_6^{7-}$	eR611+	0.2152	0.9257	-1.1409	13.94	0.62
VO$_6^{7-}$	eB41	-0.1383	-0.3986	0.5370	6.56	0.48
VO$_6^{7-}$	eB411	-0.0983	-0.4015	0.4998	6.11	0.61
VO$_6^{7-}$	eB411+	not converge				
VO$_6^{7-}$	eB61	-0.0424	-0.4113	0.4537	5.54	0.81
VO$_6^{7-}$	eB611	0.0164	0.5686	-0.5850	7.15	0.94
VO$_6^{7-}$	eB611+	-0.0783	-0.4114	0.4898	5.98	0.68
VO$_5^{5-}$	iR41	0.1695	0.6560	-0.8255	10.09	0.59
VO$_5^{5-}$	iR411	0.1823	0.6351	-0.8174	9.99	0.55
VO$_5^{5-}$	iR411+	0.1315	0.4394	-0.5709	6.98	0.54
VO$_5^{5-}$	iR61	-0.0077	-0.6649	0.6726	8.22	0.98
VO$_5^{5-}$	iR611	0.0554	0.6284	-0.6838	8.35	0.84
VO$_5^{5-}$	iR611+	0.1830	0.2084	-0.3914	4.78	0.10
VO$_5^{5-}$	iB41	0.0902	0.4985	-0.5888	7.19	0.69
VO$_5^{5-}$	iB411	0.0590	0.5174	-0.5764	7.04	0.80
VO$_5^{5-}$	iB411+	not converge				
VO$_5^{5-}$	iB61	0.0220	0.5169	-0.5389	6.59	0.92
VO$_5^{5-}$	iB611	0.0603	0.4982	-0.5585	6.82	0.78
VO$_5^{5-}$	iB611+	0.0614	0.3178	-0.3792	4.63	0.68
VO$_5^{5-}$	eR41	0.1450	0.4990	-0.6439	7.87	0.55
VO$_5^{5-}$	eR411	-0.0592	-0.4722	0.5314	6.49	0.78
VO$_5^{5-}$	eR411+	0.3280	1.3934	-1.7214	21.03	0.62
VO$_5^{5-}$	eR61	0.5884	0.8619	-1.4502	17.72	0.19
VO$_5^{5-}$	eR611	0.1686	0.7863	-0.9549	11.67	0.65
VO$_5^{5-}$	eR611+	0.2152	0.9257	-1.1409	13.94	0.62
VO$_5^{5-}$	eB41	0.0176	0.4645	-0.4822	5.89	0.93
VO$_5^{5-}$	eB411	-0.0551	-0.4628	0.5180	6.33	0.79
VO$_5^{5-}$	eB411+	not converge				
VO$_5^{5-}$	eB61	-0.0424	-0.4113	0.4537	5.54	0.81
VO$_5^{5-}$	eB611	0.0164	0.5686	-0.5850	7.15	0.94
VO$_5^{5-}$	eB611+	-0.0783	-0.4114	0.4898	5.98	0.68

[a-f] See footnotes of Table A.2.1; [f] obtained from reference [3].

Table A.3.1. Summary of X-ray crystallographic data for $CpNbCl_4$•THF, 7.

Compound Number	(η^5-C_5H_5)$NbCl_4$•THF
Empirical formula	$C_9H_{13}Cl_4NbO$
Formula weight / g mol^{-1}	371.9
Temperature / K	173(2)
Wavelength / Å	0.71073
Crystal system	Triclinic
Space group	*P-1*
Unit cell dimensions:	
a, b, c / Å	7.0665(5), 7.1523(5), 13.3112(9)
α, β, γ / °	76.8130(10), 86.6070(10), 69.3700(10)
Volume / Å^3	612.86(7)
Z	2
Density (calculated) / g cm^{-3}	2.015
Absorption coefficient / mm^{-1}	1.823
F(000)	368
Crystal size / mm	0.40 x 0.20 x 0.20
θ range for data collection /°	3.44 to 27.55
Index ranges:	$-9 \le h \le 9$, $-8 \le k \le 9$, $-17 \le l \le 17$
Reflections collected	5994
Independent reflections	2820 [R(int) = 0.0167]
Completeness to θ / %	99.5
Absorption correction	None
Refinement method	Full matrix least squares on F^2
Data / restraints / parameters	2820 / 0 / 127
Goodness-of-fit (S)[a] on F^2	1.05
Final R indices [I>2σ(I)][b]	*R1* = 0.0285, *wR2* = 0.0657
R indices (all data)[b]	*R1* = 0.0305, *wR2* = 0.0667
Largest diff. peak and hole / e A^{-3}	0.779 and -0.607

[a] $S = [\Sigma w(|F_o|^2 - |F_c|^2)^2]/(n-p)^{1/2}$, where n is the number of reflections and p is the number of parameters used. [b] $R1(F) = \{\Sigma(|F_o| - |F_c|)/\Sigma|F_o|\}$ for reflections with $F_o > 4((F_o))$. $wR2(F^2) = \{\Sigma w(|F_o|^2 - |F_c|^2)^2/\Sigma w(|F_o|^2)^2\}^{1/2}$, where w is the weight given each reflection.

Table A3.2. Selected metrical parameters for CpNbCl$_4$•THF, 7[a]

O-Nb	2.3108(19)[b]
Cl(1)-Nb	2.4260(7)
Cl(2)-Nb	2.4044(7)
Cl(3)-Nb	2.3955(7)
Cl(4)-Nb	2.4021(7)
Nb-Cp[c]	2.133(3) [2.116(4)]
Nb-C(11)	2.417(5) [2.424(8)]
Nb-C(12)	2.465(5) [2.401(7)]
Nb-C(13)	2.476(5) [2.419(7)]
Nb-C(14)	2.441(5) [2.441(7)]
Nb-C(15)	2.411(5) [2.440(8)]
O-Nb-Cl(1)	77.94(5)
O-Nb-Cl(2)	77.05(6)
O-Nb-Cl(3)	77.99(5)
O-Nb-Cl(4)	78.55(6)
Cl(3)-Nb-Cl(4)	87.19(3)
Cl(3)-Nb-Cl(2)	88.69(3)
Cl(4)-Nb-Cl(1)	86.97(3)
Cl(2)-Nb-Cl(1)	87.04(3)
Cl(4)-Nb-Cl(2)	155.58(3)
Cl(3)-Nb-Cl(1)	155.90(3)
O-Nb-Cp	179.40(8) [177.92(13)]
Cl(1)-Nb-Cp	101.53(7) [103.46(11)]
Cl(2)-Nb-Cp	102.66(7) [101.42(11)]
Cl(3)-Nb-Cp	102.55(7) [100.64(11)]
Cl(4)-Nb-Cp	101.73(7) [102.99(11)]

[a] distances are reported in angstroms and angles are given in degrees; [b] the comparable values found for the minor component are given in brackets; [c] Cp refers to the centroid of the cyclopentadienyl ring with the greatest occupancy.

Table A.6.1. Theoretical Cd CS Tensor parameters of Hexagonal and Cubic CdSe.

Source[a]	δ_{11}[b]	δ_{22}	δ_{33}	δ_{iso} (ppm)[c]	Ω (ppm)	κ
Experiment	**595**	**542**	**534**	**557(1)**	**61(2)**	**-0.75(10)**
hexagonal $CdSe_4^{6-}$ clusters						
RHF/Huzinaga[d]	995	984	984	987	11	-1.00
RHF/A-VDZ	939	921	921	972	18	-1.00
RHF/A-TZV	987	977	977	981	10	-1.00
RHF/cc-pVDZ	977	958	958	964	19	-1.00
RHF/cc-pVTZ	938	923	923	928	15	-1.00
RHF/cc-pVQZ	933	933	923	929	10	1.00
B3LYP/Huzinaga	1189	1189	1186	1188	3	0.94
B3LYP/A-VDZ	858	858	855	857	3	0.90
B3LYP/A-TZV	819	819	816	818	3	0.79
B3LYP/cc-pVDZ	898	898	895	897	3	0.87
B3LYP/cc-pVTZ	845	844	841	843	4	0.71
B3LYP/cc-pVQZ	930	929	926	928	4	0.69
hexagonal $Cd_{13}Se_4^{18+}$ clusters						
RHF/Huzinaga	995	984	984	987	11	-1.00
RHF/A-VDZ	939	921	921	972	18	-1.00
RHF/A-TZV	987	977	977	981	10	-1.00
RHF/cc-pVDZ	977	958	958	964	19	-1.00
RHF/cc-pVTZ	938	923	923	928	15	-1.00
RHF/cc-pVQZ	933	933	923	929	10	+1.00
B3LYP/Huzinaga	1073	1057	1056	1062	17	-0.84
B3LYP/A-VDZ	1040	1012	1011	1021	29	-0.92
B3LYP/A-TZV	1092	1073	1072	1079	20	-0.90
B3LYP/cc-pVDZ	1073	1043	1042	1053	30	-0.92
B3LYP/cc-pVTZ	1024	1001	999	1008	26	-0.83
B3LYP/cc-pVQZ	1007	1005	999	1004	9	0.36
cubic $CdSe_4^{6-}$ clusters						
RHF/cc-pVDZ	786	785	785	785	0	0.01
B3LYP/cc-pVDZ	898	897	897	898	0	-0.59
cubic $Cd_{13}Se_4^{18+}$ clusters						
RHF/cc-pVDZ	976	976	976	976	0	0.05

B3LYP/cc-pVDZ	1063	1061	1061	1062	2	-0.50

[a] An all-electron DZVP basis set is applied on Cd atoms in all cases; [b] δ_{ii} are the principal components of the Cd/Se CS tensors such that $\delta_{11} \geq \delta_{22} \geq \delta_{33}$; [c] δ_{iso}, Ω and κ are defined as $(\delta_{11} + \delta_{22} + \delta_{33})/3$, $\delta_{11} - \delta_{33}$ and $3(\delta_{22} - \delta_{iso})/\Omega$, respectively; [d] basis sets used for Se atoms. Theoretical Cd chemical shifts are referenced to a full geometry-optimized $Cd(OH_2)_6^{2+}$ ion.

Table A.6.2. Theoretical Se CS Tensor parameters of Hexagonal and Cubic CdSe.

Source[a]	δ_{11}[b]	δ_{22}	δ_{33}	δ_{iso} **(ppm)**[c]	Ω **(ppm)**	κ
Experiment	**-461**	**-461**	**-505**	**-476(1)**	**44(2)**	**1.00(10)**
hexagonal $CdSe_4^{6-}$ clusters						
RHF/Huzinaga[d]	-1119	-1120	-1120	-1120	2	-1.00
RHF/A-VDZ	-967	-968	-968	-968	1	-1.00
RHF/A-TZV	-1011	-1012	-1012	-1012	1	-1.00
RHF/cc-pVDZ	-948	-950	-950	-949	1	-1.00
RHF/cc-pVTZ	-846	-847	-847	-847	1	-1.00
RHF/cc-pVQZ	-922	-923	-923	-922	1	-1.00
B3LYP/Huzinaga	-1133	-1136	-1136	-1135	3	-0.83
B3LYP/A-VDZ	-886	-887	-887	-887	1	-0.88
B3LYP/A-TZV	-934	-935	-936	-935	2	-0.93
B3LYP/cc-pVDZ	-869	-870	-871	-870	2	-0.86
B3LYP/cc-pVTZ	-800	-802	-802	-801	2	-0.98
B3LYP/cc-pVQZ	-880	-882	-882	-881	2	-0.93
hexagonal $Cd_{13}Se_4^{18+}$ clusters						
RHF/Huzinaga	-1013	-1013	-1123	-1050	110	1.00
RHF/A-VDZ	-796	-796	-841	-811	45	1.00
RHF/A-TZV	-911	-911	-932	-918	21	1.00
RHF/cc-pVDZ	-767	-767	-813	-782	46	1.00
RHF/cc-pVTZ	-784	-784	-795	-788	11	1.00
RHF/cc-pVQZ	-943	-943	-946	-944	3	1.00
B3LYP/Huzinaga	-1044	-1054	-1175	-1091	132	0.85
B3LYP/A-VDZ	-739	-742	-795	-759	56	0.89
B3LYP/A-TZV	-955	-957	-964	-959	8	0.54
B3LYP/cc-pVDZ	-703	-706	-757	-722	54	0.90
B3LYP/cc-pVTZ	-834	-851	-857	-847	23	-0.47
B3LYP/cc-pVQZ	-1065	-1067	-1078	-1070	13	0.67

cubic $CdSe_4^{6-}$ clusters						
RHF/cc-pVDZ	-949	-949	-949	-949	0	—
B3LYP/cc-pVDZ	-870	-870	-870	-870	0	—
cubic $Cd_{13}Se_4^{18+}$ clusters						
RHF/cc-pVDZ	-783	-783	-783	-783	0	—
B3LYP/cc-pVDZ	-735	-735	-735	-735	0	—

[a] An all-electron DZVP basis set is applied on Cd atoms in all cases; [b] δ_{ii} are the principal components of the Cd/Se CS tensors such that $\delta_{11} \geq \delta_{22} \geq \delta_{33}$; [c] δ_{iso}, Ω and κ are defined as $(\delta_{11} + \delta_{22} + \delta_{33})/3$, $\delta_{11} - \delta_{33}$ and $3(\delta_{22} - \delta_{iso})/\Omega$, respectively; [d] basis sets used for Se atoms. Theoretical Se chemical shifts are referenced to a full geometry-optimized $Se(CH_3)_2$ molecule.

Bibliography

[1] Nielsen, U.G., Jakobsen, H.J., Skibsted, J. *J. Phys. Chem. B* **2001**, *105*, 420.

[2] Skibsted, J., Jacobsen, C.J.H., Jakobsen, H.J. *Inorg. Chem.* **1998**, *37*, 3083.

[3] Nielsen, U.G., Jakobsen, H.J., Skibsted, J. *Inorg. Chem.* **2000**, *39*, 2135.

Appendix B – Supplementary Figures

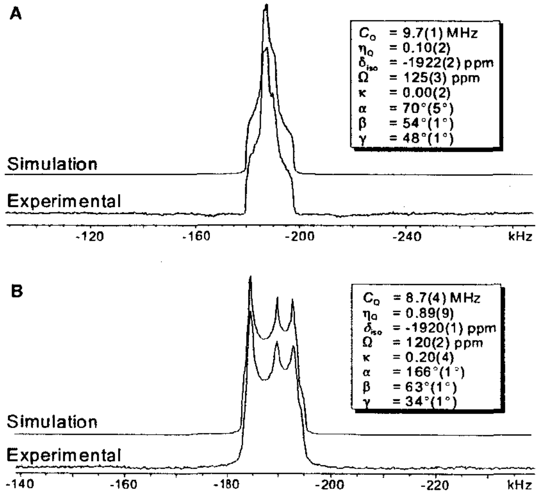

Figure B.3.1. static ^{93}Nb NMR spectra acquired at 9.4 T, along with their analytical simulation, of (A) **2** and (B) **4**. The niobium CS tensor parameters (shown in boxes) are similar to those are found in other singly substituted tetracarbonyl niobium analogues (**3** and **5**).

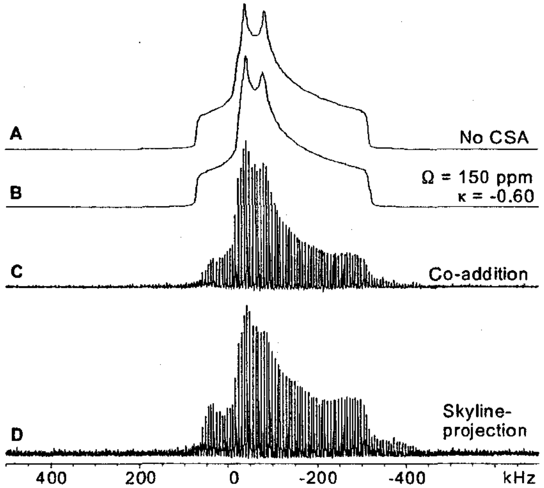

Figure B.3.2. Analytical simulations of static ^{93}Nb QCPMG NMR spectra of $CpNbCl_4$ (**6**), with (A) no and (B) small CSA contribution. (C) and (D) are experimental NMR spectra (at 9.4 T) obtained with two different spectral processings.

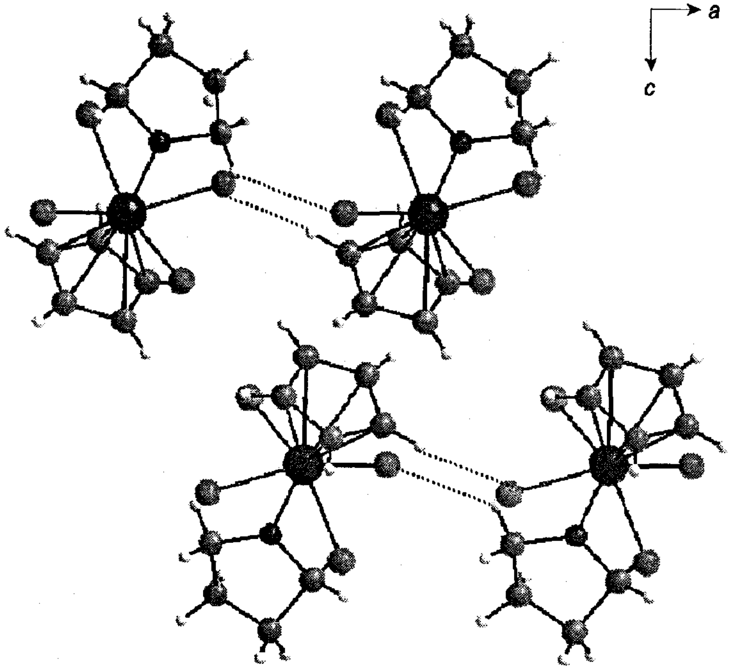

Figure B.3.3. Long-range structure in **7** reveals weak intermolecular interaction between Cl ligands and the nearest H atom on the Cp ring (dashed lines with Cl···H distance ≈ 3.0 Å).

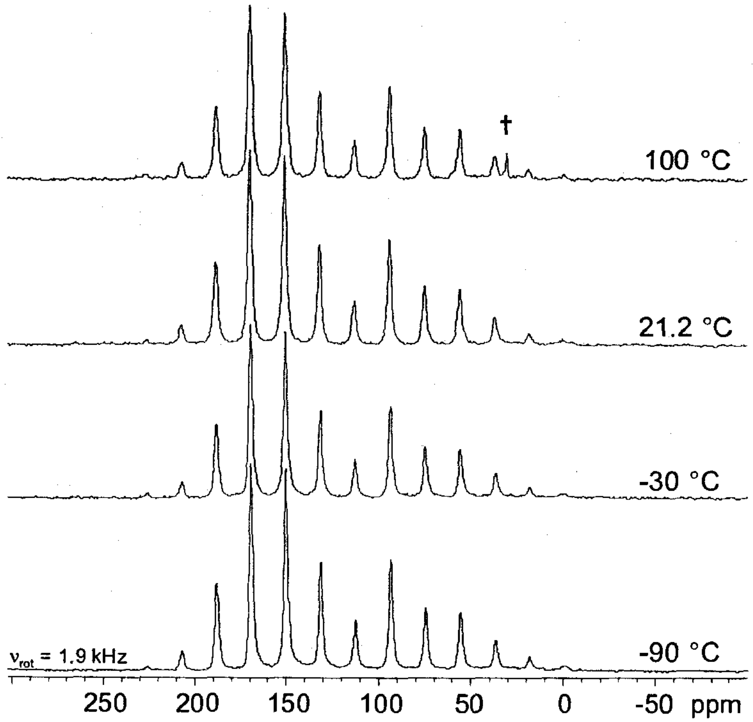

Figure B.3.4. Variable-temperature ^{13}C CP/MAS NMR spectra of **6** at 9.4 T. "†" indicates carbon NMR resonance resulted from decomposition of the air-tight parafilm cap of the NMR rotor.

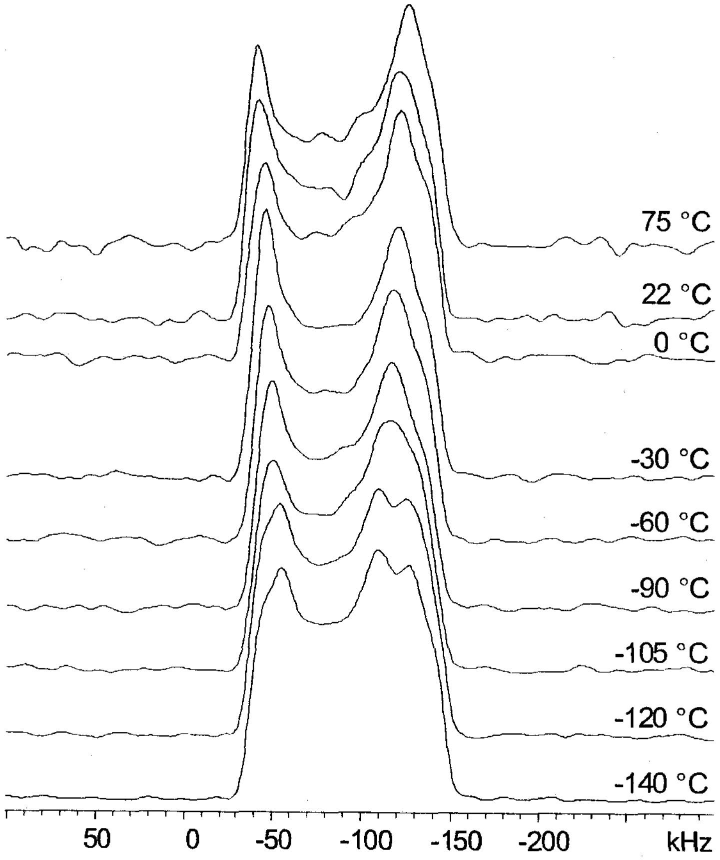

Figure B.3.5. VT static ^{93}Nb NMR spectra of **7** at 9.4 T.

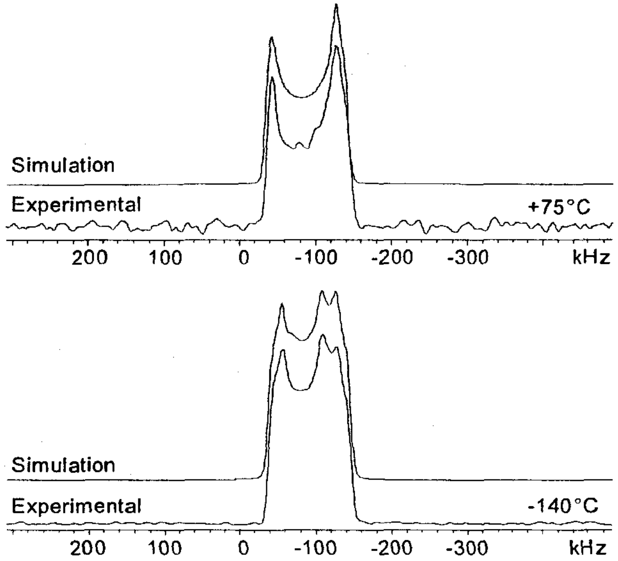

Figure B.3.6. VT static ^{93}Nb NMR spectra along with corresponding analytical simulations of **7** at 9.4 T. At 75 °C, $C_Q = 39.1(4)$ MHz, $\eta_Q = 0.10(2)$, $\delta_{iso} = -700(20)$ ppm, $\Omega = 335(35)$ ppm, $\kappa = -0.55(10)$, α, β and $\gamma = 130(20)°$, $90(3)°$ and $5(5)°$, respectively; while at -140 °C, $C_Q = 35.5(5)$ MHz, $\eta_Q = 0.23(2)$, $\delta_{iso} = -760(20)$ ppm, $\Omega = 310(30)$ ppm, $\kappa = 0.0(2)$, α, β and $\gamma = 150(10)°$, $75(4)°$ and $35(10)°$, respectively.

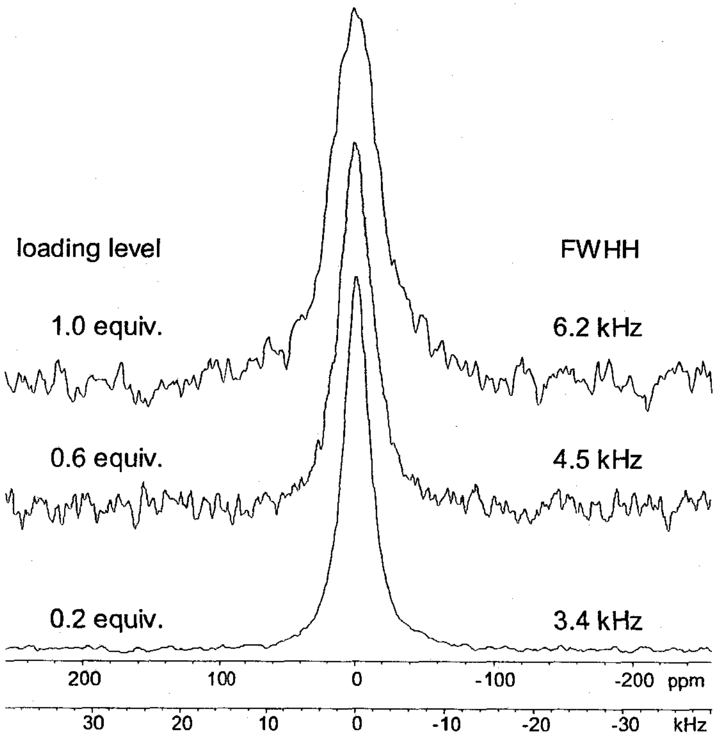

Figure B.4.1. ^{7}Li static NMR spectra of mesoporous Ti oxides loaded with various loading levels of Li-naphthalenides, along with their corresponding full width at half height (FWHH) shown on the right column. NMR spectra were acquired at 9.7 T.

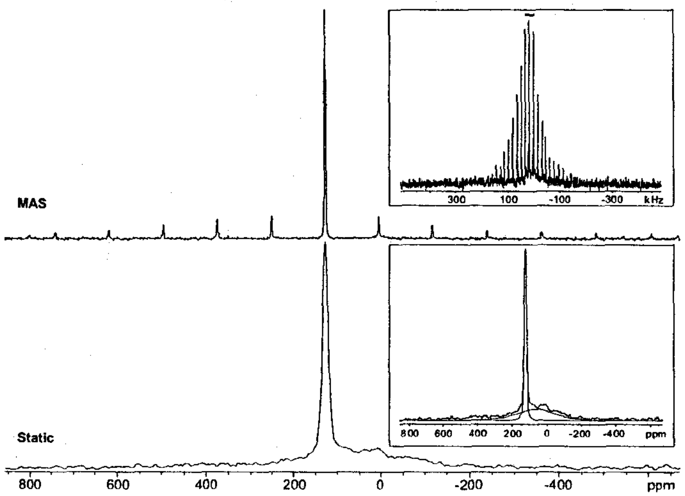

Figure B.4.2. (A) ^{87}Rb MAS and (B) static ^{87}Rb NMR spectra of mesoporous Ta oxide reduced with 0.5 equiv. Rb- naphthalenides. Insets: (top) full spectrum with vertical expansion of (A) and (bottom) deconvolution of powder patterns in (B). Sharp peak: δ_{iso} = 128 ppm, FWHH = 2.1 kHz; broad pattern: δ_{iso} = 66 ppm, FWHH = 35 kHz; relative integrated intensity of sharp to broad powder patterns = 24:31.

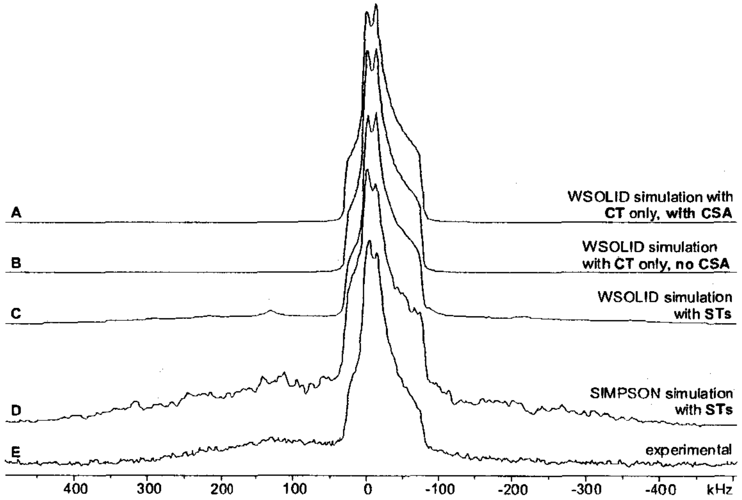

Figure B.5.1. Experimental static ^{139}La NMR spectra and spectral simulations of bulk LaF_3 at 9.4 T. In (A), La CS tensor parameters of $\Omega = 35$ ppm, $\kappa = 0.6$, $\alpha = \gamma = 0°$ and $\beta = 10°$ were employed (*ref.* 55), and no significant difference was observed when compared with (B). In (D), a CT selective $\pi/2$ pulse (with the same value as in the experimental) was utilized in the numerical simulation.

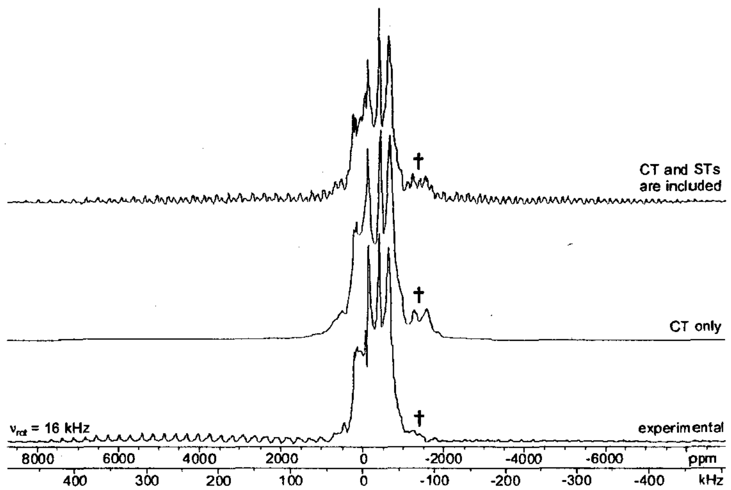

Figure B.5.2. Experimental and numerically simulated ^{139}La NMR spectra at 9.4 T of bulk LaF_3. The signal intensity of spinning sideband of CT (marked by a "†") is largely reduced by the presence of STs.

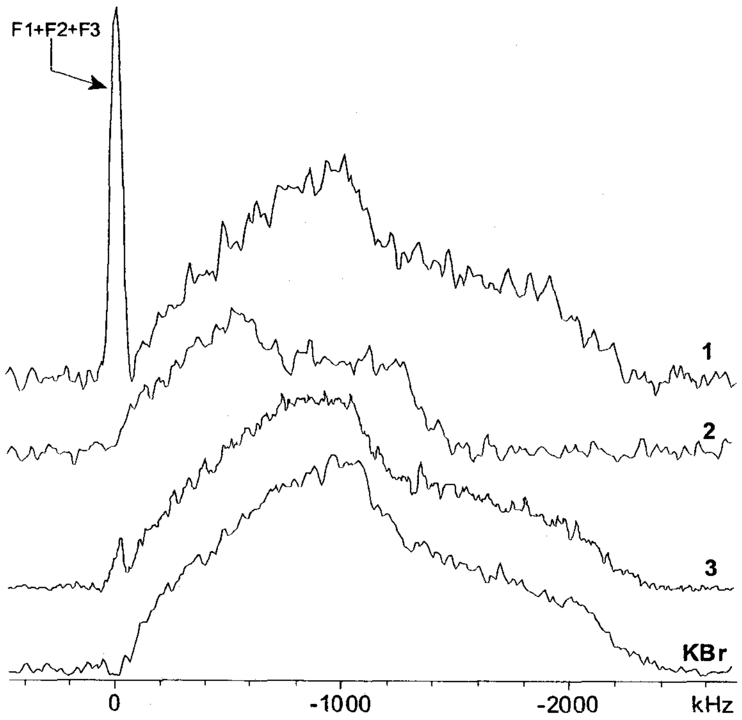

Figure B.5.3. Static ^{19}F NMR spectra of bulk LaF3 (**1**), pure LaF_3 (**2**) and 5 % Yb^{3+}–doped LaF_3 nanoparticles (**3**), and KBr sample, showing the ^{19}F NMR signal from the rotor (2.5 mm for all samples except a 4 mm zirconia rotor was used for **2**) spacers and/or the probe backgroud. All spectra were acquired with 1.0 s recycle delays.

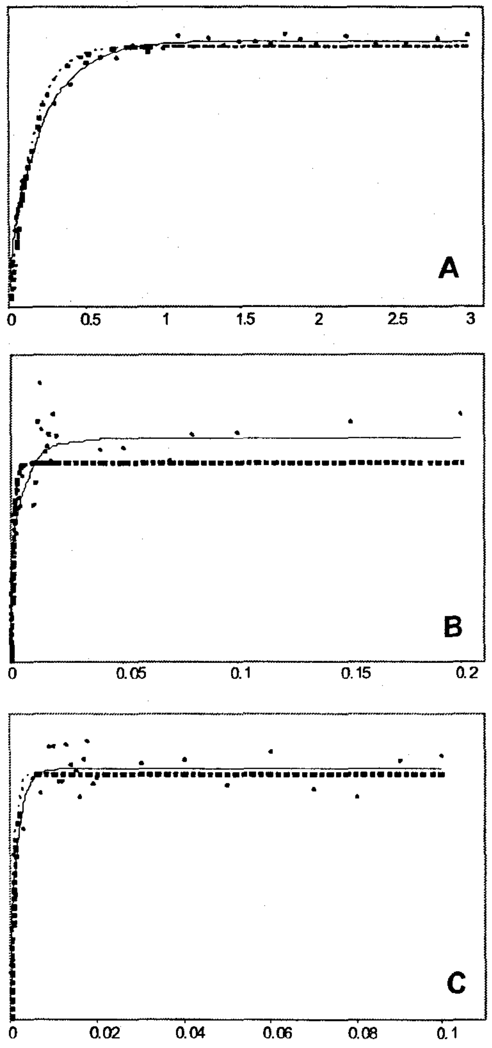

Figure B.5.4. Mono- (dashed line) and biexponential (solid line) curve fits for ^{139}La T_1 relaxation time constant in (A) bulk LaF_3, (B) pure LaF_3 and 10 % Yb^{3+}-doped LaF_3 NPs. *y*-axes: normalized intensity and *x*–axes: time in s.

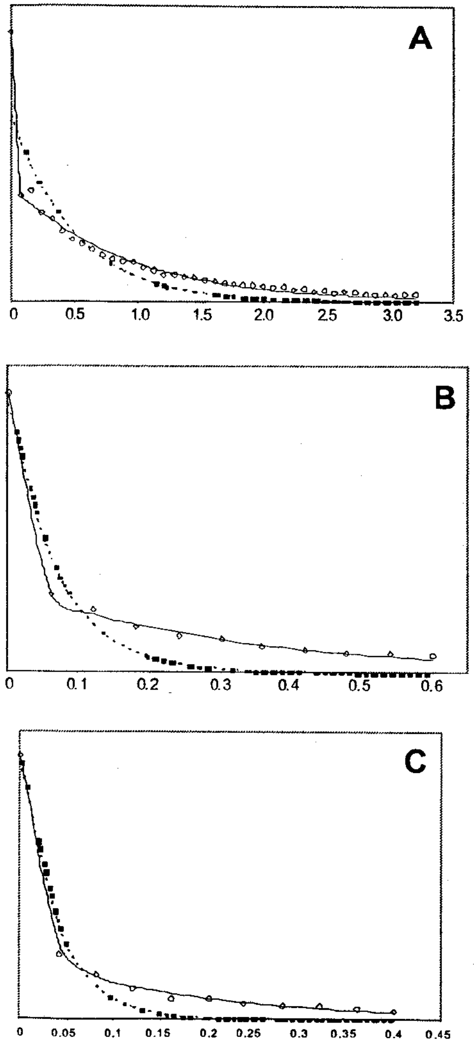

Figure B.5.5. Mono (dashed line) and biexponential (solid line) curve fits for ^{139}La T_2 relaxation time constant in (A) bulk LaF_3, (B) pure LaF_3 and 10 % Yb^{3+}–doped LaF_3 NPs. y–axes: normalized intensity and x–axes: time in s.

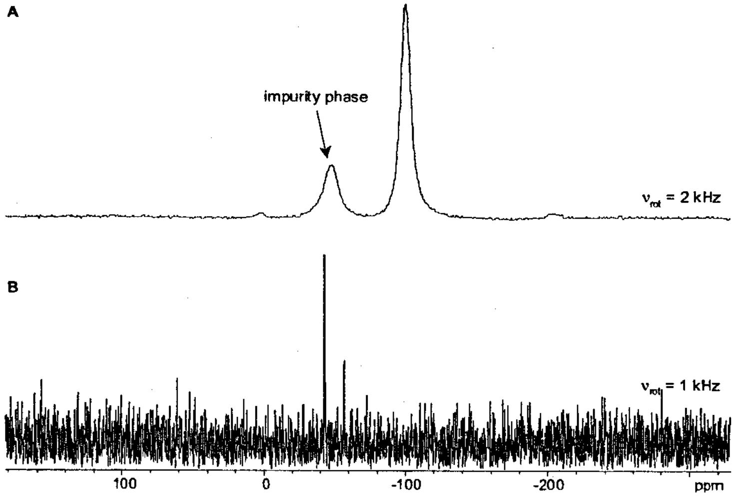

Figure B.5.6. ^{19}F–^{89}Y CP/MAS NMR spectrum of (A) bulk YF_3 and 10 % Y^{3+}–doped LaF_3 nanoparticles acquired at 9.4 T. The impurity phase may arise from hygroscopic contaminations of the moisture–sensitive YF_3 sample ($YF_3 \bullet xH_2O$).

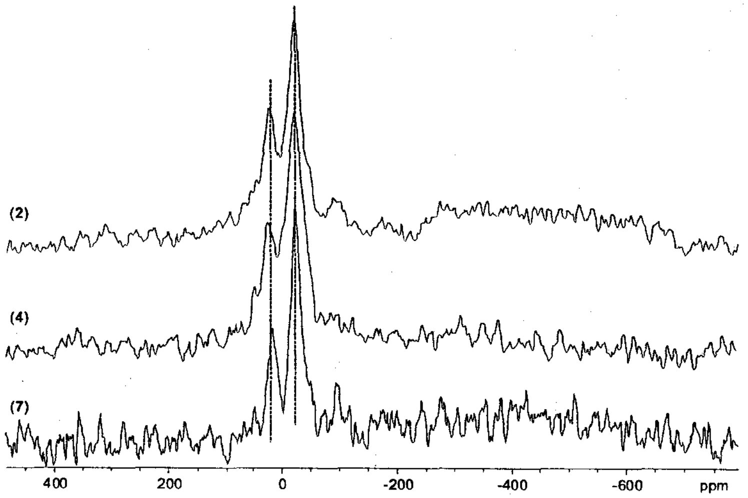

Figure B.5.7. ^{19}F MAS NMR spectra of pure (**2**), 10 % Y^{3+}–doped (**4**), and 10 % Sc^{3+}–doped (**7**) LaF_3 nanoparticles acquired at 9.4 T. All spectra exhibit similar line shape except that of **7** which experienced a lower S/N ratio.

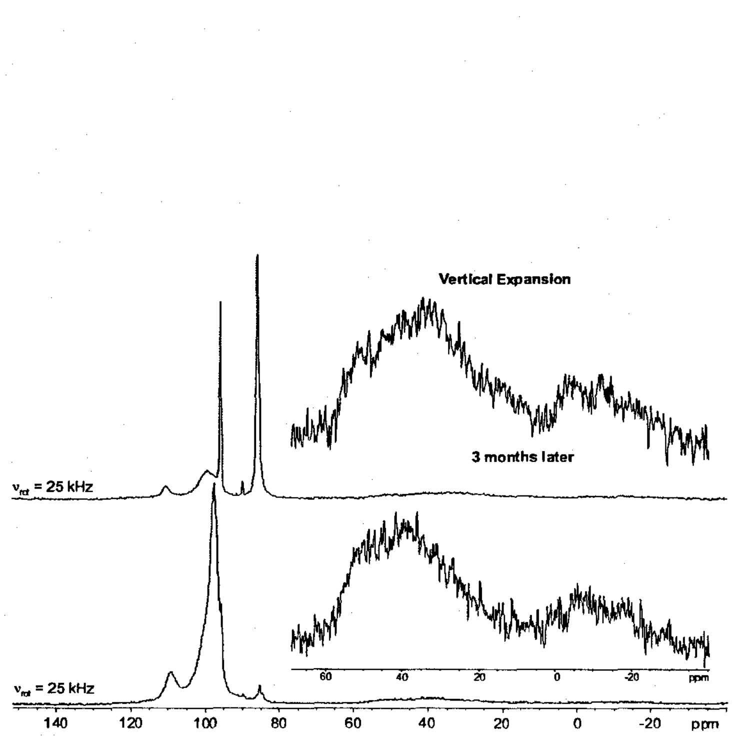

Figure B.5.8. ^{31}P MAS NMR spectra of 10 % Yb^{3+}–doped LaF_3 nanoparticles acquired at 9.4 T. Significant changes are observed in the dithiophosphate region (ca. 100 ppm), while the thiophosphate and the phosphate regions (vertical expansion) are relatively stable. An estimation to the ratio of integrated area of dithiophosphate powder pattern to the unidentified peak to the combination of thiophosphate and phosphate resonances before and after the three months period is 1.00:0.06:0.25 and 1.00:0.95:1.21, respectively, indicating that most of the ^{31}P signals in originally from the dithiophosphate powder pattern are redistributed into the unidentified peak as well as both thiophosphate and phosphate resonances.

Vita Auctoris

Andy Yu Ho Lo was born on November 24th, 1976 in Kowloon, Hong Kong. He completed his secondary school at Ying Wa College, Hong Kong in 1994. In 1995, he immigrated to Canada. He spent two years to complete the grade-12 and OAC levels and graduated from Assumption College School, Windsor, Ontario in 1997. From there he went on to the University of Windsor where he obtained a Bachelor of Science (B.Sc.) degree in Chemical Physics in 2001. He is currently a candidate for the Philosophiae Doctor (Ph.D.) in Chemistry at the University of Windsor, and expecting his graduation in the summer of 2007.